Channel Characterization and Modeling for Future Wireless Communication Systems

Zhang, Guojin

DOI (link to publication from Publisher):
10.54337/aau561771065

Publication date:
2023

Document Version
Publisher's PDF, also known as Version of record

CHANNEL CHARACTERIZATION AND MODELING FOR FUTURE WIRELESS COMMUNICATION SYSTEMS

BY
GUOJIN ZHANG

DISSERTATION SUBMITTED 2023

AALBORG UNIVERSITY
DENMARK

Channel Characterization and Modeling for Future Wireless Communication Systems

Ph.D. Dissertation

Guojin Zhang

Dissertation submitted May, 2023

Dissertation submitted: May, 2023

PhD supervisor: Prof. Gert Frølund Pedersen
Aalborg University

Assistant PhD supervisors: Assoc. Prof. Jesper Ødum Nielsen
Aalborg University

Asst. Prof. Xuesong Cai
Lund University

PhD committee: Associate Professor Jan Dimon Bendtsen (chairman)
Aalborg University, Denmark

Professor Luis M. Correia
University of Lisbon, Portugal

Professor Joseph Wout
Ghent University, Belgium

PhD Series: Technical Faculty of IT and Design, Aalborg University

Department: Department of Electronic Systems

ISSN (online): 2446-1628
ISBN (online): 978-87-7573-708-6

Published by:
Aalborg University Press
Kroghstræde 3
DK – 9220 Aalborg Ø
Phone: +45 99407140
aauf@forlag.aau.dk
forlag.aau.dk

Printed in Denmark by Stibo Complete, 2023

Curriculum Vitae

Guojin Zhang

Guojin Zhang received her B.S. in Information Engineering from the China University of Mining and Technology, China, in 2013. She received her M.S. in Information and Communication Engineering from China University of Petroleum (East China), China, in 2016. Since then, she had been a Network Engineer at Ericsson Communications, China. In 2018 she was employed as a Guest Researcher in the section of Antennas Propagation and Millimeter-wave Systems (APMS) at Aalborg University, Denmark. Since 2019, she has been employed as a Ph.D. student in the same section. In 2022 she visited the Department of Electrical and Information Technology at Lund University, Sweden, as a Visiting Researcher. Her research interests include channel measurement, parameter estimation, and channel modeling for 5G and beyond communication systems.

Abstract

Because of the shortage of spectrum at the sub-6 GHz frequency bands, the millimeter wave (mm-wave) has become a popular choice for the fifth generation (5G) and beyond wireless systems. Despite offering high-speed data transfer, mm-wave signals also have the disadvantage of significant attenuation and blockage caused by atmospheric absorption, reflection, diffraction, and scattering. Consequently, this results in poor signal quality and unreliable communication. However, ultra-massive multiple-input multiple-output (UM-MIMO) technology can provide high directional beams to overcome the shortage of mm-wave frequency signals. Due to its ability to offer high-speed and reliable communication systems in the mm-wave frequency bands, UM-MIMO technology is crucial for the advancement of future wireless communication systems. As a result, it is crucial to perform measurement-based investigations to accurately characterize and model the UM-MIMO channel at mm-wave frequency bands in different scenarios. This is necessary for evaluating system performance and designing effective communication systems. In this thesis, measurement campaigns were conducted using two vector network analyzer (VNA)-based channel sounders, i.e., coaxial-cable-based and fiber-optic-based channel sounders, both equipped with a large-scale uniform circular array (UCA) to investigate the spatial channel characteristics. Because of the high power loss of the coaxial cables, the coaxial-cable-based channel sounder is limited to short-range indoor scenarios in Paper [A-C], with the same height of the transmitter (Tx) and receiver (Rx) antennas to simulate device-to-device (D2D) wireless communication. The fiber-optic-based channel sounder was utilized for long-range measurement campaigns in [D] and [E], with the Rx antenna set as 18 m and 3 m to simulate the base station-to-device (B2D) wireless communication in outdoor and indoor scenarios, respectively.

In Paper [A-E], a high-resolution parameter estimation (HRPE) algorithm was applied to estimate the propagation parameters, i.e., complex amplitude, delay, direction (azimuth and elevation) of departure or arrival, the distance between the antenna array and the first-hop or last-hop scatterers, of the multipath components (MPCs) under the spherical wavefront assumption. Paper [A] investigates the channel characteristics based on the measurement campaigns

conducted in the classroom, office, and hall scenarios at the frequency bands of 27-29 GHz. The study also investigates the effects of furniture density and indoor layout on the propagation channel. Paper [D] explores the cluster-level channel characteristics obtained in an outdoor scenario at the frequency band of 28-30 GHz. To constitute a geometry-based stochastic channel model (GSCM), a novel clustering algorithm is proposed to group the MPCs according to their physical objects using 3-D Ray Tracing simulations. Additionally, the study explores the power contributions of clusters that experience multiple bounces from each IOs. It is worth noting that in the NLoS scenario, clusters may experience up to 7 bounces. Paper [E] investigates the characteristics of the propagation channel using measurements conducted from an indoor hall to an indoor corridor within the 28-30 GHz frequency band. A novel algorithm is proposed to identify and track dynamic clusters. Their composite and cluster-level characteristics and dynamic behaviors are analyzed to constitute a dynamic model.

Moreover, as the channel characteristics at mm-wave frequencies exhibit significant differences from those at sub-6 GHz, it is crucial to study the frequency dependence of channel characteristics. Paper [B] compares the channel characteristics obtained in a hall scenario at 9-11 GHz and 27-29 GHz frequencies. Similarly, Paper [C] compares the channel characteristics obtained in a classroom and a hall scenario at 2-4, 9-11 and 27-29 GHz frequencies. A novel clustering algorithm is proposed to group the MPCs into clusters across multiple frequency bands.

To constitute a GSCM for the UM-MIMO channel, a novel scatterer localization algorithm is proposed in Paper [F], which can be further used to group the MPCs into clusters according to the estimated locations of the scatterers. Previously, the locations of scatterers were estimated using the estimated angular information and distances, i.e., the distances from the array to the scatterers, under the spherical wavefront assumption. However, searching the extra parameter of distance based on the entire array can result in high computational complexities. To decrease the complexity, the novel scatterer localization algorithm only utilized the estimated angular information obtained from each sub-array, which is divided from the large-scale antenna array. The algorithm was verified through simulation and applied to an indoor measurement carried out in a hall scenario at 27-29 GHz.

Resumé

Millimeterbølger (mm-bølger) er blevet brugt i vid udstrækning til femte generation (5G) og senere trådløse systemer på grund af knapheden på spektrum på sub-6 GHz frekvensbåndene. Mm-bølge signaler kan give høj hastighed til at overføre data, men har også ulemper som betydelig dæmpning og blokering på grund af atmosfærisk absorption, refleksion, diffraktion og spredning, hvilket kan resultere i dårlig signalkvalitet og upålidelig kommunikation. Imidlertid kan ultramassiv multiple-input multiple-output (UM-MIMO) teknologi give meget retningsbestemte stråler som kan modvirke begrænsningerne ved mm-bølge signaler. På grund af evnen til at levere højhastigheds- og pålidelige kommunikationssystemer i mm-bølge frekvensbåndene, spiller UM-MIMO teknologi en nøglerolle i udviklingen af fremtidige trådløse kommunikationssystemer. Derfor er målebaserede undersøgelser afgørende for systemdesign og ydeevneevaluering, samt for realistisk karakterisering og modellering af UM-MIMO-kanalen ved mm-bølgebånd i forskellige scenarier. I dette afhandling blev målekampagnerne udført med vektornetværksanalysator (VNA)-baserede kanal-soundere, dvs. koaksialkabel-baserede og fiberoptik-baserede kanal-soundere, begge udstyret med et stort *uniform circular array (UCA)* for at undersøge de rumlige kanalkarakteristika af kanalen. På grund af koaksialkablernes høje effekttab, kan den koaksialkabelbaserede sounder kun bruges til de indendørsscenarier med korte afstande som behandles i artiklerne [A-C], med samme højde på sender- (Tx) og modtager- (Rx) antenner for at simulere enhed-til-enhed (D2D) trådløs kommunikation. Den fiberoptik-baserede sounder blev brugt til målekampagnerne med store afstande i artiklerne [D] og [E], med Rx-antennen indstillet til 18 m og 3 m for at simulere basestation-til-enhed (B2D) trådløs kommunikation i henholdsvis udendørs og indendørs scenarier.

I artiklerne [A-E] blev der anvendt en *high-resolution parameter estimation (HRPE)* algoritme til at estimere udbredelsesparametrene for *multipath components (MPC)* under antagelse af sfærisk bølgeudbredelse, dvs. kompleks amplitude, forsinkelse, retning (azimut og elevation) af både afsendelse og ankomst, afstanden mellem antennearrayet og objektet i kanalen for første hop eller sidste hop. Artiklen [A] undersøger kanalens karakteristika baseret på målekampagner udført i et klasseværelse, et kontor og en hall ved frekvens-

båndene 27-29 GHz. Indvirkningen af mængden af møbler og den indendørs geometri på udbredelseskanalen undersøges og sammenlignes. Artiklen [D] undersøger kanalkarakteristika på klyngeniveau opnået i et udendørs scenarie ved frekvensbåndet 28-30 GHz. For at opstille en geometribaseret stokastisk kanalmodel (GSCM) foreslås en geometribaseret klyngealgoritme til at gruppere MPC'erne baseret på fysiske interaktionsobjekter (IO'er) ved at bruge Ray Tracing 3-D-simuleringer. Desuden undersøges bidragene af effekt fra klyngerne med flere hop fra hver IO. Det maksimale antal af hop er op til 7 i NLoS-scenariet. Artiklen [E] undersøger kanalens karakteristika baseret på målekampagnen udført fra en indendørs hall til en indendørs korridor i frekvensbåndet 28-30 GHz. En ny klyngeidentifikations- og sporingsalgoritme foreslås til at spore dynamiske klynger. Med henblik på at opstille en dynamisk model undersøges sammensatte kanalkarakteristika, klyngeniveauparametre og klyngers dynamiske adfærd.

Da kanalkarakteristikkerne ved mm-bølger adskiller sig fra dem ved sub-6 GHz frekvenser, er det desuden nødvendigt at undersøge frekvensafhængigheden af kanalkarakteristiske parametre. Artiklen [B] sammenligner kanalkarakteristika opnået i et hall-scenarie ved frekvensbåndene 9-11 GHz og 27-29 GHz. Artiklen [C] sammenligner kanalkarakteristika opnået i klasseværelse og hall scenarier ved frekvensbåndene 2-4, 9-11 og 27-29 GHz. En ny klyngeidentifikationsalgoritme baseret på KPowerMeans-algoritmen foreslås til at gruppere de estimerede MPC'er i klynger på flere frekvensbånd.

Med henblik på at opstille en GSCM for UM-MIMO-kanalen foreslås en ny scatterer-lokaliseringsalgoritme i artiklen [F], som yderligere kan bruges til at gruppere MPC'erne i klynger baseret på de estimerede placeringer af scatterne. Tidligere blev placeringerne af scatterers estimeret ved hjælp af den estimerede vinkelinformation og afstande, dvs. afstandene fra arrayet til scattererne, under en sfærisk bølgefrontantagelse. Det fører dog til en høj beregningkompleksitet med det store array. For at mindske kompleksiteten er det store antennearray opdelt i flere subarrays, så den såkaldte *space-alternating generalized expectation-maximization (SAGE)* algoritme kan anvendes under antagelse af plane bølgefronter. Ud fra den estimerede vinkelinformation fra hver sub-array kan placeringen af tilsvarende scatterere opnås. Den foreslåede algoritme verificeres i en simulering af et stort array og anvendes på data fra en indendørs målekampagne udført i et hallscenarie ved 27-29 GHz.

Contents

Thesis Details

Thesis Title:	Channel Characterization and Modeling for Future Wireless Communication Systems
Ph.D. Student:	Guojin Zhang
Supervisors:	Prof. Gert Frølund Pedersen, Aalborg University Assoc. Prof. Jesper Ødum Nielsen, Aalborg University Asst. Prof. Xuesong Cai, Lund University

This thesis is submitted as partial fulfilment of the requirements for the degree of Doctor of Philosophy (PhD) from Aalborg University, Denmark. The thesis is structured as a collection of papers with the main part of the thesis being scientific papers published in, or submitted to, peer-reviewed journals and conferences. The thesis is a result of four years of research, in the period February 2018-October 2022, as a PhD student in the Section of Antennas, Propagation and Millimetre-wave Systems (APMS), Department of Electronic Systems, Aalborg University.

The papers included in this thesis are:

[A] Guojin Zhang, Kentaro Saito, Wei Fan, Xuesong Cai, Panawit Hanpinitsak, Jun-ichi Takada, and Gert F. Pedersen, "Experimental Characterization of Millimeter-wave Indoor Propagation Channels at 28 GHz," *IEEE Access*, vol.6, pp. 76516–76526, 2018.

[B] Guojin Zhang, Panawit Hanpinitsak, Xuesong Cai, Wei Fan, Kentaro Saito, Jun-ichi Takada, and Gert F. Pedersen, "Millimeter-Wave Channel Characterization in Large Hall Scenario at the 10 and 28 GHz Bands," *13th European Conference on Antennas and Propagation (EuCAP)*, 2019.

[C] Guojin Zhang, Jesper Ø. Nielsen, Xuesong Cai, Saito Kentaro, Panawit Hanpinitsak, Jun-ichi Takada, Gert F. Pedersen, and Wei Fan, "Modeling Multi-frequency Characteristics for Classroom and Hall Scenarios at 2-4, 9-11 and 27-29 GHz Bands," *IEEE Access*, vol. 9, pp. 14549–14563, 2021.

[D] Guojin Zhang, Jesper Ø. Nielsen, Xuesong Cai, Gert F. Pedersen, and

Wei Fan, "Geometry-Based Clustering Characteristics for Outdoor Measurements at 28-30 GHz," *IEEE Antennas and Wireless Propagation Letters*, vol. 21, no. 9, pp. 1797-1801, Sept. 2022.

[E] Xuesong Cai, Guojin Zhang, Chao Zhang, Wei Fan, Jinxing Li, and Gert F. Pedersen, "Dynamic Channel Modeling for Indoor Millimeter-Wave Propagation Channels Based on Measurements," *IEEE Transactions on Communications*, vol. 68, no.9, pp. 5878–5891, 2020.

[F] Guojin Zhang, Xuesong Cai, Jesper Ø. Nielsen, Gert F. Pedersen, and Fredrik Tufvesson, "A Scatterer Localization Method Using Large-Scale Antenna Array Systems," *IEEE Conference on Antenna Measurement and Applications (CAMA)*, 2022.

According to the Ministerial Order no. 1039 of August 27, 2013, regarding the PhD Degree § 12, article 4, statements from each co-author about the PhD students contribution to the above-listed papers have been provided to the PhD school for approval prior to the submission of this thesis. These co-author statements have also been presented to the PhD committee and included as a part of their assessment.

In addition to the listed papers as the main content of this thesis, the following paper was also authored during the PhD studies. As this paper is not a part of the main body of this thesis it has not been included in print. The reader is therefore kindly referred to the publishing channel as listed hereafter.

[1] Guojin Zhang, Xuesong Cai, Wei Fan, and Gert F. Pedersen, "A USRP-based Channel Sounder for UAV Communications," *14th European Conference on Antennas and Propagation (EuCAP)*, 2020.

Preface

The past four years of my PhD program have been an incredible journey filled with challenges, discoveries, and personal growth. During this time, I not only gained expertise in wireless communication and developed my research abilities, but I also gained the role of a mother. My journey began when I joined the Antenna Propagation and Millimeter-wave Systems (APMS) section as a guest researcher, and after a year, I decided to pursue a PhD in the same field. I am profoundly grateful to all those who have supported, encouraged and stood by me throughout this journey.

I would like to express my heartfelt appreciation to Professor Gert Frølund Pedersen, my supervisor, for granting me the opportunity to pursue my studies in this section. I am truly grateful for the inspiring encouragement and unwavering support that he provided me during my PhD journey. I would also like to extend my sincere gratitude to Associate Professor Jesper Ødum Nielsen, my co-supervisor, for his professionalism, kindness, and patient guidance throughout this period. Jesper's erudition, enthusiasm, and engaging discussions motivated me to complete my PhD, and I firmly believe that the knowledge I gained from him will benefit my academic career and my life as a whole. Further, I would like to express my deepest gratitude to my co-supervisor, Assistant Professor Xuesong Cai, for his guidance and support since I began as a guest researcher and throughout my PhD journey. Additionally, I would like to extend my thanks to Professor Fredrik Tufvesson for providing me with the opportunity to visit Lund University and for his support of my research.

Finally, I would like to acknowledge the love and support of my family and friends. Especially my husband, who has been a constant source of encouragement and inspiration throughout this journey. His constant support has allowed me to pursue my academic goals while also fulfilling my responsibilities as a mother. I would like to extend my sincere appreciation to my son Max for his good sleep and strong physique, which enabled me to devote uninterrupted time to complete my PhD. In addition, I would like to express my gratitude to my friend Yilin Ji, who provided extensive support to me in my research, despite not being named as a co-author in my papers.

Guojin Zhang

Aalborg University, May 8, 2023

Part I

Introduction

1 Mm-wave Channel

Wireless communication technologies have become an integral part of our daily lives and find extensive usage in diverse applications such as mobile communication, GPS, Bluetooth, Wi-Fi, and satellite communication. However, with the proliferation of user devices and applications, the need for higher data rates and additional bandwidth is on the rise. Because of the spectrum scarcity at the sub-6 GHz frequency bands, the millimeter wave (mm-wave) bands were introduced for the fifth-generation (5G) and beyond communication systems [1–3]. The mm-wave systems are expected to offer higher data transfer speeds and larger system capacity [1, 4]. However, the channel characteristics of mm-wave bands differ from lower frequency bands. Compared with lower frequencies, the mm-wave transmission suffers more significant air attenuation and more significant shadowing due to the obstacle [5]. Moreover, it is found that the reflection is more dominant than diffraction and diffuse scattering at mm-wave bands [5–7]. Therefore, due to these channel characteristics, highly directional antennas, large antenna arrays, and adaptive beamforming techniques are required for mm-wave wireless systems [8]. Therefore, to facilitate the development of mm-wave systems, it is necessary to investigate the channel propagation characteristics in different scenarios at mm-wave bands and compare the mm-wave channel characteristics with lower frequency bands channel [6].

In addition, the small wavelength of mm-wave makes it possible to pack a large number of antennas in a small area to form a large-scale antenna array, which has gained considerable interest in both academia and industry for the 5G and beyond communication systems [9]. For example, the massive multiple-input-multiple-output (MIMO) with beamforming techniques are applied to provide the high-gain beams to compensate for the high attenuation at mm-wave bands [10]. Therefore, with the channel characteristics of mm-wave mentioned above, the mm-wave communication systems are planned to be utilized for various applications, such as short-range wireless networks, on-body wireless devices, inter-chip communication, and high-precision localization systems.

1.1 Channel Sounding

The channel characteristics at mm-wave have been investigated extensively based on measurement campaigns in both indoor and outdoor scenarios for frequencies up to 100 GHz [11]. The channel sounders used in the measurement campaigns are either based on time-domain or frequency-domain techniques [12]. For the time-domain-based systems, the channel impulse response (CIR) is obtained by the correlation between the transmitted and received pseudorandom noise (PN) sequence signals, which are also known as correlation-based channel sounders [12]. For example, the Universal Software-defined Radio Peripheral (USRP) based channel sounder is a kind of correlation-based channel sounder, which was widely used for UAV communication systems, due

to its light weight [13, 14]. For the frequency domain channel sounders, the CIR is obtained by an inverse discrete Fourier transform (IDFT) of the measured channel transfer functions (CTFs), with the frequency points swept over the interesting bands [10]. However, the channel must be kept static, while the frequency points are swept. Therefore, due to its ease of calibration, low cost, and the ability to sweep over a large bandwidth, vector network analyzer (VNA)-based channel sounders are widely used in static channel measurements [12, 15]. Moreover, a cable connection between the transmitter (Tx) and the receiver (Rx) is required for antenna control and phase synchronization. Since the power attenuation of the coaxial cable increases, as the length and frequency increase, the measurement distance range is limited at mm-wave frequencies. Therefore, the coaxial-cable-based VNA channel sounders are mainly used in short-range deployment scenarios, such as indoor scenarios [16, 17]. In this thesis, a coaxial-cable-based channel sounder is applied in Paper [A-C] with Tx and Rx antennas set as the same height of 1.5 m, to investigate the device-to-device (D2D) wireless communication. To increase the VNA measurement range, a fiber-optic-based VNA channel sounder is utilized for long-range measurement campaigns in both indoor and outdoor scenarios [12]. A phase compensation scheme was used to compensate for the phase changes caused by the thermal and mechanical stress in the optic cables [12]. The fiber-optic-based channel sounder is applied in Paper [D] with Rx antenna fixed on the roof of the building and Paper [E] with Rx antenna set as 3 m above the ground, to investigate the base station-to-device (B2D) wireless communication in outdoor and indoor scenarios, respectively.

Moreover, to investigate the channel characteristics in space, rotated directional antenna-based and uniform virtual array (UVA)-based measurement systems are widely used [7]. The former method is to steer a highly directional antenna, e.g., a horn antenna, to scan each angular direction. However, the antenna pattern is embedded and the spatial resolution is limited by the narrow beamwidth of the antenna [10, 16]. On the other hand, the latter UVA-based method uses an antenna that is moved to form uniform virtual arrays, such as a uniform linear array (ULA), a uniform rectangular array (URA), and a uniform circular array (UCA). The space between each element of the UVA is less than a half wavelength to avoid spatial aliasing effects [16, 18]. However, the ULA cannot resolve symmetrical angles with respect to the array line [16]. Therefore, to investigate the spatial channel characteristics, UCA is utilized in this thesis, due to its uniform beam pattern around the azimuth plane.

1.2 Measurement Campaigns

In this thesis, with the channel sounders mentioned above, the measurement campaigns were mainly conducted at 28 GHz, which was one of the main candidates for the 5G systems with extensive research in this band. Besides, 28 GHz was applied into use for 5G systems by the US Federal Communications Com-

mission (FCC) [6]. Two kinds of VNA-based UCA channel sounders were used in the measurement campaigns, e.g., a coaxial-cable-based in Paper [A-C] and a fiber-optic-based channel sounder in Paper [D] and Paper [E].

1.2.1 Coaxial-cable-based channel sounder

In order to simulate D2D communication for 5G, both Tx and Rx antennas were placed at a height of 1.5 m. Two types of biconical antennas were used: a commercially available SZ−2003000/P [19] and a homemade antenna [20]. These antennas are omnidirectional in the horizontal plane and narrow beamwidth in the elevation plane [5]. The SZ−2003000/P and the homemade antenna have an elevation half-power-beamwidth (HPBW) of less than 30° and between 30°-65° over the covered bands, respectively. The Rx antenna was rotated clockwise to create a UCA with $M = 360$ elements and a pre-set radius r of 0.24 m. To avoid angular aliasing, the UCA elements were positioned with a spacing of 4.2 mm, which is below half the wavelength at 28 GHz [10]. The VNA swept over N =750 frequency points across three frequency bands: 2-4, 9-11, and 27-29 GHz [21].

R1-Classroom The experiment was conducted in a classroom measuring $8.54\times6.70\times2.71$ m^3, with measurements taken at the 2-4, 9-11, and 27-29 GHz frequency bands. The classroom contained several tables that were 0.74 m in height and lower than the Tx and Rx antennas. Fig. 1 shows that the Rx antenna was positioned at the front of the classroom, while the Tx antenna was moved to 20 different positions along the tables with a spacing of 0.8 m.

R2-Hall Measurements in an irregular hall scenario at 2-4, 9-11 and 27-29 GHz bands were also conducted. The dimension of the hall is approximately $39\times20\times10$ m^3. As illustrated in Fig. 2, the Rx antenna was positioned close to four ventilation tubes, which are indicated by yellow circles. Meanwhile, the Tx antenna was placed at 20 different positions that were 1 m apart. There are six pillars made of concrete located around the Tx positions. The stairs and a big table are located in the southeast part of the hall scenario.

R3-Classroom The measurements in a classroom, similar in size to R1-Classroom, but with a different tables layout (marked with the number "No."), are depicted in Fig. 3. The Rx antenna was placed at the center of the classroom and the Tx antenna was located in the northwest corner. The measurements were conducted in 11 steps, as indicated in Table 1. In each step, the tables were gradually moved outside or inside the classroom. At steps No.1 and No.10 all the tables are in the classroom, and at steps No.4 and No.7 the classroom is totally empty. At step No.11, the classroom is empty, and the curtains on the windows (marked as blind part) and a shelf were removed.

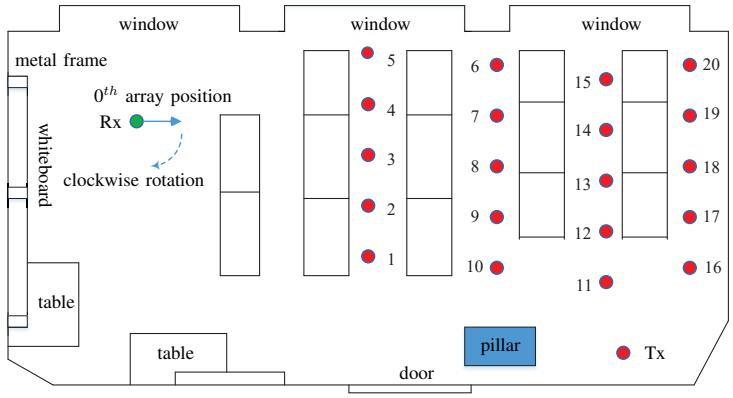

(a)

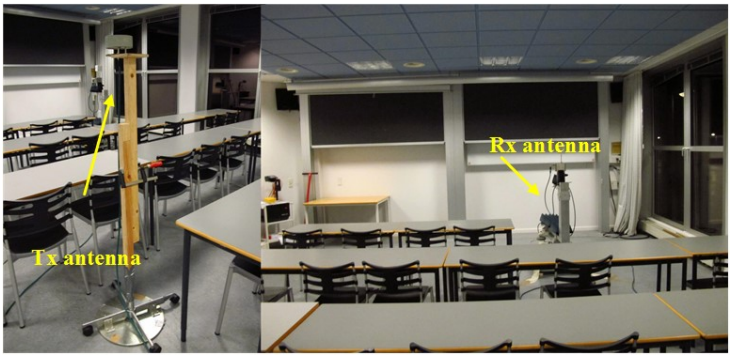

(b)

Fig. 1: (a) The layout of R1-Classroom with 20 Tx locations. (b) A photograph of Tx and Rx antennas. [3]

R4-Office As shown in Fig. 4, the dimension of R4-Office is 3.44×4.78×2.85 m^3. Similar to the measurement campaign in the R3-Classroom, the measurements in the R4-Office were started with from step No.1 with the shelves fully loaded with books, as shown in Fig. 4(b), and ended with a totally empty office in step No.11, as shown in Fig. 5(b). From step No.2 to No.6, the books were removed from the office step by step, and the shelves were removed from steps No.7 to No.11.

1.2.2 Fiber-optic-based channel sounder

To overcome the disadvantage of the coaxial-cable-based channel sounder, a fiber-optic-based channel sounder was applied in Paper [D] and [E] for long distance measurement in both outdoor and indoor scenarios [12]. The measurements were conducted at 28-30 GHz, with $N = 2000$ frequency points swept

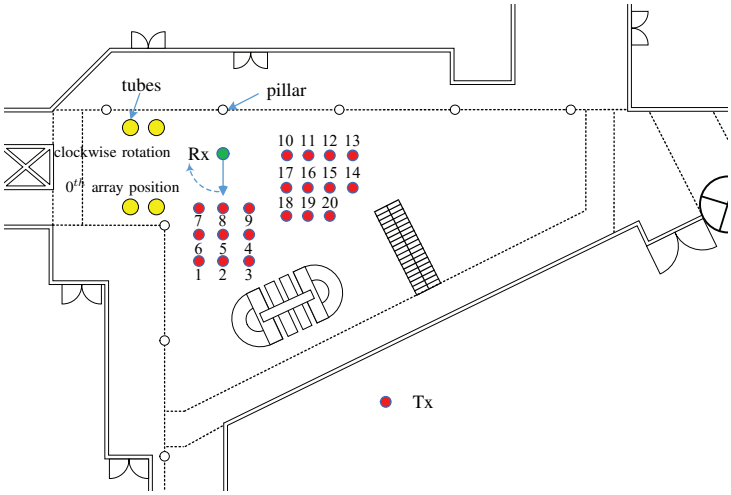

(a)

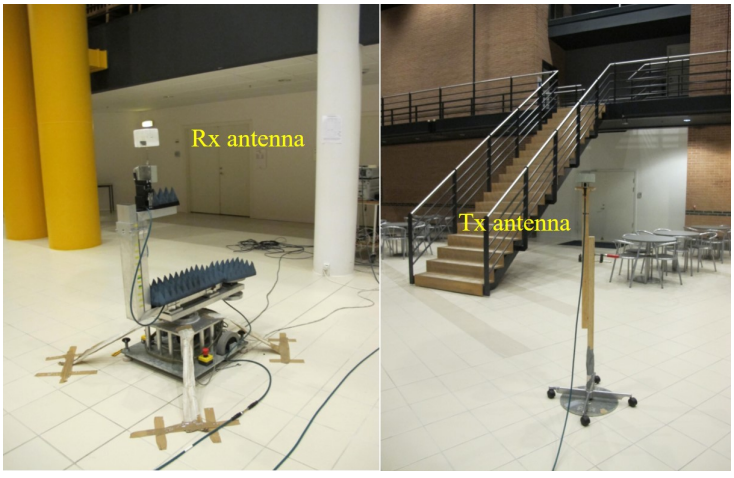

(b)

Fig. 2: (a) The layout of R2-Hall with 20 Tx locations. (b) The photograph of Tx and Rx antennas. [3]

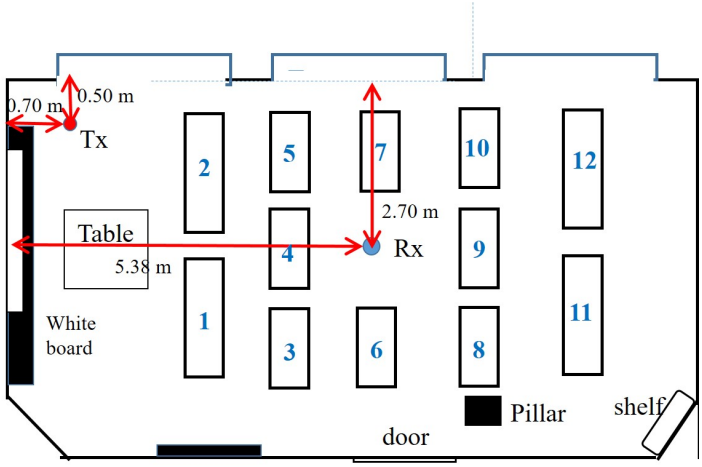

(a)

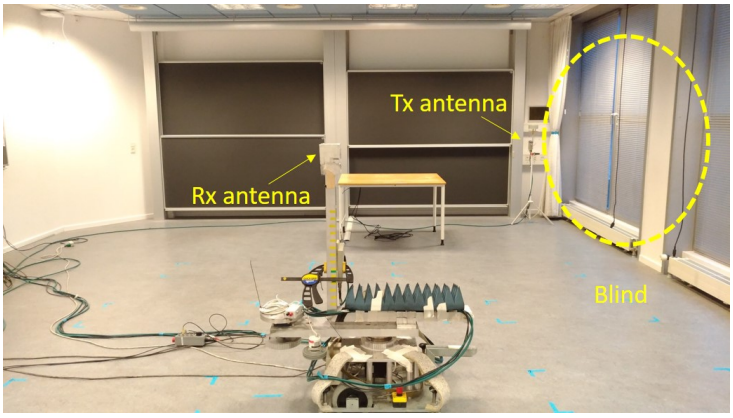

(b)

Fig. 3: (a) The layout of R3-Classroom. (b) The photograph of the empty classroom with Tx and Rx antennas. [3]

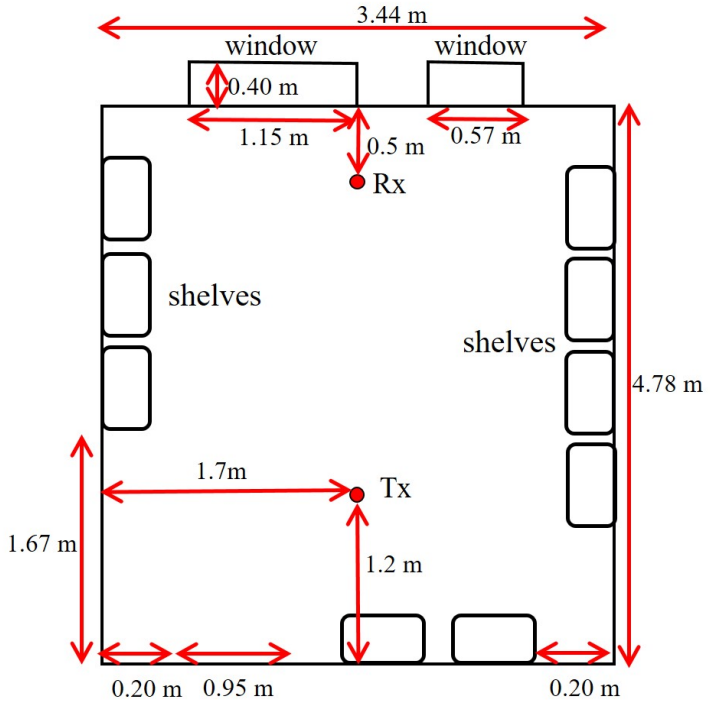

(a)

(b)

Fig. 4: (a) The layout of R4-Office. (b) The photograph of R4-Office full of books on the shelves. [3]

(a)

(b)

Fig. 5: (a) The photograph of R4-Office with only shelves on the walls and the Rx antenna. (b) The photograph of totally empty R4-Office and the Tx antenna. [3]

Table 1: Measurement procedure.

Steps	Measurement Procedure
1	Full classroom with 12 tables as shown in Fig. 3(a)
2	Remove the tables No.1, 2, 11, 12
3	Remove the tables No.3, 5, 8, 10
4	Remove the tables No.4, 6, 7, 9 (Empty classroom)
5	Add the tables No.4, 9
6	Remove the tables No.4, 9 and add the tables No.6, 7
7	Remove the tables N0.6, 7 (Empty classroom)
8	Add the tables No. 1, 2, 11, 12
9	Add the tables No. 3, 5, 8, 10
10	Add the tables No. 4, 6, 7, 9 (Full classroom)
11	Empty classroom and all blind is open, a shelf is removed

by the VNA. The Rx antenna was placed at a height of 18 m for the outdoor scenario and 3 m above the ground in the indoor scenario, to simulate the B2D communication. The Tx antenna was placed on a rotating pedestal to form a UCA with a height of 1.15 m and a pre-set radius of 0.25 m.

Hall to Corridor The measurement campaign depicted in Fig. 6 covered the hall to the corridor scenarios, with a total of 50 Tx positions ranging from a line-of-sight (LoS) to a Non-LoS (NLoS) scenarios [10]. The hall scenario used in this campaign was the same as the R2-Hall scenario. The dimension of the corridor is 3.6 m wide and 33 m long. One side of the corridor is made of glass windows, and the other side is made of concrete walls. Two biconical antennas, e.g., SZ−2003000/P [19] and a homemade biconical antenna [20], were exploited as Rx and Tx antennas in the measurement, respectively. As shown in Fig. 7(a), the Rx antenna was fixed on a wooden pole with a height of 3 m. The Tx positions are 0.9 m, 0.85 m and 0.9 m apart for position No.1 to No.6, position No.6 to No.18 and No.18 to No.50, respectively. The total distance from position No.1 to No.50 is about 43.5 m.

Outdoor As depicted in Fig. 8, the measurement campaign was conducted between the two buildings, with a bicycle shelter and a parking lot nearby. A horn antenna (LB-SJ-180400-KF [22]) was utilized as the Rx fixed on the top of the building as shown in Fig. 8(b), with its main beam down tilted towards the Tx positions [23]. A homemade biconical antenna [20] (the same as mentioned above) was used as the Tx UCA as illustrated in Fig. 8(c), and moved along the route in-between the building, with a total of 15 Tx positions from LoS to NLoS scenario.

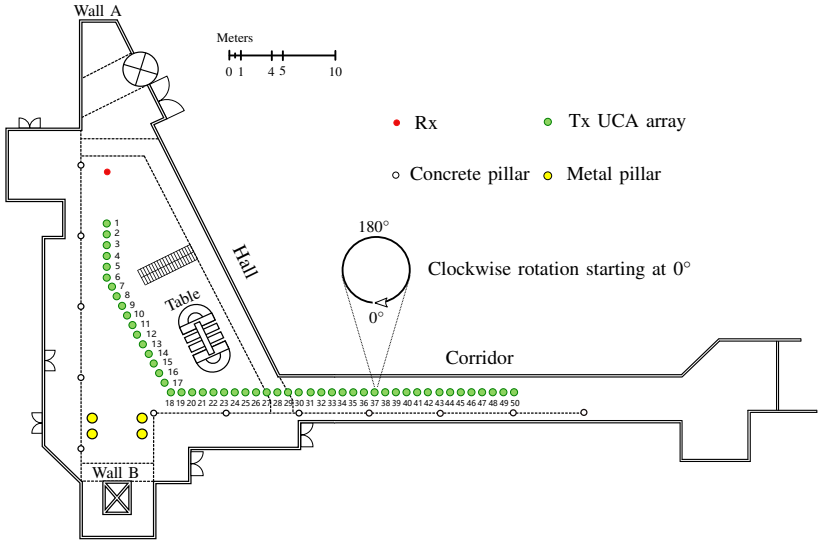

Fig. 6: The top-view of the indoor hall and corridor scenarios. [10]

1.3 Channel Characteristics

Fig. 9 presents examples of measured CIRs obtained using the channel sounder system mentioned above with ultra-wide bandwidth and large-scale UCA configuration. The CIRs were recorded in the hall to corridor scenario of Paper [E] at the frequency bands of 28-30 GHz in an LoS to an NLoS scenario. The IDFT is applied to convert the measured frequency response recorded by the VNA into CIRs, with N=2000 frequency points swept for each frequency band, and M=360 elements of the UCA. Because of the wide bandwidth of 2 GHz, a significant variation in the delay of each propagation path can be observed as the antenna moves across the elements of the UCA. In Fig. 9(a), it is observed that the delay of the LoS path is minimum at the 180th array, which indicates the angle information of this path. In addition, combined with the geometry of the hall and delay information, it can be deduced that the paths are contributed from Wall A and Wall B as shown in Fig. 9(a). Moreover, due to the spatial non-stationarity, the variability of path gains across the UCA elements can also be seen from the paths contributed from Wall A and Wall B in Fig. 9(a) [10]. We conjecture that it can be caused by the blockage, as the mm-wave has a weak ability to diffract around the obstacles such as the human body and furniture [10, 24]. Fig. 9(b) illustrates the CIRs in an NLoS scenario with the LoS path blocked. It can also be found that the power of the channel also decreases significantly in the NLoS scenario compared to the LoS scenario.

To investigate realistic channel models, a suitable algorithm is required for estimating the propagation parameters of the multipath components (MPCs),

(a)

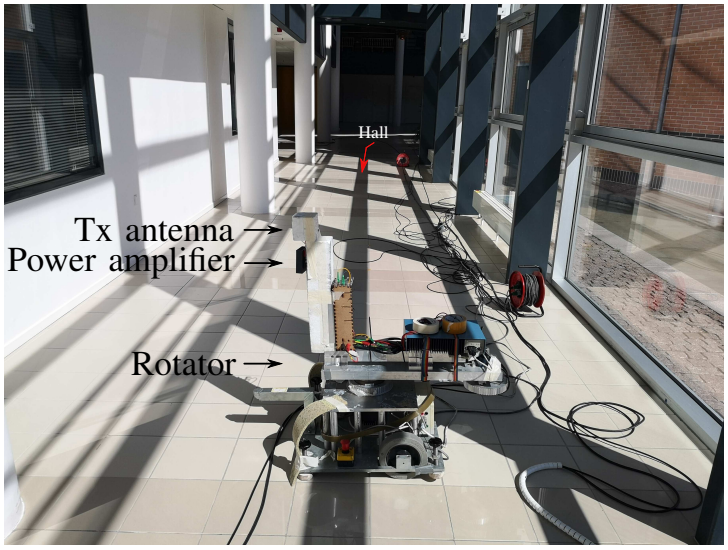

(b)

Fig. 7: (a) A photograph of the Rx antenna in the hall scenario. (b) A photograph of the Tx antenna in the corridor scenario. [10]

(a)

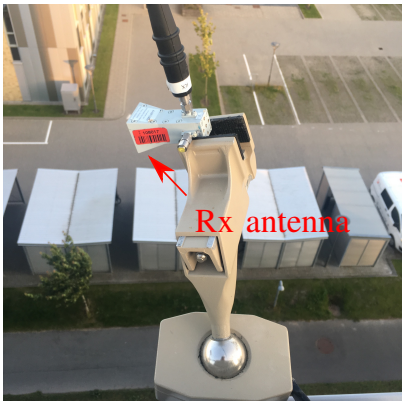

(b)

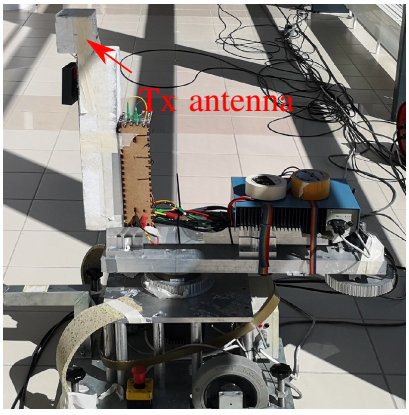

(c)

Fig. 8: (a) The top-view of the outdoor scenario. Image by Google Maps. (b) The photograph of the Rx antenna on the roof of the building. (c) The photograph of the Tx antenna. [10]

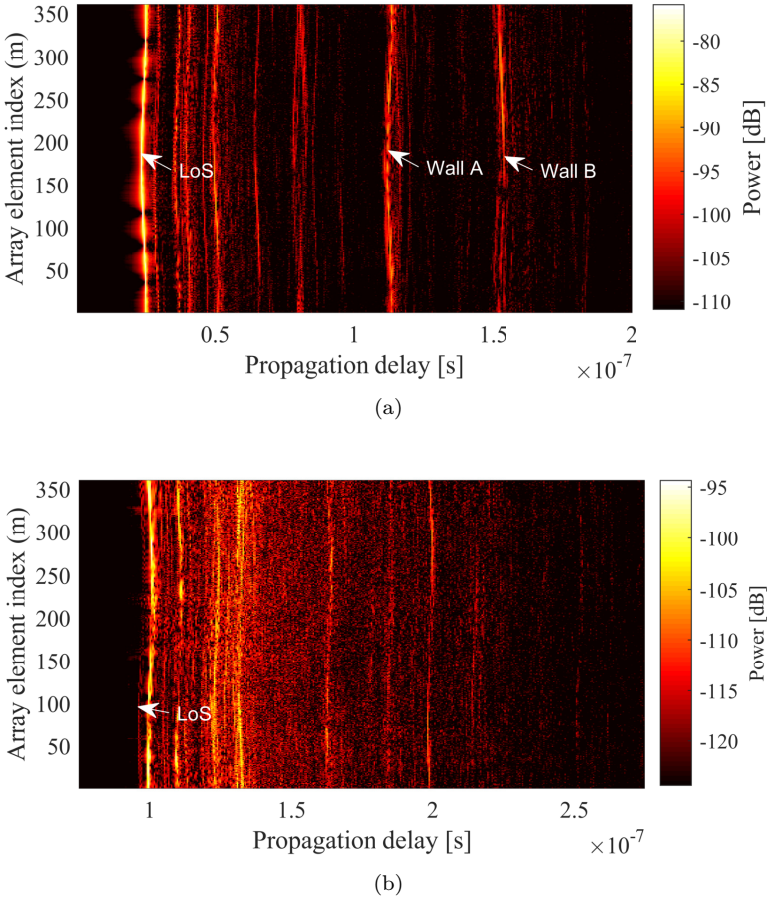

Fig. 9: Example CIRs obtained in the LoS and NLoS scenarios. [10]

such as delay, amplitudes, direction (azimuths and elevations) of arrival or departure, etc., based on measured data. Moreover, due to the size of the large-scale antenna arrays, the channel characteristics are significantly affected by the antenna's position, which is called the "near-field" effect. Therefore, the spherical wavefront assumption needs to be considered instead of the plane-wavefront assumption to avoid model mismatch [18]. Furthermore, due to spatial non-stationarity, the variability of path gains across the array elements can be significant. As a result, it is crucial to include it in channel models for ultra-wideband mm-wave communication systems with large-scale antenna array configurations.

2 Estimation Methods

The propagation channel is described by the multipath components (MPCs) caused by the reflection and diffraction of scattering mechanisms [25]. To establish a realistic propagation channel model, an accurate estimation of the propagation parameters of the MPCs is required. The Space Alternating Generalized Expectationmaximization (SAGE) algorithm [26] and Richter's Maximum likelihood estimation (RiMAX) algorithm [27] were widely used for the channel estimation under the plane wave assumption. For prior communication systems, such as the Long Term Evolution (LTE) system, the far-field assumption was utilized, as the antenna aperture was significantly smaller than the distance between the Tx, Rx, and scatterers [18]. Nevertheless, in the case of the mm-wave propagation channel with large-scale antenna array configurations, the large array aperture and the small mm-wave wavelength lead to significantly increased Fraunhofer distance D_{fr} [18]. The Fraunhofer distance [28] is expressed as

$$D_{fr} = \frac{2D^2}{\lambda}, \tag{1}$$

where D denotes the array aperture and λ is the wavelength [18]. The plane wave assumption is solely applicable if the distance between the source point and the array exceeds the Fraunhofer distance [29]. As the propagation distance is small in mm-wave bands, it is essential to take into account the spherical wave propagation model in parameter estimation for mm-wave communication systems with large-scale arrays to avoid model mismatch [18, 30, 31].

In Paper [A-E], a high-resolution propagation parameter estimation (HRPE) algorithm [29, 32] under the spherical wave propagation was utilized to extract the spherical propagation parameters of the MPCs from the measured data across the entire UCA. To model the spatial non-stationarity across the entire UCA and localize the source scatterers with lower complexity, the entire UCA is divided into multiple sub-arrays in Paper [F]. Then, the SAGE algorithm can be utilized independently on the parameter estimation of the MPCs from each sub-array under the plane wave assumption, resulting in lower complexity.

2.1 HRPE Estimation–Spherical Wave Based

The spherical propagation assumption needs to be considered for the mm-wave communication systems with a large-scale antenna array configuration. As shown in Fig. 10, it is assumed that the CIRs consist of a finite number of L spherical waves impinge into the UCA [29]. To overcome the limitations of 2D, narrow bands and plane wave assumptions of the SAGE algorithm, an HRPE algorithm [29, 32] was utilized to extract the propagation parameters of the ℓth propagation path, i.e., the complex amplitude α_ℓ, the delay τ_ℓ, the directions

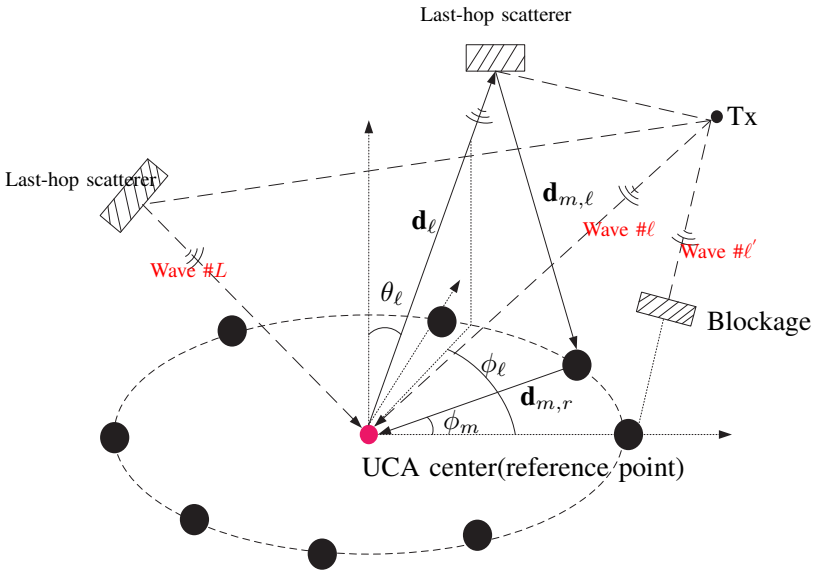

Fig. 10: Multipath prorogation with UCA. [32]

of arrival (i.e., azimuth ϕ_ℓ and elevation θ_ℓ) and the distance from the center of the Rx UCA to the last-hop scatterers d_ℓ, with low complexity. Besides, the realistic spatial non-stationarity for a large-scale array is also considered in the HRPE algorithm [10, 29].

The HRPE algorithm mainly consists of three parts as follows: [29, 32]

1) The SAGE algorithm is applied to estimate the element-wise delay $\tau_{m,\ell}$ and amplitude $\alpha_{m,\ell}$ of the ℓth path in the delay domain.

2) The trajectory identification is performed by the phase mode excitation method to obtain rough delay, azimuth, and elevation information of this path trajectory.

3) According to prior initialization obtained from the 2) step, the identified path trajectory was reconstructed. The estimated parameters are updated by the maximization estimation algorithm with low complexity. Then, update the original transfer function by removing this path, called the " identification-removing" operation.

The 2) and 3) steps are repeated until the power is fully extracted. The advantages of the HRPE algorithm are spatial non-stationarity considered and its low complexity. Readers can refer to [29, 32] for detailed information on the HRPE algorithm. Using the HRPE algorithm, the propagation parameters Θ of the MPCs at each snapshots are obtained, where $\Theta = [\alpha_\ell, \tau_\ell, \theta_\ell, \phi_\ell, d_\ell; \ell = 1, \ldots, L]$ [29, 32].

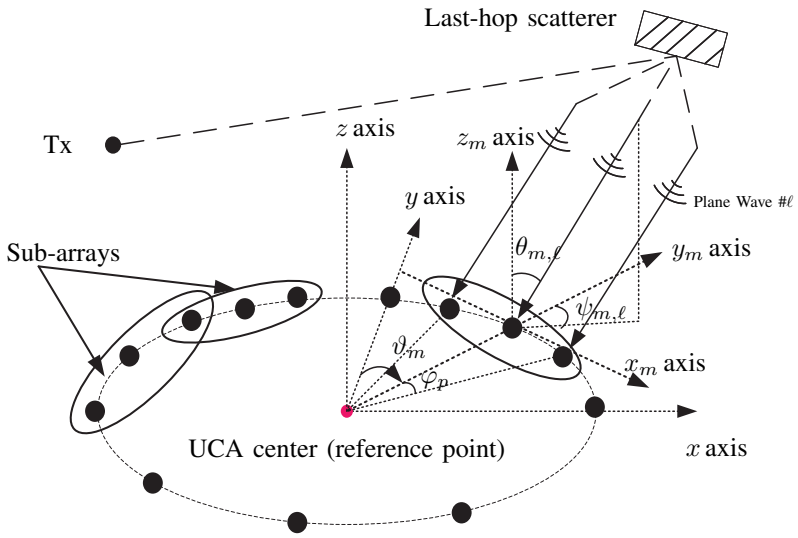

Fig. 11: Approximation of linear antenna sub-arrays moving across the UCA. [21]

2.2 SAGE Estimation–Plane Wave Based

In Paper [F], to investigate the spatial non-stationary phenomenon observed across the large-scale antenna array, the antenna array is split into multiple sub-arrays as shown in Fig. 11, and SAGE algorithm is applied for the parameters estimation of the MPCs from each sub-array under the plane wave assumption. Fig. 11 illustrates the setup of a UCA with M elements and the radius r in the x-y-z coordinate system. The center of the UCA is set as the origin point. Each virtual sub-array containing P elements of the UCA is located in the x_m-y_m-z_m system with its center as the origin point. A finite number of L plane waves are assumed to impinge into the sub-array with the center moving to the mth element across the UCA [21]. The SAGE algorithm is applied independently to estimate the propagation parameter set $\Psi_m = [\alpha_{m,\ell},\ \tau_{m,\ell},\ \psi_{m,\ell},\ \theta_{m,\ell};\ \ell = 1,\ldots,L]$ of the MPCs for each sub-array in the x_m-y_m-z_m coordinate system when the center of the sub-array moves to the mth element across the UCA [21]. However, the final angular values $\phi_{m,\ell}$ in the x-y-z coordinate system should be compensated with the rotation angle of the x_m-y_m-z_m coordinate, which can be expressed as $\phi_{m,\ell} = \psi_{m,\ell} + \vartheta_m$ as shown in Fig. 11. Therefore, the final target is to obtain the estimation of Θ_m=$[\alpha_{m,\ell},\ \tau_{m,\ell},\ \phi_{m,\ell},\ \theta_{m,\ell};\ \ell = 1,\ldots,L]$, m is the sub-array index across the UCA [21].

This thesis considers each virtual sub-array containing P=11 elements, which is approximately a virtual linear sub-array, with a Fraunhofer distance of 0.53 m at 28 GHz. Thus, the plane wave assumption can be utilized for the parameter estimation of the MPCs impinging into each sub-array by the SAGE algorithm.

Without estimating the source distance, the 3D parameters of the MPCs (i.e., delays, azimuths, elevations) are independently estimated by the SAGE algorithm with low complexity. Furthermore, the spatial non-stationary across the entire array can also be revealed from the estimated parameters at each sub-array [21].

3 Clustering Method

In wireless channel analysis, the MPCs with similar propagation parameters are grouped as a cluster, which is widely used for channel modeling. Parameter-based and physical-based clustering methods are widely used for grouping the estimated MPCs into clusters. The parameter-based method includes the KpowerMeans [33] and multipath component distance (MCD)-threshold principle [34], which are based on the estimated propagation parameters of the MPCs. To constitute a dynamic channel model, an MCD-threshold-based clustering and tracking method was proposed in Paper [E]. Furthermore, as the initialization for an optimum number of clusters is required in advance for the KpowerMeans method, and the prior assumption of the optimum MCD threshold is also required in advance for the MCD-threshold principle, which is not easy to obtain in low frequency bands with rich MPCs. Therefore, to cluster the MPCs at multiple frequency bands, a frequency-based clustering method based on the KPowerMeans algorithm [33] is proposed in Paper [C] linking the clusters obtained at high frequency bands to lower frequency bands. Additionally, to constitute a geometry-based stochastic channel model (GSCM), a geometry-based clustering method based on MCD-threshold algorithm [33] is proposed in Paper [D] linking the MPCs to their corresponding physical interaction objects (IOs) obtained from the Ray Tracing (RT) simulations, resulting in more physical interpretation [35–37]. In addition, to establish a GSCM, a novel scatterer localization method is also proposed in Paper [F], which can be used for the scatterer-based clustering and tracking method according to the estimated locations of the scatterers.

3.1 MCD-threshold-based clustering and tracking algorithm

In Paper [E], to establish a dynamic model, an MCD-threshold-based clustering and tracking algorithm is proposed, which mainly contains two parts as follows:

1) The initial step involves identifying clusters for each position separately, based on the estimated propagation parameters set $\Theta = [\alpha_\ell,\ \tau_\ell,\ \theta_\ell,\ \phi_\ell,\ \ell = 1, \ldots, L]$. Firstly, set the highest power as the reference point, and then calculate the MCDs [33] between all the MPCs with this reference point. The MCD is used as a basic distance function to quantify the MPCs separation by combining delay and angular domains. Secondly, if the MCDs are lower than the pre-defined MCD threshold $\eta_{\mathrm{MCD},1}$, then these paths are assigned to the same cluster set $\mathcal{L}_i$, otherwise, these paths are stored as remaining paths. Thirdly, repeat the first and second steps iteratively among the remaining paths and update the cluster centroids iteratively. The cluster centroid with the MPCs in the cluster set $\mathcal{L}_i$ can be calculated as

$$\mu_i = \frac{\sum_{\ell \in \mathcal{L}_i} |\alpha_\ell|^2 \cdot [\tau_\ell, \phi_\ell, \theta_\ell]^T}{\sum_{\ell \in \mathcal{L}_i} |\alpha_\ell|^2} \tag{2}$$

To obtain optimum pre-defined MCD threshold $\eta_{\mathrm{MCD},1}$, a range of the MCD threshold $[\eta_{\min}, \eta_{\max}]$ is set for evaluating the score fusion SF [38], which is computed as the geometrical mean of all the cluster validity indices (CVIs) for each possible threshold value η [5]. The compactness, separation, and exclusiveness of the clusters are represented by these CVIs, i.e., Calinski Harabasz index, Xie and Beni index, Pakhira-Bandyopadhyay-Maulik index [38–41].

2) The second part involves tracking clusters between adjacent positions by computing the MCDs between the cluster centroids. If the clusters from neighbor positions are mutually closest, and the MCDs between their cluster centroids are below the pre-defined threshold $\eta_{\mathrm{MCD},2}$, then they are tracked together, otherwise, the old cluster is considered as "dead" cluster at the previous position, and the new cluster is considered as "born" cluster at next position.

3.2 Frequency-based clustering algorithm

According to the channel characteristics at multiple frequency bands, it is inferred that the specular reflections dominate at multiple frequencies, and the frequency dependence of these reflections is not significant [42–44]. Therefore, the clusters at high frequency bands can be used as initialization for lower bands, leading to better accuracy and low complexity. Moreover, as the MPCs are sparse in high frequency bands, the physical IOs that the clusters contributed from can be identified based on the geometry, estimated delay, and angular information. Then, dominant clusters at lower frequencies can be linked to these physical IOs. The proposed frequency-based clustering method based on the KPowerMeans algorithm [33] mainly contains two parts as follows:

1) The first part is to cluster the estimated MPCs obtained from high frequency band, i.e. 27-29 GHz, using the KPowerMeans method [33]. A range of the number of the clusters $[K_{\min}, K_{\max}]$ is established to determine optimum number of clusters K_{opt} by considering the score fusion SF [38]. To enhance the visual representation, any clusters with power below 0.1% of the total power are eliminated.

2) The cluster centroids $\mu_i = [\mu_{i,\tau}, \mu_{i,\phi}, \mu_{i,\theta}]^T$ of identified clusters at 27-29 GHz are used as initialization for clustering the MPCs at lower frequency bands, i.e., 2-4 and 9-11 GHz. Then, the MCD between the MPCs from lower frequency and nearest cluster centroids μ_i obtained at high frequency band are calculated. In addition, a range of the MCD threshold $[\eta_{\min}, \eta_{\max}]$ is also set to obtain optimum MCD threshold η_{opt} for separating the MPCs at lower frequency band belonging to the clusters $\mathcal{L}_i$ linked

to clusters obtained from high frequency band or belonging to a new cluster $\mathcal{L}_{\text{new}}$. An extra range for the number of new clusters $[K^{'}_{min}, K^{'}_{max}]$ is set, and the KPowerMeans algorithm [33] is only performed in this range, leading to the low complexity of the algorithm. Then the centroids of the clusters $\mathcal{L}_i$ and $\mathcal{L}_{\text{new}}$ are updated. Finally, the clusters with power below 0.1% of the total power are also eliminated.

3.3 Geometry-based clustering algorithm

The RT tool [45, 46] developed by University of Bologna is utilized for simulating the outdoor scenario in this thesis, including the reflection, diffraction, transmission, and diffuse scattering mechanisms. To reduce computational time, only the basic structure of the two buildings and the bicycle shelter are modeled in the RT simulations [23]. Additionally, the material of the building is considered concrete and the bicycle shelter is set as metal. For simplicity, the reflections contributed from the ground are also ignored, due to the close distance between the Tx and the ground. Using the RT tool, the realistic physical propagation properties of each MPCs are obtained, i.e., the IOs (IO#, marked with the white label as shown in Fig. 8(a)) and the number of bounces, making it possible to group the MPCs based on their corresponding IOs and the number of bounces.

The geometry-based clustering method mainly contains two parts as follows:

1) For each Tx position, ℓ_e paths are estimated by the HRPE algorithm from the measured data, and ℓ_r paths are obtained from the RT simulation. As the material properties in the outdoor scenario are not easy to obtain, the power of the ℓ_r paths in the RT simulations are not precise. Therefore, to align the estimated ℓ_e paths with the simulated ℓ_r paths, the minimum MCD between them is calculated. All the dominant estimated paths can be matched with the simulated paths in the RT simulations, with only a few weak paths remaining unaligned. These aligned paths contributed from the same IO# and the same number of bounces are grouped into clusters, with their cluster centroids μ_c calculated by the equation (6). These cluster centroids are used as initialization for clustering all the estimated ℓ_e paths.

2) The MCDs between each estimated path and its nearest initialization cluster centroids are calculated. If the MCD is below the pre-defined MCD threshold η_{MCD}, this estimated path is assigned to this cluster, otherwise, this path is assigned to new clusters for further clustering with the MCD threshold-based clustering algorithm in Sect. 3.1. The optimum threshold η_{MCD} is determined by the score fusion SF of the CVIs. Finally, the clusters with power below 0.1% of the total power are removed.

3.4 Scatterer-based clustering algorithm

In Paper [F], a novel scatterer localization method is proposed, which can be applied for further scatterer-based clustering identification and tracking algorithm based on the estimated locations of the scatterers.

The scatterer-based clustering identification and tracking algorithm mainly contains two parts as follows:

1) The first part is to estimate the locations of the scatterers using the estimated angular information of the MPCs observed at each sub-array. The propagation parameters set Ψ_m and Θ_m of the ℓth path for each sub-array in the x_m-y_m-z_m and x-y-z coordinate systems are obtained from the estimation algorithm as described in Section 2.2, respectively, where $\Psi_m = [\alpha_{m,\ell},\ \tau_{m,\ell},\ \psi_{m,\ell},\ \theta_{m,\ell};\ \ell = 1,\ldots,L]$ and Θ_m=$[\alpha_{m,\ell},\ \tau_{m,\ell},\ \phi_{m,\ell},\ \theta_{m,\ell};\ \ell = 1,\ldots,L]$, m is the sub-array index across the UCA [21]. An MCD threshold method [10] is used to track the estimated parameters observed at each sub-array that belong to the same ℓth path, by combining the estimated delay $\tau_{m,\ell}$ and angular parameters (i.e., $\psi_{m,\ell}$ and $\theta_{m,\ell}$). Moreover, note that as the sub-array is approximately a linear antenna array, the symmetrical angular value of $\psi_{m,\ell}$ and $\theta_{m,\ell}$ should also be considered in the tracking method. According to final tracked angular values $\phi_{m,\ell}$ and $\theta_{m,\ell}$ for the ℓth path, the location of its corresponding scatterer $\mathbf{V}_\ell$ can be obtained by an iterative non-linear least squares approach, i.e. the Levenberg and Marquard algorithm [47].

2) Based on the MCD threshold-based clustering algorithm proposed in Paper [E], the MCDs are calculated by combining estimated delay and locations of the scatterers, the MCDs between ℓth and $\ell^{'}$th path can be described as

$$\mathrm{MCD}_{\ell\ell'} = \sqrt{\left\|\mathrm{MCD}_{\mathrm{Tx},\ell\ell'}\right\|^2 + \left\|\mathrm{MCD}_{\mathrm{Rx},\ell\ell'}\right\|^2 + \mathrm{MCD}^2_{\tau,\ell\ell'}} \tag{3}$$

where $\mathrm{MCD}_{\mathrm{Tx/Rx},\ell\ell'}$ denotes the MCD based on their corresponding locations of the first-hop or last-hop scatterers, which can be calculated as

$$\mathrm{MCD}_{\ell\ell'} = \frac{\|\mathbf{V}_\ell - \mathbf{V}_{\ell'}\|}{\zeta_v} \tag{4}$$

where ζ_v is an appropriate scaling factor for the location information in x-y-z coordinate system, which are based on the maximum extension of the physical objects in the scenarios. And $\mathrm{MCD}_{\tau,\ell\ell'}$ is the MCD in delay domain, with

$$\mathrm{MCD}_{\tau,\ell\ell'} = \frac{\|\tau_\ell - \tau_{\ell'}\|}{\zeta_\tau} \tag{5}$$

where ζ_τ denotes an appropriate delay scaling factor, which is calculated as $\zeta_\tau = 2 \times \zeta_v/c$, with c as the speed of light. Then, by evaluating the CVIs, an optimum MCD threshold η_{opt} is selected for separating the MPCs into clusters. If either condition, i.e., $\|\mathbf{V}_\ell - \mathbf{V}_{\ell'}\| \geq \zeta_v$ or $\|\tau_\ell - \tau_{\ell'}\| \geq \zeta_\tau$ is satisfied, then the ℓth and $\ell^{'}$th paths are belonging to different clusters, otherwise, if both conditions are not satisfied, the $\text{MCD}_{\ell\ell'}$ is compared with the optimum MCD threshold η_{opt}. If $\text{MCD}_{\ell\ell'}$ is larger than η_{opt}, then the ℓth and $\ell^{'}$th paths are belonging to different clusters, otherwise, they are grouped into the same cluster. Then, the cluster centroids $\mu_i = [\mu_{i,v}, \mu_{i,\tau}]^T$ with the MPCs in the cluster set $\mathcal{L}_i$ can be calculated as

$$\mu_i = \frac{\sum_{\ell \in \mathcal{L}_i} |\alpha_\ell|^2 \cdot [\mathbf{V}_\ell, \tau_\ell]^T}{\sum_{\ell \in \mathcal{L}_i} |\alpha_\ell|^2} \tag{6}$$

Finally, the cluster tracking algorithm is performed by calculating the MCDs between the cluster centroids at neighbor positions, as described in Sect. 3.1.

4 Channel Modeling

Accurate channel propagation characteristics and modeling at mm-wave bands are important for the development of future communication systems. A suitable channel model is required to accurately predict the wireless propagation behavior and explore corresponding propagation mechanisms. The primary approaches for channel modeling are stochastic, deterministic, and hybrid channel models. Ray tracing [48] and the finite-difference time-domain (FDTD) methods [49] are used for deterministic models. The drawback of both methods is their high computational complexity. Stochastic channel models describe the statistical properties of the channel. Correlation-based stochastic channel models calculate the correlation between the channel coefficients of each Tx and Rx antenna for the MIMO channel with low computational complexity. However, the geometry-based stochastic channel models (GSCM) are the most widely used, as they can provide a comprehensive channel description with the geometry details of the scenarios. The standard channel models, such as COST2100 [50], 3GPP [11], and the WINNER II models [51] belong to GSCM.

4.1 Composite level paramaters

In Paper [A-C] and [E], the composite level parameters are investigated. Decay factor, the root mean square (RMS) delay spread and angle spread, LoS power ratio of the channel in four scenarios at 27–29 GHz are investigated and compared in Paper [A]. In Paper [B] and [C], the frequency dependence of the composite parameters is explored in classroom and hall scenarios, including path loss, delay spread, and angle spread. And in addition, the number of the paths L is also analyzed in Paper [C]. In Paper [E], path loss, RMS delay spread, and angle spread of the channel from the hall to corridor scenario are also investigated.

Power Decay Factor

The exponential decay rate for modeling the decay tail of the average power delay profile (APDP) is known as the power decay factor β. The decay tail consists of the specular spectrum and distributed diffuse scattering components [52, 53], which can be modeled by a linear regression line. The decay factor β can be calculated using the slope of the fitting line s as [54]

$$\beta = -\frac{10\log(e)}{s}, \tag{7}$$

where e represents Euler's number.

Path Loss

Both the close-in free space reference distance (CI) path loss model and the floating-intercept (FI) path loss model are utilized in this thesis. FI model has been extensively applied in various models such as the WINNER II model, the 3GPP SCM, and the COST 2100 model [55]. Only one single parameter n is used to fit PL in the CI model, which is represented as [56, 57]

$$\begin{aligned} \mathrm{PL}^{\mathrm{CI}}(f,d)[\mathrm{dB}] = \mathrm{FSPL}(f,d_0) + 10\cdot n\log_{10}(d/d_0) + X_{\varsigma}^{\mathrm{CI}} \\ \text{for } d \geq d_0, \text{ where } d_0 = 1\,m \end{aligned} \tag{8}$$

where $\mathrm{FSPL}(f,d_0) = 10\log_{10}(\frac{4\pi d_0}{\lambda})^2$ represents the free space path loss at the measured frequency band, with the physically-based reference distance $d_0 = 1\,\mathrm{m}$. d is the distance between the Tx and Rx antennas. The linear slope n is commonly referred to as the path loss exponent (PLE), and $X_{\varsigma}^{\mathrm{CI}}$ is denoted as the shadowing effect.

Two parameters α and β are used for fitting PL in FI model, which is established as [55]

$$\mathrm{PL}^{\mathrm{FI}}(d)[\mathrm{dB}] = \alpha + 10\cdot\beta\log_{10}(d) + X_{\varsigma}^{\mathrm{FI}} \tag{9}$$

where α and β denote the intercept and the slope of the fitting line and $X_{\varsigma}^{\mathrm{FI}}$ is the shadow fading [5].

Root-mean-square (RMS) delay spread and angle spread

The RMS delay spread and angle spread are commonly utilized in channel models to describe the delay and angle dispersion of the channel, respectively. In Paper [B], two methods are employed to compute the RMS delay spread. The first method involved utilizing the raw APDP data, while the second method used estimated parameters of the MPCs by the HRPE algorithm. The RMS delay spread σ_τ can be calculated using raw APDPs P_{ave} as [3, 58]

$$\sigma_\tau = \sqrt{\frac{\sum_{n=1}^{N} P_{ave}(\tau)\cdot\tau^2}{\sum_{n=1}^{N} P_{ave}(\tau)} - \bar{\tau}^2}. \tag{10}$$

with

$$\bar{\tau} = \frac{\sum_{n=1}^{N} P_{ave}(\tau)\cdot\tau}{\sum_{n=1}^{N} P_{ave}(\tau)}. \tag{11}$$

Based on the estimated parameters $\Theta = [\alpha_\ell,\ \tau_\ell,\ \theta_\ell,\ \phi_\ell;\ \ell = 1,\ldots,L]$, of the MPCs by the HRPE algorithm, the RMS delay spread σ_τ can be expressed as [10]

$$\sigma_\tau = \sqrt{\overline{\tau^2} - \overline{\tau}^2} \tag{12}$$

with

$$\overline{\tau^2} = \frac{\sum_{\ell=1}^{L} |\alpha_\ell|^2 \cdot \tau_\ell^2}{\sum_{\ell=1}^{L} |\alpha_\ell|^2}, \quad \overline{\tau} = \frac{\sum_{\ell=1}^{L} |\alpha_\ell|^2 \cdot \tau_\ell}{\sum_{\ell=1}^{L} |\alpha_\ell|^2} \tag{13}$$

The azimuth spread σ_ϕ can be calculated as [3, 11]

$$\sigma_\phi = \sqrt{-2\log\left(\left|\frac{\sum_{\ell=1}^{L} \exp(j\phi_\ell) \cdot |\alpha_\ell|^2}{\sum_{\ell=1}^{L} |\alpha_\ell|^2}\right|\right)} \tag{14}$$

LoS power ratio

The LoS power ratio R_{LoS} is used to investigate the power ratio of the LoS or dominant components to the rest components of the channel, which is defined as [3]

$$R_{LoS} = \frac{\sum_{\ell=1}^{\ell_{LoS}} |\alpha_\ell|^2}{\sum_{\ell_{LoS}}^{L} |\alpha_\ell|^2} \tag{15}$$

where $\ell = [1, \ldots, \ell_{LoS}]$ belong to the LOS path or the most dominant components of the channel and $\ell = [\ell_{LoS}, \ldots, L]$ is the sum of the rest paths except LoS or the most dominant paths.

4.2 Dynamic channel model

A dynamic channel model is developed for the hall and corridor scenarios in Paper [E] based on the "hall to corridor" measurement described in Sect. 1.2, including cluster-level parameters and the "birth-death" behaviors of clusters [10]. To fairly compare the cluster-level parameters between the hall and corridor scenarios, the LoS and NLoS clusters in the hall scenario are separate. The cluster-level parameters include cluster power decay behavior, intra-cluster delay spread, and azimuth spread, and the correlations of these parameters [10]. The dynamic clusters are identified and tracked using the MCD-threshold-based clustering and tracking method as detailed in Sect. 3.1. The results of the tracked clusters in both delay and angular domains from the hall to corridor scenarios are depicted in Fig. 12. As presented in Fig. 13, linear lines are used to fit the tracked clusters in both delay and angular domains. Therefore, the tracked clusters in both delay and angular domains can be modeled as [10]

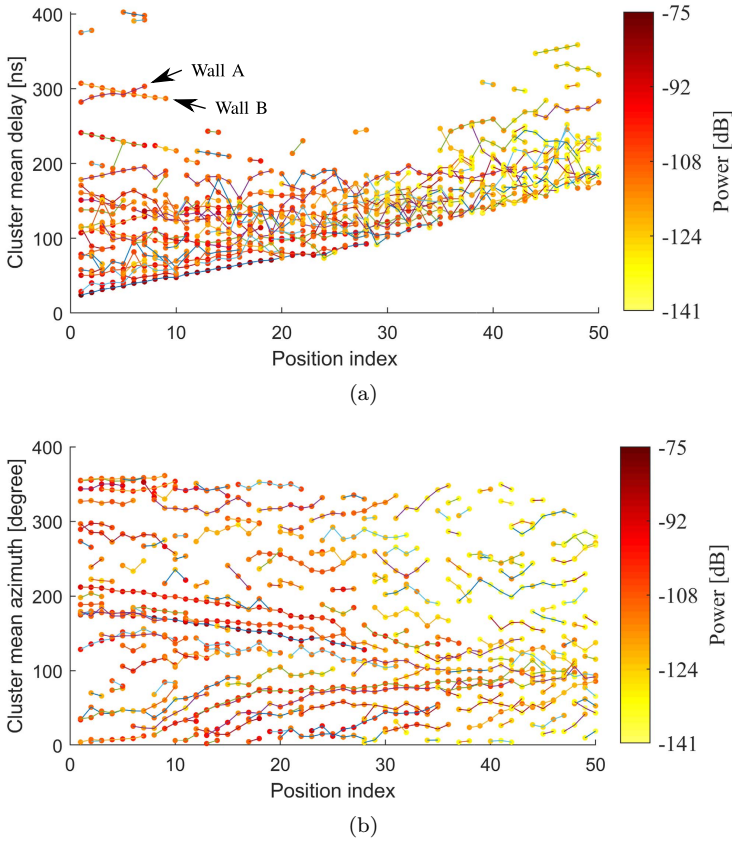

Fig. 12: The identified and tracked dynamic clusters at each position in both delay and angular domain. (a) Delay domain. (b) Azimuth domain. [10]

$$\bar{\tau}_c = a_\tau d + b_\tau + \varsigma_\tau, \bar{\phi}_c = a_\phi d + b_\phi + \varsigma_\phi \tag{16}$$

where d is the distance that the UCA moves. a and b represent the slope and intercept of the linear fitting line, respectively. ς represents the fluctuation. In addition, their subscripts τ and ϕ denote delay and angular domains, respectively. Moreover, to model the "birth-death" behaviors of clusters, the dynamic parameters as illustrated in Fig. 13, i.e., cluster survival length d_s, cluster birth location (τ_0 and ϕ_0) and slopes of the linear fitting line (a_τ and a_ϕ) in delay and azimuth domains, and born clusters number at each position N are investigated and compared for hall and corridor scenarios.

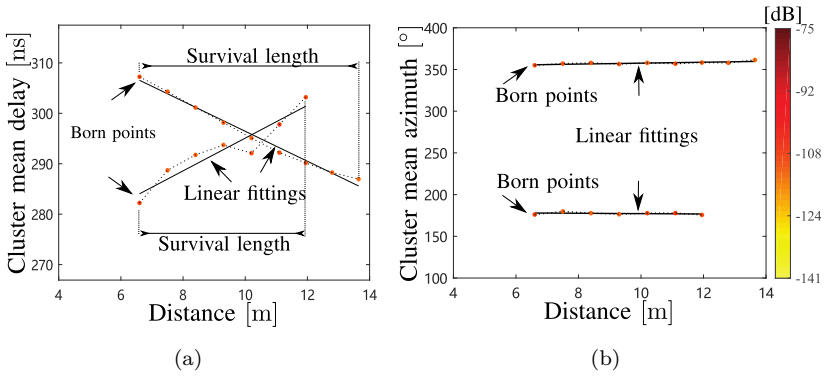

Fig. 13: The parameters of the linear fitting lines for the identified and tracked clusters. [10]

4.3 Geometry-based channel model

A geometry-based channel model is investigated in Paper [D] with the aid of RT tool [48] based on the outdoor measurement described in Sect. 1.2. Using the geometry-based clustering method proposed in Sect. 3.3, the estimated MPCs are grouped into clusters based on their corresponding physical IOs. The cluster-level characteristics, i.e., cluster power decay behavior, cluster number, intra-cluster delay spread, and azimuth spread are investigated. The intra-cluster delay spread and azimuth spread based on all the clusters, LoS cluster, and the clusters contributed from each IO are compared. In addition, the power contributions of the clusters at each position with multiple bounces from IOs are also studied. The clusters that are absent in the RT simulations are considered with unknown IOs and the number of bounces -1, which contribute less than 3% of the total power [23].

5 Contribution

This section briefly summarizes the main contributions of this thesis, including the motivation, main content and results of the papers presented in Section II.

5.1 Paper A

Experimental Characterization of Millimeter-wave Indoor Propagation Channels at 28 GHz
Guojin Zhang, Kentaro Saito, Wei Fan, Xuesong Cai, Panawit Hanpinitsak, Jun-ichi Takada, and Gert Frølund Pedersen
Published in the *IEEE Access*, vol.6, pp. 76516–76526, 2018.

Motivation

Despite extensive efforts to investigate mm-wave propagation channels, most studies have been limited to single scenarios using different frequency bands and measurement configurations. As a result, it is challenging to fully investigate how different scenarios affect mm-wave propagation characteristics. Currently, there are rare works on the comparison of mm-wave propagation characteristics in multiple scenarios using the same measurement system and frequency bands. Additionally, conducting channel measurement at mm-wave frequency bands is often costly and challenging. Therefore, simulation tools, e.g., Ray Tracing tools, have been extensively utilized to forecast channel behavior, but their simulation accuracy depends on the realistic modeling of objects present in the environment. Hence, it is also crucial to investigate the impact of furniture richness levels and indoor geometry on the channel based on measurements.

Paper Content

Four measurements in various indoor scenarios such as classrooms, an office, and a hall were conducted using the same measurement system at the frequency band of 27-29 GHz. The channel characteristics, e.g., power delay profiles (PDPs), decay factor, delay spread, angular spread, and line of sight (LoS) power ratio, in the four scenarios, are investigated and compared. Furthermore, the study also explores the impact of furniture richness levels and indoor geometry on the channel based on the measurements.

Main Results

It is found that the channel characteristics exhibit variations in different scenarios. The delay spread values in R2-Hall are significantly larger than those in R4-Office, whereas the angle spread values in R2-Hall are significantly lower than those observed in R4-Office. It indicates that the dimensions of the indoor environments have a noteworthy influence on the characteristics of the channel. Furthermore, it is also found that channel characteristics within each

scenario differ depending on the Tx location, which can be observed through the noticeable fluctuations in channel characteristics at different Tx positions within R1-Classroom and R2-Hall. Moreover, in R3-Classroom and R4-Office, minimal fluctuation of channel characteristics is observed as furniture is progressively removed, indicating a weak impact of furniture richness on channel propagation in indoor scenarios. In general, the mm-wave frequency band of 27-29 GHz exhibits dominant LoS and specular propagation mechanisms, particularly in the larger R2-Hall scenario. Moreover, it is noteworthy that the LoS power ratio in R3-Classroom is notably lower than that of R1-Classroom, mostly due to the strong reflection from the aluminous frame of the blackboard in the corner where the Tx is located in R3-Classroom.

5.2 Paper B

Millimeter-Wave Channel Characterization in Large Hall Scenario at the 10 and 28 GHz Bands

Guojin Zhang, Panawit Hanpinitsak, Xuesong Cai, Wei Fan, Kentaro Saito, Jun-ichi Takada, and Gert Frølund Pedersen

Published in the *13th European Conference on Antennas and Propagation (EuCAP)*, 2019.

Motivation

Most studies on indoor channel characteristics have been limited to power spectrum and delay spread analysis across various frequency bands, with few focusing on the comparison of angular spread in multiple frequency bands.

Paper Content

The measurements were carried out in a large hall scenario, covering frequency bands of 9-11 GHz and 27-29 GHz, and included a total of 20 Tx locations for each frequency band. The high-resolution parameter estimation (HRPE) algorithm is utilized to extract estimated channel parameters such as delay, angle, and amplitude. Following this, the channel characteristics including path loss, delay spread, and angle spread were analyzed and compared across the 9-11 GHz and 27-29 GHz frequency bands.

Main Results

The results indicate minor differences between the frequency bands of 9-11 GHz and 27-29 GHz. It is observed that the path loss at 27-29 GHz is close to free space path loss, attributed to dominant LoS paths. The path loss exponents (PLEs) were found to be higher than 1.5 at both frequency bands, which is likely due to the large dimension of the hall scenario. Furthermore, delay spread was calculated using two methods, based on the raw measured data and estimated delay parameters from the HRPE algorithm. It was observed that

the HRPE algorithm provided more accurate delay spread values ranging from 6-20 ns compared to the values obtained from the raw data. In addition, the angle spread values were found to range mainly between 12.75° and 41°.

5.3 Paper C

Modeling Multi-frequency Characteristics for Classroom and Hall Scenarios at 2-4, 9-11 and 27-29 GHz Bands
Guojin Zhang, Jesper Ødum Nielsen, Xuesong Cai, Saito Kentaro, Panawit Hanpinitsak, Jun-ichi Takada, Gert Frølund Pedersen, and Wei Fan
Published in the *IEEE Access*, vol. 9, pp. 14549–14563, 2021.

Motivation

The current works lack the analysis of cluster-level and frequency-dependent channel characteristics at mm-wave bands and below 6 GHz in different indoor scenarios using a consistent channel sounder and measurement configuration. Additionally, the effect of indoor room conditions such as dimensions and furniture on channel characteristics at mm-wave bands and below 6 GHz has not been comprehensively studied.

Paper Content

The study involved the measurements conducted in both a classroom and large hall scenarios. The measurements covered three frequency bands, e.g., 2-4, 9-11, and 27-29 GHz. Each frequency band and each scenario were tested at 20 different Tx locations. To achieve a more precise and realistic estimation, a complexity-efficient HRPE algorithm was used to estimate spherical channel propagation parameters of the multipath components (MPCs), based on the measured data. The spatial non-stationarity of path gain was also taken into account in the HRPE algorithm. Furthermore, estimated parameters were used to calculate composite level parameters, including path loss, number of paths, root-mean-square (RMS) delay spreads, and azimuth spreads. A novel cluster identification algorithm was proposed to categorize estimated MPCs into clusters at multiple frequency bands, considering both consistency and differences between different bands. Since specular reflections dominate at multiple frequency bands and their frequency dependence is not significant, the clustering results obtained from high frequency bands can be used as initialization for lower bands with more abundant MPCs. Using this approach, similarities between different frequency bands of the channel can be tracked and unique characteristics at lower bands can be identified. Statistical models of the cluster-level parameters, i.e., the number of clusters, cluster delay spread, cluster azimuth spread, and cluster power loss behavior, were also investigated. Finally, to investigate the frequency dependence of the channel, composite level, and cluster level parameters at 2-4, 9-11, and 27-29 GHz were

compared. To investigate the effect of dimensions and furniture on the channel, composite level, and cluster level parameters in both scenarios were compared.

Main Results

It is found that the PLE observed in the hall scenario at 27-29 GHz, exceeded the theoretical PLE value of 2 in free space. We speculate that this overestimation may be attributed to the strong reflections from the elevator and yellow steel tubes, as well as the short distance between the transmitter and receiver, which is less than 10 meters. Furthermore, similar to the results of previous research on the PLEs of indoor scenarios, it is revealed that the PLEs were independent of frequency in both hall and classroom scenarios. Furthermore, the study has shown a decrease in the number of MPCs and clusters as the frequency bands increase in both scenarios. It is reasonable that the density of MPCs in the mm-wave band is significantly lower than those below 6 GHz, a phenomenon commonly known as channel sparsity, due to scattering and diffraction becoming more dominant at lower frequency bands. Moreover, as the frequency bands decrease in both scenarios, composite and cluster-level delay spread and azimuth spread all increase.

For the same frequencies in both scenarios, the number of MPCs and clusters in the hall was smaller than that in the classroom, possibly because of the large dimension and fewer objects in the hall. Furthermore, the composite and intra-cluster delay spread in the hall were generally larger than those in the classroom across all frequency bands. Conversely, the composite and intra-cluster azimuth spread in the classroom were larger than those in the hall across all frequency bands, primarily due to sparse objects in the hall, resulting in dominant paths.

5.4 Paper D

Geometry-Based Clustering Characteristics for Outdoor Measurements at 28-30 GHz
Guojin Zhang, Jesper Ødum Nielsen, Xuesong Cai, Gert Frølund Pedersen, and Wei Fan
Published in the *IEEE Antennas and Wireless Propagation Letters*, vol. 21, no. 9, pp.1797-1801, Sept. 2022.

Motivation

Traditional clustering algorithm group MPCs based on their similar delay and angular information, however, lacking a relationship with physical scatterers. It is particularly challenging in complicated outdoor scenarios such as narrow corridors, where high-order reflections (up to 7 bounces) occur. To address this issue, a geometry-based clustering algorithm is required to group MPCs based on their corresponding physical interaction objects (IOs) in realistic scenarios.

Paper Content

An outdoor measurement campaign was conducted from LoS to NLoS (narrow corridor) scenarios. To address the challenge of linking MPCs to their corresponding physical interaction objects (IOs) in complex outdoor scenarios with multiple bounces, a fully automatic geometry-based clustering method was proposed with the assistance of the 3D Ray Tracing (RT) tool. Finally, the paper investigates the cluster-level channel characteristics, i.e., cluster power decay behavior, intra-cluster delay and azimuth spread linked to their corresponding physical IOs, the number of the clusters, as well as the power contributions of multiple bounces.

Main Results

In this paper, the geometry-based channel characteristics, i.e., cluster-level parameters based on their physical IOs in both LoS and NLoS scenarios for the complex outdoor scenario in the 28-30 GHz frequency band were investigated. The results indicate that LoS clusters have a non-zero intra-cluster delay and azimuth spread due to ground reflections. Furthermore, clusters from the walls IO#4 inside the narrow corridor have the largest intra-cluster delay spread and smallest azimuth spread. Conversely, the clusters from IO#5 have the smallest intra-cluster delay spread and the largest azimuth spread. We speculate that the narrow size of the corridor leads to multiple bounces, resulting in increased dispersion of the clusters in the angle domain, consequently, a smaller delay spread. In addition, compared to indoor scenarios, the outdoor scenario has fewer clusters and a higher slope value for the floating-intercept (FI) path loss model of cluster power decay behavior. It is also found that, in most cases, the higher number of bounces contributes less power.

5.5 Paper E

Dynamic Channel Modeling for Indoor Millimeter-Wave Propagation Channels Based on Measurements
Xuesong Cai, Guojin Zhang, Chao Zhang, Wei Fan, Jinxing Li, and Gert Frølund Pedersen
Published in the *IEEE Transactions on Communications*, vol.68, no.9, pp.5878-5891, 2020.

Motivation

Due to the high power attenuation in the coaxial cable, long distance measurements were not widely explored in previous work. Furthermore, appropriate estimation algorithms are also required for extracting MPC parameters with low complexity. The spatial consistency of the channel should also be considered in the estimation algorithm. In addition, the dynamic behaviors ("birth-death") of the channel as the Tx or Rx moves have not been thoroughly investigated

yet. It is essential to investigate dynamic characteristics for evaluating system performance, i.e., the application of beam management between the base station (BS) and the user equipment (UE).

Paper Content

Utilizing a fiber-optic-based channel sounder, measurements were conducted in both indoor hall and corridor scenarios at the frequency band of 28-30 GHz. A total of 50 antenna positions were collected along a pre-defined route of approximately 48 m, enabling investigation of the dynamic behaviors of the channel. Furthermore, a complexity-efficient HRPE algorithm was applied for extracting MPC parameters, while taking spherical propagation into account. As a result, the accuracy and resolution of the estimated results are significantly improved. In addition, a novel algorithm was proposed to cluster the estimated MPCs and track the clusters as the antenna moves along the pre-defined route. Finally, composite-level and cluster-level parameters of the channel were explored. To develop a realistic dynamic channel model, the dynamic behaviors ("birth-death") of clusters were also investigated.

Main Results

The study found that the PLE observed in the corridor is higher than that in the hall, which is mainly due to the significant power loss caused by multiple reflections in the corridor. Moreover, while the composite delay spread in the corridor is similar to that in the hall, the composite azimuth spread is significantly greater in the hall than in the corridor. Furthermore, cluster-level delay spread and azimuth spread in the hall are smaller than those observed in the corridor, primarily because the objects in the hall can create dominant paths.

To compare the NLoS clusters in the hall and corridor, the LoS clusters in the hall were extracted and analyzed separately. The results indicated a significant difference in the PLE observed between the NLoS clusters present in the corridor scenario, which exhibit notably higher PLE, and those in the hall scenario, which show relatively low PLE.

To investigate the dynamic characteristics of the clusters, the parameters, i.e., cluster survival length, cluster born point, slopes of cluster trajectories in both delay and azimuth domains, and born cluster number were also investigated. It was found that the cluster survival length in both hall and corridor scenarios exhibited a good fit with the lognormal distributions. It has also been observed that the cluster born delay in both scenarios follows a log-normal distribution, while the born azimuth follows a uniform distribution. Moreover, the born cluster number was found to be similar in both scenarios.

5.6 Paper F

A Scatterer Localization Method Using Large-Scale Antenna Array Systems

Guojin Zhang, Xuesong Cai, Jesper Ødum Nielsen, Gert Frølund Pedersen, and Fredrik Tufvesson

Published in the *IEEE Conference on Antenna Measurement and Applications (CAMA)*, 2022.

Motivation

In ultra-massive multiple-input multiple-output (UM-MIMO) technology used in millimeter-wave and terahertz communications systems, it's essential to account for spherical wavefronts. As a result, analyzing the position and dynamic characteristics of scatterers becomes crucial. The conventional approach for locating scatterers relies primarily on estimating angular information and the distance between the scatterer and the array, utilizing the whole large-scale antenna array under spherical wave assumptions. However, it leads to high complexity for searching the two parameters, i.e., angular and distance information. Therefore, to lower the complexity of the algorithm, a novel scatterer localization method is required.

Paper Content

A novel algorithm for localizing scatterers has been proposed in this contribution. The large-scale antenna array was divided into multiple sub-arrays, where the space-alternating generalized expectation-maximization (SAGE) estimation approach can be applied under the plane wave assumptions. With the estimated angular information observed at all the sub-array, the location of the scatterers can be obtained. Furthermore, the proposed algorithm was demonstrated through simulations and applied to measured data obtained in a hall scenario. The results indicate that the estimated scatterers are in good agreement with the actual scenario.

Main Results

The simulation results show the error distance between the estimated and simulated scatterer, which is mainly due to the model mismatch. As the short distance between the scatterer and the sub-array, the near field effect still exists. The proposed method was also applied to the measurement campaigns conducted in hall scenarios using a large-scale antenna array. The estimated dominant scatterers show good consistency with the actual physical objects in the hall scenario.

6 Conclusion

The main scope of this thesis is to investigate the ultra-massive multiple-input multiple-output (UM-MIMO) channel characteristics in millimeter wave (mm-wave) frequency bands for the fifth generation (5G) and beyond wireless systems. This thesis includes a total of six papers, which encompass data collection at the mm-wave frequency bands in both indoor and outdoor scenarios, the investigation of channel characteristics and modeling for device-to-device (D2D) and base station-to-device (B2D) wireless communication, and a novel scatterer localization algorithm.

To investigate the channel characteristics of D2D communication, in Paper A four measurement campaigns were conducted in the classroom, office, and hall scenarios at the frequency bands of 27-29 GHz. Composite characteristic parameters of the channel in the four measurement campaigns were compared to study the influence of the objects and geometry in the scenario on the channel.

Paper B and Paper C investigate the multi-frequency characteristics of the channel in hall and classroom scenarios. Composite channel characteristics of the channel in the hall scenario at the frequency bands of 9-11 GHz and 27-29 GHz were compared in Paper B. Composite and cluster-level characteristics of the channel in a classroom and a hall scenarios at the frequency bands of 2-4, 9-11 and 27-29 GHz was compared in Paper C.

In Paper D, an outdoor measurement campaign was conducted for the B2D communication at the frequency band of 28-30 GHz. To constitute a geometry-based stochastic channel model (GSCM), cluster-level characteristics were investigated with the assistance of Ray Tracing 3-D simulations. Furthermore, the power contributions of the clusters with multiple bounces were also investigated.

In Paper E, an indoor measurement campaign conducted from an indoor hall to an indoor corridor at the frequency band of 28-30 GHz was presented for the B2D communication. To constitute a dynamic model, composite channel characteristics, cluster-level parameters, and dynamic behaviors of clusters are investigated.

Finally, a novel scatterer localization algorithm with low complexity was proposed in Paper F, which can be further used to constitute a GSCM based on the estimated locations of the scatterers.

References

[1] Theodore S. Rappaport, Shu Sun, Rimma Mayzus, Hang Zhao, Yaniv Azar, Kevin Wang, George N. Wong, Jocelyn K. Schulz, Mathew Samimi, and Felix Gutierrez. Millimeter Wave Mobile Communications for 5G Cellular: It Will Work! *IEEE Access*, 1:335–349, 2013.

[2] Sana Salous, Vittorio Degli Esposti, Franco Fuschini, Reiner S Thomae, Robert Mueller, Diego Dupleich, Katsuyuki Haneda, Jose-Maria Molina Garcia-Pardo, Juan Pascual Garcia, Davy P Gaillot, et al. Millimeter-wave propagation: Characterization and modeling toward fifth-generation systems.[wireless corner]. *IEEE Antennas and Propagation Magazine*, 58(6):115–127, 2016.

[3] Guojin Zhang, Kentaro Saito, Wei Fan, Xuesong Cai, Panawit Hanpinitsak, Jun-Ichi Takada, and Gert Frølund Pedersen. Experimental Characterization of Millimeter-Wave Indoor Propagation Channels at 28 GHz. *IEEE Access*, 6:76516–76526, 2018.

[4] Mamta Agiwal, Abhishek Roy, and Navrati Saxena. Next Generation 5G Wireless Networks: A Comprehensive Survey. *IEEE Communications Surveys Tutorials*, 18(3):1617–1655, 2016.

[5] Guojin Zhang, Jesper Ødum Nielsen, Xuesong Cai, Kentaro Saito, Panawit Hanpinitsak, Jun-Ichi Takada, Gert Frølund Pedersen, and Wei Fan. Modeling Multi-Frequency Characteristics for Classroom and Hall Scenarios at 2-4, 9-11 and 27-29 GHz Bands. *IEEE Access*, 9:14549–14563, 2021.

[6] Junghoon Ko, Yeon-Jea Cho, Sooyoung Hur, Taehwan Kim, Jeongho Park, Andreas F. Molisch, Katsuyuki Haneda, Michael Peter, Dong-Jo Park, and Dong-Ho Cho. Millimeter-Wave Channel Measurements and Analysis for Statistical Spatial Channel Model in In-Building and Urban Environments at 28 GHz. *IEEE Transactions on Wireless Communications*, 16(9):5853–5868, 2017.

[7] Xianyue Wu, Cheng-Xiang Wang, Jian Sun, Jie Huang, Rui Feng, Yang Yang, and Xiaohu Ge. 60-GHz Millimeter-Wave Channel Measurements and Modeling for Indoor Office Environments. *IEEE Transactions on Antennas and Propagation*, 65(4):1912–1924, 2017.

[8] Wonil Roh, Ji-Yun Seol, Jeongho Park, Byunghwan Lee, Jaekon Lee, Yungsoo Kim, Jaeweon Cho, Kyungwhoon Cheun, and Farshid Aryanfar. Millimeter-wave beamforming as an enabling technology for 5G cellular communications: theoretical feasibility and prototype results. *IEEE Communications Magazine*, 52(2):106–113, 2014.

[9] Vittorio Degli-Esposti, Franco Fuschini, Enrico M. Vitucci, Marina Barbiroli, Marco Zoli, Li Tian, Xuefeng Yin, Diego Andres Dupleich, Robert Müller, Christian Schneider, and Reiner S. Thomä. Ray-tracing-based mm-wave beamforming assessment. *IEEE Access*, 2:1314–1325, 2014.

[10] Xuesong Cai, Guojin Zhang, Chao Zhang, Wei Fan, Jinxing Li, and Gert Frølund Pedersen. Dynamic Channel Modeling for Indoor Millimeter-Wave Propagation Channels Based on Measurements. *IEEE Transactions on Communications*, 68(9):5878–5891, 2020.

[11] Study on channel model for frequencies from 0.5 to 100 GHz. Technical report, 3GPP TR 38.901 V15.0.0, Jun. 2018.

[12] Allan Wainaina Mbugua, Wei Fan, Kim Olesen, Xuesong Cai, and Gert Frølund Pedersen. Phase-Compensated Optical Fiber-Based Ultrawideband Channel Sounder. *IEEE Transactions on Microwave Theory and Techniques*, 68(2):636–647, 2020.

[13] Aziz Altaf Khuwaja, Yunfei Chen, Nan Zhao, Mohamed-Slim Alouini, and Paul Dobbins. A Survey of Channel Modeling for UAV Communications. *IEEE Communications Surveys Tutorials*, 20(4):2804–2821, 2018.

[14] Guojin Zhang, Xuesong Cai, Wei Fan, and Gert Frølund Pedersen. A USRP-Based Channel Sounder for UAV Communications. In *2020 14th European Conference on Antennas and Propagation (EuCAP)*, pages 1–4, 2020.

[15] Timo Dammes, Wolfgang Endemann, and Ruediger Kays. Frequency domain channel measurements for wireless localization - practical considerations and effects of the measurement. In *European Wireless 2012; 18th European Wireless Conference 2012*, pages 1–8, 2012.

[16] Wei Fan, Ines Carton Llorente, Jesper Ødum Nielsen, Kim Olesen, and Gert F. Pedersen. Measured Wideband Characteristics of Indoor Channels at Centimetric and Millimetric Bands. *EURASIP Journal on Wireless Communications and Networking*, 2016(58), 2016. special issue on Radio Channel models for higher frequency bands.

[17] Panawit HANPINITSAK, Kentaro SAITO, Wei Fan, Jun ichi Takada, and Gert F. Pedersen. Frequency Characteristics of Path Loss and Delay-Angular Profile of Propagation Channels in An Indoor Room Environment in SHF Bands. In *TECHNICAL REPORT OF IEICE*, volume 116 of *IEICE Technical Report*, pages 153–158. The Institute of Electronics, Information and Communication Engineers, 2017. Mobile Communication Workshop ; Conference date: 01-03-2017 Through 03-03-2017.

[18] Yilin Ji, Wei Fan, and Gert F. Pedersen. Near-Field Signal Model for Large-Scale Uniform Circular Array and Its Experimental Validation. *IEEE Antennas and Wireless Propagation Letters*, 16:1237–1240, 2017.

[19] Ainfoinc. SZ-2003000-P.pdf [online]. Technical report, Available: http: //www.ainfoinc.com/en/pro_ pdf/new_ products/antenna/Bi-Conical% 20Antenna/tr_ SZ-2003000-P.pdf, (2018, June 5).

[20] S. S. Zhekov, A. Tatomirescu, and G. F. Pedersen. Antenna for Ultrawideband Channel Sounding. *IEEE Antennas Wireless Propag. Lett.*, 16:692–695, 2017.

[21] Guojin Zhang, Xuesong Cai, Jesper Ødum Nielsen, Gert Frølund Pedersen, and Fredrik Tufvesson. A Scatterer Localization Method Using Large-Scale Antenna Array Systems. In *2022 IEEE Conference on Antenna Measurements and Applications (CAMA)*, pages 1–4, 2022.

[22] LB-SJ-180400-KF Datasheet. Technical report.

[23] Guojin Zhang, Jesper Ødum Nielsen, Xuesong Cai, Gert Frølund Pedersen, and Wei Fan. Geometry-Based Clustering Characteristics for Outdoor Measurements at 28-30 GHz. *IEEE Antennas and Wireless Propagation Letters*, June 2022.

[24] Vasanthan Raghavan, Andrzej Partyka, Ashwin Sampath, Sundar Subramanian, Ozge Hizir Koymen, Kobi Ravid, Juergen Cezanne, Kiran Mukkavilli, and Junyi Li. Millimeter-Wave MIMO Prototype: Measurements and Experimental Results. *IEEE Communications Magazine*, 56(1):202–209, 2018.

[25] Jinwen Liu, David W. Matolak, Mohanad Mohsen, and Jinming Chen. Path Loss Modeling and Ray-Tracing Verification for 5/31/90 GHz Indoor Channels. In *2019 IEEE 90th Vehicular Technology Conference (VTC2019-Fall)*, pages 1–6, 2019.

[26] B.H. Fleury, M. Tschudin, R. Heddergott, D. Dahlhaus, and K. Ingeman Pedersen. Channel parameter estimation in mobile radio environments using the SAGE algorithm. *IEEE Journal on Selected Areas in Communications*, 17(3):434–450, 1999.

[27] A. Ritcher, M. Landmann, and R.S. Thoma. Maximum likelihood channel parameter estimation from multidimensional channel sounding measurements. In *The 57th IEEE Semiannual Vehicular Technology Conference, 2003. VTC 2003-Spring.*, volume 2, pages 1056–1060 vol.2, 2003.

[28] Constantine A Balanis. *Antenna theory: analysis and design*. John wiley & sons, 2015.

[29] Xuesong Cai, Wei Fan, Xuefeng Yin, and Gert Frølund Pedersen. Trajectory-Aided Maximum-Likelihood Algorithm for Channel Parameter Estimation in Ultrawideband Large-Scale Arrays. *IEEE Transactions on Antennas and Propagation*, 68(10):7131–7143, 2020.

[30] Xuefeng Yin, Stephen Wang, Nan Zhang, and Bo Ai. Scatterer Localization Using Large-Scale Antenna Arrays Based on a Spherical Wave-Front Parametric Model. *IEEE Transactions on Wireless Communications*, 16(10):6543–6556, 2017.

[31] Yilin Ji, Wei Fan, and Gert Frølund Pedersen. Channel Characterization for Wideband Large-Scale Antenna Systems Based on a Low-Complexity Maximum Likelihood Estimator. *IEEE Transactions on Wireless Communications*, 17(9):6018–6028, 2018.

[32] Xuesong Cai and Wei Fan. A Complexity-Efficient High Resolution Propagation Parameter Estimation Algorithm for Ultra-Wideband Large-Scale Uniform Circular Array. *IEEE Transactions on Communications*, 67(8):5862–5874, 2019.

[33] Nicolai Czink, Pierluigi Cera, Jari Salo, Ernst Bonek, Jukka-pekka Nuutinen, and Juha Ylitalo. A Framework for Automatic Clustering of Parametric MIMO Channel Data Including Path Powers. In *IEEE Vehicular Technology Conference*, pages 1–5, 2006.

[34] Carl Gustafson, Katsuyuki Haneda, Shurjeel Wyne, and Fredrik Tufvesson. On mm-Wave Multipath Clustering and Channel Modeling. *IEEE Transactions on Antennas and Propagation*, 62(3):1445–1455, 2014.

[35] Meifang Zhu. *Geometry-based Radio Channel Characterization and Modeling: Parameterization, Implementation and Validation*. PhD thesis, Department of Electrical and Information Technology, Lund University, 2014.

[36] Panawit Hanpinitsak, Kentaro Saito, Jun-ichi Takada, Minseok Kim, and Lawrence Materum. Multipath Clustering and Cluster Tracking for Geometry-Based Stochastic Channel Modeling. *IEEE Transactions on Antennas and Propagation*, 65(11):6015–6028, 2017.

[37] Fengyu Luan, Andreas F. Molisch, Limin Xiao, Fredrik Tufvesson, and Shidong Zhou. Geometrical Cluster-Based Scatterer Detection Method with the Movement of Mobile Terminal. In *2015 IEEE 81st Vehicular Technology Conference (VTC Spring)*, pages 1–6, 2015.

[38] Krzysztof Kryszczuk and Paul Hurley. Estimation of the Number of Clusters Using Multiple Clustering Validity Indices. In Neamat El Gayar, Josef Kittler, and Fabio Roli, editors, *Multiple Classifier Systems*, pages 114–123, Berlin, Heidelberg, 2010. Springer Berlin Heidelberg.

[39] S. Cheng, M. Martinez-Ingles, D. P. Gaillot, J. Molina-Garcia-Pardo, M. Liénard, and P. Degauque. Performance of a Novel Automatic Identification Algorithm for the Clustering of Radio Channel Parameters. *IEEE Access*, 3:2252–2259, 2015.

[40] U. Maulik and S. Bandyopadhyay. Performance evaluation of some clustering algorithms and validity indices. *IEEE Transactions on Pattern Analysis and Machine Intelligence*, 24(12):1650–1654, 2002.

[41] Malay K. Pakhira, Sanghamitra Bandyopadhyay, and Ujjwal Maulik. Validity index for crisp and fuzzy clusters. *Pattern Recognition*, 37(3):487 – 501, 2004.

[42] Panawit Hanpinitsak, Kentaro Saito, Wei Fan, Johannes Hejselbæk, Jun-Ichi Takada, and Gert Frølund Pedersen. Frequency Characteristics of Geometry-Based Clusters in Indoor Hall Environment at SHF Bands. *IEEE Access*, 7:75420–75433, 2019.

[43] David Ferreira, Iñigo Cuiñas, Rafael F.S. Caldeirinha, and Telmo R. Fernandes. A Review on the Electromagnetic Characterisation of Building Materials at Micro- and Millimetre Wave Frequencies. In *The 8th European Conference on Antennas and Propagation (EuCAP 2014)*, pages 145–149, 2014.

[44] Guillaume Tesserault, Nadine Malhouroux, and Patrice Pajusco. Determination of Material Characteristics for Optimizing WLAN Radio. In *2007 European Conference on Wireless Technologies*, pages 225–228, 2007.

[45] V. Degli-Esposti, D. Guiducci, A. de'Marsi, P. Azzi, and F. Fuschini. An Advanced Field Prediction Model Including Diffuse Scattering. *IEEE Transactions on Antennas and Propagation*, 52(7):1717–1728, 2004.

[46] Vittorio Degli-Esposti, Franco Fuschini, Enrico M. Vitucci, and Gabriele Falciasecca. Measurement and modelling of scattering from buildings. *IEEE Transactions on Antennas and Propagation*, 55(1):143–153, 2007.

[47] Martin Schmidhammer, Christian Gentner, and Benjamin Siebler. Localization of Discrete Mobile Scatterers in Vehicular Environments Using Delay Estimates. In *2019 International Conference on Localization and GNSS (ICL-GNSS)*, pages 1–6, 2019.

[48] G.E. Corazza, V. Degli-Esposti, M. Frullone, and G. Riva. A Characterization of Indoor Space and Frequency Diversity by Ray-tracing Modeling. *IEEE Journal on Selected Areas in Communications*, 14(3):411–419, 1996.

[49] Stanislav Stefanov Zhekov, Ondrej Franek, and Gert Frølund Pedersen. Numerical Modeling of Indoor Propagation Using FDTD Method With Spatial Averaging. *IEEE Transactions on Vehicular Technology*, 67(9):7984–7993, 2018.

[50] Lingfeng Liu, Claude Oestges, Juho Poutanen, Katsuyuki Haneda, Pertti Vainikainen, François Quitin, Fredrik Tufvesson, and Philippe De Doncker. The COST 2100 MIMO channel model. *IEEE Wireless Communications*, 19(6):92–99, 2012.

[51] Winner II channel models. Technical report, IST-4-027756 WINNER II D1.1.2 V1.2, 02 2008.

[52] Katsuyuki Haneda, Jan Järveläinen, Aki Karttunen, Mikko Kyrö, and Jyri Putkonen. A Statistical Spatio-Temporal Radio Channel Model for Large Indoor Environments at 60 and 70 GHz. *IEEE Transactions on Antennas and Propagation*, 63(6):2694–2704, 2015.

[53] Gerhard Steinböck, Troels Pedersen, Bernard Henri Fleury, Wei Wang, and Ronald Raulefs. Experimental Validation of the Reverberation Effect in Room Electromagnetics. *IEEE Transactions on Antennas and Propagation*, 63(5):2041–2053, 2015.

[54] A. Bamba, W. Joseph, J. B. Andersen, E. Tanghe, G. Vermeeren, D. Plets, J. Ø. Nielsen, and L. Martens. Experimental Assessment of Specific Absorption Rate Using Room Electromagnetics. *IEEE Trans. Electromagn. Compat.*, 54(4):747–757, Aug 2012.

[55] J. Ko, Y. Cho, S. Hur, T. Kim, J. Park, A. F. Molisch, K. Haneda, M. Peter, D. Park, and D. Cho. Millimeter-Wave Channel Measurements and Analysis for Statistical Spatial Channel Model in In-Building and Urban Environments at 28 GHz. *IEEE Transactions on Wireless Communications*, 16(9):5853–5868, Sep. 2017.

[56] G. R. Maccartney, T. S. Rappaport, S. Sun, and S. Deng. Indoor Office Wideband Millimeter-Wave Propagation Measurements and Channel Models at 28 and 73 GHz for Ultra-Dense 5G Wireless Networks. *IEEE Access*, 3:2388–2424, 2015.

[57] Mathew K. Samimi, Theodore S. Rappaport, and George R. MacCartney. Probabilistic Omnidirectional Path Loss Models for Millimeter-Wave Outdoor Communications. *IEEE Wireless Communications Letters*, 4(4):357–360, 2015.

[58] Xuesong Cai, Xuefeng Yin, Xiang Cheng, and Antonio Pérez Yuste. An Empirical Random-Cluster Model for Subway Channels Based on Passive Measurements in UMTS. *IEEE Transactions on Communications*, 64(8):3563–3575, 2016.

Part II

Papers

Paper A

Experimental Characterization of Millimeter-wave Indoor Propagation Channels at 28 GHz

Guojin Zhang, Kentaro Saito, Wei Fan, Xuesong Cai, Panawit Hanpinitsak, Jun-ichi Takada, Gert Frølund Pedersen

The paper has been published in the
IEEE Access Vol. 6, pp.76516–76526, 2018.

The layout has been revised.

Abstract

The increasing requirement for the mobile data traffic accelerates the research of millimeter-wave (mm-wave) for future wireless systems. Accurate characterization of the mm-wave propagation channel is fundamental and essential for the system design and performance evaluation. In this paper, we conducted measurement campaigns in various indoor scenarios, including classroom, office and hall scenarios at the frequency bands of 27-29 GHz. The spatial channel characteristics were recorded by using a large-scale uniform circular array (UCA). A high resolution parameter estimation (HRPE) algorithm was applied to estimate the mm-wave spherical propagation parameters i.e., the azimuth angle, elevation angle, delay, source distance and complex amplitude of multipath components (MPCs). With the same measurement system, the channel parameters including decay factor, delay spread, angular spread and line of sight (LOS) power ratio are investigated thoroughly in individual indoor scenarios and compared in different indoor scenarios. Furthermore, the impact of the furniture richness level and indoor geometry on the propagation parameters are also investigated.

1 Introduction

The utilization of millimeter-wave (mm-wave) frequencies for the fifth generation communications (5G) and beyond has gained considerable interest in both academic and industrial community recently due to the spectrum scarcity at the sub-6 GHz frequency bands [1–4]. Mm-wave frequency bands have been identified as the promising candidate frequencies for future cellular networks [2]. However, the mm-wave propagation characteristics are very different from that observed in the sub-6 GHz frequency bands. Accurate understanding of the mm-wave propagation channels are essential and have attracted increasing attention recently [5–7].

Extensive measurement campaigns have been conducted at mm-wave frequency bands [8–15]. In [8, 9], measurement campaigns were conducted in high-speed trains scenarios, and extensive ray tracing simulations were applied to understanding the propagation mechanisms. In [10], the measurement was performed at 81−86 GHz (E-band) in a street canyon scenario, and a geometry-based single-bounce channel model was developed for investigating the characteristics in the delay domain. Considerable efforts have been devoted to study the channel characteristics at 60 GHz frequency bands [11–13], which have been exploited for unlicensed wireless HD and Wireless Gigabit Alliance (WiGig) WLAN applications [14] with Gbps transmission in short range indoor communications. In addition, several radio channel sounding campaigns were performed at 60 GHz and 70 GHz frequency bands in various short-range scenarios, including offices, shopping mall and station in [15]. Furthermore, various inves-

tigations for the propagation channels at the frequency bands of 28 GHz have been conducted [16–18]. Channel characteristics such as path loss, signal outage [16], reflection coefficients, penetration losses caused by common building materials [17] and angular characteristics [18] have been thoroughly analyzed. More recently, in [19], measurements in two important cellular scenarios, i.e., an urban microcell and an open indoor hall, were conducted at the frequency bands of 28 GHz, with a focus on spatio-temporal channel characteristics parameters.

Although extensive measurement efforts have been taken to understand the propagation channels, most of them were performed in a single scenario, e.g. the indoor scenario or the outdoor scenario. Furthermore, the frequency bands and measurement configurations differ in these works. This poses challenge on understanding the influence of different scenarios on the mm-wave propagation characteristics. To the authors' best knowledge, the comparison among the mm-wave propagation characteristics observed in several different scenarios with the same measurement system and frequency band applied has not been investigated so far. Moreover, it is usually expensive and difficult to carry out channel measurement at mm-wave frequency bands. Thus, simulation tools such as ray tracing have been widely exploited to predict the channel behaviors. However, the simulation accuracy relies on the realistic modeling of the various objects existing in the environment, i.e. the detailed database of electrical properties for the structure and random minor objects. This also necessitate the measurement-based investigation for the impact of the furniture richness level and indoor geometry on the radio propagation parameters.

In this paper, the mm-wave propagation channels in different indoor scenarios including classroom, office and hall are recorded by using the same measurement system. The measurement system is based on the virtual antenna array scheme to sound the mm-wave channel at the frequency band of 27 GHz-29 GHz. Channel characteristics, including power delay profiles (PDPs), decay factor, delay spread, angular spread and line of sight (LOS) power ratio are thoroughly investigated in individual scenarios and compared among different scenarios. Moreover, we also gain insights into the impact of the indoor geometry, materials and furniture richness level on the channel characteristics.

The rest of the paper is organized as follows. Section 2 describes four measurement campaigns. Section 3 briefly describes the post-processing for extracting the parameters of interest. The resulted channel models are discussed in Section 4. Finally, Section 5 concludes the paper.

2 Measurement campaign

In this section, the measurement scenarios and setup of the four indoor measurements are detailed. The scenarios include two classroom scenarios, an office scenario and a hall scenario, with measurement settings specified in Table A.1.

Table A.1: Measurement Setup

Room	R1-Classroom	R2-Classroom	R3-Office	R4-Hall
Dimension (m^3)	$8.54 \times 6.70 \times 2.71$	$8.54 \times 6.70 \times 2.71$	$4.78 \times 3.44 \times 2.85$	$39 \times 20 \times 10$
Tx antenna	Antenna A	Antenna A	Antenna B	Antenna A
Rx antenna	Antenna B	Antenna B	Antenna A	Antenna B
Center frequency	28 GHz	28 GHz	28 GHz	28 GHz
Transmit power	15 dBm	12 dBm	15 dBm	15 dBm
Tx\Rx antenna height	1.50 m	1.30 m	1.50 m	1.50 m
Frequency sweep points	360	360	360	360
UCA radius	0.24 m	0.24 m	0.24 m	0.24 m
Details	20 positions	Remove and restore tables and chairs	Remove contents and shelves	20 positions

2.1 Measurement setup

The measurement system is a vector network analyzer (VNA) based virtual array channel sounding system. Readers can refer to [20, 21] for details. Two types of biconical antenna are used in the measurements, which are commercial biconical antenna SZ-2003000/P (marked as A) [22] and homemade biconical antenna (marked as B) [23]. Both biconical antennas are wideband and omnidirectional in the horizontal plane and has narrow elevation patterns in elevation plane. The antenna gains of commercial and homemade biconical antennas are 6 dB and 4.8 dB at 28 GHz, respectively. The biconical antenna is rotated clockwise on a rotating pedestal with a pre-set radius (as shown in Table A.1) with 1 degree rotating steps to form a UCA for the four measurement campaigns. In the measurements, the channel propagation from 27-29 GHz was swept by using the VNA, giving a delay resolution of 0.5 ns. 750 frequency points were collected, limiting the maximum delay to 375 ns.

2.2 Measurement Scenario

R1-Classroom

The measurement was performed in a typical small classroom [21] as shown in Fig. A.1, where three sides of the room are covered by the concrete walls and three windows on the other side. The height of the tables is 0.74 m. A total of 20 spatial snapshots (i.e. locations) were measured by moving the Tx antenna between the tables. Each Tx location in each row was spaced 0.8 m apart. An illustration of the classroom and antennas used in R1-Classroom are presented in Fig. A.1.

R2-Classroom

The measurements were performed in the same classroom as R1-Classroom, where the Tx antenna was fixed at the corner and Rx antenna set in the center of the classroom, as shown in Fig. A.2. In the measurement, we removed four tables and chairs in the classroom and repeated the measurements for each step

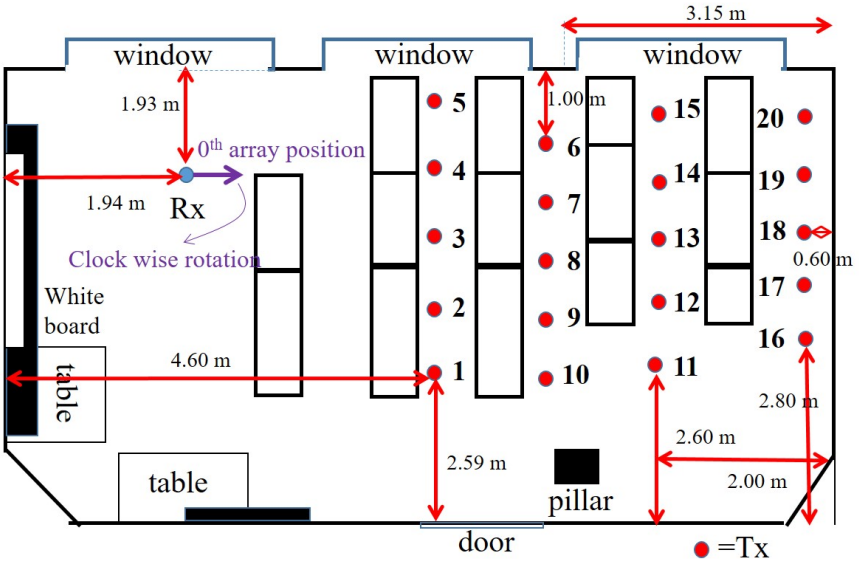

(a)

(b)

Fig. A.1: (a) The sketch of R1-Classroom with 20 Tx locations. (b) The photograph of R1-Classroom and Tx (left), Rx (right) antennas.

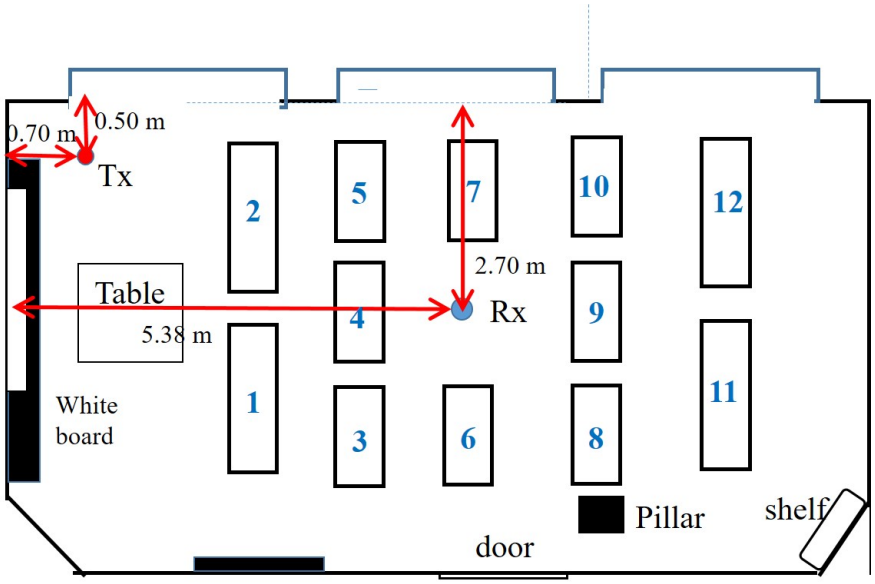

Fig. A.2: The sketch of R2-Classroom with 12 tables.

(in 5 steps). Then we restored and brought back two or four tables and chairs and repeated the measurements for each step (in 5 steps). The classroom is full of tables and chairs in step 1 and 10, and totally empty in step 4 and 7. The last measurement was conducted with the classroom totally empty and all blind windows open as shown in Fig. A.3(b). The objective is to investigate the impact of tables and chairs on the channel characteristics.

R3-Office

To study the impact of furniture richness level on the channel characteristics, we performed measurements in a typical office scenario, which is equipped with metallic shelves and loaded with books, as shown in Fig. A.4. In the measurement, we removed the contents on the shelves one by one from step 2 to step 6 and then removed shelves from step 7 to step 11. A total of 11 measurements were performed in the campaign, starting from fully loaded shelves in step 1 and ending with no shelves in the room in step 11.

R4-Hall

To investigate the channel characteristics in irregular large indoor scenarios, the measurement was conducted in a hall scenario, as shown in Fig. A.5. The shape of the hall is irregular, and the ceiling of the hall is 10 m high. There is also a big table and stairs along the south wall. The four big ventilation tubes

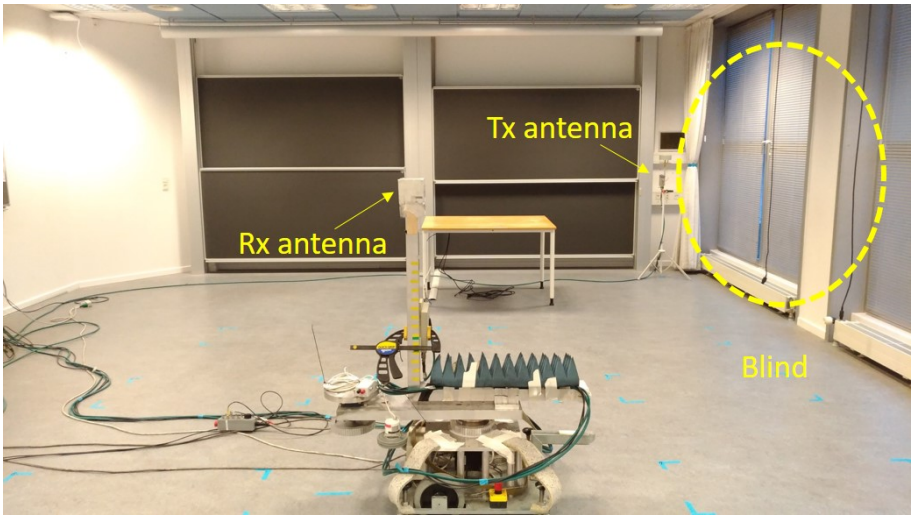

(a)

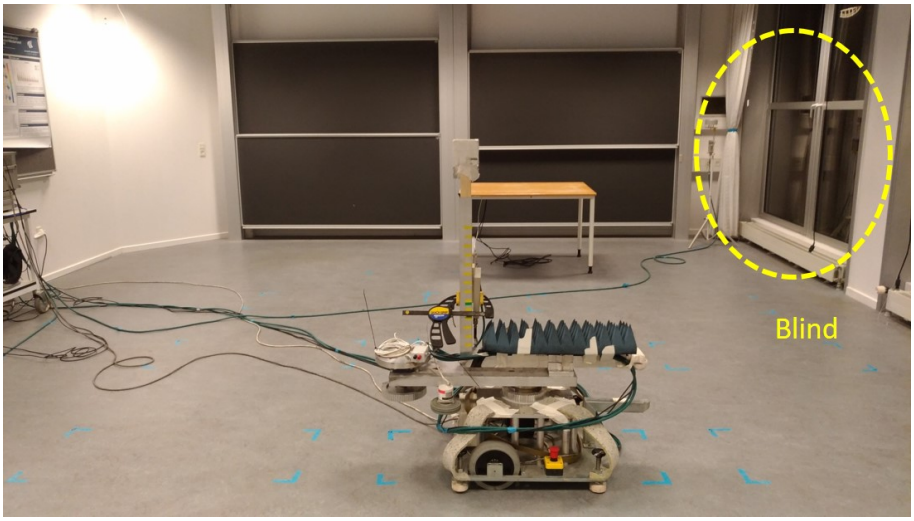

(b)

Fig. A.3: (a) The photograph of R2-Classroom and Tx/Rx antennas location with all room furniture removed. (b) The photograph of empty R2-Classroom with blind windows open.

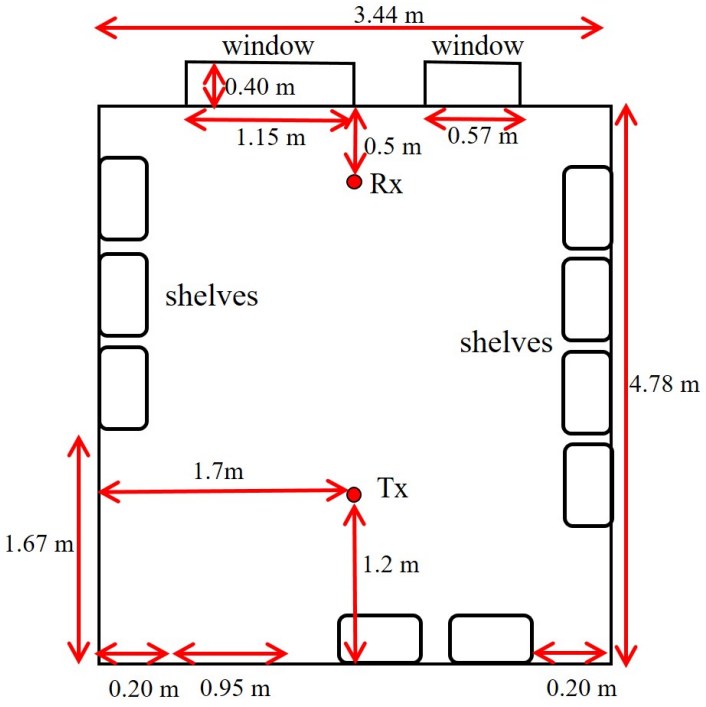

(a)

(b)

Fig. A.4: (a) The sketch of R3-Office. (b) The photograph of R3-Office and Tx (down), Rx (top) antennas.

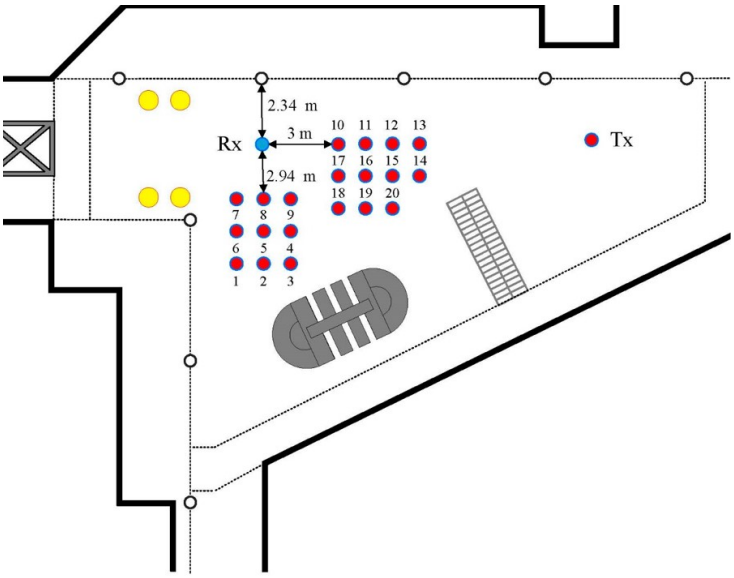

(a)

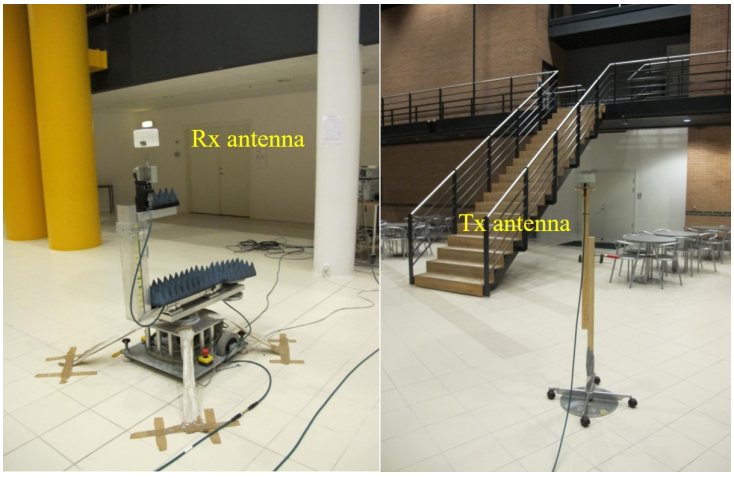

(b)

Fig. A.5: (a) The sketch of R4-Hall with 20 Tx locations. (b) The photograph of R4-Hall and Rx (left), Tx (right) antennas.

(shown as yellow circles) and six pillars (shown as white circles) are located around the hall. The Rx was located near the four big pillars in the west side of the hall, and the Tx was located at 20 different points distributed around the Rx, as shown in Fig. A.5. Each Tx location is 1 m apart from each other.

3 Parameter Analysis

3.1 Power Decay Factor

When modeling the radio propagation channel, the PDPs are expressed as a combination of primary and decay components [15, 24]. The primary component contains the direct propagation and possibly first-order reflections, and the decay component is from the specular spectrum and distributed diffuse scattering. The decay tail of the power-delay profile can be typically modeled as a tail with an exponential decay rate, defined as decay factor β.

As explained, the Rx antenna was mounted at uniform angles around a circle to obtain a UCA with N=360 elements, and M=750 frequency points were recorded for each frequency band. The Hanning window and the inverse Fourier transom (IFT) computation are used to processing the raw data in the frequency domain. The average power delay profiles (APDPs) can be obtained by

$$P_m(\tau) = \frac{1}{N} \sum_{n=1}^{N} |h_{m,n}(\tau)|^2 \tag{A.1}$$

where $h_{m,n}(\tau)$ represents the channel impulse response (CIR) at m-th sample in delay domain, and n-th measured element.

For the accuracy of analysis, we need to define the fixed range of the linear regression of the decay tail. The end time of the regression line τ_{noise} corresponds to the noise floor P_{noise}. The beginning of the linear regression fit line $\bar{\tau}$ can be defined as [25]

$$\bar{\tau} = \frac{\sum_{m=1}^{M} P_m(\tau) \cdot \tau}{\sum_{m=1}^{M} P_m(\tau)}, \tag{A.2}$$

where P_m is the power value of the APDPs at m-th delay sample.

According to the regression line, we obtain the slope of the decay tail and decay factor β, which can be described as [25]

$$\beta = -\frac{10 \log(e)}{s}, \tag{A.3}$$

where e is Euler's number, and s is the slope of the power decay tail in APDPs, represented as dB/ns.

3.2 Delay Spread

The delay spread of the channels is widely used for characterizing the multipath components (MPCs) richness in the wireless channel, which is calculated as the second-order central moments of the APDPs [26]. The mean delay $\bar{\tau}$ is defined in (A.2), and root mean square (RMS) delay spread σ_τ can be computed from the measured as [26]

$$\sigma_\tau = \sqrt{\frac{\sum_{m=1}^{M} P_m(\tau) \cdot \tau^2}{\sum_{m=1}^{M} P_m(\tau)} - \bar{\tau}^2}. \tag{A.4}$$

3.3 Angle Spread

In this paper, we utilized the HRPE algorithm [27] to estimate the mm-wave spherical propagation parameters of the UCA channels, i.e. azimuth angle, elevation angle, delay, source distance and amplitude of MPCs. Then the spatial-temporal CIR $h(\tau, \theta, \phi, d)$ can expressed as

$$h(\tau, \theta, \phi, d) = \sum_{l=1}^{L} \alpha_l \delta(\tau - \tau_l)\delta(\theta - \vartheta_l)\delta(\phi - \varphi_l)\delta(d - d_l), \tag{A.5}$$

where L is the number of spherical waves impinge into the UCA, τ_l is the propagation delay, ϑ_l and φ_l represent the azimuth and elevation angles of the l-th path, respectively. α_l denotes the complex amplitude, and d_l is the propagation distance between the UCA center and the last source point during the propagation route of the l-th path, respectively.

As most of the estimated elevation angles are close to 90 degree, we only focus on the azimuth angles. Then the spatial-temporal CIR can be expressed as $h(\tau, \varphi)$. The circular angle spread σ_φ can be calculated, as defined in [27, 28],

$$\sigma_\varphi = \sqrt{-2\log\left(\left|\frac{\sum_{l=1}^{L} \exp(j\varphi_l) \cdot |h(\tau_l, \varphi_l)|^2}{\sum_{l=1}^{L} |h(\tau_l, \varphi_l)|^2}\right|\right)}. \tag{A.6}$$

3.4 LOS Power Ratio

To figure out the dominant components of the channel, the LOS power ratio K is defined as the ratio of the power in the LOS component or most dominant component to the power in the non-line of sight (NLOS) or the other MPCs components [26]. LOS power ratio plays a vital role in estimating statistics, which is identified as,

$$K = \frac{P_{\text{LOS}}(\tau)}{P_{\text{NLOS}}(\tau)} \tag{A.7}$$

where, $P_{\mathrm{LOS}}(\tau)$ is the power of LOS path (i.e. in most dominant component) and $P_{\mathrm{NLOS}}(\tau)$ is the sum of the power of all the MPCs components except the most dominant path.

4 Measurement Results

4.1 R1-Classroom

The calculated APDPs with corresponding decaying lines at Tx positions 1, 12, and 19 at 27 GHz-29 GHz in R1-Classroom are illustrated in Fig. A.6 for an example. It can be observed from Fig. A.6 that, the strongest path is contributed by LOS propagation, with power values of -67.7 dB, -69.4 dB and -72.3 dB with Tx at position 1, 12 and 19, respectively. The power of the LOS path decreases, as the distance between the Tx and Rx increases for the three example locations. The noise level is about -100 dB, leading to the dynamic range around 30 dB.

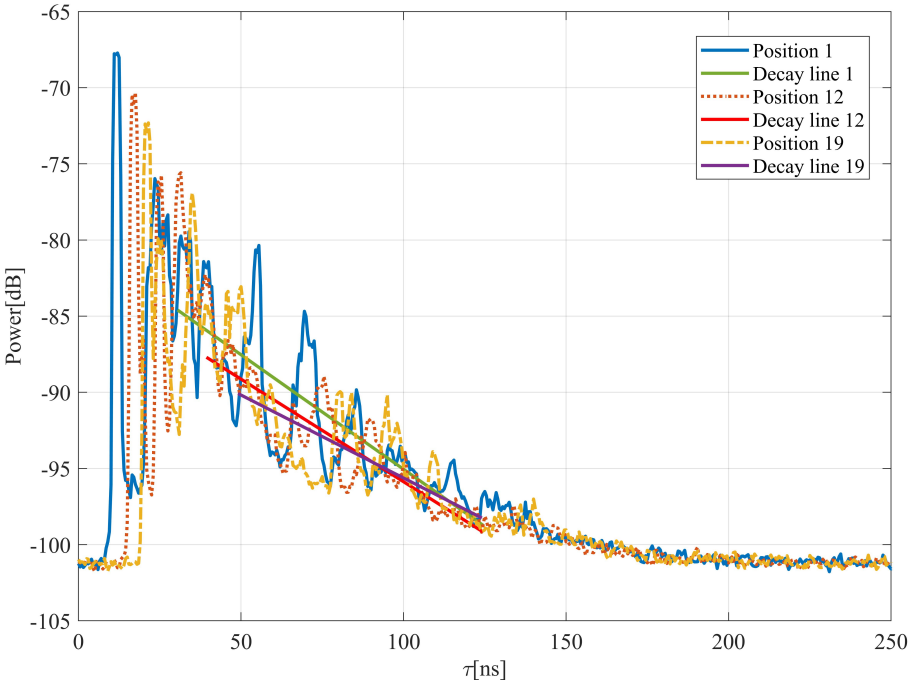

Fig. A.6: The APDPs of total 20 Tx locations observed at 27 GHz-29 GHz in R1-Classroom.

The characteristic parameters of total 20 Tx locations are plotted in Fig. A.7(a)-A.7(d). It can be observed that the values of decay factor β in Fig. A.7(a), delay spread in Fig. A.7(b) and angle spread in Fig. A.7(c) are relatively lower at position 1-5 than other positions and the values of LOS power ratio in

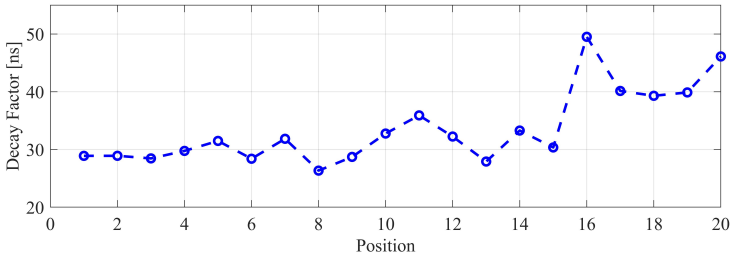

(a)

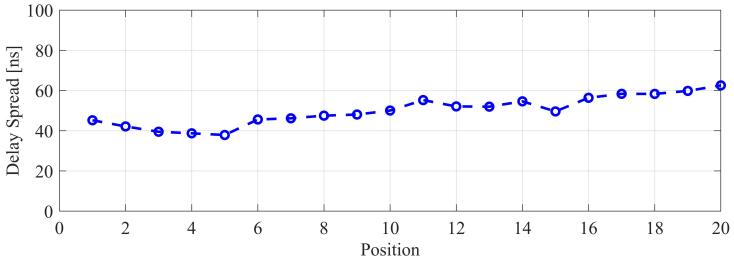

(b)

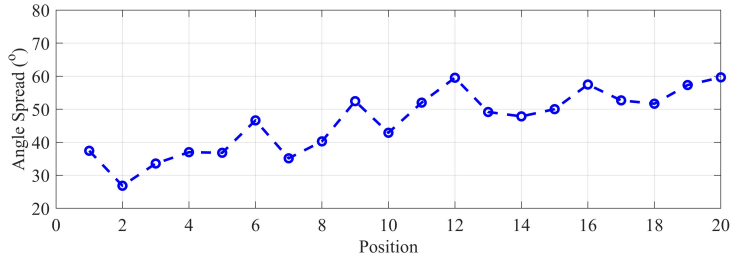

(c)

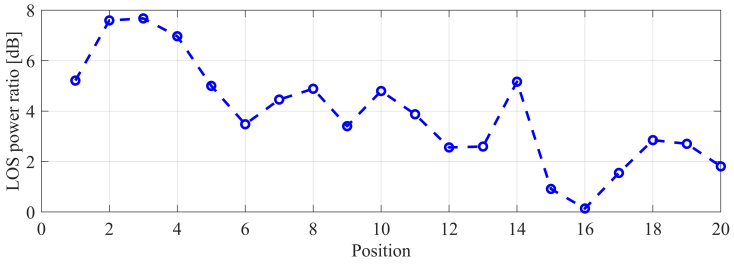

(d)

Fig. A.7: The channel characteristics of total 20 Tx locations observed at 27 GHz-29 GHz in R1-Classroom. (a) Decay factor. (b) Delay Spread. (c) Angle Spread. (d) LOS power ratio.

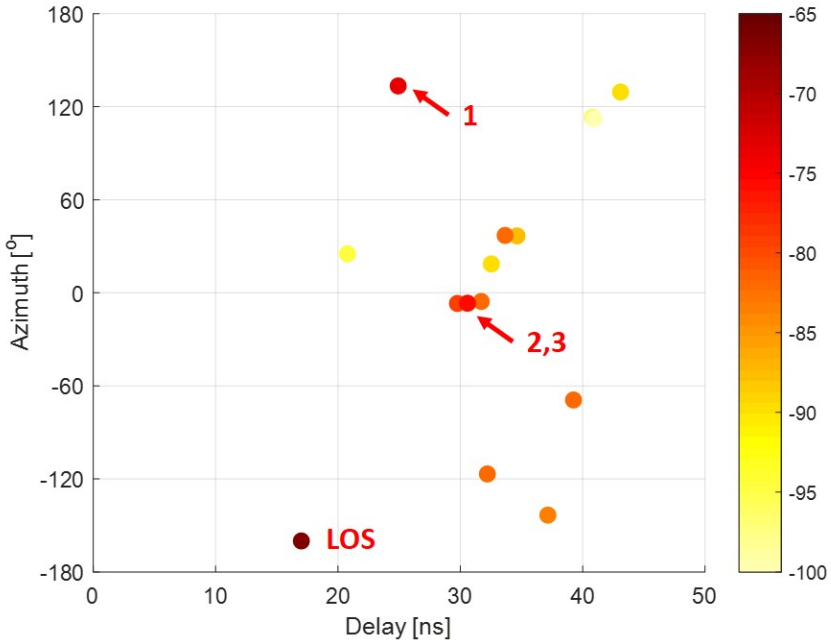

Fig. A.8: The PADPs of Tx position 12 at 27 GHz-29 GHz in R1-Classroom.

Fig. A.7(d) are higher than others. That is due to the fact that dominant LOS path has less path loss and strong reflections from the whiteboard and windows at position 1-5.

It is also found that the values of decay factor β, delay spread and angle spread are higher and the values of LOS power ratio are lower at positions 16-20 than other positions. That is probably due to the fact that the distance between Tx and Rx antenna is much larger, and the Tx antenna is much closer to the back wall with the distance of 0.6 m at the positions 16-20, leading to the lower power of the LOS path and richer multipath components from the back walls.

The power angle delay profiles (PADPs) of position 12, corresponding to the position with the highest angle spread, is shown in Fig. A.8. The large difference in angle spread among locations is most likely caused by the difference in path 1 (reflection from the windows) and path 2,3 (from the whiteboard on the west wall) among locations.

4.2 R2-Classroom

The APDPs with corresponding decaying lines of the measurement step 1 and 11 measured in R2-Classroom at 27 GHz-29 GHz are described in Fig. A.9 for an example, which show little relationship with the furniture moving out and in on the decay lines. Two strongest paths with the same power values of about -66.7 dB are found in APDPs shown in Fig. A.9. The two strongest paths are from LOS propagation and probably strong reflection from the corner, respectively. The strong reflection may be from the poles of the blackboard, as they are aluminum which reflects the radio wave well.

The characteristic parameters of total 11 steps are shown in Fig. A.10(a)-A.10(d). With removing the tables and chairs and moving back in the classroom, the values of decay factor β in Fig. A.10(a) and delay spread in Fig. A.10(b) remains stable. It can be observed that, there is little influence on the propagation channel for our measurements. One possible reason is that the Tx and Rx antennas were located higher than the objects in the room, resulting in little interaction between the objects and multipath components. The elevation half power beam width of commercial biconical is narrow, leading to the low power of reflection and scattering from tables.

It is noticed that with blind windows open in step 11, there will be small difference in the values of the decay factor in Fig. A.10(a), delay spread in Fig. A.10(b) and angle spread in Fig. A.10(c), which is perhaps due to the strong reflections from the open blind windows in the corner.

The similar tendency has been observed in Fig. A.10(d) that the values of LOS power ratio are distributed in the range between -2 and -3 dB, indicating that the measurements in the classroom are all not LOS dominated. That is because of the strong reflection from the aluminous poles of the blackboard near the

Tx located, with almost the same power of the LOS path propagation.

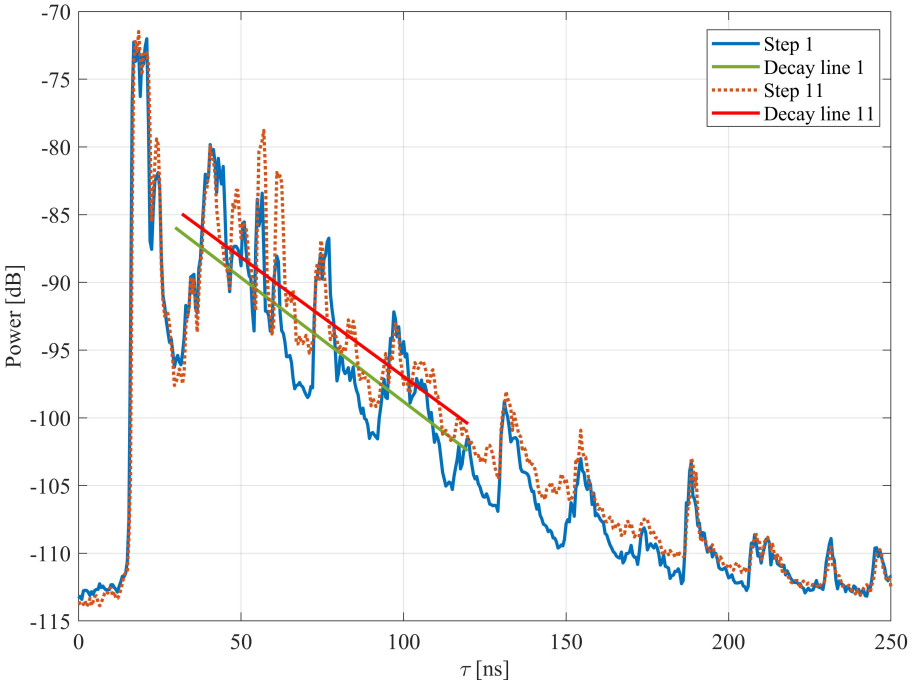

Fig. A.9: The APDPs of 11 steps at 27 GHz-29 GHz in R2-Classroom.

4.3 R3-Office

Fig. A.11 shows the APDPs with corresponding decaying lines of step 1, 6 and 11, which again shows slight relationship with the furniture richness in the office. The strongest paths of each step are from LOS path propagation, with the same power values of -66.7 dB. As we remove the contents on the shelves till with only shelves in step 6, the power level of specular paths is higher than fully occupied in step 1 shown in Fig. A.11. When we continue to remove the shelves till empty office in step 11, the power level of specular paths remains stable, due to the fact that the surface of the shelves is relatively small compared with the surface of the walls.

The characteristic parameters of total 11 steps measured in R3-Office at 27 GHz-29 GHz are plotted in Fig. A.12(a)-A.12(d). The similar tendency has been observed in Fig. A.12(a)-A.12(d), with minor variations in the values of decay factor, delay spread, angle spread and LOS power ratio, respectively. For the measurement steps from 1 to 6, the values of decay factor, delay spread and angle spread increase slightly and the values of LOS power ratio decrease, mostly due to the fact that less waves will be absorbed by the contents on the shelves,

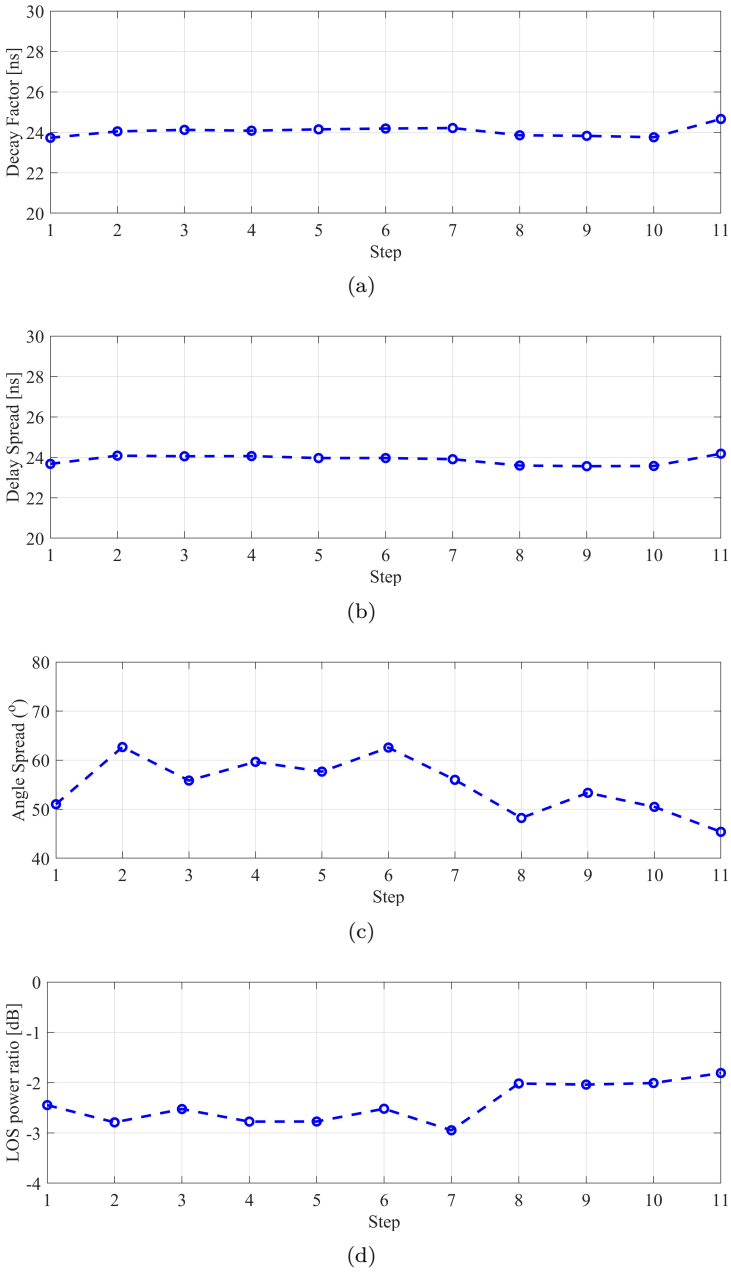

Fig. A.10: The channel characteristics of 11 steps at 27 GHz-29 GHz in R2-Classroom. (a) Decay factor. (b) Delay Spread. (c) Angle Spread. (d) LOS power ratio.

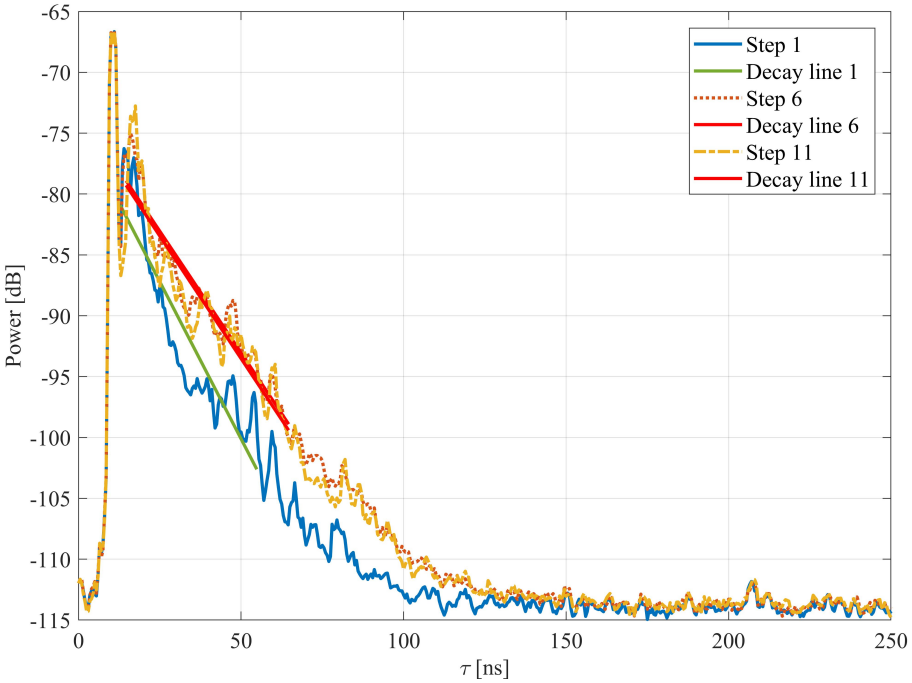

Fig. A.11: The APDPs of 11 steps at 27 GHz-29 GHz in R3-Office.

as the contents are removed from the shelves one by one. An explanation for the values of decay factor, delay spread, angle spread remain stable from step 7 to 11, is that the surfaces of the shelves are relatively small comparing with the walls, leading to little impact on the MPCs components in the office.

4.4 R4-Hall

The APDPs with corresponding decaying lines at position 1, 8, 15 measured in R4-Hall scenario at 27 GHz-29 GHz are plotted in Fig. A.13 for an example. It can be observed that there is little diffuse spectrum in Fig. A.13, due to the large dimension of the hall scenario. In this case, it makes no sense to study the decay factor in such large hall scenario, since the multipath components are dominated by specular components, with little diffuse components.

The characteristic parameters of total 20 Tx positions are shown in Fig. A.14(a)-A.14(c). It is observed that the values of delay spread and angle spread are relatively low as shown in Fig. A.14(a) and Fig. A.14(b), and the values of LOS power ratio in Fig. A.14(c) are small, because of the small Tx-Rx distance at the position 7-9, 10, 17 and 18.

Especially, the large deviation in the values of delay spread, angle spread,

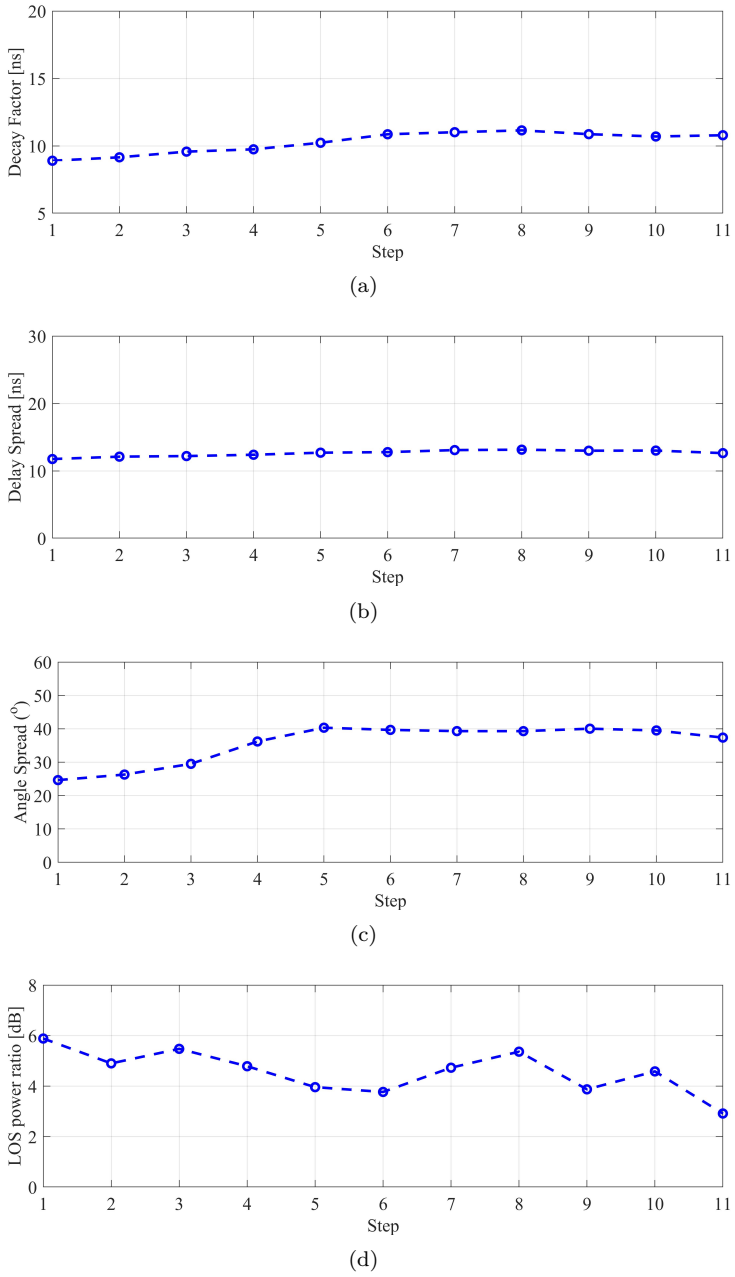

Fig. A.12: The channel characteristics of 11 steps at 27 GHz-29 GHz in R3-Office. (a) Decay factor. (b) Delay Spread. (c) Angle Spread. (d) LOS power ratio.

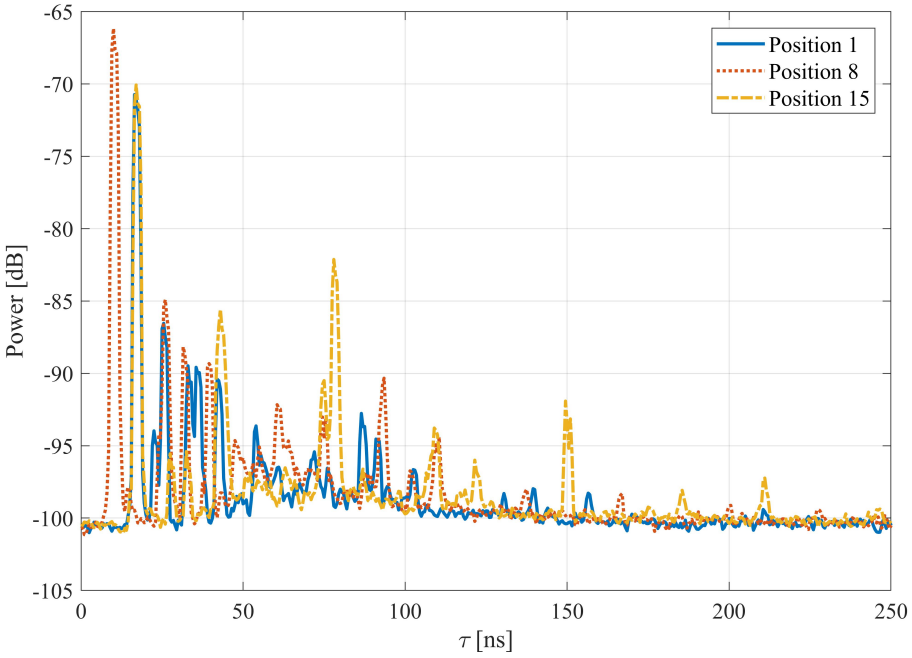

Fig. A.13: The APDPs of 20 positions at 27 GHz-29 GHz in R4-Hall.

Table A.2: Summary of the characteristic parameters.

Room	R1-Classroom	R2-Classroom	R3-Office	R4-Hall
Decay factor (ns)	26.33-49.51	23.73-24.66	8.90-11.15	N/A
Delay Spread (ns)	37.89-62.55	23.57-24.18	11.76-13.15	53.82-83.78
Angle Spread (°)	36.81-59.64	45.40-62.68	24.63-40.33	12.75-35.12
LOS power ratio (dB)	0.14-7.67	-2.95-(-1.81)	2.92-5.88	8.07-13.42

and LOS power ratio as shown in Fig. A.14(a)-A.14(c) at position 8 and 14, are mostly due to the distance between Tx and Rx. According to PADPs of position 8 and 14 obtained by the HRPE algorithm shown in Fig. A.15, the main specular components after the LOS path are sparse. Besides that, the strong reflections at position 8 are mainly from the white pillars and yellow ventilation tubes nearby as shown in Fig. A.15(a) with small range of azimuth, while mainly from the walls around at Tx position 14 in Fig. A.15(b) with large range of azimuth.

4.5 Discussion

The channel characteristics summarized in Table A.2 provide us with the similarities and difference between the propagation channels in different scenarios.

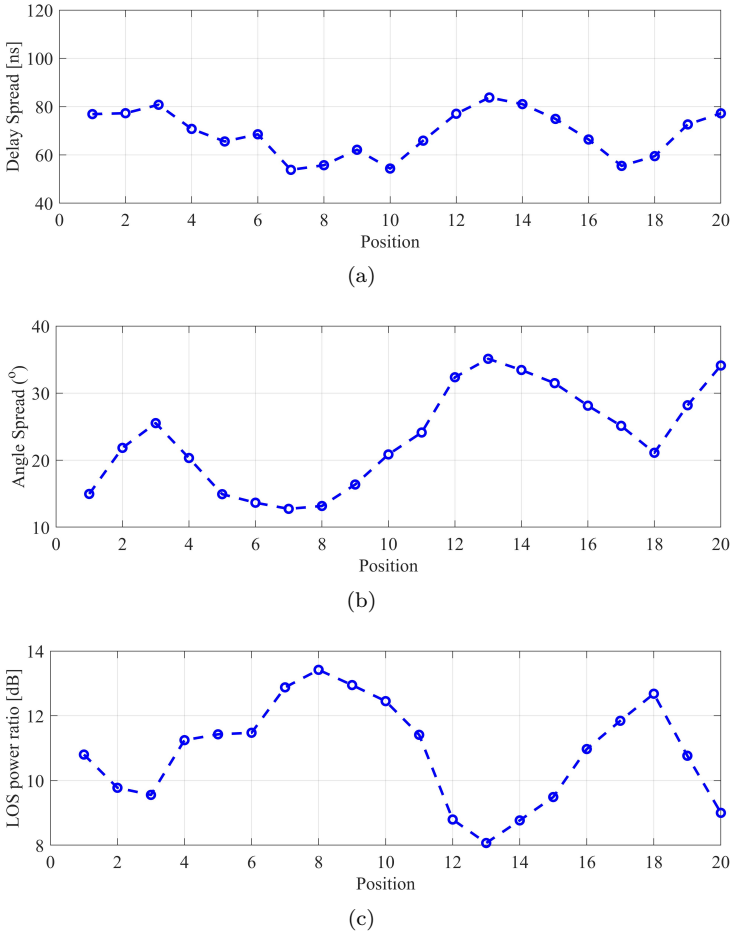

Fig. A.14: The channel characteristics of 20 positions at 27 GHz-29 GHz in R4-Hall. (a) Decay factor. (b) Delay Spread. (c) Angle Spread. (d) LOS power ratio.

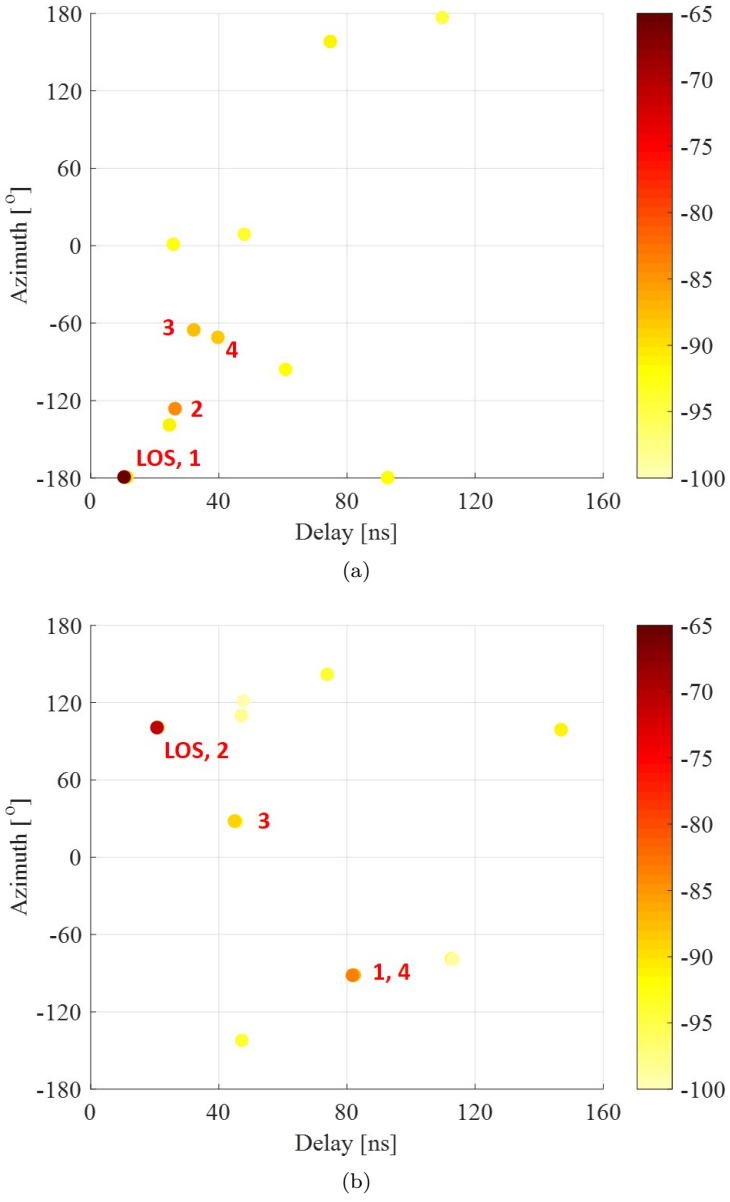

Fig. A.15: The PADPs of Tx positions 8 and 14 at 27 GHz-29 GHz in R4-Hall. (a) Position 8 (b) Position 14.

It can be found that the characteristic parameters are closely related to the room size of the scenarios. The values of the decay factor are similar in the same classroom of two scenarios, while the values in R3-Office are much lower, due to the small volume of the office. The diffuse spectrum can be observed in small room size of R3-Office, while in large dimension of R4-hall scenario, there is little diffuse spectrum observed, resulting in no decay factor.

The large values of the delay spread are observed in R4-Hall scenario, and smallest values of delay spread are seen in R3-Office with small room size. The values of delay spread in R1-Classroom are larger than that in R2-Classroom with the same room size, because of strong reflection from the poles of the blackboard in R2-Classroom. The LOS dominance and specular components are most apparent in open hall environment, according to the highest values of LOS power ratio.

The results of the measurements with Tx antenna at different positions in R1-Classroom and R4-Hall scenarios indicate that the characteristic parameters are also associated with the antenna locations in the scenario. The values of characteristic parameters are significantly affected by the antenna locations, due to the strong reflections from the objects, walls and corners around the antenna. As the Tx antenna was located in the corner of the R2-Classroom, there are strong reflection components from the poles of the blackboard in the corner, leading to the values of LOS power ratio in R2-Classroom lower than the values in other scenarios, presenting the NLOS dominance in R2-Classroom.

As ray tracing simulation mainly suffers from inaccurate database and computational complexity. The room furniture richness level on the characteristic parameters of the propagation channel is also investigated. This is beneficial for ray tracing simulation as detailed database description might not be needed in some scenarios. Our observation is that furniture richness might in some cases not relevant to the channel parameters. Since the channel parameters derived here may be dominated by the LOS path, the impact of furniture richness on channels may be interesting to consider the analysis in case of NLOS and obstructed-LOS as well in the further.

5 Conclusion

In this contribution, four indoor measurements in classrooms, office and hall were conducted at the frequency band of 27 GHz-29 GHz. Channel characteristics, i.e. decay factor, delay spread, angle spread and line of sight (LOS) power ratio, were investigated and compared in different scenarios.

The channel characteristics differ in different scenarios. It is found that the values of the delay spread in R4-Hall are much larger than that in R3-Office, and values of angle spread in R4-Hall are much smaller than that in R3-Office. It reveals that the size of the indoor scenarios has significant impact on the channel

characteristics. In individual scenarios, the channel characteristics vary with respect to different Tx locations, which can be seen from the apparent fluctuation of the channel characteristics at different Tx position in R1-Classroom and R4-Hall. Furthermore, in R2-Classroom and R3-Office, little fluctuation of the channel characteristics can be found with the furniture removing step by step, which indicates weakly impact of the furniture richness in indoor scenario on channel propagation. Generally speaking, the LOS and specular propagation mechanisms are dominant at 27 GHz-29 GHz mm-wave band, especially more apparent in large R4-Hall scenario. In addition, it is interested to notice the value of LOS power ratio in R2-Classroom is much lower than that in R1-Classroom. That is caused by the strong reflection from the aluminous poles of the blackboard in the corner Tx located in R2-Classroom.

References

[1] T. S. Rappaport, S. Sun, R. Mayzus, H. Zhao, Y. Azar, K. Wang, G. N. Wong, J. K. Schulz, M. Samimi, and F. Gutierrez. Millimeter wave mobile communications for 5G cellular: It will work! *IEEE Access*, 1:335–349, 2013.

[2] S. Salous, V. Degli Esposti, F. Fuschini, R. S. Thomae, R. Mueller, D. Dupleich, K. Haneda, J. Molina Garcia-Pardo, J. Pascual Garcia, D. P. Gaillot, S. Hur, and M. Nekovee. Millimeter-wave propagation: Characterization and modeling toward fifth-generation systems. [wireless corner]. *IEEE Antennas Propag. Mag.*, 58(6):115–127, Dec 2016.

[3] Yong Niu, Yong Li, Depeng Jin, Li Su, and Athanasios V. Vasilakos. A survey of millimeter wave communications (mmWave) for 5G: opportunities and challenges. *Wireless Networks*, 21(8):2657–2676, Nov 2015.

[4] R. He, B. Ai, G. L. Stüber, G. Wang, and Z. Zhong. Geometrical-based modeling for millimeter-wave mimo mobile-to-mobile channels. *IEEE Trans. Veh. Technol.*, 67(4):2848–2863, April 2018.

[5] T. S. Rappaport, Y. Xing, G. R. MacCartney, A. F. Molisch, E. Mellios, and J. Zhang. Overview of millimeter wave communications for fifth-generation (5G) wireless networks with a focus on propagation models. *IEEE Trans. Antennas Propag.*, 65(12):6213–6230, Dec 2017.

[6] C. T. Neil, M. Shafi, P. J. Smith, P. A. Dmochowski, and J. Zhang. Impact of microwave and mmwave channel models on 5G systems performance. *IEEE Trans. Antennas Propag.*, 65(12):6505–6520, Dec 2017.

[7] Jianhua Zhang, Pan Tang, Lei Tian, Zhixue Hu, Tan Wang, and Haiming Wang. 6–100 GHz research progress and challenges from a channel perspective for fifth generation (5G) and future wireless communication. *Science China Information Sciences*, 60(8):080301, Jun 2017.

[8] K. Guan, B. Ai, B. Peng, D. He, G. Li, J. Yang, Z. Zhong, and T. Kuerner. Towards realistic high-speed train channels at 5G millimeter-wave band – part I: Paradigm, significance analysis, and scenario reconstruction. *IEEE Trans. Veh. Technol.*, pages 1–1, 2018.

[9] D. He, B. Ai, K. Guan, Z. Zhong, B. Hui, J. Kim, H. Chung, and I. Kim. Channel measurement, simulation, and analysis for high-speed railway communications in 5G millimeter-wave band. *IEEE Trans. Intell. Transp. Syst.*, pages 1–15, 2018.

[10] M. Kyro, V. Kolmonen, and P. Vainikainen. Experimental propagation channel characterization of mm-wave radio links in urban scenarios. *IEEE Antennas Wireless Propag. Lett.*, 11:865–868, 2012.

[11] P. F. M. Smulders. Statistical characterization of 60-GHz indoor radio channels. *IEEE Trans. Antennas Propag.*, 57(10):2820–2829, Oct 2009.

[12] T. S. Rappaport, J. N. Murdock, and F. Gutierrez. State of the art in 60-GHz integrated circuits and systems for wireless communications. *Proc. IEEE*, 99(8):1390–1436, Aug 2011.

[13] C. Gustafson, K. Haneda, S. Wyne, and F. Tufvesson. On mm-wave multipath clustering and channel modeling. *IEEE Trans Antennas Propag*, 62(3):1445–1455, March 2014.

[14] T. S. Rappaport, G. R. MacCartney, M. K. Samimi, and S. Sun. Wideband millimeter-wave propagation measurements and channel models for future wireless communication system design. *IEEE Trans. Commun.*, 63(9):3029–3056, Sept 2015.

[15] K. Haneda, J. Järveläinen, A. Karttunen, M. Kyrö, and J. Putkonen. A statistical spatio-temporal radio channel model for large indoor environments at 60 and 70 GHz. *IEEE Trans. Antennas Propag.*, 63(6):2694–2704, June 2015.

[16] Y. Azar, G. N. Wong, K. Wang, R. Mayzus, J. K. Schulz, H. Zhao, F. Gutierrez, D. Hwang, and T. S. Rappaport. 28 GHz propagation measurements for outdoor cellular communications using steerable beam antennas in new york city. In *2013 IEEE International Conference on Communications (ICC)*, pages 5143–5147, June 2013.

[17] H. Zhao, R. Mayzus, S. Sun, M. Samimi, J. K. Schulz, Y. Azar, K. Wang, G. N. Wong, F. Gutierrez, and T. S. Rappaport. 28 GHz millimeter wave cellular communication measurements for reflection and penetration loss in and around buildings in new york city. In *2013 IEEE International Conference on Communications (ICC)*, pages 5163–5167, June 2013.

[18] M. Samimi, K. Wang, Y. Azar, G. N. Wong, R. Mayzus, H. Zhao, J. K. Schulz, S. Sun, F. Gutierrez, and T. S. Rappaport. 28 GHz angle of arrival and angle of departure analysis for outdoor cellular communications using steerable beam antennas in new york city. In *2013 IEEE 77th Vehicular Technology Conference (VTC Spring)*, pages 1–6, June 2013.

[19] J. Ko, Y. Cho, S. Hur, T. Kim, J. Park, A. F. Molisch, K. Haneda, M. Peter, D. Park, and D. Cho. Millimeter-wave channel measurements and analysis for statistical spatial channel model in in-building and urban environments at 28 GHz. *IEEE Trans. Wireless Commun.*, 16(9):5853–5868, Sept 2017.

[20] Wei Fan, Ines Carton, Jesper Ø. Nielsen, Kim Olesen, and Gert F. Pedersen. Measured wideband characteristics of indoor channels at centimetric and millimetric bands. *EURASIP Journal on Wireless Communications and Networking*, 2016(1):58, Feb 2016.

[21] P. Hanpinitsak, K. Saito, W. Fan, J. Takada, G. F. Pedersen. Frequency Characteristics of Path Loss and Delay-Angular Profile of Propagation Channels in An Indoor Room Environment in SHF Bands. In *IEICE Technical report, SRW2016-96,*, Mar 2017.

[22] Ainfoinc. SZ-2003000-P.pdf [online]. Technical report, Available: http: //www.ainfoinc.com/en/pro_ pdf/new_ products/antenna/Bi-Conical% 20Antenna/tr_ SZ-2003000-P.pdf, (2018, June 5).

[23] S. S. Zhekov, A. Tatomirescu, and G. F. Pedersen. Antenna for ultrawideband channel sounding. *IEEE Antennas Wireless Propag. Lett.*, 16:692–695, 2017.

[24] G. Steinböck, T. Pedersen, B. H. Fleury, W. Wang, and R. Raulefs. Experimental validation of the reverberation effect in room electromagnetics. *IEEE Trans. Antennas Propag.*, 63(5):2041–2053, May 2015.

[25] A. Bamba, W. Joseph, J. B. Andersen, E. Tanghe, G. Vermeeren, D. Plets, J. Ø. Nielsen, and L. Martens. Experimental assessment of specific absorption rate using room electromagnetics. *IEEE Trans. Electromagn. Compat.*, 54(4):747–757, Aug 2012.

[26] X. Cai, X. Yin, X. Cheng, and A. Pérez Yuste. An empirical random-cluster model for subway channels based on passive measurements in UMTS. *IEEE Trans. Commun.*, 64(8):3563–3575, Aug 2016.

[27] Xuesong Cai and Wei Fan. A Complexity-Effcient High Resolution Propagation Parameter Estimation Algorithm for Ultra-Wideband Large-Scale Uniform Circular Array. *IEEE Transactions*, 2018.

[28] 3GPP. Study on channel model for frequencies from 0.5 to 100 GHz. *(3GPP TR25.996 version 14.0.0 Release 14)*, 2018.

Paper B

Millimeter-Wave Channel Characterization in Large Hall Scenario at the 10 and 28 GHz Bands

Guojin Zhang, Panawit Hanpinitsak, Xuesong Cai, Wei Fan, Kentaro Saito, Jun-ichi Takada, and Gert Frølund Pedersen

The paper has been published in the
13th European Conference on Antennas and Propagation (EuCAP), 2019.

The layout has been revised.

Abstract

This paper presents the characteristics of the mm-wave propagation channel in hall scenario at the frequency bands of 9−11 GHz and 27−29 GHz. The spherical propagation parameters, i.e. delay, azimuth, elevation, source distance and complex amplitude are estimated by the high resolution parameter estimation (HRPE) algorithm. Based on the results, the channel characteristics, e.g. path loss, delay spread, and angle spread are analyzed for different mm-wave bands. The results reveal that the line of sight and specular components are dominant in such large size scenario at 9−11 GHz and 27−29 GHz bands, and little differences in the characteristics between the two bands can be observed.

1 Introduction

The next generation communication system (5G) is moving towards frequency bands above 6 GHz, due to the plenty of available spectrum and higher data traffic supported at millimeter wave (mm-wave) bands. Accurate knowledge of the channel propagation characteristics in mm-wave frequencies band is important for mm-wave system design and performance evaluation [1].

Extensive measurement campaigns have been conducted for mm-wave channels, with focusing on the comparison of channels in different frequency bands in the same environment [2–4]. In [2], the measurements were conducted in a typical indoor office environment at 28 GHz and 73 GHz frequency bands. Large-scale path loss and temporal statistic are provided, using rotatable directional horn antennas. In [5], the frequency dependency of propagation parameters, e.g. power delay profile, delay spread, path loss and shadow fading were investigated in three different indoor environments, such as hall, meeting room and corridor scenarios. In [6], the large scale parameters, i.e. path-loss, shadowing, cross-polarization power ratio, delay spread and coherence bandwidth were investigated in various indoor environments at 11 GHz, including two hall scenarios and three rooms. To the author's best knowledge, the analysis of the channel characteristics at different frequency bands in these indoor cases, is still limited comparing the power spectrum and delay spread in most papers.

In this paper, the comparison of propagation characteristics with total 20 Tx antenna locations at 9−11 GHz and 27−29 GHz bands in large hall scenario are investigated. The high resolution parameter estimation (HRPE) algorithm is used for extracting the information of delay, angle and amplitude, which are used for calculating the characteristics, such as path loss, delay spread and angle spread.

The rest of this paper is organized as follows. In Sect. 2, the measurement campaign is presented. Sect. 3 describes the channel characteristics, and the results of propagation parameters are analyzed. Sect. 4 summarizes the conclusions.

Table B.1: Measurement Setup.

Room	Hall
Dimension (m^3)	$39 \times 20 \times 10$
Tx antenna	Commercial biconical SZ-2003000/P
Rx antenna	Homemade biconical antenna
Center frequency	10, 28 GHz
Bandwidth	2 GHz
Tx\Rx antenna height	1.50 m
Frequency sweep points	360
Frequency samples	750
UCA radius	0.24 m

2 Measurement campaign

Fig. B.1 illustrates the top-view sketch of the hall scenario in Aalborg University, where the measurement campaign was conducted at the frequency band of 9−11 GHz and 27−29 GHz, using a channel sounder [3, 7] based on a vector network analyzer (VNA). The measurement setup parameters are depicted in Table. B.1. The shape of the hall is irregular, with 39 m from west to east, 20 m from north to south and 10 m height from the ground to the ceiling. The four big yellow ventilation tubes and six small white pillars are located around the hall.

The commercial biconical antenna SZ-2003000/P [8] was used as transmitter (Tx) antenna and homemade biconical antenna [9] was used as receiver (Rx) antenna, as shown in Fig. B.2. The Rx antenna was rotated clockwise on a rotating pedestal with a pre-set radius of 0.24 m with 1 degree rotating steps, to form a large-scale uniform circular array (UCA) with 360 elements. The antenna gains of commercial antenna are 2.75 dBi at 10 GHz and 4.8 dBi at 28 GHz. For the homemade antenna, the gains are 3.5 dBi at 10 GHz and 6 dBi at 28 GHz. A total of 20 spatial snapshots were measured by moving the Tx antenna and the Rx antenna was located near the yellow ventilation tubes as shown in Fig. B.1. Each Tx in each row was spaced 1 m apart. The height of the Tx and Rx antennas is mounted at 1.50 m. The measurement was conducted with a bandwidth of 2 GHz and 750 samples were collected for each frequency band.

3 Radio channel characterization

The measured raw data is processed by the hanning window and inverse Fourier transform (IFT), then the average power delay profiles (APDPs), which can be

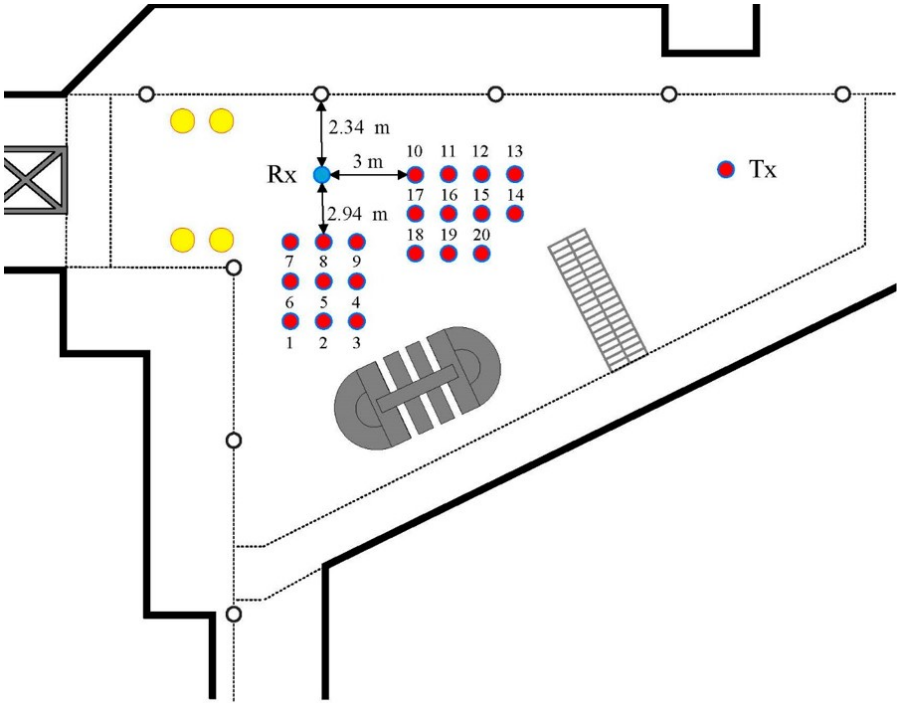

Fig. B.1: Top view of the hall scenario with 20 Tx locations and single Rx location.

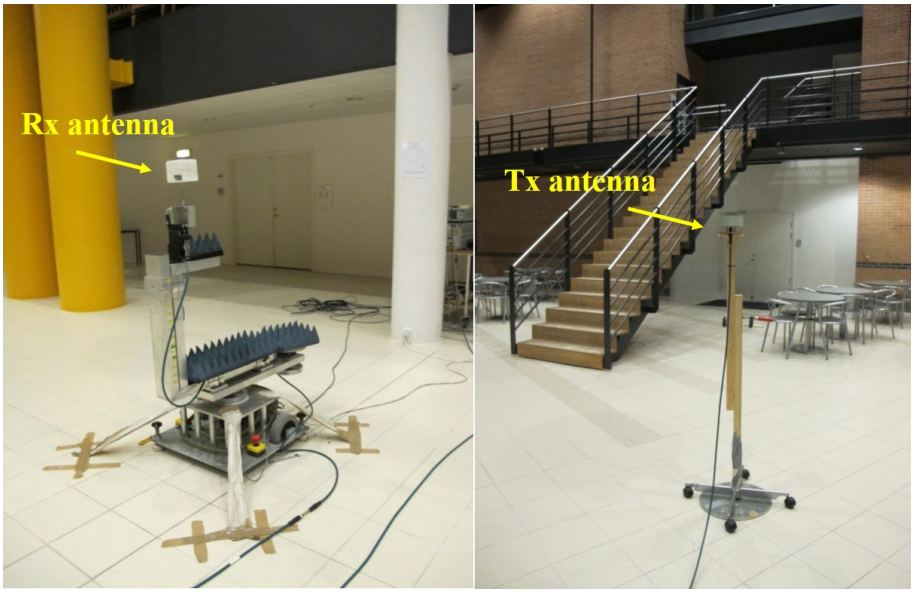

Fig. B.2: The photograph of Rx (left) and Tx (right) antennas.

obtained by the channel impulse response (CIR) $h_{m,n}(\tau)$ as

$$P_m(\tau) = \frac{1}{N}\sum_{n=1}^{N}|h_{m,n}(\tau)|^2 \tag{B.1}$$

where $h_{m,n}(\tau)$ represents the CIR at m-th delay sample and n-th measured element.

In order to study the channel characteristics of the mm-wave spherical propagation, the HRPE algorithm [10] is applied to derive the parameters of the UCA channels, i.e. azimuth angles, elevation angles, delays, source distances and amplitudes of multipath components (MPCs). The spatial-temporal CIR $h(t;\tau,\theta,\phi,d)$ can be described as

$$h(t;\tau,\theta,\phi,d) = \sum_{l=1}^{L}\alpha_l\delta(\tau-\tau_l)\delta(\theta-\theta_l)\delta(\phi-\phi_l)\delta(d-d_l), \tag{B.2}$$

where L is the number of spherical waves impinge into the UCA, α_l represents the complex amplitude, τ_l is the propagation delay, θ_l and ϕ_l represent the azimuth and elevation angles of the l-th path, respectively. d_l is the propagation distance between the UCA center and the last source point during the propagation route of the l-th path, respectively. These parameters are used for calculating the characteristics of the channel propagation in this section.

3.1 Path loss

Path Loss is a fundamental channel model for estimating the link budget and coverage in cellular network [11]. The path loss of each Tx location can be calculated by the sum power of the CIRs, which can be represented as

$$PL = P_{\mathrm{Tx}} - P_{\mathrm{Rx}} + G_{\mathrm{Tx}} + G_{\mathrm{Rx}}[\mathrm{dB}] \tag{B.3}$$

where P_{Tx} and P_{Rx} are the transmit and received power, respectively. G_{Tx} and G_{Rx} are the the gains of the Tx and Rx antennas used at the measurement frequency, respectively. The path loss can be represented by the integrating all the power of the paths, can be obtained by the CIRs as

$$P_{Tx} - P_{Rx} = \sum_{m=1}^{M} P_m(\tau) \tag{B.4}$$

Table. B.2 shows the path loss model fitting results, in which the path loss model is expressed by

$$PL(d)[\mathrm{dB}] = a + 10\cdot b\log_{10}(d[\mathrm{m}]) + X_\sigma \tag{B.5}$$

where a is the fading constant and b is the path loss exponent, which are both the least-square fits of floating intercept and the slope. d represents the

Table B.2: path loss model parameters.

Frequency band (GHz)	a	b	X_σ
10	51.651	1.712	0.195
28	63.725	1.525	0.468

distance between Tx and Rx antennas, with the reference distance set as 1 m. X_σ denotes the shadowing variation, which is represented by the log-normal random variable with standard deviation σ.

Fig. B.3(a) shows the measured path loss compared with the free space path loss at the frequency bands of 9-11 GHz and 27-29 GHz. The measured path loss at 9-11 GHz is little lower than free space path loss. While, in case of 27-29 GHz band, the measured path loss was roughly the same as free space path loss. It can also be seen from the results in Table. B.2 that the path loss exponents b are similar to 2 due to large size of the hall scenario. These results match the results in [2] which reported that the b decreases with frequencies and values are higher than 1.5.

3.2 Delay Spread

The delay spread is widely used for characterizing the MPCs richness of the channels [12]. In this section, delay spread is calculated by two methods. The first method is based on the measured raw data with dynamic range of 25 dB, and the second is based on the delay information estimated by HPRE algorithm.

The delay spread is calculated as the second-order central moments of APDPs. The mean delay $\bar{\tau}$ and root mean square delay spread σ_τ with the first method can be computed as [12]

$$\bar{\tau} = \frac{\sum_{m=1}^{M} P_m(\tau) \cdot \tau}{\sum_{m=1}^{M} P_m(\tau)}, \tag{B.6}$$

$$\sigma_\tau = \sqrt{\frac{\sum_{m=1}^{M} P_m(\tau) \cdot \tau^2}{\sum_{m=1}^{M} P_m(\tau)} - \bar{\tau}^2}. \tag{B.7}$$

For the second method, $P_m(\tau)$ need to be replaced by the square of complex amplitude $|\alpha_l|^2$ obtained by the HPRE algorithm. Besides that, the delay sample m and M should be exchanged with the number of the estimated paths l and L, respectively.

The similar trend by the two methods at 10 GHz and 28 GHz can be observed from Fig. B.3(b). The difference between the two methods at the same frequency is due to the affect of the sidelobes in measured raw data. Thus, more

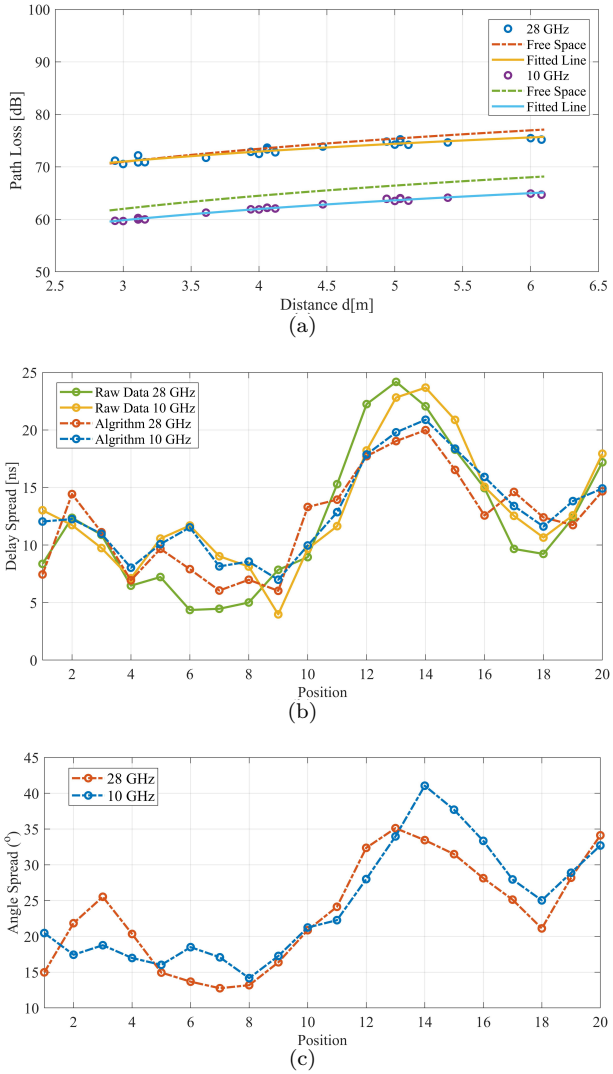

Fig. B.3: The channel characteristics in hall scenario at total 20 Tx locations. (a) Path Loss. (b) Delay Spread. (c) Angle Spread.

accurate results can be achieved by the HPRE algorithm. The lowest values of delay spread can be seen at position 7-10 and 17-18, where is the smallest Tx-Rx distance.

3.3 Angle Spread

Because the estimated elevation angles are almost close to 90 degrees, only azimuth angles are investigated. The angle spread σ_θ can be calculated, as defined in [10, 13],

$$\sigma_\theta = \sqrt{-2\log\left(\left|\frac{\sum_{l=1}^{L}\exp(j\theta_l)\cdot|\alpha_l|^2}{\sum_{l=1}^{L}|\alpha_l|^2}\right|\right)}. \tag{B.8}$$

The large deviation in the values of angle spread is depicted in Fig. B.3(c) at positions 5-10 and 12-16, 20. That is because positions 5-10 are much close to the Rx antenna, yellow ventilation tubes and pillars, the strong reflections at these positions are mainly from the white pillars and yellow ventilation tubes nearby with small range of azimuth. While positions 12-16 and 20 are relatively far from the Rx antenna, yellow ventilation tubes and pillars, the reflections are mainly from the walls around with large range of azimuth.

According to the power angle delay profiles (PADPs) of position 8 obtained by the HRPE algorithm in Fig. B.4(a), the main specular components after the LOS path are identified and plotted in Fig. B.4(b). It could be seen that strong specular reflected paths are mainly contributed by the yellow ventilation tubes and white pillars. On the other hand, the main specular components after the LOS path are sparse at 10 and 28 GHz bands and the LOS components are dominant at the positions with small Tx-Rx distance.

4 Conclusion

In this paper, the radio channel of hall scenario is characterized at frequency bands of 9−11 GHz and 27−29 GHz. Based on the virtual uniform circular array (UCA) system and high resolution parameter estimation (HRPE) algorithm, specular propagation paths are identified and their delay, azimuth and elevation information are estimated. The properties of the radio channel at 9−11 GHz and 27−29 GHz bands are studied in terms of path loss, angle spread, and delay spread. The result shows that the differences between two frequency bands are mostly minor. The measured path loss at 27−29 GHz is similar with the free space path loss, duo to dominant LOS path. The path loss exponents b are higher than 1.5 at 9−11 GHz and 27−29 GHz, due to the large size of the hall scenario. It can also be observed that the values of delay spread obtained by HRPE algorithm are more accurate than that by measured raw

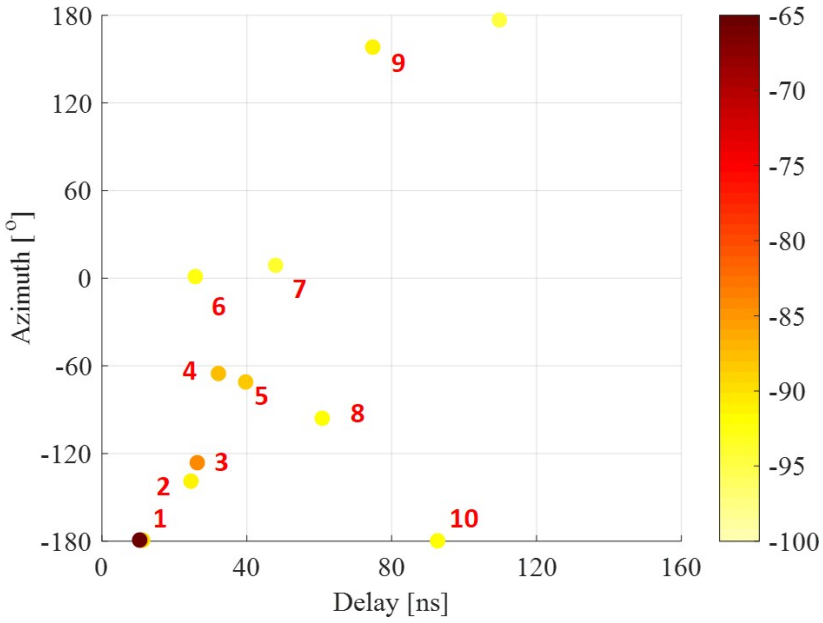

(a)

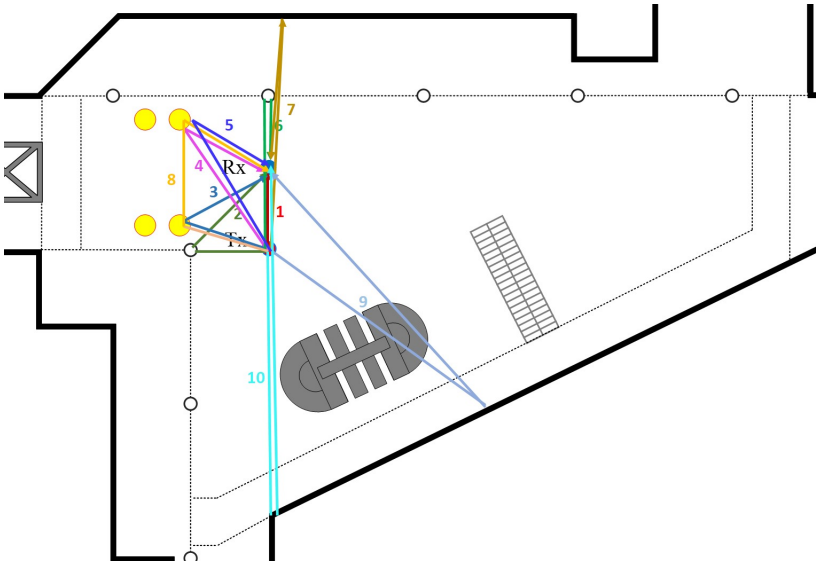

(b)

Fig. B.4: The PADPs and identified paths of Tx positions 8 at 27 GHz-29 GHz in Hall.

data, with the range of 6−20 ns. The values of angle spread are mainly ranged between 12.75 ° and 41 °. In order to reveal further channel characteristics in non-line of sight scenarios, more measurements and simulation data are still needed.

References

[1] T. S. Rappaport, S. Sun, R. Mayzus, H. Zhao, Y. Azar, K. Wang, G. N. Wong, J. K. Schulz, M. Samimi, and F. Gutierrez. Millimeter wave mobile communications for 5G cellular: It will work! *IEEE Access*, 1:335–349, 2013.

[2] G. R. Maccartney, T. S. Rappaport, S. Sun, and S. Deng. Indoor office wideband millimeter-wave propagation measurements and channel models at 28 and 73 GHz for ultra-dense 5G wireless networks. *IEEE Access*, 3:2388–2424, 2015.

[3] Wei Fan, Ines Carton, Jesper Ø. Nielsen, Kim Olesen, and Gert F. Pedersen. Measured wideband characteristics of indoor channels at centimetric and millimetric bands. *EURASIP Journal on Wireless Communications and Networking*, 2016(1):58, Feb 2016.

[4] J. Vehmas, J. Jarvelainen, S. L. H. Nguyen, R. Naderpour, and K. Haneda. Millimeter-wave channel characterization at helsinki airport in the 15, 28, and 60 GHz bands. In *2016 IEEE 84th Vehicular Technology Conference (VTC-Fall)*, pages 1–5, Sept 2016.

[5] S. Geng and P. Vainikainen. Frequency and bandwidth dependency of UWB propagation channels. In *2006 IEEE 17th International Symposium on Personal, Indoor and Mobile Radio Communications*, pages 1–5, Sept 2006.

[6] M. Kim, Y. Konishi, Y. Chang, and J. Takada. Large scale parameters and double-directional characterization of indoor wideband radio multipath channels at 11 GHz. *IEEE Transactions on Antennas and Propagation*, 62(1):430–441, Jan 2014.

[7] Panawit Hanpinitsak, Kentaro Saito, Wei Fan, Jun-ichi Takada, and Gert F Pedersen. Frequency characteristics of path loss and delay-angular profile of propagation channels in an indoor room environment in SHF bands. In *Mobile Communication Workshop*, 2017.

[8] ainfoinc. SZ-2003000-P.pdf [online]. Technical report, Available: http: //www.ainfoinc.com/en/pro_ pdf/new_ products/antenna/Bi-Conical% 20Antenna/tr_ SZ-2003000-P.pdf, (2018, June 5).

[9] S. S. Zhekov, A. Tatomirescu, and G. F. Pedersen. Antenna for ultrawideband channel sounding. *IEEE Antennas and Wireless Propagation Letters*, 16:692–695, 2017.

[10] Xuesong Cai and Wei Fan. A complexity-effcient high resolution propagation parameter estimation algorithm for ultra-wideband large-scale uniform circular array. *submitted to IEEE Trans. Commun.*, 2018.

[11] J. Ko, Y. Cho, S. Hur, T. Kim, J. Park, A. F. Molisch, K. Haneda, M. Peter, D. Park, and D. Cho. Millimeter-wave channel measurements and analysis for statistical spatial channel model in in-building and urban environments at 28

GHz. *IEEE Transactions on Wireless Communications*, 16(9):5853–5868, Sept 2017.

[12] X. Cai, X. Yin, X. Cheng, and A. Pérez Yuste. An empirical random-cluster model for subway channels based on passive measurements in UMTS. *IEEE Trans. Commun.*, 64(8):3563–3575, Aug 2016.

[13] 3GPP. Study on channel model for frequencies from 0.5 to 100 GHz. *(3GPP TR 38.901 version 14.0.0 Release 14)*, 2018.

Paper C

Modeling Multi-frequency Characteristics for Classroom and Hall Scenarios at 2-4, 9-11 and 27-29 GHz Bands

Guojin Zhang, Jesper Ødum Nielsen, Xuesong Cai, Kentaro Saito, Panawit Hanpinitsak, Jun-Ichi Takada, Gert Frølund Pedersen and Wei Fan

The paper has been published in the
IEEE Access Vol. 9, pp. 14549-14563, 2021.

The layout has been revised.

Abstract

This paper investigates the wideband channel characteristics obtained in a classroom and a hall indoor scenarios at 2-4, 9-11 and 27-29 GHz. A virtual uniform circular array (UCA) based channel sounding system was utilized to capture wideband spatial channel characteristics. The propagation parameters of multipath components (MPCs) were estimated by using a high resolution parameter estimation (HRPE) algorithm. The estimated MPCs are further grouped into clusters via a novel clustering identification algorithm based on the KPower-Means algorithm. The comparison of the composite and cluster-level characteristics at multiple frequency bands in both scenarios is investigated. Moreover, the impact of the indoor room environment, i.e. dimension and furniture, on the propagation channel is also analyzed. The statistics of channel parameters at multiple frequency bands extracted constitute a stochastic clustered spatial channel model.

1 Introduction

The centimeter-wave (cm-wave) and millimeter-wave (mm-wave) spectra have been envisioned to support more data traffic and higher system capacity in the fifth generation (5G) communications [1–3]. The frequency bands from 450 MHz to 85 GHz are considered as candidates for 5G communications by "Mobile and wireless communications Enablers for the Twenty-twenty Information Society" (METIS) project [4]. Since the channel characteristics at mm-wave frequencies differ from those below 6 GHz [5], it is necessary to establish realistic spatio-temporal channel models at different frequency bands for 5G communication networks.

Extensive research on channel characteristics at different cm-wave and mm-wave frequencies have been done [5–8]. It is found that mm-wave transmission suffers significant atmospheric attenuation and cannot penetrate most solid materials very well compared with lower frequency. Besides, reflection is more dominant than diffraction and diffuse scattering at mm-wave bands [7, 9]. Because of these channel characteristics at mm-wave frequencies, 5G communication systems require highly directional antennas, large antenna array, and adaptive beamforming techniques [10]. Understanding the angular characteristics is critical for 5G communications. For this purpose, a considerable amount of measurement-based investigations can be found in the literature, which are mainly divided into two categories: those using a rotated directional antenna (RDA)-based method [9, 11–14] or a uniform virtual array (UVA)-based method [14–17]. *i*) For the RDA-based method, a highly directional antenna with a certain half-power-beamwidth (HPBW), such as a horn antenna, is rotated to scan the azimuth and elevation directions. The drawback of this method is the spatial resolution limited by the beamwidth of the an-

tenna. In [11], directional horn antennas with 17° HPBW at 25.5 and 28 GHz, 11° HPBW at 37.5 and 39.5 GHz, connected with a time-domain mm-wave channel sounder were utilized to conduct measurement campaigns in a conference room. Frequency-dependent channel parameters with different polarimetric combinations, including root-mean-square (RMS) delay and angular spread, were investigated. Besides, in [9] directional horn antennas with 10° HPBW in both the azimuth and elevation planes were used for the in-building and urban cellular communication systems at 28 GHz. Spatio-temporal channel characteristics and detailed cluster analysis of both the intra- and inter-cluster distributions were investigated. Moreover, in [12] the measurement was conducted at Helsinki Airport in the 15, 28, and 60 GHz bands by means of directional wideband channel sounding using directive horn antennas with 10° and 40° HPBWs in the azimuth and elevation domains, respectively. Channel characteristics at 15, 28, and 60 GHz bands were analyzed and compared by the parameters of the specular propagation paths, specular and diffuse power contributions, polarization, and the delay and angular spreads. In addition, extensive wideband indoor propagation measurements were conducted using rotatable directional horn antennas with 28.8°/30° azimuth/elevation HPBW and 15°/15° azimuth/elevation HPBW, for 28 GHz and 73 GHz, respectively in [13]. Channel characteristics including large-scale path loss models and temporal statistics derived from these measurements were investigated. *ii*) For the UVA-based method, an antenna is moved to different positions with a step less than a half wave-length to form a uniform virtual array, which usually takes a long time to finish one measurement snapshot. In [14], both RDA and UVA methods were adopted and compared to investigate the channel at 60 GHz in a 3D space, including the azimuth and elevation information. In [15], massive multiple-input multiple-output (MIMO) channel measurements at 11, 16, 28, and 38 GHz bands in indoor office environments were conducted by using a vector network analyzer (VNA) and large virtual rectangular arrays. Massive MIMO propagation properties, such as spherical wavefront, cluster birth-death, and non-stationarity over the antenna array were investigated. By applying a virtual uniform cylindrical array in [16], the diffuse scattering of radio waves in 3, 10 and 28 GHz bands were evaluated. It was found that the power and the angular spread of diffuse scattering tend to decrease as the frequency increased. In [17], the authors studied the frequency dependent characteristics at the 5.8, 14.8, and 58.7 GHz bands by a virtual uniform cubic array. However, these works lack the comparison of channel propagation characteristics at multiple frequency bands in different indoor scenarios with the same channel sounding and measurement configuration. Moreover, the impact of the indoor room environment, i.e. dimension and furniture, on channel propagation characteristics has not been fully investigated.

The current work will analyze data measured in the frequency bands of 2-4, 9-11 and 27-29 GHz obtained in a classroom and a hall scenarios using a virtual uniform circular array (UCA) based channel sounding system. The

data at 2-4, 9-11 and 27-29 GHz was previously analyzed in [18–21] and the data at 27-29 GHz was previously investigated in [22]. In [18], the frequency characteristics of geometry-based clusters at the frequency bands 2-4, 9-11 and 27-29 GHz in the hall scenario were investigated. The cluster intensity and spread characteristics of geometry-based clusters in the classroom scenario at 9-11 and 27-29 GHz, and in both the hall and classroom scenarios at 27-29 GHz were also investigated in [19] and [20], respectively. In [18–20], the space-alternating generalized expectation-maximization algorithm (SAGE) was utilized for extracting the parameters of multipath components (MPCs) by assuming the same number of paths for different frequency bands. However, the actual number of MPCs in the frequency bands can be different, due to the channel sparsity at mm-wave frequency bands [23]. Suitable number of paths assuming for each frequency band is necessary to obtain accurate estimation results. Moreover, spatial non-stationarity in realistic channel, such as the power variation across the antenna elements should also be considered [24]. Therefore, to fully and realistically extract the parameters of the MPCs, a complexity-efficient high resolution parameter estimation (HRPE) algorithm is needed. Meanwhile, geometry-based clusters were estimated by the enhanced scattering point-based KPowerMeans (SPKPM) algorithm in [18–20] and categorized into different groups based on the propagation mechanism. The results show that specular reflections are not significantly frequency dependent, while shadowing, scattering, diffraction, and the Fresnel zone plate effect had significant frequency dependency. However, [18–20] lacks the comparison of channel characteristics in different scenarios at different frequency bands. In [21], the characteristics of path loss and delay-angular profile in the classroom scenario at the frequency bands 2-4, 9-11 and 27-29 GHz were analyzed, where a beamforming method with low angular resolution was exploited. In addition, in [22], four large-scale UCA based measurement campaigns were conducted in various indoor scenarios, including classroom, office, and hall scenarios, at the frequency band 27-29 GHz. The spatial channel characteristics were investigated and compared in the composite level parameters, such as decay factor, delay spread, angular spread and line of sight power ratio. But these works [21, 22] lack the analysis of cluster-level parameters and frequency dependence of these channel parameters.

To address the above-mentioned gaps, we present measurement-based results for indoor measurement campaigns at the frequency bands of 2-4, 9-11 and 27-29 GHz in classroom and hall scenarios. To the best of authors' knowledge, no publication has considered all of these contributions listed as follows:

- A complexity-efficient high-resolution parameter estimation (HRPE) algorithm [24] is utilized for fully extracting spherical channel propagation parameters of the MPCs with the spatial non-stationarity of path gain considered, resulting in more accurate and realistic estimation. Besides that, based on the HRPE estimation results, composite level parameters, such as path loss, number of paths, RMS delay spreads and azimuth

spreads at 2-4, 9-11 and 27-29 GHz frequency bands are investigated.

- A novel cluster identification algorithm based on the automatic KPowerMeans method [25] is proposed to group the estimated MPCs into clusters at multiple frequency bands. The novelty is that we consider both the consistency and difference at different bands. That is, the specular reflections are dominant at multiple frequency bands, and the frequency dependence of specular reflections is not significant [26, 27], which was shown in [18]. Therefore, we utilize the clustering results at mm-wave bands as initialization for lower bands with richer MPCs. This enables us to track the similarities at different bands, identify the additional characteristics at lower bands and compare them realistically. The cluster-level parameters at 2-4, 9-11 and 27-29 GHz frequency bands are statistically modeled, which is essential for performance evaluation for 5G and beyond systems.
- Using the same measurement system in different scenarios and frequency bands, the frequency dependence of channel parameters and the impact of the indoor room environment (i.e. dimension and furniture) are also investigated.

The rest of the paper is organized as follows. Sect. 2 elaborates the scenarios and specifications in the measurement campaigns. Sect. 3 presents some typical channels at multiple frequency bands in both scenarios. The HRPE results and composite level parameters are investigated. In Sect. 4, a novel cluster identification algorithm based on KPowerMeans algorithm is introduced. Moreover, cluster-level parameters are elaborated. Finally, conclusions are in Sect. 5.

2 Measurement campaign

In this section, two measurement campaigns conducted in classroom and hall scenarios at 2-4, 9-11 and 27-29 GHz frequency bands are introduced. The measurements were performed with a virtual UCA-based VNA channel sounding system, see [21, 22, 28] for more details. A commercial omnidirectional biconical antenna (A-INFO-SZ-2003000/P [29]) is exploited as the transmitter (Tx) antenna and a homemade biconical antenna [30] is used as the receiver (Rx) antenna. The Rx antenna is rotated from the 0th array position clockwise with a pre-set radius $r = 0.24$ m to form $P = 360$ UCA elements. A total of 20 positions were measured for each scenario by moving the Tx. The HPBW in elevation plane of the commercial omnidirectional biconical antenna is less than 30° for 3, 10, and 28 GHz, and the elevation HPBW of the homemade biconical antenna varies from 30° to 65° over the covered band. Due to the narrow beamwidth of the antennas in the elevation plane and typical handset level height [13] for Device-to-device (D2D) connections of 5G communications, the height of both Tx and Rx antennas is set as 1.50 m [31]. Considering the sweep time and the maximum propagation distance for the indoor scenarios,

Table C.1: Measurement specifications.

Frequency range	2-4, 9-11 and 27-29 GHz
UCA array radius	0.24 m
Tx/Rx height	1.50 m
UCA elements number	360
Frequency points	750

750 frequency sweeping points were collected for the frequency range 2-4, 9-11 and 27-29 GHz. Table C.1 summarizes the measurement specifications.

The first scenario is a classroom with desks and whiteboard as depicted in Fig C.1(a), and each Tx location in each row was spaced 0.8 m apart. The dimension of the classroom is $8.54\times6.70\times2.71\,\mathrm{m}^3$. The second scenario is a hall with four ventilation tubes and seven white pillars as shown in Fig C.1(b). The dimension of the hall is $39\times20\times10\,\mathrm{m}^3$, which is much larger than the classroom. In the hall scenario, the Tx grid spacing is 1 m. The details of the measurement scenarios can be found in [22]. Note that, due to the small antenna aperture of the UCA available for the elevation angle information, we only consider the azimuth angle for the angular parameters of the channel in this work. Besides that, it should also be noted that all the measured Tx antenna positions in both classroom and hall scenarios result in LoS scenarios.

3 Channel characteristics

3.1 Concatenated channel impulse responses

As mentioned above, at each Tx position $P = 360$ UCA elements were collected and 750 frequency points were recorded for each frequency band. The inverse discrete Fourier transform (IDFT) was applied for processing the measured channel transfer functions (CTFs) $H(p, f)$ to obtain the channel impulse responses (CIRs) $h(p, \tau)$, where p is the UCA element index and f is the frequency. To compare the channel characteristics in different scenarios at all bands, we plot the power of 360 CIRs at each Tx position as concatenated CIRs (CCIRs) i.e. $|h(p, \tau)|^2$. Note that the delay resolution is 0.5 ns (corresponding to 0.15 m in distance), due to the 2 GHz bandwidth set for the three frequency bands. Thus, the delay variations of propagation trajectories across the array aperture with radius of 0.24 m can also be observed.

In the classroom Position 5 alongside the window and in the hall scenario Position 5 surrounded by pillars and tubes are chosen as typical positions for the investigation. Figs. C.2(a) and C.2(b) illustrate the CCIRs for Tx position 5 in the classroom and hall scenarios, respectively, at 2-4, 9-11 and 27-29 GHz. As MPCs rarely have delays larger than 100 ns in both classroom and hall scenarios, it is plotted with a maximum delay of 100 ns to show the details of

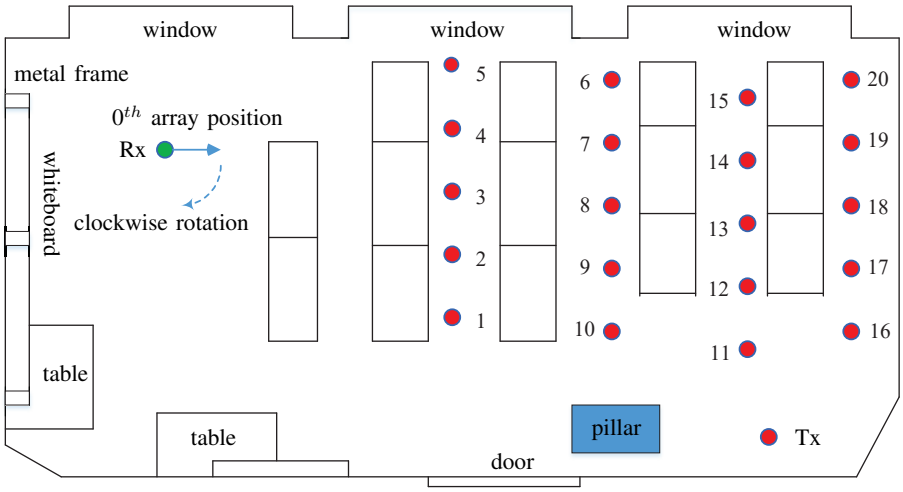

(a)

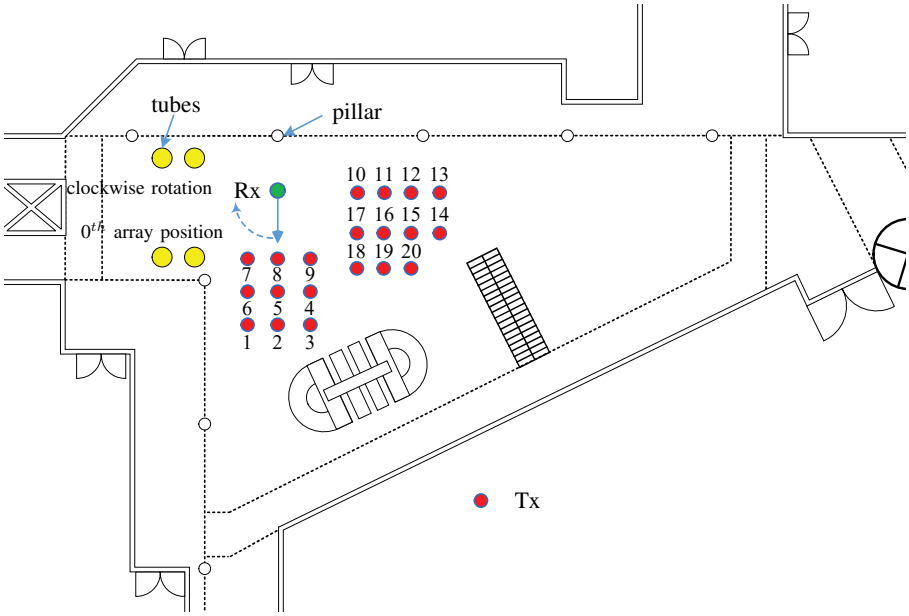

(b)

Fig. C.1: The top-view of the classroom and hall where measurement campaigns were conducted. (a) The classroom scenario. (b) The hall scenario.

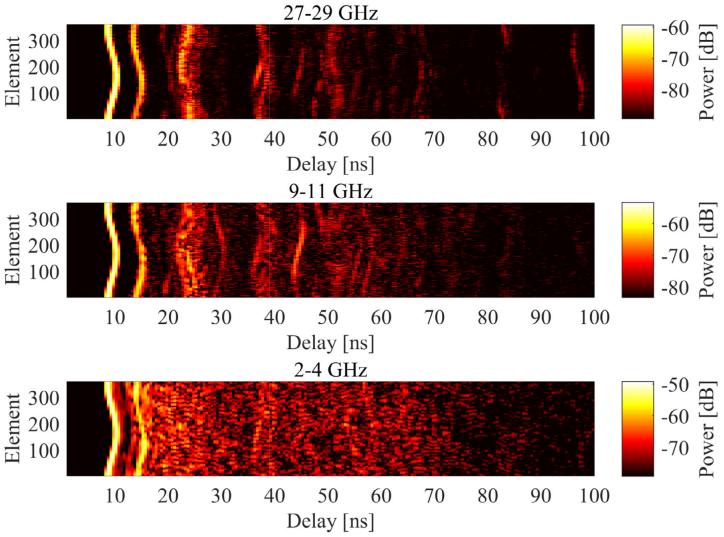

(a)

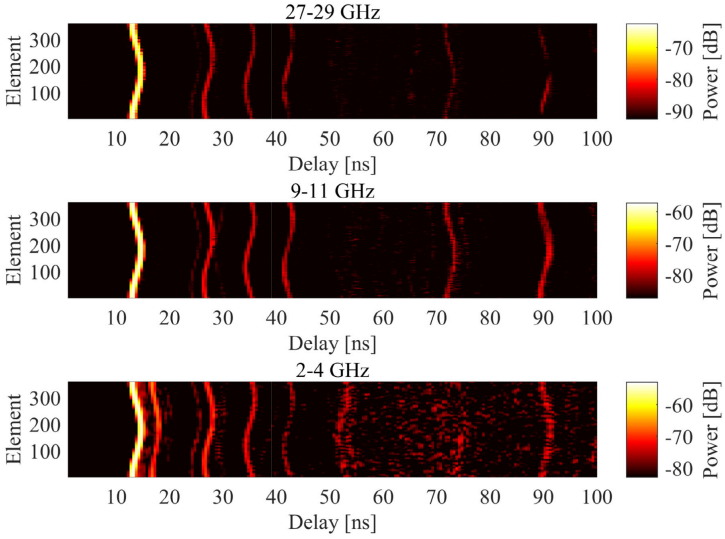

(b)

Fig. C.2: The example CCIRs for Tx position 5 in the classroom and hall scenarios at 2-4, 9-11 and 27-29 GHz. (a) Classroom scenario. (b) Hall scenario.

LoS path and strong reflections more clearly. The noise floor is about -95, -100 and -95 dB for the classroom and hall scenarios at 27-29 GHz, 9-11 GHz and 2-4 GHz, respectively. For fair observation and comparison from Figs. C.2(a) and C.2(b), the dynamic range 30 dB is set for different frequency bands in both scenarios. We have the following observations shown as below.

- In Figs. C.2(a) and C.2(b), the shapes of the LoS paths are ")"-alike curves, due to the fact that it is close to the maximum delay and minimum power at the 180th UCA element as well as the minimum delay and maximum power at the 360th or 0th UCA elements at position 5 in both classroom and hall scenarios. That means that the shapes of the paths can reflect the information of the angles-of-arrivals (AoAs). It can be inferred that the LoS paths are approximately from 0 or 360 degree in the azimuth plane. Besides that, another strong reflection path can also be observed after the LoS path in Fig. C.2(a). Considering the similar shape of the strong reflection path with LoS path and the delay information, it can be inferred that this path is contributed by the window as indicated in Fig. C.1(a).
- The MPCs with different shapes can be observed in both Figs. C.2(a) and C.2(b), which are contributed by other furniture, windows, the sidewalls in the classroom and hall. Different from the "clean" trajectories at 9-11 GHz and 27-29 GHz in both Figs. C.2(a) and C.2(b), the trajectories may be blurred at 2-4 GHz. It can also be observed that the trajectories of the MPCs are rather sparse at 27-29 GHz in both Figs. C.2(a) and C.2(b), while much richer at 2-4 GHz. This phenomenon matches the condition known as channel sparsity in [23] that the number of significant MPCs associated with the mm-wave band may be lower than that in sub-6 GHz frequency bands.
- By comparing Fig. C.2(a) and Fig. C.2(b) at the same frequency bands, it is found that the CCIRs in Fig. C.2(a) are much richer than that in Fig. C.2(b). We conjecture that it is mostly due to the larger dimension and less furniture of the hall scenario. Besides that, there are more high order reflections and more scattering effects from furniture and sidewalls in the small classroom.

The above observations demonstrate that the propagation parameters (e.g. delays and azimuths) of MPCs can be roughly obtained by the CCIRs. However, due to the interference among the paths caused by the effect of the IDFT sidelobes and the shapes of different trajectories shifting with respect to the AoAs, the trajectories of the MPCs are blurred in CCIR figures. Therefore, a HRPE algorithm is applied in this paper for estimating high-resolution information of the channel.

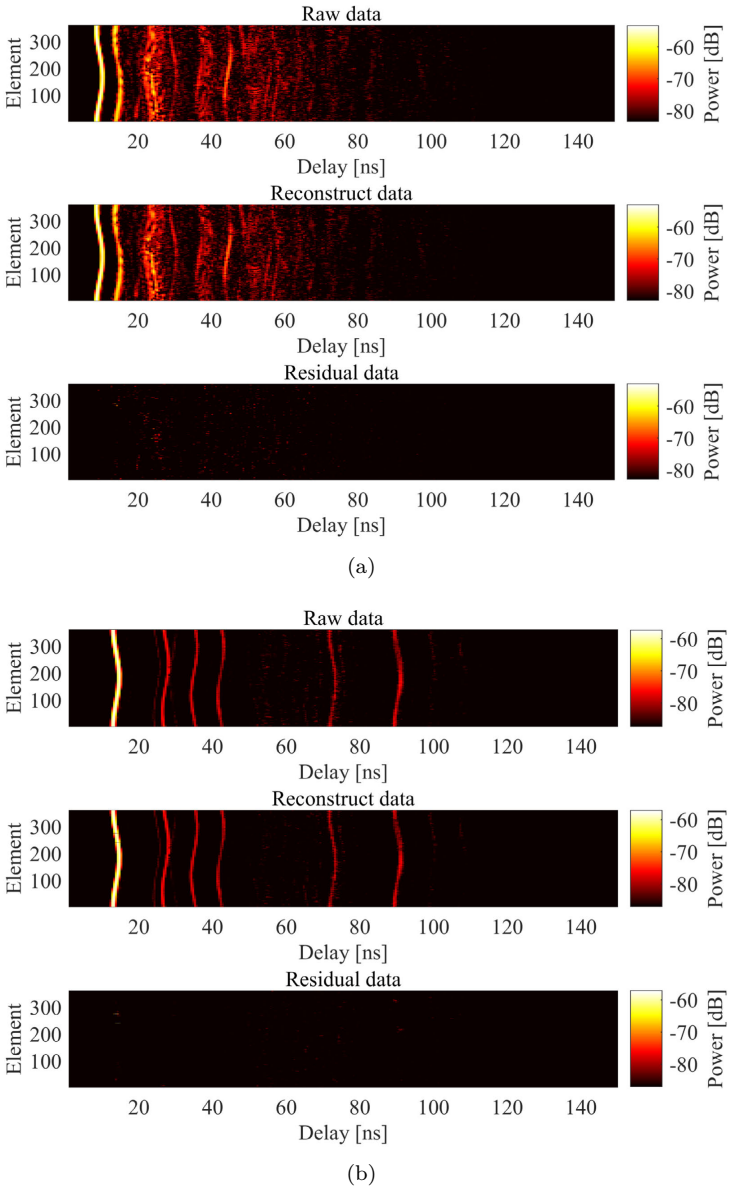

Fig. C.3: The CCIRs of raw data, reconstructed data based on the HRPE estimation results and residual data, respectively, for Tx position 5 in the hall and classroom scenario at 9-11 GHz. (a) Classroom scenario. (b) Hall scenario.

3.2 Parameter estimation

To establish an accurate and realistic channel model, comprehensive and complexity-efficient HRPE algorithms are required for extracting the spherical propagation parameters in ultra-wideband large-scale arrays for future communications. Furthermore, the realistic spatial non-stationarity in path gain across the array elements should be considered as well [24]. Therefore, based on the ultra-wideband and spherical wave propagation model assumption, the HRPE algorithm [24] is exploited to fully extract the spherical channel propagation parameters, i.e. delays, azimuths, elevations, complex amplitudes of the MPCs from the measured CTFs $H(p, f)$. As mentioned above, the UCA radius r was set as 0.24 m. Due to the large aperture, the spherical propagation model must be assumed to avoid the model mismatch that may occur with the plane wave assumption [32]. With a finite number of L spherical waves assumed to impinge on the UCA, the underlying signal model for the measured CTFs $H(p, f)$ contributed by all the L paths can be formulated as [24]

$$H(p,f) = \sum_{\ell=1}^{L} \frac{d_\ell}{d_{p,\ell}} \alpha_\ell e^{-j2\pi f(\frac{d_{p,\ell}-d_\ell}{c}+\tau_\ell)} + n(p,f) \tag{C.1}$$

with

$$d_{p,\ell} = \sqrt{{d_\ell}^2 + r^2 - 2rd_\ell \sin\theta_\ell \cos(\phi_\ell - \phi_p)} \tag{C.2}$$

where f is frequency points, α_ℓ, τ_ℓ, θ_ℓ and ϕ_ℓ represent the complex amplitude, propagation delay, elevation and azimuth of the ℓth path, d_ℓ is the distance between the UCA center and the last source point during the propagation, $d_{p,\ell}$ denotes the distance from the pth UCA element to the last source point, c is the light speed, ϕ_p is the azimuth of the pth UCA element calculated as $\frac{2\pi(p-1)}{P}$ and $n(p, f)$ denotes the complex Gaussian noise.

The HRPE algorithm[1] [24] mainly includes three parts. *i)* Firstly, the high resolution estimation results of delays and amplitudes at each element are obtained based on the SAGE principle. In this step, the number of paths should be set large enough to fully extract all the propagation paths at individual antenna elements above the noise floor. *ii)* Secondly, a single path trajectory is identified by the phase mode excitation technique roughly with the delay and angular information [33]. *iii)* Thirdly, reconstruct the CTFs for this identified path from the second step and update the estimated parameters based on the maximum likelihood principle. Then, update the trajectories by removing this identified path. Go through this "identification-removing" operation by repeating steps *ii)* and *iii)*, until the channel power is adequately extracted within the

[1]The reader is referred to [24] for details of the extraction of spherical channel propagation parameters using the HRPE algorithm.

dynamic range. Moreover, the number L of the MPCs can be automatically estimated.

In [24], it is validated that the computation complexity is decreased significantly compared to the maximum likelihood estimator (MLE) algorithm [32] with exhaustive 4D parameter searchings. Considering that a trajectory may be spatially non-stationary across the array elements, a trajectory with a low number of array elements will not be extracted as a valid path. In this way, a complexity-efficient algorithm and more realistic results will be achieved by avoiding the artificial paths with the stationary gain being estimated. The final extracted number of paths L is illustrated in Table C.2. To show that the HRPE algorithm has the ability to fully extract the propagation trajectories, we compare the CCIRs of raw data and reconstructed data based on the HRPE estimation results, and residual data obtained by subtracting the reconstructed data from the raw data for Tx position 5 in the classroom and hall scenarios in Fig. C.3. It is observed that reconstructed CCIRs are close to raw CCIRs in both Fig. C.3(a) and Fig. C.3(b). It is found that on average, about 95.5% of total measured power can be extracted for all Tx positions in both scenarios at all bands.

Figs. C.4 and C.5 illustrate the example estimated power-delay-azimuth spectrums (PDAS) at position 5 for both classroom and hall scenarios in all frequency bands. By comparing Figs. C.4 and C.5, we have the observations as follows: *i)* The estimated number of paths L is least in Fig. C.5(a) and most in Fig. C.4(c), which is consistent with the observation from CCIRs in Fig. C.2. *ii)* In both Figs. C.4 and C.5, the azimuths of LoS paths are close to 360° or 0°, which also matches the observation in Fig. C.2. *iii)* Using the delays, azimuths of the MPCs and the geometry of the scenarios, it can be inferred that the strong reflections in Fig. C.4 are contributed by the metal frame of the whiteboard and window, while the reflections in Fig. C.5 are from the pillars and yellow ventilation tubes. *iv)* The delays and azimuths of the LoS path and the strong MPCs are almost the same at different frequencies in the same scenarios in Figs. C.4 and C.5, respectively. In this way, the weak MPCs around these strong MPCs with similar delays and angles can be considered as clusters.

3.3 Composite level parameters

Based on the estimated propagation parameters of the channel, composite-level parameters that include the number of paths, path loss, composite root-mean-square (RMS) delay spreads and composite RMS azimuth spreads are investigated.

Path Loss PL

The path loss for each location in both the classroom and hall scenarios can be calculated as follows

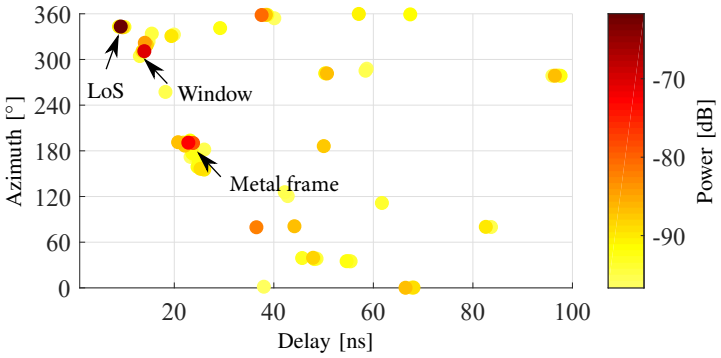

(a)

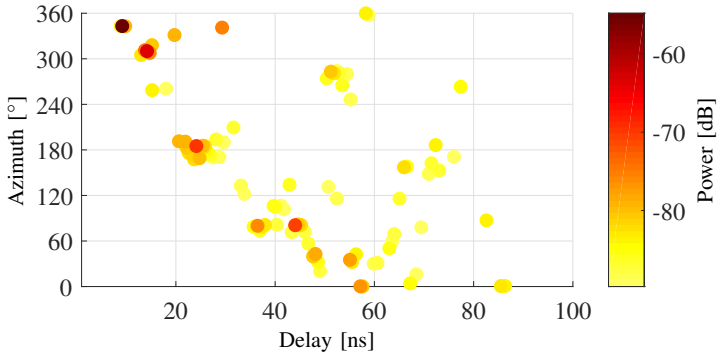

(b)

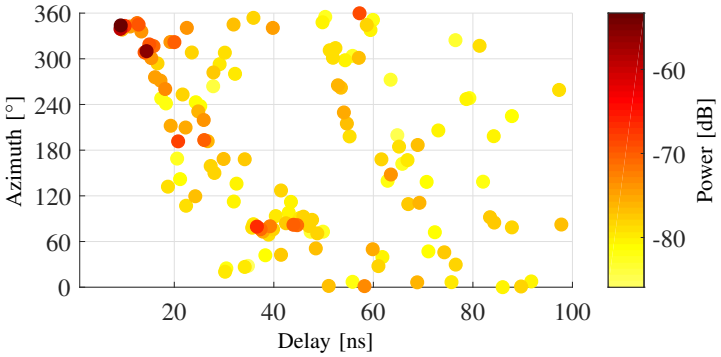

(c)

Fig. C.4: The example estimated PDASs for Tx position 5 in the classroom scenario at multiple frequency bands. (a) 27-29 GHz. (b) 9-11 GHz. (C) 2-4 GHz.

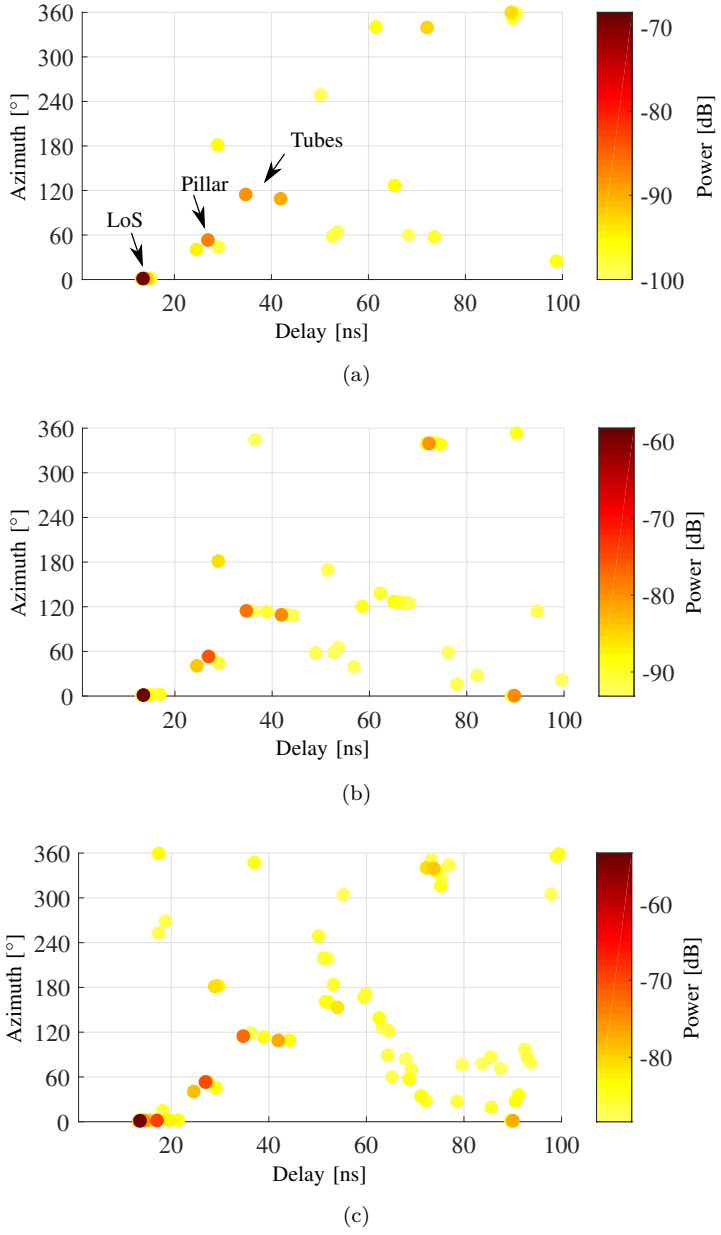

Fig. C.5: The example estimated PDASs for Tx position 5 in the hall scenario at multiple frequency bands. (a) 27-29 GHz. (b) 9-11 GHz. (C) 2-4 GHz.

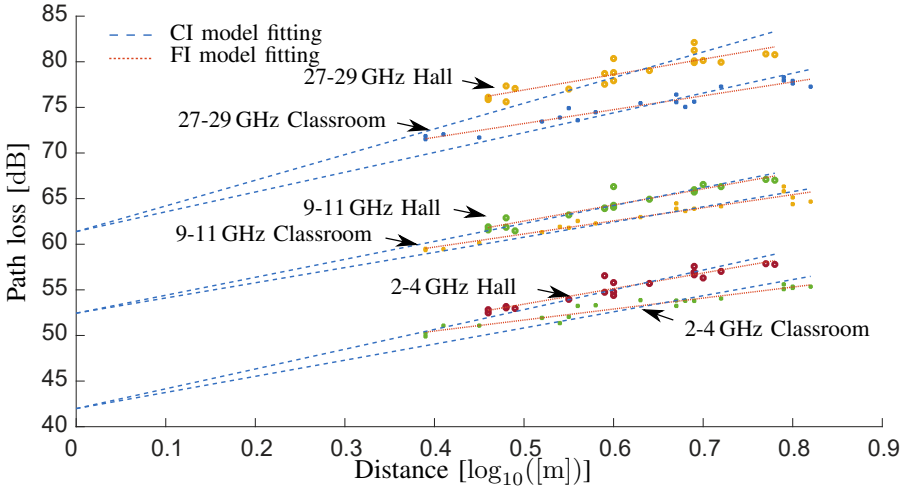

Fig. C.6: Path loss fitting for the path loss calculated based on the estimated data in classroom and hall scenarios at 2-4, 9-11, 27-29 GHz.

Table C.2: Statistics extracted for the composite-level parameter.

	Parameters	Classroom	Hall
27-29 GHz	$\mathrm{PL}^{\mathrm{CI}}(n, \varsigma)$	(2.17, 1.06)	(2.81, 1.41)
	$\mathrm{PL}^{\mathrm{FI}}(\alpha, \beta, \varsigma)$	(65.63, 1.52, 0.51)	(68.47, 1.69, 0.83)
	L (μ, σ)	(64.25, 18.83)	(26.75, 12.41)
	σ_τ[ns] (μ, σ)	(11.53, 1.77)	(14.89, 31.92)
	σ_ϕ[°] (μ, σ)	(50.30, 70.01)	(24.79, 56.92)
9-11 GHz	$\mathrm{PL}^{\mathrm{CI}}(n, \varsigma)$	(1.67, 0.61)	(1.97, 0.60)
	$\mathrm{PL}^{\mathrm{FI}}(\alpha, \beta, \varsigma)$	(53.95, 1.44, 0.51)	(53.71, 1.77, 0.56)
	L (μ, σ)	(100.60, 56.88)	(60, 138.42)
	σ_τ[ns] (μ, σ)	(14.30, 3.99)	(16.55, 27.81)
	σ_ϕ[°] (μ, σ)	(50.91, 84.17)	(26.48, 70.77)
2-4 GHz	$\mathrm{PL}^{\mathrm{CI}}(n, \varsigma)$	(1.77, 0.90)	(2.17, 0.70)
	$\mathrm{PL}^{\mathrm{FI}}(\alpha, \beta, \varsigma)$	(45.67, 1.20, 0.41)	(44.90, 1.71, 0.52)
	L (μ, σ)	(140.65, 15.08)	(104.45, 298.89)
	σ_τ[ns] (μ, σ)	(17.03, 2.00)	(22.00, 33.80)
	σ_ϕ[°] (μ, σ)	(54.53, 128.22)	(30.99, 99.45)

$$\begin{aligned} \mathrm{PL} &= P_{Tx} - P_{Rx} + G_{Tx} + G_{Rx} \\ &= -\sum_{\ell=1}^{L} |\alpha_\ell|^2 + G_{Tx} + G_{Rx} \end{aligned} \tag{C.3}$$

where P_{Tx} and P_{Rx} are the transmit power and received power, respectively. In addition, G_{Tx} and G_{Rx} are the gains of the Tx and Rx antennas used at the measured frequency, respectively. The gains of the commercial antenna [29] at the Tx side are 0.75 dBi at 3 GHz, 3.25 dBi at 10 GHz and 6 dBi at 28 GHz. The gains of the homemade antenna [30] at the Rx side are 1.25 dBi at 3 GHz, 2.8 dBi at 10 GHz and 4.8 dBi at 28 GHz.

The close-in free space reference distance (CI) path loss model is utilized for fitting the PL with a single parameter n as [13, 34]

$$\begin{aligned} \mathrm{PL}^{\mathrm{CI}}(f,d)[\mathrm{dB}] = \mathrm{FSPL}(f,d_0) + 10\cdot n\log_{10}(d/d_0) + X_\varsigma^{\mathrm{CI}} \\ \text{for } d \geq d_0, \text{ where } d_0 = 1\,m \end{aligned} \tag{C.4}$$

where d_0 is the physically-based reference distance set as 1 m and $\mathrm{FSPL}(f,d_0) = 10\log_{10}(\frac{4\pi d_0}{\lambda})^2$. d is the Tx-to-Rx distance, the linear slope n is well known as the path loss exponent (PLE), and $X_\varsigma^{\mathrm{CI}}$ is the shadowing effect described by a Gaussian random variable with zero mean and standard deviation ς. In our case, $\mathrm{FSPL}(f, 1\,\mathrm{m})$ is 42.0 dB, 52.4 dB and 61.4 dB for 2-4, 9-11 and 27-29 GHz, respectively.

The floating-intercept (FI) path loss model for fitting the measured PL with two parameters, which has been widely used in the WINNER II model, the 3GPP SCM and the COST 2100 model, is established as [9]

$$\mathrm{PL}^{\mathrm{FI}}(d)[\mathrm{dB}] = \alpha + 10\cdot\beta\log_{10}(d) + X_\varsigma^{\mathrm{FI}} \tag{C.5}$$

where α and β denote the intercept and the slope obtained via least-square fitting, and $X_\varsigma^{\mathrm{FI}}$ is the shadow fading considered as a Gaussian random variable with zero mean and standard deviation ς. Fig. C.6 and Table C.2 show the path loss fitting and the model fitting parameters by both CI and FI path loss models for classroom and hall scenarios at 2-4, 9-11, 27-29 GHz. It can be observed that the PLE at 27-29 GHz in the hall scenario is much larger than theoretical PLE (n=2) in free space, which mismatches the results of the LoS scenarios in [9, 13, 35, 36]. We conjecture that it is because of the short-measured distance range (less than 10 m) and strong reflections contributed from the PEC materials of elevator and tubes in the hall scenario, which may lead to the overestimation of PLEs by the CI path loss model. Besides that, it is found that the PLEs are frequency independent in both classroom and hall scenarios, with similar conclusions for indoor scenarios found in [13, 35, 36]. In addition, it can also be found that both of the PLEs and β in the FI model in the classroom are smaller than those of the hall scenario at the same frequency. We

speculate that it is because the Tx moves towards the east wall from Position 16 to Position 20 in the classroom scenario, there are strong reflections from the wall, which may lead to the underestimation of PLEs. Furthermore, the values of β in the FI model increase as the frequencies increase in the classroom scenario, with similar observation in [21]. However, similar values of β in the FI model at all bands are found in the hall scenario.

The number of paths L

The cumulative distribution functions (CDFs) of the number of paths L based on all the 20 Tx positions in both classroom and hall scenarios at multiple frequency bands are illustrated in Fig. C.7(a), with statistical parameters (μ, σ) [2] in Table C.2. It can be observed that the estimated L is smallest in the hall scenario at 27-29 GHz and largest in the classroom at 2-4 GHz. It can be found that the number of paths L increases as the frequency band decreases. Similar results were found in [9, 23] that the number of significant MPCs in the mm-wave band is much lower than that for below 6 GHz in similar scenarios. This is reasonable since mm-waves suffer more attenuation compared with lower frequency waves and less MPCs can be extracted within the same dynamic range, leading to a sparser channel at higher frequencies [23]. Besides that diffraction and diffuse scattering are more dominant at lower frequency bands [18, 21, 28], which are extracted as specular reflections in this paper, resulting in more specular paths at lower frequency bands. However, in the 3GPP model [37], the number of paths and the number of clusters are defined as the same for different frequency bands, which is inconsistent with the results found in the current work as well as the referred works. Furthermore, the number of paths L in the classroom is larger than that in the hall at the same frequency bands. It is reasonable as the dimension of the classroom is much smaller than the hall and more objects exist in the classroom, leading to more MPCs in the classroom.

Composite delay spread σ_τ and azimuth spread σ_ϕ

The RMS delay spread and azimuth spread are the parameters for characterizing the delay and azimuth dispersion of the channel. The RMS delay spread σ_τ is calculated as [38, 39]

$$\sigma_\tau = \sqrt{\overline{\tau^2} - \overline{\tau}^2} \tag{C.6}$$

with

$$\overline{\tau^2} = \frac{\sum_{\ell=1}^{L} |\alpha_\ell|^2 \cdot \tau_\ell^2}{\sum_{\ell=1}^{L} |\alpha_\ell|^2}, \quad \overline{\tau} = \frac{\sum_{\ell=1}^{L} |\alpha_\ell|^2 \cdot \tau_\ell}{\sum_{\ell=1}^{L} |\alpha_\ell|^2} \tag{C.7}$$

[2] μ and σ represent mean value and variance, respectively.

The RMS azimuth spread σ_ϕ is calculated as [37]

$$\sigma_\phi = \sqrt{-2\ln\left(\left|\frac{\sum_{\ell=1}^{L}\exp(j\phi_\ell)\cdot|\alpha_\ell|^2}{\sum_{\ell=1}^{L}|\alpha_\ell|^2}\right|\right)} \tag{C.8}$$

Fig. C.7(b) and Fig. C.7(c) illustrate the CDFs of σ_τ and σ_ϕ for the classroom and hall scenarios at all frequency bands, with statistical parameters (μ, σ) in Table C.2. It can be seen that the mean values of RMS delay spreads are 11.53 ns and 14.89 ns for the classroom scenario and hall scenario at 28 GHz, respectively, which are similar with the mean RMS delay spreads 12 ns for open office LoS scenario and smaller than 37 ns for shopping mall LoS scenario [40]. It can also be observed that the delay spreads increase as frequencies decrease in both classroom and hall scenarios. Similar to results reported in [13] when comparing RMS delay spreads of 28 and 73 GHz for indoor office LoS scenario. Furthermore, the mean values of RMS azimuth spreads are 50.30° and 24.79° for the classroom scenario and hall scenario at 28 GHz, respectively, which are larger than the mean azimuth spreads 19.6° at 28 GHz for the airport LoS scenario in [12] and also reported in the mmMAGIC project [31]. Besides that, the azimuth spreads are slightly larger at 2-4 GHz than those at higher frequency bands and mean azimuth spreads at 9-10 GHz and 27-29 GHz are similar in both classroom and hall scenario. Similar observation can be found in [12] that mean azimuth spreads are also similar at 15 and 28 GHz and larger than that at 60 GHz in airport LoS scenario. We conjecture that larger delay spreads and azimuth spreads at lower frequency bands are caused by the fact that more MPCs and more reflection orders exist at lower frequency bands, resulting in larger delay spreads and azimuth spread at lower frequency bands. Particularly, the azimuth spreads are similar at 9-11 and 27-29 GHz, due to the fact that the dominant reflections are mainly from similar azimuth angles at higher frequency bands. Furthermore, it can also be observed from Fig. C.7(b) that in most cases, the delay spreads in the hall scenario are larger than that observed in the classroom scenario at the same frequencies. We postulate that the larger dimension of the hall leads to the MPCs with larger relative delays. While, in some cases, the delay spreads in the hall are smaller than that of the classroom, possibly due to that the pillars or tubes in the hall cause dominant paths leading to the whole spread being compressed. Moreover, it can also be observed from Fig. C.7(c) that the azimuth spreads in the classroom are larger than that in the hall at all frequencies. It is probably due to the fact that the larger dimension of the hall and the reflections in the hall are mainly contributed by the pillar and tubes nearby, resulting in the compressed azimuth spread.

4 Cluster characteristics

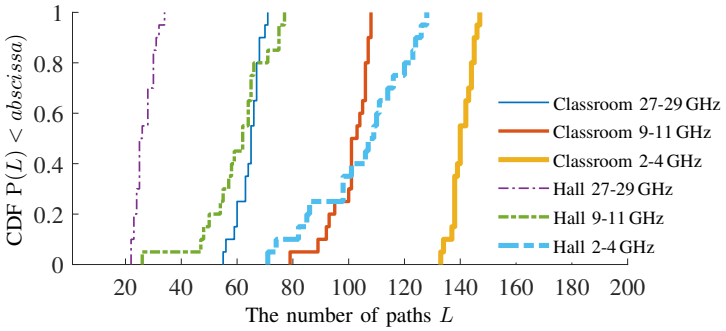

(a)

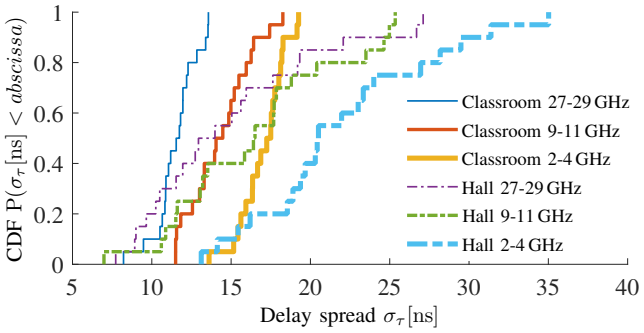

(b)

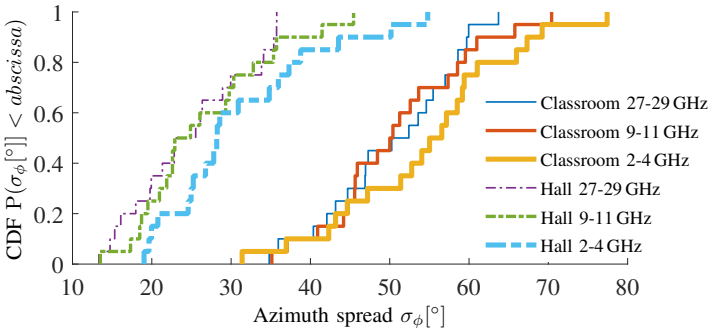

(c)

Fig. C.7: Empirical CDFs of composite parameters for the classroom and hall scenarios at 2-4, 9-11 and 27-29 GHz frequency bands. (a) The number of paths L. (b) Delay spread σ_τ. (c) Azimuth spread σ_ϕ.

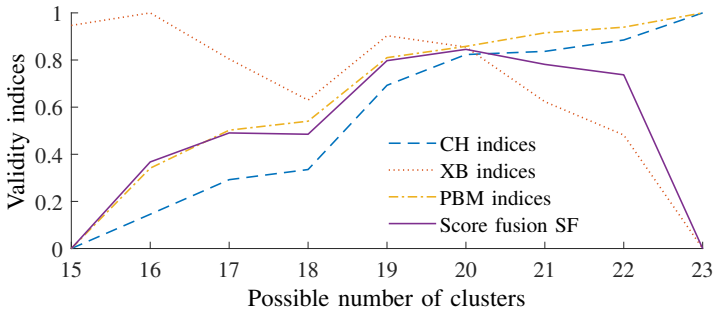

Fig. C.8: The examples of the CVIs for the classroom scenario at position 5 in 27-29 GHz frequency band.

4.1 Cluster identification

There exist several methods, e.g. visual inspection [41], KPowerMeans [42, 43] and multipath component distance (MCD)-threshold principle [44] for grouping the MPCs. Visual inspection is not available in the case of multi-dimensions, i.e., considering the delay, azimuth, and elevation of the MPCs. The MCD-threshold principle requires prior assumptions of the optimum threshold, which is physically linked to the cluster size or distribution. For the automatic KPowerMeans method [25], the cluster validation provides a trustworthy estimate of the optimum number of clusters, and the cluster pruning algorithm improves visibility. However, the automatic KPowerMeans method lacks the ability of the initialization for the number of clusters and centroids at different bands, which are difficult to obtain in advance. In [18], it is found that the identified clusters with similar delay and azimuth are basically contributed from similar physical objects in the same Tx position at multiple frequency bands. In this work, a novel cluster identification algorithm based on the automatic KPowerMeans method [25] is proposed to group the MPCs into clusters at multiple frequencies, considering both the consistency and difference at different bands. Besides that, the specular reflections are dominant at 27-29 GHz and the frequency dependence of specular reflections was not found to be significant [26] [27]. Thus we group the estimated MPCs at middle and low frequency bands based on the cluster results (e.g. the number of the clusters and centroids) from the same Tx position at the high frequency bands, which enables us to track the similarities at different bands with low complexity and better accuracy. Note that, we only focus on the angular information at the Rx UCA side in this work, i.e., AOA, without considering the angles-of-departure (AOD).

Specifically, the MPCs at 27-29 GHz are clustered based on the automatic KPowerMeans method [25] by setting a range $[K_{min}, K_{max}]$ for the expected number of clusters firstly. Then for each possible K, the KPowerMeans pro-

Algorithm 1 The proposed cluster identification algorithm based on KPowerMeans algorithm.

Input: MPC parameters α_ℓ, τ_ℓ, θ_ℓ at high and middle/low frequency.

Output: Middle/low frequency clustering results $\mathcal{L}_c^{(k^{'})}$.

1: Cluster the MPCs at high frequency by the automatic KPowerMeans method [25], and obtain the cluster centroids $\mu_c^{(k)}$ and final clusters number K_{final},

2: Do for all number of clusters $K^{'} = K_{\text{final}} + K^{'}_{min}$ to $K_{\text{final}} + K^{'}_{max}$, Do for all MCD distance threshold $\eta_{\text{MCD}} = \eta_{min}$ to η_{max}

   a. Assign MPCs at middle/low frequency to nearest cluster centroids $\mu_c^{(k)}$ and store the MCD distance

   b. Set the MCD distance threshold η_{MCD} and initialize $\mathcal{L}^{(k)}$, $\mathcal{L}^{(k^{'})}$.

   c. Find the centroid index c_n with minimum MCD to the current MPC: $c_n = \arg\min_{c \in \mathcal{C}^{(k)}} \text{MCD}_{\ell, \mu_c^{(k)}}$

   d. for $\ell \in \mathcal{L}$ do
      if $\text{MCD}_{\ell, \mu_{c_n}^{(k)}} \leq \eta_{\text{MCD}}$ then
         $\mathcal{L}^{(k)}_{c_{\text{previous}}} \leftarrow \mathcal{L}^{(k)}_{c_{\text{previous}}} + \{\ell\}$
      else $\mathcal{L}^{(k^{'})}_{c_{\text{new}}} \leftarrow \mathcal{L}^{(k^{'})}_{c_{\text{new}}} + \{\ell\}$
      end if
      end for

   e. Recalculate the cluster centroids $\mu^{(k^{'})}_{c_{\text{previous}}}$ from $\mathcal{L}^{(k^{'})}_{c_{\text{previous}}}$, and cluster the $\mathcal{L}^{(k^{'})}_{c_{\text{new}}}$ by the automatic KPowerMeans method [25], obtain the cluster centroids $\mu^{(k^{'})}_{c_{\text{new}}}$

3: Find optimum number of clusters and optimum MCD distance threshold at middle/low frequency: $[K^{'}_{\text{opt}}, \eta_{\text{opt}}] = \arg\max_{K^{'}, \eta_{\text{MCD}}} \text{SF}$

4: Prune optimum cluster set by removing the cluster power lower than 0.1% of total power

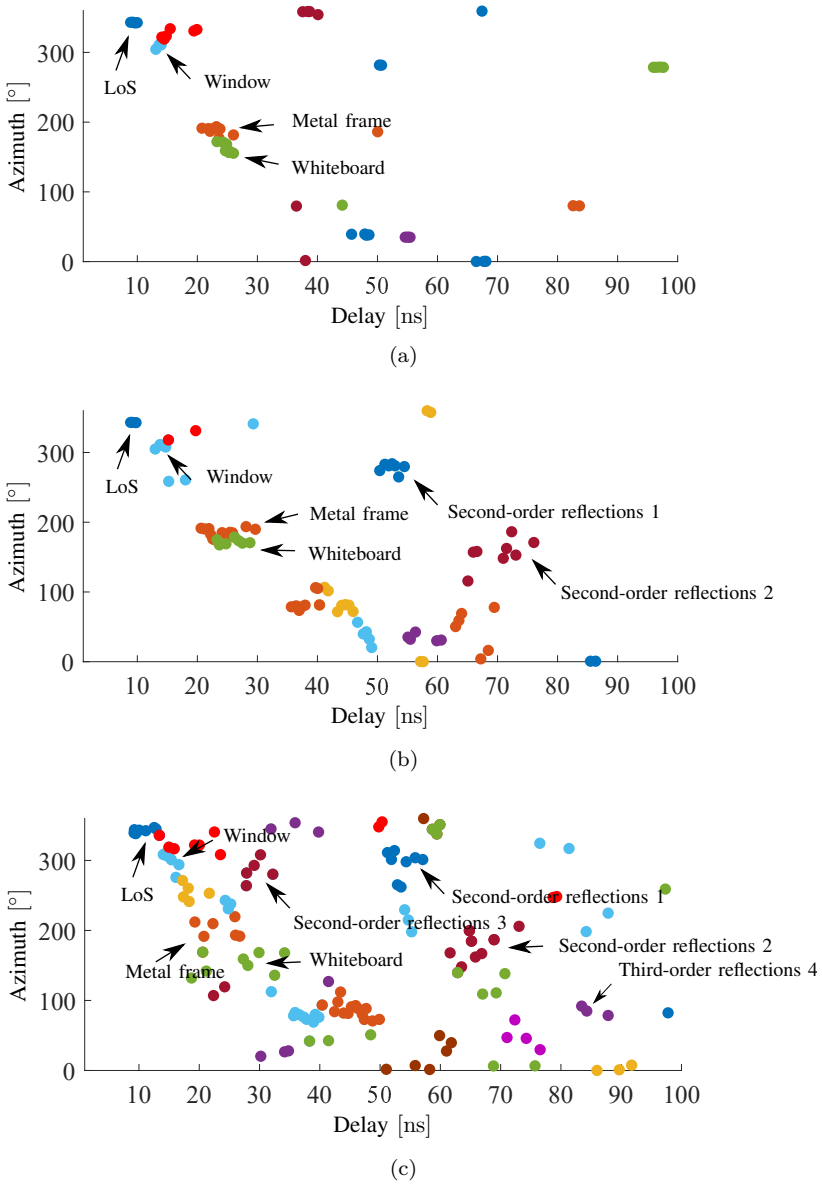

Fig. C.9: The examples of the cluster identification results for the classroom at position 5 in multiple frequency bands. (a) 27-29 GHz. (b) 9-11 GHz. (C) 2-4 GHz.

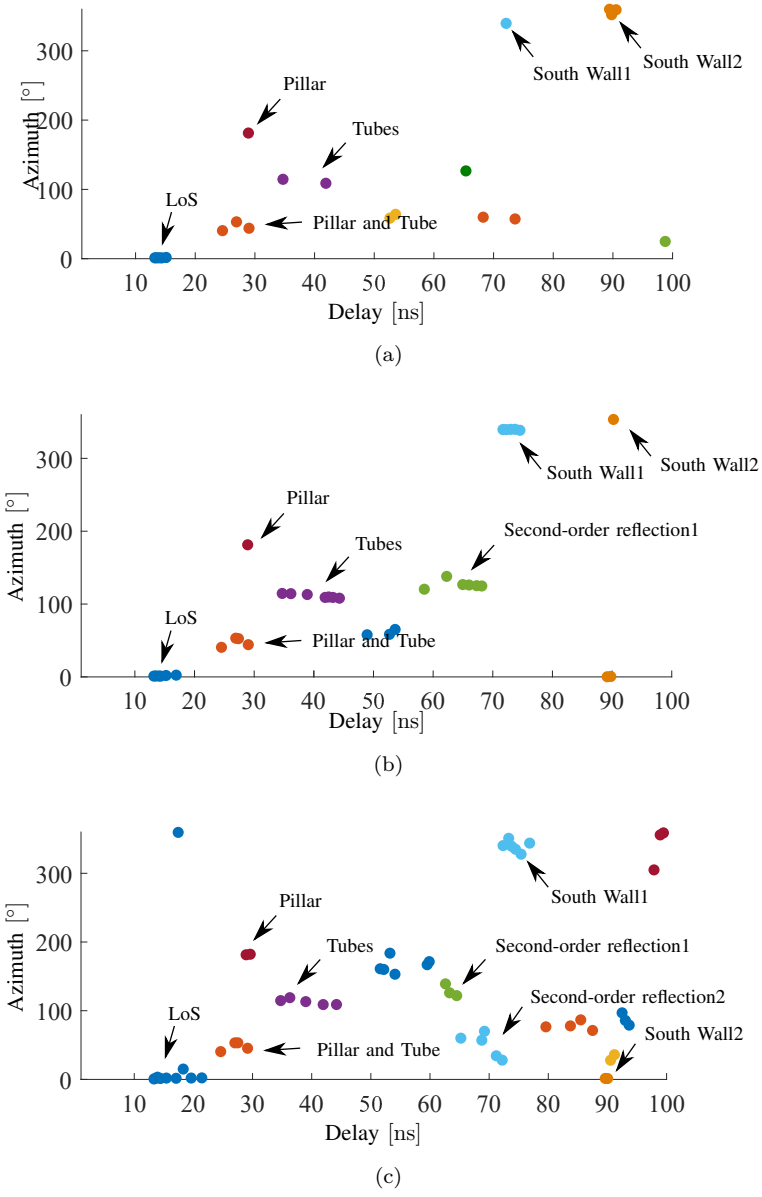

Fig. C.10: The examples of the cluster identification results for the hall at position 5 in multiple frequency bands. (a) 27-29 GHz. (b) 9-11 GHz. (C) 2-4 GHz.

cedure is performed to assign a cluster index to each MPC, and the result is validated by the cluster validity indices (CVIs), such as Calinski Harabasz index, Xie and Beni index, Pakhira-Bandyopadhyay-Maulik index [45–48]. These CVIs indicate the cluster's compactness, separation, and exclusiveness. The optimum number of clusters K_{opt} is determined according to the score fusion SF [47, 49] calculated as the geometrical mean of all the CVIs. Fig. C.8 illustrates the example for the range of the number of clusters in 27-29 GHz at position 5 in the classroom scenario. Then the cluster pruning algorithm is implemented by discarding the clusters with power lower than 0.1% of the total power for improved visualization, resulting in the final number of clusters K_{final} lower than K_{opt}.

For the 2-4 and 9-11 GHz bands, the MPCs are clustered using the proposed cluster identification algorithm, according to the identified clusters at 27-29 GHz. The proposed cluster identification algorithm is elaborated in Algorithm 1. Firstly, assign the MPCs at middle and low frequency to the nearest cluster centroids $\mu_c^{(k)}$ obtained at high frequency and store the MCD distance. MCD distance [25] is used as the basic distance function between the MPC and nearest cluster centroid by the combination of delay and angular domain. A range of the MCD distance threshold $[\eta_{min}, \eta_{max}]$ is tested for choosing the optimum MCD distance threshold η_{opt} to separate the MPCs belonging to previous clusters $\mathcal{L}_{c_{\text{previous}}}^{(k')}$ obtained at the high frequency band and new clusters $\mathcal{L}_{c_{\text{new}}}^{(k')}$. At the middle and low frequency bands, the clusters found at the high frequency band are evaluated using the MCD distance for each of the MPCs, and the clusters only resulting in MCD distance larger than η_{MCD} are omitted. If the MCD distances are larger than η_{MCD}, these MPCs are stored for the new clusters $\mathcal{L}_{c_{\text{new}}}^{(k')}$ to be grouped using the automatic KPowerMeans method by adding the number of clusters range $[K'_{min}, K'_{max}]$. In this way, the KPowerMeans procedure only need be performed for each possible K' in the range $[K'_{min}, K'_{max}]$ to iteratively initialize the cluster centroids and validate the results for the optimum number of clusters, which reduces the complexity of the clustering algorithm. The optimum number of clusters K'_{opt} and the optimum MCD distance threshold η_{opt} at middle and low frequency bands will be determined by the maximum value of the score fusion SF for all combinations of η_{MCD} and K'. Besides that, the cluster centroids of previous and new clusters are recalculated as

$$\mu_c = \frac{\sum_{\ell \in \mathcal{L}_c} |\alpha_\ell|^2 \cdot [\tau_\ell, \phi_\ell]^T}{\sum_{\ell \in \mathcal{L}_c} |\alpha_\ell|^2} \tag{C.9}$$

where T indicates transpose operation. Finally, we discard the clusters with power lower than 0.1% of the total power. Fig. C.9 and Fig. C.10 illustrate the examples of cluster identification results for the classroom and hall scenarios at position 5. In each figure, the dots with the same color represent the MPCs belonging to the same cluster. It can be observed from Fig. C.9 that the clusters contributed from LoS paths, window, the metal frame of the whiteboard and the

whiteboard in the classroom can be identified at all bands. Due to more diffuse scattering, diffraction and high order reflections at lower frequencies [18], the clusters of second-order reflection from the windows and whiteboard are marked as "Second-order reflection 1" and "Second-order reflection 2", respectively, in both Fig. C.9(b) and Fig. C.9(c). Besides that, the clusters contributed by the second-order reflection from the window and third-order reflection from the southwest corner are marked as "Second-order reflection 3" and "Third-order reflection 4", respectively, in Fig. C.9(c). Moreover, it can also be observed from Fig. C.10 that the clusters from LoS, pillars, tubes and south wall in the hall can be identified at all bands. The clusters of second-order reflection from the tubes marked as "Second-order reflection 1" in both of Fig. C.10(b) and Fig. C.10(c), and the clusters contributed by the second-order reflection from the pillar marked as "Second-order reflection 2" in Fig. C.10(c) are identified. Thus, the proposed novel cluster identification algorithm has the ability to cluster the MPCs contributed from similar objects at the same position in all bands reasonably.

4.2 Cluster level parameters

Based on the cluster identification results, the cluster-level parameters, i.e. the number of clusters, cluster delay spread, cluster azimuth spread and cluster power loss behavior are investigated. The statistics extracted for the cluster-level parameters of the proposed novel cluster identification algorithm and the automatic KPowerMeans method are detailed in Table C.3.

Cluster power loss behavior

To investigate the relationship between cluster power and delay, we analyze the cluster path loss behavior here. The cluster power loss was computed as the negative cluster total power and the propagation distance d_c was calculated based on the delay of the cluster centroid. Besides that, the standard deviation of cluster shadow fading was denoted as ς_c. The cluster power losses versus propagation distances in logarithmic scale fitted by the FI path loss model in (C.5) with linear regression lines for classroom and hall scenarios at 2-4, 9-11 and 27-29 GHz frequency bands are plotted in Fig. C.11. It can be observed that the values of β increase as frequencies increase in the classroom, while it is different in the hall scenario, which is similar to the phenomenon of FI path loss β in Sect. 3.3. In the classroom scenario, the higher frequency band waves have larger values of β, resulting in more rapid variations of cluster power versus distance.

The number of clusters K

Fig. C.12(a) illustrates the CDFs of the number of clusters K for the classroom and hall scenarios at all bands. It can be observed that the number of clusters K increases as the frequency decreases in both the classroom and hall scenario,

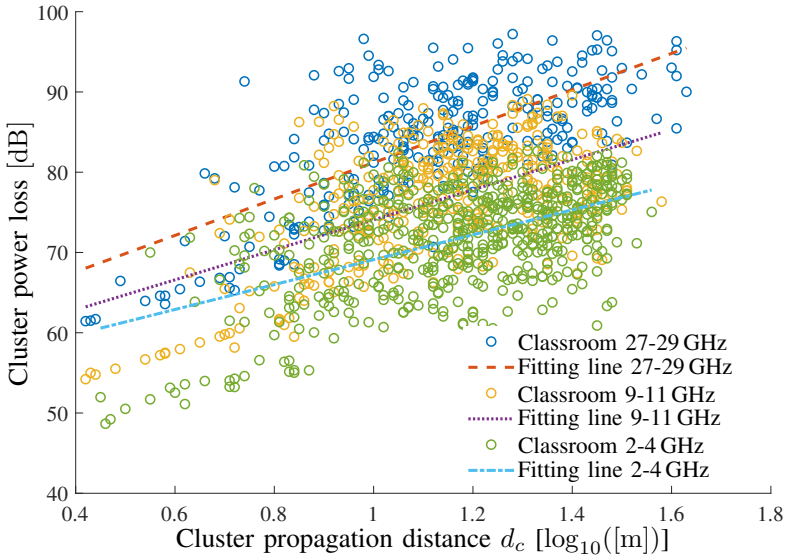

(a)

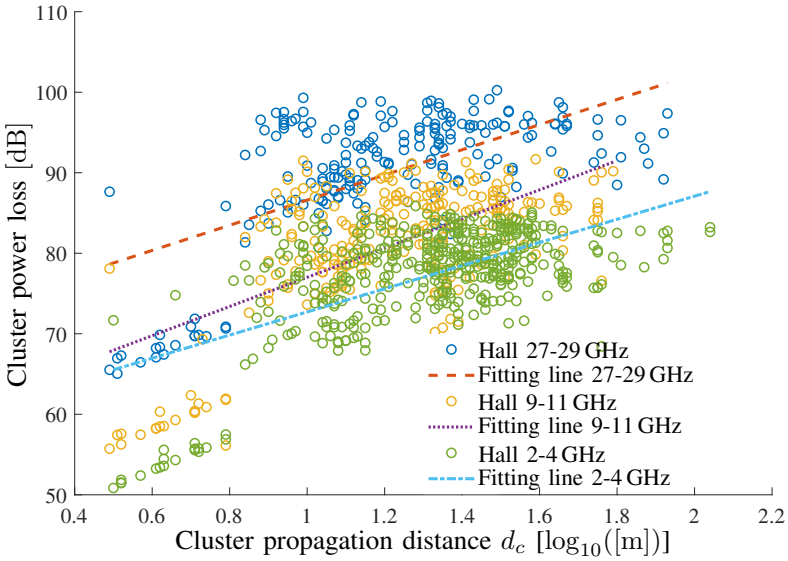

(b)

Fig. C.11: Cluster power loss behavior for classroom and hall scenarios at 2-4, 9-11 and 27-29 GHz frequency bands. (a) Classroom. (b) Hall.

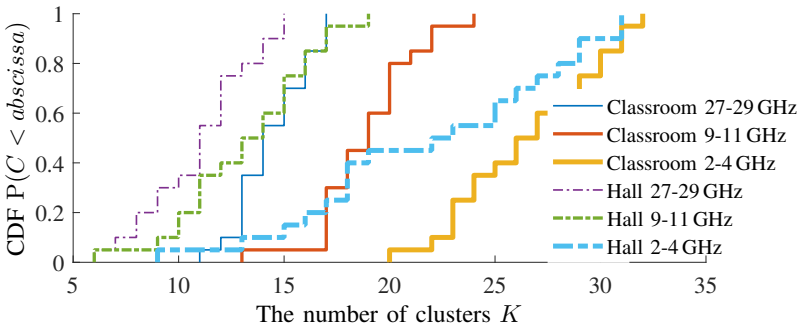

(a)

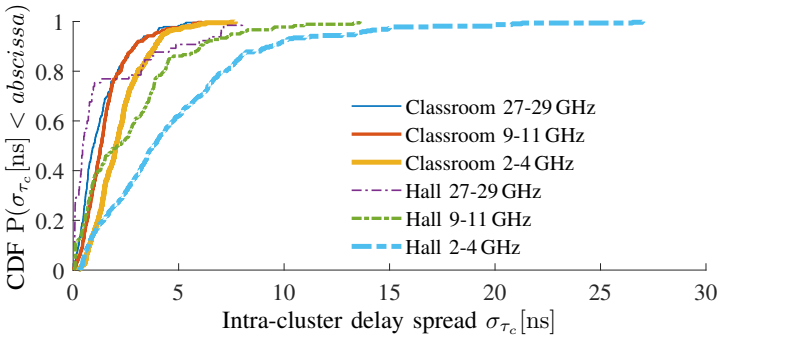

(b)

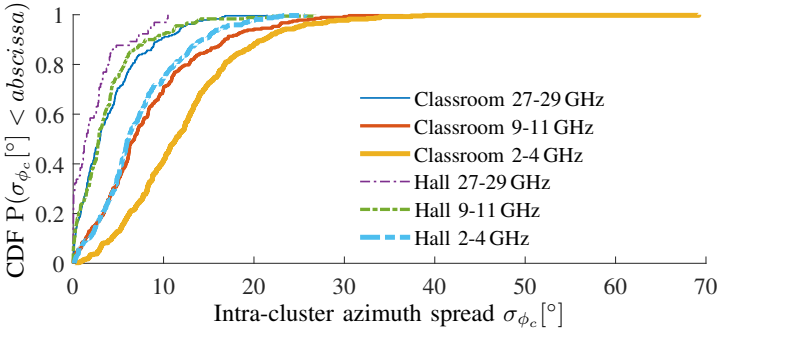

(c)

Fig. C.12: The CDFs of cluster-level parameters for classroom and hall scenarios at 2-4, 9-11 and 27-29 GHz frequency bands. (a) The number of clusters K. (b) Intra-cluster delay spread σ_{τ_c}. (c) Intra-cluster azimuth spread σ_{ϕ_c}.

Table C.3: Statistics extracted for the cluster-level parameters.

		Parameters	Classroom	Hall
	27-29 GHz	$PL_c(\alpha, \beta, \varsigma_c)$	(58.52, 2.27, 5.49)	(70.98, 1.56, 6.53)
		K (μ, σ)	(14.40, 2.99)	(11, 6.63)
		σ_{τ_c} [ns] (μ, σ)	(1.33, 1.31)	(1.45, 4.55)
		σ_{ϕ_c} [°] (μ, σ)	(4.06, 15.34)	(2.34, 7.41)
Automatic KPowerMeans	9-11 GHz	$PL_c(\alpha, \beta, \varsigma_c)$	(55.60, 1.83, 5.95)	(59.84, 1.68, 6.25)
		K (μ, σ)	(17.95, 5.94)	(12.05, 5.21)
		σ_{τ_c} [ns] (μ, σ)	(1.72, 1.52)	(3.44, 10.69)
		σ_{ϕ_c} [°] (μ, σ)	(7.06, 22.35)	(4.53, 21.62)
	2-4 GHz	$PL_c(\alpha, \beta, \varsigma_c)$	(51.72, 1.59, 5.19)	(55.95, 1.51, 5.26)
		K (μ, σ)	(21.95, 10.16)	(18.25, 8.51)
		σ_{τ_c} [ns] (μ, σ)	(2.66, 1.96)	(4.26, 7.94)
		σ_{ϕ_c} [°] (μ, σ)	(11.43, 33.06)	(9.16, 36.30)
Proposed Clustering Method	9-11 GHz	$PL_c(\alpha, \beta, \varsigma_c)$	(55.36, 1.87, 5.83)	(58.89, 1.81, 6.02)
		K (μ, σ)	(18.90, 5.78)	(13.20, 10.27)
		σ_{τ_c} [ns] (μ, σ)	(1.54, 1.26)	(2.70, 6.67)
		σ_{ϕ_c} [°] (μ, σ)	(8.28, 40.36)	(3.79, 15.94)
	2-4 GHz	$PL_c(\alpha, \beta, \varsigma_c)$	(53.59, 1.55, 5.33)	(58.34, 1.44, 5.31)
		K (μ, σ)	(28.15, 14.66)	(22.10, 39.67)
		σ_{τ_c} [ns] (μ, σ)	(2.08, 1.34)	(4.70, 14.90)
		σ_{ϕ_c} [°] (μ, σ)	(11.25, 37.02)	(7.25, 24.21)

with similar results that the number of the clusters in mm-wave band is much lower than that for below 6 GHz in [9, 23]. It is reasonable that more diffuse scattering and diffractions exist at lower frequency band [18], resulting in more clusters. Besides that, at the same frequency the number of clusters K in the classroom is larger than that in the hall. We postulate that it is caused by the smaller dimension of the classroom and more objects in the classroom contribute more scattering points.

Intra-cluster delay spread σ_{τ_c} and azimuth spread σ_{ϕ_c}

Fig. C.12(b) and Fig. C.12(c) illustrate the CDFs of intra-cluster delay spread σ_{τ_c} and azimuth spread σ_{ϕ_c} for the classroom and hall scenarios at multiple frequency bands. It can be observed from Fig. C.12(b) and Fig. C.12(c) that both intra-cluster delay spreads and azimuth spreads increase as frequencies decrease. This is reasonable since more significant diffuse scattering at lower frequency leads to more MPCs close to the strong reflections, which spread the delay and azimuth of the clusters. Moreover, it can also be observed from Fig. C.12(b) that the intra-cluster delay spreads in the hall are larger than that observed in the classroom scenario at the same frequency bands. However, it can also be observed from Fig. C.12(c) that the intra-cluster azimuth spreads in the hall are smaller than that observed in the classroom scenario at the same frequency bands. We conjecture it is because the clusters in the hall scenario are mainly from sparsely placed objects such as pillars, tubes and the sidewalls, which leads to larger cluster delay dispersion and smaller azimuth dispersion, as seen from the clusters contributed by the "Pillar and Tube" and "Tubes" in Fig. C.10.

5 Conclusions

In this paper, wideband channel characteristics obtained in a classroom and a hall at 2-4, 9-11, 27-29 GHz were investigated. A high resolution parameter estimation (HRPE) algorithm was exploited to estimate the propagation parameters of the channel. A novel clustering identification algorithm based on the automatic KPowerMeans method was proposed to cluster the multipath components (MPCs) for 2-4, 9-11 and 27-29 GHz, where the consistency and dependency at different bands were well considered. The composite level and cluster level parameters were investigated. It can be observed that the PLE at 27-29 GHz in the hall scenario is much larger than theoretical PLE (n=2) in free space, which mismatches the results of the LoS scenarios in [9, 13, 35, 36], mostly due to the short measured distance range (less than 10 m) and strong reflections contributed from the PEC materials of elevator and tubes in the hall scenario, resulting in the overestimation of PLEs by the CI path loss model. Besides that, it is found that the PLEs are frequency independent in both classroom and hall scenarios, with similar conclusions for indoor scenarios found in [13, 35, 36]. It is also found that the values of β in the FI path loss increase as the frequencies increase for the classroom scenario, but found to be frequency independent for the hall. A similar phenomenon is observed with fitting parameter β of the cluster power loss in both scenarios. Furthermore, the number of paths, composite delay spread and azimuth spread, the number of clusters, and intra-cluster delay spread and azimuth spread increase as the frequency bands decrease in both scenarios. Similar results can be found in [9, 23] that the number of MPCs and the number of clusters in the mm-wave band is much lower than that for below 6 GHz in similar scenarios, known as channel sparsity. It is reasonable that scattering and diffraction are more dominant as the frequency decreased, as found in previously published works [18, 21, 28]. Moreover, the characteristics of the channel in classroom and hall scenarios at the same frequency bands have been compared for investigating the effect of the dimension and the objects in the scenarios on the channel. It is found that the number of paths and the number of clusters in the classroom are larger than that in the hall at the same frequencies, probably due to the fact that smaller dimension and more objects in the classroom lead to more reflection orders, resulting in more MPCs within the dynamic range. Additionally, composite delay spread and intra-cluster delay spread in the hall are basically larger than that observed in the classroom at all bands. However, the composite azimuth spread and intra-cluster azimuth spread in the classroom are larger than those in the hall at the same frequencies, mostly due to the fact that the objects in the hall can cause dominant paths. The established channel model can provide a valuable reference for evaluating the performance of 5G and beyond systems.

References

[1] T. S. Rappaport, S. Sun, R. Mayzus, H. Zhao, Y. Azar, K. Wang, G. N. Wong, J. K. Schulz, M. Samimi, and F. Gutierrez. Millimeter Wave Mobile Communications for 5G Cellular: It Will Work! *IEEE Access*, 1:335–349, 2013.

[2] M. Agiwal, A. Roy, and N. Saxena. Next Generation 5G Wireless Networks: A Comprehensive Survey. *IEEE Communications Surveys Tutorials*, 18(3):1617–1655, thirdquarter 2016.

[3] J. G. Andrews, S. Buzzi, W. Choi, S. V. Hanly, A. Lozano, A. C. K. Soong, and J. C. Zhang. What will 5G be? *IEEE Journal on Selected Areas in Communications*, 32(6):1065–1082, June 2014.

[4] A. Osseiran, F. Boccardi, V. Braun, K. Kusume, P. Marsch, M. Maternia, O. Queseth, M. Schellmann, H. Schotten, H. Taoka, H. Tullberg, M. A. Uusitalo, B. Timus, and M. Fallgren. Scenarios for 5G mobile and wireless communications: the vision of the METIS project. *IEEE Communications Magazine*, 52(5):26–35, May 2014.

[5] M. Shafi, J. Zhang, H. Tataria, A. F. Molisch, S. Sun, T. S. Rappaport, F. Tufvesson, S. Wu, and K. Kitao. Microwave vs. Millimeter-Wave Propagation Channels: Key Differences and Impact on 5G Cellular Systems. *IEEE Communications Magazine*, 56(12):14–20, December 2018.

[6] V. Nurmela, A. Karttunen, et al. Deliverable D1.4, METIS Channel Models. *Tech. Rep.*, 2015.

[7] Aalto University, BUPT, CMCC, Nokia, NTT DOCOMO, New York University, Ericsson, Qualcomm, Huawei, Samsung, Intel, University of Bristol, KT Corporation, University of Southern California. 5G Channel Model for bands up to 100 GHz. *Tech. Rep.*, 2016. [Online]. Available: http://www.5gworkshops.com/5GCM.html.

[8] Study on channel model for frequency spectrum above 6 GHz (3GPP TR 38.900 version 14.2.0 Release 14). *Tech. Rep.*, 2016.

[9] J. Ko, Y. Cho, S. Hur, T. Kim, J. Park, A. F. Molisch, K. Haneda, M. Peter, D. Park, and D. Cho. Millimeter-Wave Channel Measurements and Analysis for Statistical Spatial Channel Model in In-Building and Urban Environments at 28 GHz. *IEEE Transactions on Wireless Communications*, 16(9):5853–5868, Sep. 2017.

[10] W. Roh, J. Seol, J. Park, B. Lee, J. Lee, Y. Kim, J. Cho, K. Cheun, and F. Aryanfar. Millimeter-wave beamforming as an enabling technology for 5G cellular communications: theoretical feasibility and prototype results. *IEEE Communications Magazine*, 52(2):106–113, February 2014.

[11] P. Zhang, J. Li, H. Wang, H. Wang, and W. Hong. Indoor Small-Scale Spatiotemporal Propagation Characteristics at Multiple Millimeter-Wave Bands. *IEEE Antennas and Wireless Propagation Letters*, 17(12):2250–2254, Dec 2018.

[12] J. Vehmas, J. Jarvelainen, S. L. H. Nguyen, R. Naderpour, and K. Haneda. Millimeter-Wave Channel Characterization at Helsinki Airport in the 15, 28, and 60 GHz Bands. In *2016 IEEE 84th Vehicular Technology Conference (VTC-Fall)*, pages 1–5, 2016.

[13] G. R. Maccartney, T. S. Rappaport, S. Sun, and S. Deng. Indoor Office Wideband Millimeter-Wave Propagation Measurements and Channel Models at 28 and 73 GHz for Ultra-Dense 5G Wireless Networks. *IEEE Access*, 3:2388–2424, 2015.

[14] X. Wu, C. Wang, J. Sun, J. Huang, R. Feng, Y. Yang, and X. Ge. 60-GHz Millimeter-Wave Channel Measurements and Modeling for Indoor Office Environments. *IEEE Transactions on Antennas and Propagation*, 65(4):1912–1924, April 2017.

[15] J. Huang, C. Wang, R. Feng, J. Sun, W. Zhang, and Y. Yang. Multi-Frequency mmWave Massive MIMO Channel Measurements and Characterization for 5G Wireless Communication Systems. *IEEE Journal on Selected Areas in Communications*, 35(7):1591–1605, July 2017.

[16] K. Saito, P. Hanpinitsak, W. Fan, J. Takada, and G. F. Pedersen. Frequency Characteristics of Diffuse Scattering in SHF band in Indoor Environments. In *2019 URSI Asia-Pacific Radio Science Conference (AP-RASC)*, pages 1–1, March 2019.

[17] J. Medbo, N. Seifi, and H. Asplund. Frequency Dependency of Measured Highly Resolved Directional Propagation Channel Characteristics. In *European Wireless 2016; 22th European Wireless Conference*, pages 1–6, May 2016.

[18] P. Hanpinitsak, K. Saito, W. Fan, J. Hejselbæk, J. Takada, and G. F. Pedersen. Frequency Characteristics of Geometry-Based Clusters in Indoor Hall Environment at SHF Bands. *IEEE Access*, 7:75420–75433, 2019.

[19] P. Hanpinitsak, K. Saito, W. Fan, J. Hejselbaek, J. Takada, and G. F. Pedersen. Cluster Intensity and Spread Characteristics in Classroom Scenario at 10 and 28 GHz Bands. In *2020 14th European Conference on Antennas and Propagation (EuCAP)*, pages 1–3, 2020.

[20] Panawit Hanpinitsak, Kentaro Saito, Wei Fan, Johannes Hejselbaek, Junichi Takada, and Gert Frølund Pedersen. Multi-path Cluster Characteristics in Indoor Environments at 28 GHz Band. *IEICE Technical Report*, 119(120):135–140, July 2019.

[21] Panawit Hanpinitsak, Kentaro Saito, Wei Fan, Jun ichi Takada, and Gert F. Pedersen. Frequency Characteristics of Path Loss and Delay-Angular Profile of Propagation Channels in An Indoor Room Environment in SHF Bands. In *IEICE Technical Report*, volume 116 of *IEICE Technical Report*, pages 153–158, 2017.

[22] G. Zhang, K. Saito, W. Fan, X. Cai, P. Hanpinitsak, J. Takada, and G. F. Pedersen. Experimental Characterization of Millimeter-Wave Indoor Propagation Channels at 28 GHz. *IEEE Access*, 6:76516–76526, 2018.

[23] A. Adhikary, E. Al Safadi, M. K. Samimi, R. Wang, G. Caire, T. S. Rappaport, and A. F. Molisch. Joint Spatial Division and Multiplexing for mm-Wave Channels. *IEEE Journal on Selected Areas in Communications*, 32(6):1239–1255, June 2014.

[24] X. Cai and W. Fan. A Complexity-Efficient High Resolution Propagation Parameter Estimation Algorithm for Ultra-Wideband Large-Scale Uniform Circular Array. *IEEE Transactions on Communications*, 67(8):5862–5874, Aug 2019.

[25] N. Czink, P. Cera, J. Salo, E. Bonek, J. Nuutinen, and J. Ylitalo. A Framework for Automatic Clustering of Parametric MIMO Channel Data Including Path Powers. In *IEEE Vehicular Technology Conference*, pages 1–5, 2006.

[26] D. Ferreira, I. Cuiñas, R. F. S. Caldeirinha, and T. R. Fernandes. A review on the electromagnetic characterisation of building materials at micro- and millimetre wave frequencies. In *The 8th European Conference on Antennas and Propagation (EuCAP 2014)*, pages 145–149, 2014.

[27] G. Tesserault, N. Malhouroux, and P. Pajusco. Determination of Material Characteristics for Optimizing WLAN Radio. In *2007 European Conference on Wireless Technologies*, pages 225–228, 2007.

[28] Wei Fan, Ines Carton, Jesper Ø. Nielsen, Kim Olesen, and Gert F. Pedersen. Measured wideband characteristics of indoor channels at centimetric and millimetric bands. *Eurasip Journal on Wireless Communications & Networking*, 2016(1):58, 2016.

[29] A-INFO-SZ-2003000/P Datasheet. Technical report.

[30] S. S. Zhekov, A. Tatomirescu, and G. F. Pedersen. Antenna for Ultrawideband Channel Sounding. *IEEE Antennas and Wireless Propagation Letters*, 16:692–695, 2017.

[31] Deliverable D2.2. Measurement Results and Final mmMAGIC Channel Models. Millimetre-Wave Based Mobile Radio Access Network for Fifth Generation Integrated Communications (mmMAGIC). *Tech. Rep.*, 2017.

[32] Y. Ji, W. Fan, and G. F. Pedersen. Channel Characterization for Wideband Large-Scale Antenna Systems Based on a Low-Complexity Maximum Likelihood Estimator. *IEEE Transactions on Wireless Communications*, 17(9):6018–6028, Sep. 2018.

[33] F. Zhang, W. Fan, and G. F. Pedersen. Frequency-Invariant Uniform Circular Array for Wideband mm-Wave Channel Characterization. *IEEE Antennas and Wireless Propagation Letters*, 16:641–644, 2017.

[34] Mathew K. Samimi, Theodore S. Rappaport, and George R. MacCartney. Probabilistic omnidirectional path loss models for millimeter-wave outdoor communications. *IEEE Wireless Communications Letters*, 4(4):357–360, 2015.

[35] AM Al-Samman, TA Rahman, MH Azmi, MN Hindia, I Khan, and Effariza Hanafi. Statistical modelling and characterization of experimental mm-wave indoor channels for future 5g wireless communication networks. *PloS one*, 11(9):e0163034, 2016.

[36] Ahmed M Al-Samman, Tharek Abd Rahman, and Marwan Hadri Azmi. Indoor corridor wideband radio propagation measurements and channel models for 5g millimeter wave wireless communications at 19 ghz, 28 ghz, and 38 ghz bands. *Wireless Communications and Mobile Computing*, 2018, 2018.

[37] Study on channel model for frequencies from 0.5 to 100 GHz. Technical report, 3GPP TR 38.901 V15.0.0, Jun. 2018.

[38] X. Cai, J. Rodríguez-Piñeiro, X. Yin, N. Wang, B. Ai, G. F. Pedersen, and A. P. Yuste. An Empirical Air-to-Ground Channel Model Based on Passive Measurements in LTE. *IEEE Transactions on Vehicular Technology*, 68(2):1140–1154, Feb 2019.

[39] X. Cai, B. Peng, X. Yin, and A. P. Yuste. Hough-Transform-Based Cluster Identification and Modeling for V2V Channels Based on Measurements. *IEEE Transactions on Vehicular Technology*, 67(5):3838–3852, May 2018.

[40] Lei Tian, Jianhua Zhang, Pan Tang, Fusheng Huang, and Yi Zheng. Delay characteristics for directional and omni-directional channel in indoor open office and shopping mall environments at 28 ghz. In *2016 IEEE 27th Annual International Symposium on Personal, Indoor, and Mobile Radio Communications (PIMRC)*, pages 1–4, 2016.

[41] L. Vuokko, P. Vainikainen, and J. Takada. Clusterization of measured direction-of-arrival data in an urban macro-cellular environment. In *14th IEEE Proceedings on Personal, Indoor and Mobile Radio Communications, 2003. PIMRC 2003.*, volume 2, pages 1222–1226 vol.2, Sep. 2003.

[42] N. Czink, R. Tian, S. Wyne, F. Tufvesson, J. Nuutinen, J. Ylitalo, E. Bonek, and A. F. Molisch. Tracking Time-Variant Cluster Parameters in MIMO Channel Measurements. In *the second International Conference on Communications and Networking in China*, pages 1147–1151, Aug 2007.

[43] Jerome Friedman Trevor Hastie, Robert Tibshirani. *The Elements of Statistical Learning: Data Mining, Inference, and Prediction, Second Edition (Springer Series in Statistics)*. Springer Series in Statistics. Springer, 2nd ed. 2009. corr. 3rd printing edition, 2009.

[44] C. Gustafson, K. Haneda, S. Wyne, and F. Tufvesson. On mm-Wave Multipath Clustering and Channel Modeling. *IEEE Transactions on Antennas and Propagation*, 62(3):1445–1455, March 2014.

[45] S. Cheng, M. Martinez-Ingles, D. P. Gaillot, J. Molina-Garcia-Pardo, M. Liénard, and P. Degauque. Performance of a Novel Automatic Identification Algorithm for the Clustering of Radio Channel Parameters. *IEEE Access*, 3:2252–2259, 2015.

[46] U. Maulik and S. Bandyopadhyay. Performance evaluation of some clustering algorithms and validity indices. *IEEE Transactions on Pattern Analysis and Machine Intelligence*, 24(12):1650–1654, Dec 2002.

[47] Krzysztof Kryszczuk and Paul Hurley. Estimation of the Number of Clusters Using Multiple Clustering Validity Indices. In Neamat El Gayar, Josef Kittler, and Fabio Roli, editors, *Multiple Classifier Systems*, pages 114–123, Berlin, Heidelberg, 2010. Springer Berlin Heidelberg.

[48] Malay K. Pakhira, Sanghamitra Bandyopadhyay, and Ujjwal Maulik. Validity index for crisp and fuzzy clusters. *Pattern Recognition*, 37(3):487 – 501, 2004.

[49] X. Cai, G. Zhang, C. Zhang, W. Fan, J. Li, and G. F. Pedersen. Dynamic channel modeling for indoor millimeter-wave propagation channels based on measurements. *IEEE Transactions on Communications*, 68(9):5878–5891, 2020.

Paper D

Geometry-Based Clustering Characteristics for Outdoor Measurements at 28-30 GHz

Guojin Zhang, Jesper Ødum Nielsen, Xuesong Cai, Gert Frølund Pedersen, and Wei Fan

The paper has been published in the
IEEE Antennas and Wireless Propagation Letters
Vol.21, No.9, pp.1797-1801, 2022.

The layout has been revised.

Abstract

This paper presents an analysis of channel characteristics for an outdoor scenario at the frequency band of 28-30 GHz. A geometry-based clustering algorithm is proposed to group the measured multipath components (MPCs) from the interaction points on the surrounding walls or objects according to Ray Tracing 3-D simulations, giving results that are more physically interpretable than the traditional clustering algorithms. The cluster-level characteristics at 15 positions along a pre-defined route covering both line-of-sight (LoS) and non-LoS (NLoS) scenarios are investigated. Moreover, power contributions of MPCs with multiple bounces (up to 7 bounces in NLoS scenario) from the interaction objects (IOs) are also investigated.

1 Introduction

Millimeter-wave (mm-wave) bands have been widely explored for fifth-generation (5G) communication systems due to the large amount of available frequency spectrum and the possibility to construct large-scale antenna arrays [1]. Despite many research efforts have been made in the areas of mm-wave propagation channel measurements and modeling, long-range outdoor measurements with large-scale arrays are still scarce, due to channel sounding limitations caused by high power attenuation in coaxial cables [2]. As wireless communication performance strongly depends on the propagation environments, accurate channel characterization for outdoor scenario is necessary for the design of future communication systems.

The concept of clusters has been extensively used in channel characterization to group the multipath components (MPCs) with similar delay and angular parameters. However, traditional parameter-based clustering algorithms, such as the KPowerMeans (KPM) algorithm [3] and multipath-component-distance (MCD) threshold algorithm [4], are based on the closeness of propagation parameters, lacking the relation to physical scatterers. In [5], a novel KPM-based clustering algorithm for multiple frequency bands was proposed by utilizing the clustering results at mm-wave bands as initialization for lower bands with richer MPCs, still without addressing the relation to physical scatterers. To link the clusters to their corresponding physical interaction objects (IOs) in the real environment, a geometry-based clustering algorithm was proposed by the combination of measurement and Ray Tracing (RT) simulation, resulting in a closer match to the measured channels [6]. In [7, 8], a geometry-based clustering and tracking method was proposed according to the scattering points obtained from the measurement-based ray tracer for indoor and outdoor cases. However, only single and double bounces are considered for indoor line-of-sight (LoS) environment in [7], and only single bounce and a 2-D Cartesian coordinate system are considered for a suburban scenario in [8]. For the outdoor

scenarios considered in the current work with multiple bounces (up to 7) in non-LoS (NLoS) scenarios, a more sophisticated mapping is needed. In [9], manual clustering for identifying their physical scatterers was combined with an automatic clustering algorithm to detect geometry-based clusters in an outdoor case, leading to high complexity. In summary, though a few works have been reported, a fully automatic and accurate geometry-based clustering algorithm is still missing in the literature.

To this end, the main contributions and novelties of this paper include: 1) An outdoor measurement campaign conducted with a virtual uniform circular array (UCA) in both LoS and NLoS scenarios is introduced. 2) A fully automatic geometry-based clustering method with a 3-D coordinate map is proposed for complicated outdoor scenarios with multiple bounces, linking the clusters to their corresponding physical IOs. The ability of the UCA used in the measurement to distinguish elevation angles of MPCs is not sufficient. Only delays and azimuths estimated for MPCs can be considered with adequate accuracy. This makes it difficult to obtain the full physical interactions of MPCs with the environment, especially for those with multiple bounces. Therefore, we resort to the assistance of the RT tool to obtain the physical interaction properties of each MPCs.[1] 3) Finally, the cluster-level channel characteristics linked to their corresponding physical IOs and power contributions of multiple bounces are investigated.

2 Measurement campaign

The map of the outdoor measurement environment is shown in Fig. D.1, including several buildings with bicycle shelter, parking space, and corridor in-between the buildings. A fiber-optic-based vector network analyzer (VNA) channel sounder [2, 4, 10] was used, allowing long measurement distances up to 300 m and a maximum achievable dynamic range of 112 dB. To increase the signal to noise ratio (SNR), a broadband horn antenna (LB-SJ-180400-KF [11]) was exploited as the receiver antenna (Rx) and fixed on the top of the building at a height of 18 m indicated as the yellow dot in Fig. D.1. The main beam of the Rx antenna was down tilted to appropriately cover Tx positions. For the transmitter antenna (Tx) side, an omni-directional biconical antenna [12] was located on a rotating device with a height of 1.15 m above the ground. To form a virtual UCA, the Tx was rotated clockwise in a circle with a radius of 0.25 m and 1° step. For each step, the channel transfer function from 28 GHz to 30 GHz was recorded with 2000 points. The virtual UCA was formed at 15 different positions, as indicated by the red dots in Fig. D.1. Position 1-10 are LoS scenarios, and Position 11-15 are NLoS scenarios.

[1] It is worth noting that the inaccuracy or missing of elevation information in measurements can make it challenging to distinguish, e.g., MPCs from the LoS direction and the ground reflection. It is always beneficial if the measurement system can well resolve paths in the elevation domain.

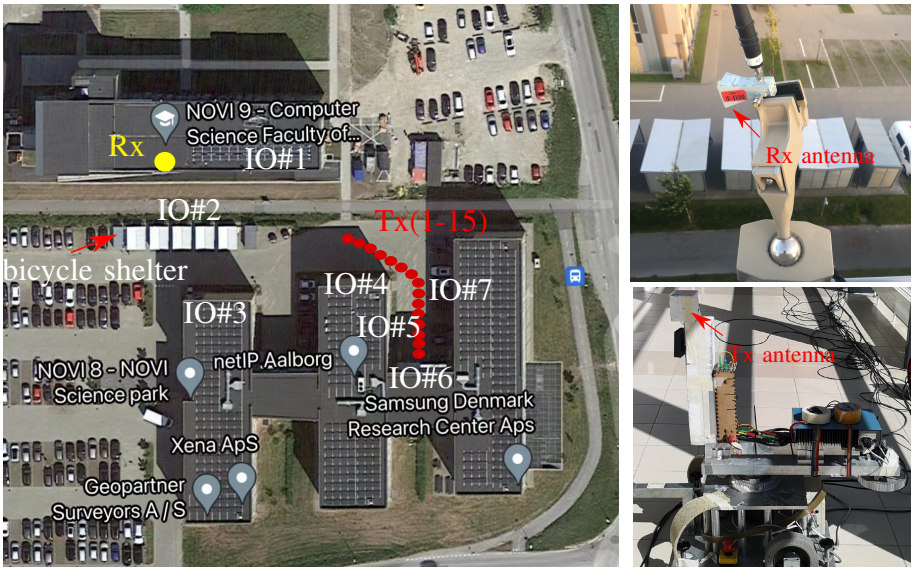

Fig. D.1: The measurement environment and channel sounder. (Left) The top view of the outdoor scenario where the measurement campaign was conducted. Image by Google Maps. (Right-top) Rx antenna on the roof of the building. (Right-bottom) Tx antenna mounted on pedestal used to form the virtual UCA.

3 Geometry-based clustering method

3.1 Ray Tracing

The RT tool [13, 14] is used to simulate the radio channels. Besides reflection, diffraction and transmission, diffuse scattering adopting an effective roughness model is also included. The accuracy of the RT tool has been validated in various indoor and outdoor scenarios [13–15]. For the simplicity of the simulations, only the outlines of the buildings and the bicycle shelter are modeled. The details of the buildings, such as the windows and the cars in the parking area, are ignored in the simulation. Note that the permittivity and conductivity of the materials in the environment is not completely known, which may lead to inaccurate powers of paths. Nevertheless, the geometry parameters including the delays and angles of the MPCs that are used for clustering in Sect. 3.2 are well obtained. To lower the computation time, the maximum numbers of reflections and diffraction combined with scattering are set as 4 and 1 for the LoS scenario, while 10 and 5 for the NLoS scenario. The physical interaction properties of each path, such as the IOs (as shown in Fig. D.1 with white texts IO#) and the number of bounces, are obtained by the RT tool. When the ground reflections are simulated, it is found that each propagation situation has one more bounce from the ground in the RT simulation with similar delay and azimuth, due to

the Tx being close to the ground. Leaving out the extra ground reflection does not affect the accuracy of the initialized clustering centroids described later in Sect. 3.2, and is therefore omitted in the simulation for simplicity. Note that the ground reflections exist in the real environment.

3.2 Cluster centroids initialization

Fig. D.2(a) and Fig. D.3(a) illustrate the delay-azimuth-power spectra estimated from the measured data at a LoS position 6 and an NLoS position 15, respectively, according to the high-resolution parameter estimation (HRPE) principle in [16, 17]. The minimum MCD principle [4] is used to match the paths identified from the RT simulation to the estimated paths from the measured data exploiting the delays and azimuths of the paths. The MCD threshold $\eta_{\mathrm{MCD},1}$ is used as a threshold distance to limit the search range of matching for a lower complexity. Matched paths identified in the RT simulations at position 6 and position 15 with their corresponding IOs are illustrated in Fig. D.2(b) and Fig. D.3(b), respectively. It can be observed that all the dominant MPCs estimated from the measured data can be identified in the RT simulation, and only a few weak MPCs are missing. The 3-D propagation mechanisms (plotted in 2-D view for clarity) in the RT simulation for each matched pair are shown in Fig. D.2(c) and Fig. D.3(c) for the two positions, respectively. The matched paths with the same IO# and the same number of bounces in the RT simulation are grouped as individual clusters. The cluster centroids μ_i are calculated as an initialization for clustering the estimated MPCs in measurements.

3.3 Main clustering algorithm

For each estimated MPC obtained by the HRPE algorithm, the minimum MCD to the RT-initialized cluster centroids is calculated. An MCD threshold $\eta_{\mathrm{MCD},2}$ is exploited to assign estimated MPCs to the RT-initialized clusters or as "new clusters". That is if the minimum MCD of a path is within $\eta_{\mathrm{MCD},2}$, it is assigned to the nearest RT-initialized cluster centroid. Otherwise, it is labeled as a component of new clusters to be grouped using the MCD threshold-based clustering algorithm [4]. The optimal threshold $\eta_{\mathrm{MCD},2}$ is determined by several cluster validity indices (CVIs). Clusters with powers less than 0.1% of the total power are finally pruned.

Fig. D.4(a) and Fig. D.4(b) show the clustering results at position 6 and position 15, respectively, with the power in descending order and the number of bounces indicated in the legend. At position 6, clusters have contributions from LoS, surrounding wall IO#4 and IO#7 as indicated in Fig. D.2(c), according to the RT-initialized cluster centroids as shown in Fig. D.2(b). However, it is worth noting that Cluster No.3 in Fig. D.4(a) is grouped as two clusters if using the traditional MCD threshold clustering method. The clusters at position 15 are contributed by multiple bounces with a maximum order of 7, all occurring in-between the buildings as indicated in Fig. D.3(c). It can be observed from

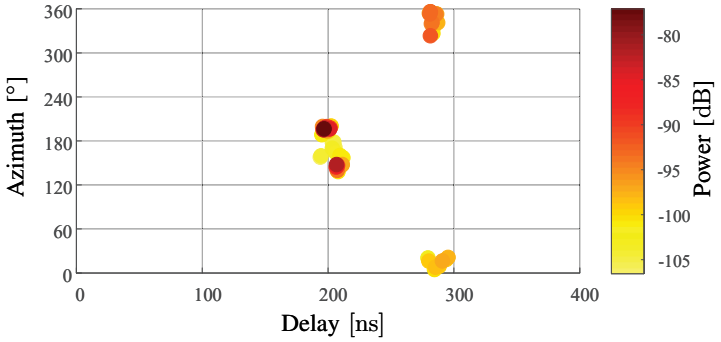

(a)

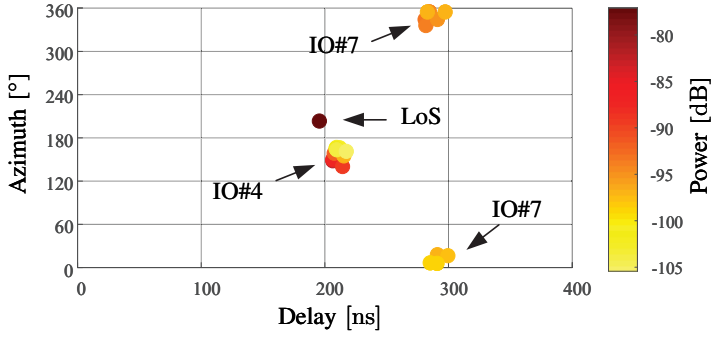

(b)

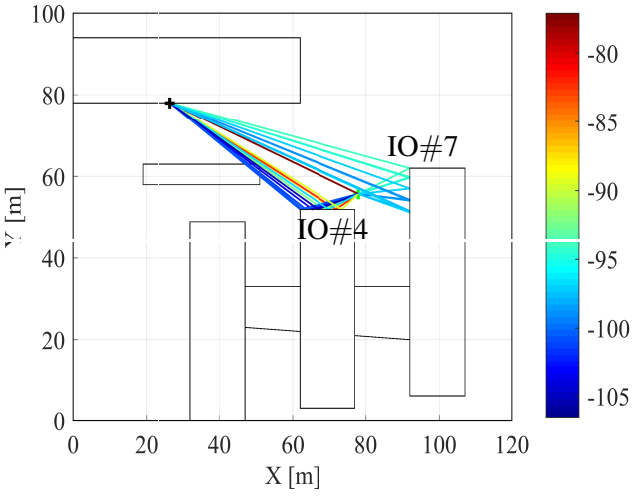

(c)

Fig. D.2: Example at Position 6: (a) Delay-azimuth-power spectrum. (b) Matched paths from RT tool. (c) RT map.

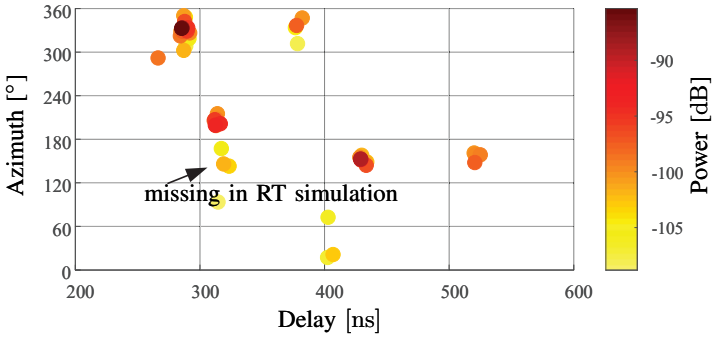

(a)

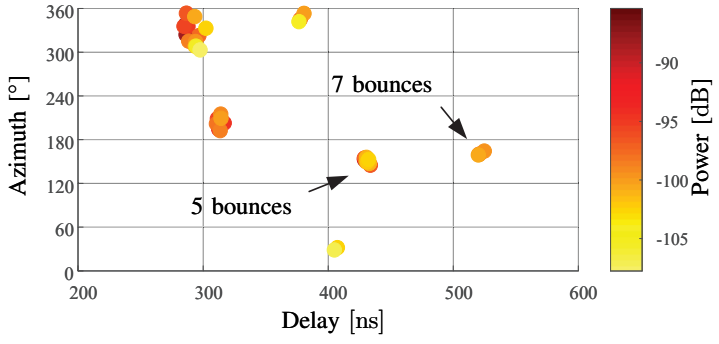

(b)

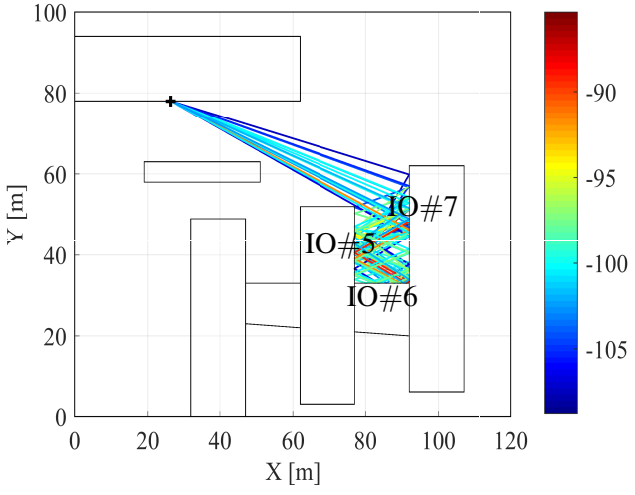

(c)

Fig. D.3: Example at Position 15: (a) Delay-azimuth-power spectrum. (b) Matched paths from RT tool. (c) RT map.

Fig. D.4(b) that Cluster No.2 and No.4 are close and both have 5 bounces. Nevertheless, they belong to different clusters, as they have different bounce sequences from the surrounding walls as IO#7→IO#5→IO#6→IO#7→IO#5 and IO#7→IO#5→IO#7→IO#6→IO#5, respectively. However, Clusters No.2 and No.4 will be seen as one cluster with the traditional MCD threshold clustering method, as they have similar delays and azimuths. Besides, Cluster No.5 with 7 bounces and Clusters No.2 and No.4 with 5 bounces have higher power than Cluster No.6 with 3 bounces and Cluster No.8 with 4 bounces. Furthermore, the measured MPCs missing in the RT simulation in Fig. D.3(a) are grouped as a "new cluster" with unknown bounces and physical IOs, which is Cluster No.7 in Fig. D.4(b).

4 Cluster-level channel characteristics

4.1 Multiple bounces

The power percentage of multiple bounces for each Tx position is depicted in Fig. D.5(a). New clusters, as defined in Sect. 3.3, have unknown numbers of interactions and are marked with -1 for the number of bounces. Since they contribute less than 3% of the total power at each Tx position, they are omitted from the analysis. It can be observed that for the LoS scenario, the power mainly comes from LoS clusters with 0 bounce, while for the NLoS scenario, the power is mostly from a single bounce. However, it is seen that the power contribution of LoS cluster at Tx3 is less than that of clusters with one bounce. This is because part of the elements of the large-scale array was blocked in the LoS direction during the measurement. Moreover, it can be observed that the more bounces, the lower the power contribution is, as generally expected. Except in the case of Tx position 15 as shown in Fig. D.4(b), the power percentage with 5 bounces is higher than that with 2 and 4 bounces. This possible reason is that the multiple reflections with 5 bounces are mainly from the windows with less power attenuation.

4.2 Cluster power decay behavior

The cluster power decays versus propagation distances d in logarithmic scale is fitted by the floating-intercept (FI) path loss model [5] with linear regression lines and plotted in Fig. D.5(b). The parameters $(\alpha, \beta, \varsigma)$ of the FI path loss model obtained from the MCD-threshold and the proposed methods are also shown in Fig. D.5(b). It can be found that the values of the slopes β of the fitting line are similar for the two methods. Additionally, the values of β of both methods are much higher than that found in indoor scenarios at similar frequency bands, which are 2.27 in the classroom, 1.56 in the hall [5], and 3.66 in the NLoS corridor scenario [4]. It means more rapid variations of cluster power versus distance in outdoor scenarios. We conjecture that the larger power loss is caused by the multiple bounces occurring between the buildings.

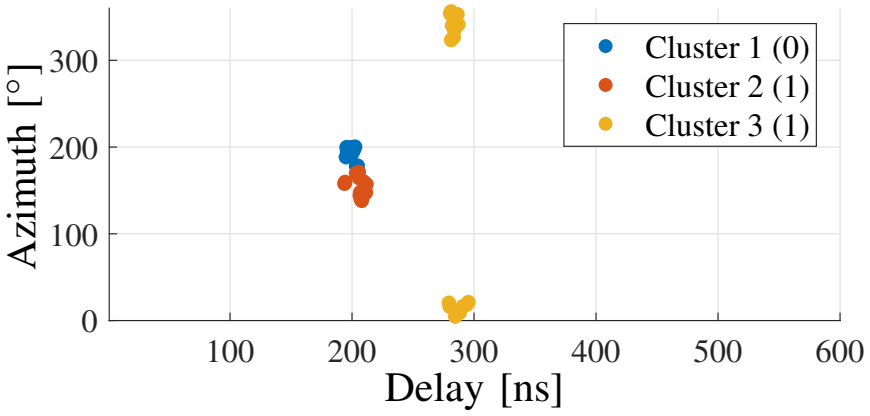

(a)

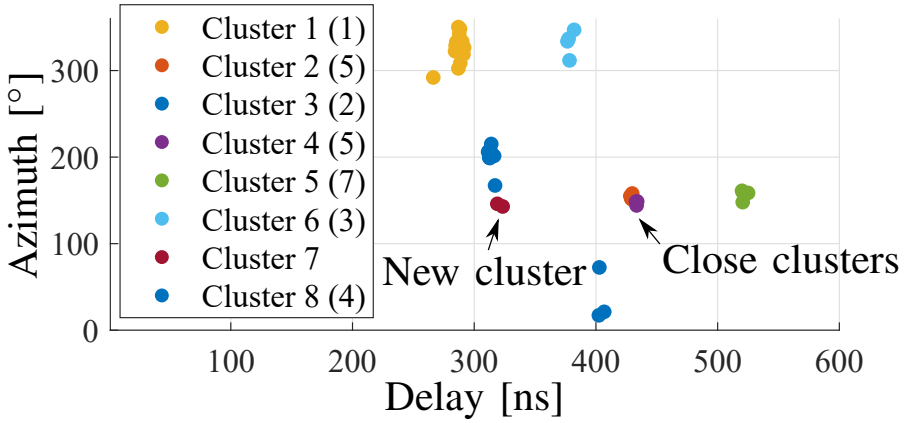

(b)

Fig. D.4: Clustering results based on the proposed clustering method. (a) Position 6. (b) Position 15.

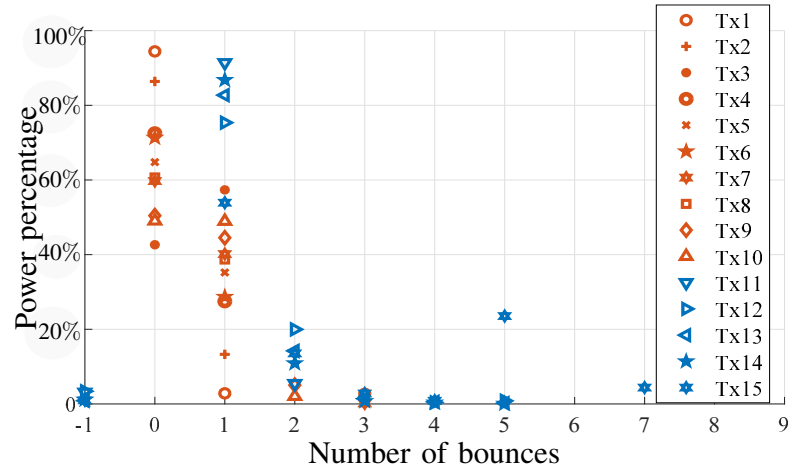

(a)

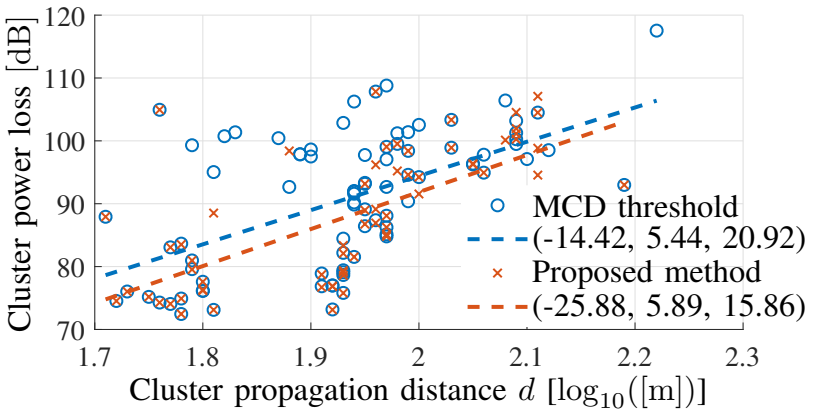

(b)

Fig. D.5: Cluster-level parameters. (a) The power percentage of the total power for different numbers of bounces. (b) Cluster power loss behavior.

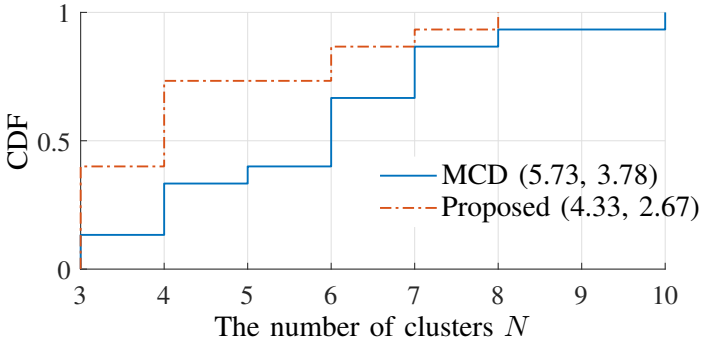

(a)

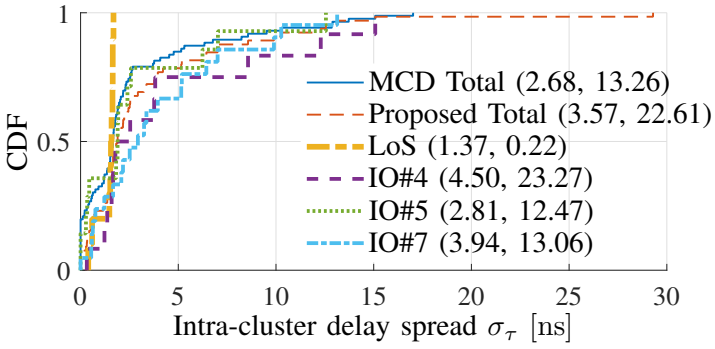

(b)

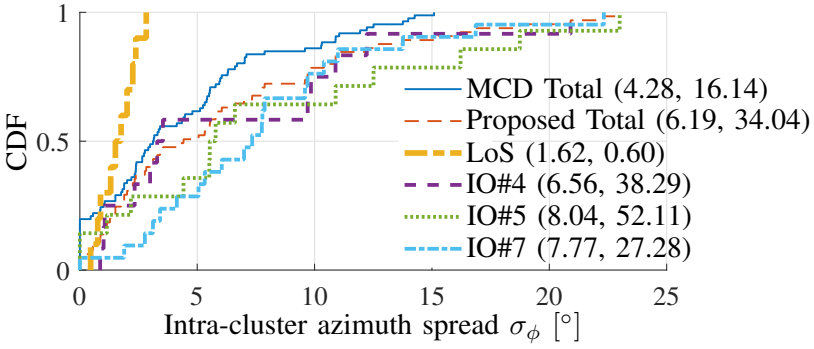

(c)

Fig. D.6: Cluster-level parameters. (a) The number of clusters N. (b) Intra-cluster delay spread σ_τ. (c) Intra-cluster azimuth spread σ_ϕ.

4.3 The number of clusters

Fig. D.6(a) illustrates the CDFs of the number of clusters N [5] of all Tx positions obtained from the MCD-threshold and the proposed methods, with means and variances indicated. The numbers of clusters from both methods are much smaller, compared to those found for LoS indoor scenarios at similar frequency bands, where a mean value of 14.4 was found for the classroom, a mean value of 11 for the hall [5], and a mean value of 21 for the hall and corridor scenario [4] including both LoS and NLoS scenarios. We postulate that it is caused by sparse IOs in outdoor scenarios. Besides, small numbers of clusters, such as less than 4, are mainly in LoS scenarios, while large numbers of clusters usually appear in NLoS scenarios, due to the multiple bounces in between the buildings.

4.4 Intra-cluster delay and azimuth spread

The CDFs of intra-cluster delay spread σ_τ and azimuth spread σ_ϕ [5] for all the clusters obtained from the MCD-threshold are plotted in Fig. D.6(b) and Fig. D.6(c). Similarly, the CDFs of σ_τ and σ_ϕ for all the clusters, LoS and the clusters contributed from each IO# obtained from the proposed method are also plotted in Fig. D.6(b) and Fig. D.6(c). Compared with the results for the indoor scenario in [4], it is found that σ_τ for all the clusters obtained using both clustering methods are much smaller, which are probably caused by the sparse IOs in the outdoor scenario. While it is also found that σ_ϕ for all the clusters are similar, mostly due to the multiple bounces in the corridor in both indoor and outdoor scenarios. It can be observed that both σ_τ and σ_ϕ of LoS clusters are non-zero and smaller than other clusters. This is reasonable, as the Tx is close to the ground, and the reflections from the ground caused non-zero σ_τ and σ_ϕ, while the high power of LoS path compresses the cluster dispersion in both domains. Besides, it can be observed that the clusters from IO#4 have the highest σ_τ and lowest σ_ϕ. However, the clusters from IO#5 have lowest σ_τ and highest σ_ϕ. We conjecture this is because the narrow and long dimension in-between IO#5 and IO#7 caused multiple bounces, which enlarges the cluster dispersion in the angle domain and leads to a smaller delay spread.

5 Conclusions

The geometry-based channel characteristics for the outdoor scenario at the frequency band of 28-30 GHz were investigated in this paper. A geometry-based clustering algorithm was proposed for the accurate determination of clusters based on the interaction objects (IOs) obtained from 3D ray tracing (RT) simulations. The complexity and generalization of the proposed algorithm both depend on the RT tool, where only a simplified model was needed. Further research is required for, e.g., THz bands. Using the measured data, cluster-level parameters contributed by different IOs in both line-of-sight (LoS) and

non-LoS (NLoS) scenarios were investigated.

References

[1] M. Agiwal, A. Roy, and N. Saxena. Next Generation 5G Wireless Networks: A Comprehensive Survey. *IEEE Communications Surveys Tutorials*, 18(3):1617–1655, thirdquarter 2016.

[2] Allan Wainaina Mbugua, Wei Fan, Kim Olesen, Xuesong Cai, and Gert Frølund Pedersen. Phase-Compensated Optical Fiber-Based Ultrawideband Channel Sounder. *IEEE Transactions on Microwave Theory and Techniques*, 68(2):636–647, 2020.

[3] N. Czink, R. Tian, S. Wyne, F. Tufvesson, J. Nuutinen, J. Ylitalo, E. Bonek, and A. F. Molisch. Tracking Time-Variant Cluster Parameters in MIMO Channel Measurements. In *the second International Conference on Communications and Networking in China*, pages 1147–1151, Aug 2007.

[4] Xuesong Cai, Guojin Zhang, Chao Zhang, Wei Fan, Jinxing Li, and Gert Frølund Pedersen. Dynamic Channel Modeling for Indoor Millimeter-Wave Propagation Channels Based on Measurements. *IEEE Transactions on Communications*, 68(9):5878–5891, 2020.

[5] Guojin Zhang, Jesper Ødum Nielsen, Xuesong Cai, Kentaro Saito, Panawit Hanpinitsak, Jun-Ichi Takada, Gert Frølund Pedersen, and Wei Fan. Modeling Multi-Frequency Characteristics for Classroom and Hall Scenarios at 2-4, 9-11 and 27-29 GHz Bands. *IEEE Access*, 9:14549–14563, 2021.

[6] Meifang Zhu. *Geometry-based Radio Channel Characterization and Modeling: Parameterization, Implementation and Validation.* PhD thesis, Department of Electrical and Information Technology, Lund University, 2014.

[7] Panawit Hanpinitsak, Kentaro Saito, Jun-ichi Takada, Minseok Kim, and Lawrence Materum. Multipath Clustering and Cluster Tracking for Geometry-Based Stochastic Channel Modeling. *IEEE Transactions on Antennas and Propagation*, 65(11):6015–6028, 2017.

[8] Fengyu Luan, Andreas F. Molisch, Limin Xiao, Fredrik Tufvesson, and Shidong Zhou. Geometrical Cluster-Based Scatterer Detection Method with the Movement of Mobile Terminal. In *2015 IEEE 81st Vehicular Technology Conference (VTC Spring)*, pages 1–6, 2015.

[9] Lawrence Materum, Jun-ichi Takada, Ichirou Ida, and Yasuyuki Oishi. Mobile Station Spatio-temporal Multipath Clustering of An Estimated Wideband MIMO Double-directional Channel of A Small Urban 4.5 GHz Macrocell. *EURASIP Journal on wireless communications and networking*, 2009:1–16, 2009.

[10] W. Fan, A. W. Mbugua, X. Cai, and K. Olesen. Development and Experimental Validation of an Ultra-wideband Channel Sounder. In *13th European Conference on Antennas and Propagation (EuCAP)*, pages 1–5, March 2019.

[11] LB-SJ-180400-KF Datasheet. Technical report.

[12] S. S. Zhekov, A. Tatomirescu, and G. F. Pedersen. Antenna for Ultrawideband Channel Sounding. *IEEE Antennas and Wireless Propagation Letters*, 16:692–695, 2017.

[13] V. Degli-Esposti, D. Guiducci, A. de'Marsi, P. Azzi, and F. Fuschini. An Advanced Field Prediction Model Including Diffuse Scattering. *IEEE Transactions on Antennas and Propagation*, 52(7):1717–1728, 2004.

[14] Vittorio Degli-Esposti, Franco Fuschini, Enrico M. Vitucci, and Gabriele Falciasecca. Measurement and modelling of scattering from buildings. *IEEE Transactions on Antennas and Propagation*, 55(1):143–153, 2007.

[15] Anders Karstensen, Wei Fan, Fengchun Zhang, Jesper Ø Nielsen, and Gert F Pedersen. Analysis of simulated and measured indoor channels for mm-wave beamforming applications. *International Journal of Antennas and Propagation*, 2018, 2018.

[16] X. Cai and W. Fan. A Complexity-Efficient High Resolution Propagation Parameter Estimation Algorithm for Ultra-Wideband Large-Scale Uniform Circular Array. *IEEE Transactions on Communications*, 67(8):5862–5874, Aug 2019.

[17] Xuesong Cai, Wei Fan, Xuefeng Yin, and Gert Frølund Pedersen. Trajectory-aided maximum-likelihood algorithm for channel parameter estimation in ultra-wideband large-scale arrays. *IEEE Transactions on Antennas and Propagation*, 68(10):7131–7143, 2020.

Paper E

Dynamic Channel Modeling for Indoor Millimeter-Wave Propagation Channels Based on Measurements

Xuesong Cai, Guojin Zhang, Chao Zhang, Wei Fan, Jinxing Li and Gert Frølund Pedersen.

The paper has been published in the
IEEE Transactions on Communications Vol. 68, No. 9, pp. 5878-5891, 2020.

The layout has been revised.

Abstract

In this contribution, a recently conducted measurement campaign for indoor millimeter-wave propagation channels is introduced. A vector network analyzer (VNA)-based channel sounder was exploited to record the channel characteristics at the frequency band from 28-30 GHz. A virtual uniform circular array (UCA) with a radius of 0.25 m was formed using a rotator with 360 steps. Moreover, by taking advantage of fiber-optic technique applied in the channel sounder, measurements at 50 positions were performed from an indoor hall to an indoor corridor along a long pre-defined route. A low-complexity high-resolution propagation estimation (HRPE) algorithm is exploited to estimate the propagation parameters of multipath components (MPCs). Based on the HRPE estimation results, a novel clustering identification and tracking algorithm is proposed to trace clusters. Composite channel characteristics, cluster-level characteristics and dynamic (or birth-death) behaviours of the clusters are investigated, which constitute a dynamic model for the indoor millimeter-wave channel.

1 Introduction

In recent years, an explosive growth of wireless communication data traffic is observed. In this context, millimeter wave (mm-wave) is expected to contribute high data-rate and large capacity for future fifth-generation (5G) communication system due to the large amount of available frequency spectrum [1, 2]. However, mm-wave transmission suffers severe attenuation caused by propagation loss and blockage compared to the sub-6 GHz bands. In order to meet the ever-increasing demands, enabling 5G technologies, e.g. massive multiple-input-multiple-output (MIMO), ultra-dense network, etc. [3–5], have been studied. Specially, beamforming with massive MIMO offers great promise as the high-gain beams can compensate the attenuation and also provide increased capacity to multiple users (so-called MU-MIMO) [6]. These technologies necessitate special strategies such as beam acquisition and tracking [7], making it a prerequisite to gain explicit knowledge of mm-wave channels (especially the dynamic behaviours) for performance evaluation of 5G techniques and communication systems.

Many research groups and organizations have made efforts to study and develop channel models in either theoretical or experimental manners for frequencies up to 100 GHz. In [8–11], ray-tracing simulation tools were exploited to investigate the mm-wave channels in outdoor and indoor scenarios. The authors in [12] applied the propagation graph theory to model 60 GHz channel power angular spectra in an office environment. Though inspiring results were provided by these numerical studies, the realistic scenarios which are far more complicated compared to simulated scenarios need to be characterized by conducting

field measurements. According to the different measurement methodologies, we classify the measurement-based investigations into three categories with several examples discussed in each category. *i) Directional scan sounding (DSS):* Horn antennas are widely used in mm-wave channel measurements since they provide a significant level of directivity and gain. The horn antennas are usually installed on a rotational platform for capturing the signals from different directions. The total received power could be obtained by summing the received powers at each steering direction [13]. Large scale omnidirectional path loss models were developed based on this concept as presented in [14, 15] for both line-of-sight (LoS) and non-LoS (NLoS) scenarios. Furthermore, the measured channels at different steering directions construct the joint delay-angle-power spectra, e.g. as shown in [12, 16]. A double-directional MIMO channel model was presented to demonstrate the consistency between extracted clusters and geometry of the conference room at 60 GHz [17]. Note that in the DSS measurements the additional phase noise introduced by the rotation-center deviation and cable bending should be carefully considered or calibrated, especially in high frequency bands [18, 19]. *ii) Virtual antenna arrays (VAA):* Different from DSS method, VAA relies on a positioner to move an antenna to different locations so that a 2D or 3D array can be formed. For examples, channel characteristics in delay and spatial domain were investigated in [20–23] for mm-wave bands with uniform arrays. The authors in [24] established intracluster and intercluster angular spread models with Laplace distribution and Gaussian mixture distribution. Moreover, the behaviour of clusters evolving across a large antenna array was investigated in [25]. Note that in both DSS and VAA measurements, it takes time for the rotator or positioner to scan the pre-set locations. Therefore, both approaches can be only applied in static environments. *iii) Real antenna arrays (RAA):* Apart from the above mentioned methods, using RAA is also an alternative. For examples, a channel sounder with antenna arrays up to 2×16 at mm-wave band and up to 16×128 at sub-6 GHz band using RAAs and switches was presented in [26]. In [27, 28], a very large RAA-based sounder with 160 dual-polarized antennas was developed and validated in LoS mobile channels, though the working frequency is below 6 GHz. RAA has the advantages in e.g. measuring channels in fast-moving scenarios. However, it requires a huge amount of resources, and the calibration and decoupling among antennas are difficult and critical especially at mm-wave bands. This is also the reason for the scarcity of RAA measurements in mm-wave bands.

Despite considerable efforts have been made in mm-wave propagation channel measurements and modeling, some important features are still inadequately considered in literature. The reasons are threefold. *i)* The measurement distance, i.e. the distance between transmitter (Tx) and receiver (Rx), is usually limited, e.g. in [29, 30], due to the high power attenuation in the coaxial-cable. These models may exhibit poor performance in scenarios like hall or airport where the distance between the users and base stations can be tens of meters. *ii)* Regarding the MPC parameter estimation, the coherent information across

a whole large-array or the whole band is usually not adequately exploited. This is basically due to the missing of appropriate estimation algorithms or the prohibitively high computation-complexity. For examples in [17, 25] the authors decompose the very large arrays into several sub-arrays (and also the whole bands into several sub-bands) to make the plane-wave assumption valid so that the space-alternating-generalized-expectation-maximization (SAGE) algorithm can be applied. However, this in turns lower the accuracy and resolution. Similarly, the radiation pattern of the horn antenna used in the DSS measurements is usually hard to be de-embedded from the raw data. *iii)* Another main deficiency of the existing models is lack of consideration of the channel spatial consistency. In other words, the channel evolution behaviours when either Tx or Rx moves are not addressed in most of the investigations. However, the dynamic characteristics are crucial for system performance evaluation e.g. in terms of beam management especially for 5G and beyond systems where beamforming (based on massive MIMO) is considered the key technology. To support for beam operations in the performance evaluation under dynamic propagation scenarios, it is desirable that moving of Rx or Tx along a long route is enabled in the measurement campaign.

To address the above mentioned gaps, we carry out mm-wave channel measurements at 28-30 GHz frequency band using virtual uniform circular array (UCA) with both indoor hall and corridor scenarios considered. The main contributions and novelties of this paper are summarized as follows:

- By exploiting the fiber-optic technology in a vector network analyzer (VNA)-based channel sounder, a decently long-distance measurement campaign with closely spaced UCA positions was conducted in the indoor scenario. Moreover, the dynamic range was also enhanced due to the low signal-attenuation in the optic fiber. Totally 50 UCA positions were applied along a pre-defined route of around 48 m, which allows us to investigate the dynamic behaviors of the mm-wave channel.
- A complexity-efficient high resolution parameter estimation (HRPE) algorithm [31] is adopted for the ultra-wideband large-scale UCA. The coherent information across the large array and the whole frequency band can be adequatedly exploited by taking the spherical propagation into account. The accuracy and resolution of the estimated multipath-component (MPC) parameters are significantly enhanced.
- Based on the HRPE estimation results, a novel cluster identification and tracking algorithm is proposed to trace the dynamic clusters along the measurement route. Composite-level parameters, cluster-level parameters and dynamic parameters that characterize the "birth-death" behaviors of clusters are investigated. The established realistic dynamic channel model is essential for performance evaluation for 5G and beyond systems.

The rest of the paper is organized as follows. Sect. 2 elaborates the mea-

surement scenarios and specifications in the measurement campaign. Sect. 3 presents some typical channels. In Sect. 4, data processing including the high-resolution propagation parameter estimation and cluster identification and tracking is elaborated. Based on Sect. 4, the established dynamic channel model is investigated in Sect. 5. Finally, conclusive remarks are included in Sect. 6.

2 Measurement campaign

In this section, a recently conducted measurement campaign in an indoor area with a hall and a corridor is presented. The measurement scenarios and measurement equipment are introduced in Sect. 2.1. The measurement configuration that includes the Tx and Rx antennas, frequency band, array configuration etc. is elaborated in Sect. 2.2.

2.1 Measurement environment and channel sounder

The measurement campaign was conducted in an indoor environment. Fig. E.1(a) illustrates its top-view geometry. As illustrated in Fig. E.1(a), the indoor area has an irregularly-shaped hall and a connecting corridor. The dimension of the hall is approximately $44\times25\times10\,\mathrm{m}^3$ (length×width×height). Fig. E.1(b) illustrates a photo taken in the hall. It can be observed that the hall is characterized by stairs, tables, metal supporting pillars (yellow circles), concrete supporting pillars (white circles) and walls. The connecting corridor is around 3.6 m wide and 33 m long. As illustrated in Fig. E.1(c), the corridor has a concrete wall on one side and a glass wall on the other side. A vector network analyzer (VNA) and fiber-optic based channel sounder was used in the measurement. The VNA was exploited to excite the channel and record the channel transfer functions (CTFs), and the fiber optic cable was employed for prolonging the measurement distance (Tx-Rx distance) by taking advantage of its low attenuation to signals in the cable. It has been demonstrated in [32] that a maximum dynamic range of 112 dB can be obtained at 30 GHz using a fiber-optic cable of length 300 m.[1] Furthermore, a phase compensation scheme was applied using photo detector, optic power splitter, optic circulator, etc. to calibrating the phase changes in the optic cable caused by e.g. thermal and mechanical stress. Readers are referred to [32, 33] for the detailed design of the measurement system. The model numbers of the different components used in the channel sounder can be found in Table E.1 in [32]. The performance of the channel sounder has also been validated in [32, 33].

[1] The channel sounder was designed with maximum Tx-Rx distance as 300 m to also cope with, e.g., outdoor measurements. Considering the fiber-optic cable has very low attenuation (which is less than 1 dB/km at 30 GHz [32]), the long cable was kept for the indoor scenarios, although the Tx-Rx distance was less than 300 m.

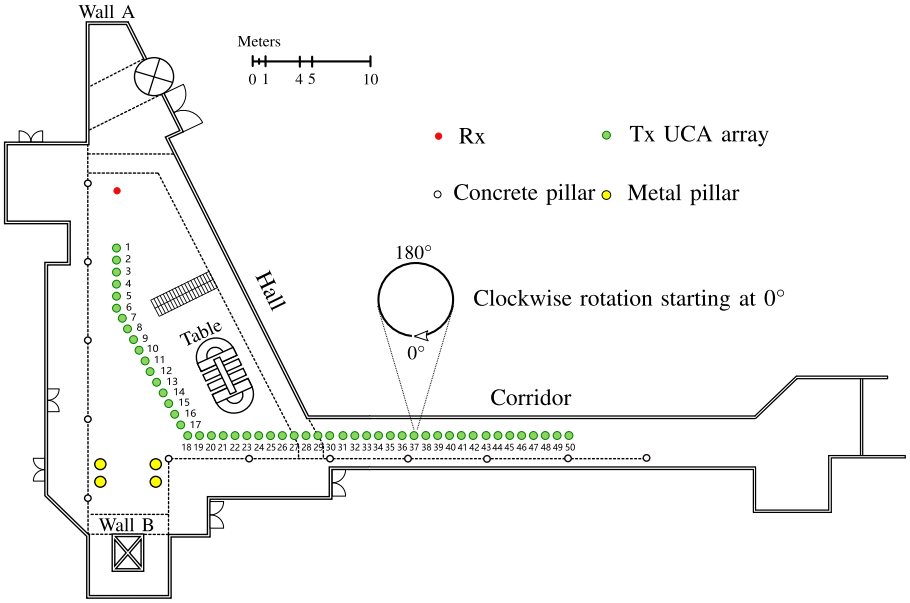

(a)

(b)

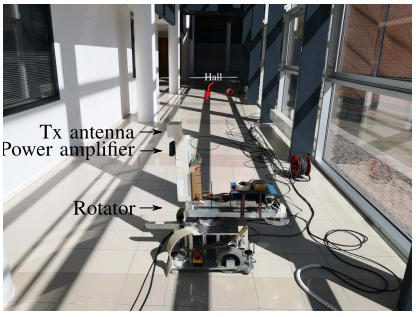

(c)

Fig. E.1: The indoor hall and corridor where the measurement campaign was conducted. (a) The top-view sketch of the indoor area with measurement points marked. (b) A photo taken in the indoor hall. (c) A photo taken in the indoor corridor.

Table E.1: Measurement specifications applied in the measurement campaign.

Measurement specifications			
Tx UCA height (above ground)	1.15 m	Rx height (above ground)	3 m
UCA array radius	0.25 m	Frequency range	28-30 GHz
UCA elements number	360	Frequency points	2000

2.2 Measurement setup

During the measurement, an omni-directional biconical antenna (A-INFO-SZ-2003000/P [34]) was exploited in the Rx side and fixed at the location indicated by the red dot in Fig. E.1(a). As illustrated in Fig. E.1(b), the height (above ground) of Rx was set as 3 m. At the Tx side, another omni-directional biconical antenna [35] was placed on the rotator with a height (above ground) of 1.15 m as illustrated in Figs. E.1(b) and E.1(c). The Tx was moving in the indoor area from position to position as indicated by the green dots in Fig E.1(a). Therefore, it is possible to regard the Rx and Tx as a base-station and a mobile user, respectively. Totally $K = 50$ different positions were performed along a predefined route. The distance of the whole route was 43.5 m, and the distances between neighboring positions were 0.9 m, 0.85 m and 0.9 m for positions 1 to 6, 6 to 18 and 18 to 50, respectively. At each position, a virtual UCA was formed by rotating the Tx antenna clockwise along a circle. The radius r, steps number M and starting point were kept the same for all the 50 positions. As shown in the zoomed-in sketch in Fig. E.1(a) for position 36, the radius was $r = 0.25$ m, the number of steps to complete the circle was $M = 360$, and the starting point (i.e. the first UCA element) was at 0°. The distance between neighboring UCA elements was 4.4 mm which is smaller than the half wavelength at 30 GHz, so that the angular aliasing can be avoided [36]. The frequency range in the VNA was set from 28 GHz to 30 GHz with 2000 sweeping points. The intermediate bandwidth and average factor were set as 1 kHz and 1, respectively. It took 1.844 s to sweep 2000 frequency points for one UCA element. With guard time needed to move the antenna mechanically, the time gap between two sweeps was set as 3 s. Note that a back-to-back calibration for the channel sounder was performed before the formal measurements to remove the system response. It can be calculated that the frequency step was around 1 MHz which corresponds to a propagation distance window with length of 300 m. It was appropriately set to capture all paths with far propagation distances in the indoor environment.[2] Table E.1 and Table E.2 summarize the measurement specifications and antenna specifications applied in the measurement, respectively.

[2]It is worth noting that by applying the measurement configuration, all paths with power above the noise floor can be appropriately captured since no delay aliasing was observed, and the noise floor observed in the channel impulse response was around -140 dB. The dynamic ranges of the color-bars in Figs. E.2 and E.3 are confined referring to the maximum power just for illustration purpose.

Table E.2: Specifications of Tx and Rx antennas applied in the measurement campaign.

Antenna specifications		
Antenna	Rx Biconical [33]	Tx Biconical [34]
Operating frequency range	2-30 GHz	1.5-41 GHz
Typical gain	6 dBi @29 GHz	4.5 dBi @29 GHz
Azimuth pattern	Omni	Omni
Polarization	Vertical	Vertical

3 Channel characterization

As elaborated in Sect. 2.2, at each Tx position 360 CTFs $H(m, f)$ were recorded where m and f represent the step index and frequency, respectively. By applying the inverse discrete Fourier transform (IDFT) to $H(m, f)$ with respect to f, 360 channel impulse responses (CIRs) $h(m, \tau)$ for the array can be obtained. We denote the 360 CIRs for a position as concatenated CIRs (CCIRs). In this section, some typical measured CCIRs are presented, and the underlying propagation mechanisms are discussed.

i) CCIRs in hall scenario:

Figs. E.2(a) and E.2(b) illustrate the CCIRs, i.e. $|h(m, \tau)|^2$, for positions 1 and 18 respectively in the hall. It can be observed that multiple curves exist in the figures. This is due to the 2 GHz bandwidth, i.e., a delay resolution of 0.5 ns or a distance resolution of 0.15 m. That is, the delay variation of a propagation path across the array aperture with radius of 0.25 m can present as a curve in a CCIRs figure. At position 1 as illustrated in Fig. E.2(a), it can be clearly observed that the shape of the LoS path is a "("-alike curve. This is consistent with the fact that the delay of LoS path at the 180th array element is minimum for position 1. This also indicates the fact that the shape of a curve can reflect the angle information of a path to a certain extent. For example, as indicated by the arrow with text "Wall A" in Fig. E.2(a), a curve with a similar shape to that of the LoS path can be observed. By checking its propagation delay, it can be inferred that this curve is contributed by "Wall A" as indicated in Fig. E.1(a).[3] Moreover, the curve attributed to "Wall B" as indicated in Fig. E.1(a) is also marked in Fig. E.2(a). It can be observed that its shape is opposite to that of the LoS path and the "Wall A" curve. Furthermore, we can observe some other curves with different shape orientations.[4] They are contributed by the pillars, side walls, etc. in the hall. Different from the "clean" LoS trajectory, it can be observed that these NLoS curves may blur in the CCIRs figure. This indicates that multiple paths can occur with similar delays and angles, e.g. possibly caused by the scattering effects at pillars and walls. Fig. E.2(b) illustrates the

[3]The signal interacted with "Wall A" but not necessarily only with "Wall A".

[4]Orientation herein can be interpreted as the index of the element with minimum delay in a curve.

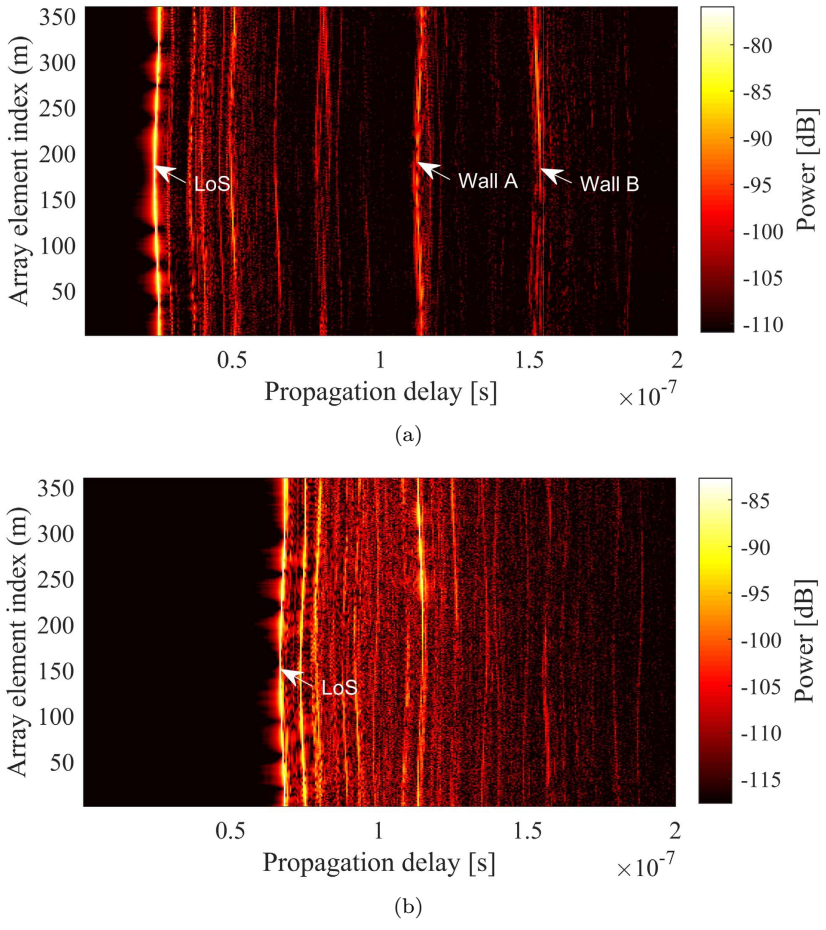

Fig. E.2: Example CCIRs obtained in the hall. (a) Position 1. (b) Position 18.

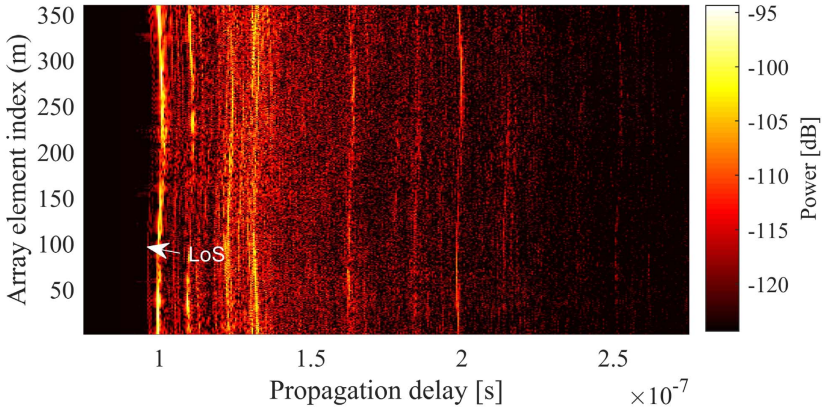

Fig. E.3: An example CCIRs obtained at position 31 in the corridor.

CCIRs figure at position 18. It can be observed that the index of the array element with minimum delay in the LoS curve shifts to a value smaller than 180, which demonstrates that the LoS path angle is less than 180°. This is consistent with the geometry between Tx and Rx at this position. Moreover, due to the distance between Tx and Rx becomes larger, the channel power also decreases. *ii) CCIRs in corridor scenario:* Fig. E.3 illustrates an example CCIRs at position 31 in the corridor. Since the hall wall and corridor wall lie in between the Rx and Tx at this position as shown in Fig. E.1(a), it can be observed from Fig. E.3 that the LoS path is blocked. The channel power also decreases more.

4 Data processing

By examining the CCIRs figures in Figs. E.2 and E.3, it can be observed that the channel experiences obvious changes from the hall to the corridor in delay, angle and power domains. To gain more insights into how the channel evolves in the indoor area, high-resolution information of the channel is required. In this section, a HRPE algorithm is exploited to obtain the high-resolution propagation parameters, i.e. delays, azimuth angles, complex amplitudes, etc. of MPCs from the measured CTFs $H(m, f)$, which is discussed in Sect. 4.1. Based on the HRPE estimation results, a multipath-component-distance (MCD) threshold-based cluster identification and tracking algorithm is proposed in Sect. 4.2 to track the dynamic behaviours of the channel.

4.1 High-resolution MPC parameter estimation

As elaborated in Sect. 2.2, the UCA radius r was set as 0.25 m. The large aperture is advantageous to obtain a high angle-resolution [36]. Meanwhile, the

Fraunhofer distance [37, Ch. 2.2.3], i.e. $\frac{8r^2}{\lambda}$, for the UCA is calculated as 50 m at 30 GHz where λ denotes the wavelength. This means that in the indoor environment, the spherical propagation is non-negligible since plane wave assumption can only be considered valid when the distance from a spherical-wavefront center to an array is much larger than the Fraunhofer distance. Therefore, to gain accurate high-resolution estimation results, spherical propagation must be considered in the propagation parameter estimation to avoid model mismatch [38]. The underlying signal model for the channel impulse response can be formatted as

$$h(\tau, \phi, \theta, d) = \sum_{\ell=1}^{L} \alpha_\ell \delta(\tau - \tau_\ell)\delta(\phi - \phi_\ell)\delta(\theta - \theta_\ell)\delta(d - d_\ell), \tag{E.1}$$

and considering the UCA configuration, the measured array CTFs $H(m, f)$ can be written as [31]

$$H(m, f) = \sum_{\ell=1}^{L} \frac{d_\ell}{d_{\ell,m}} \alpha_\ell e^{-j2\pi f(\tau_\ell + \frac{d_{\ell,m} - d_\ell}{c})} + n(m, f) \tag{E.2}$$

with

$$d_{\ell,m} = \sqrt{{d_\ell}^2 + r^2 - 2rd_\ell \cos\theta_\ell \cos\left(\phi_\ell - \frac{2\pi(m-1)}{M}\right)} \tag{E.3}$$

where L denotes the total number of MPCs, α_ℓ, τ_ℓ, θ_ℓ and ϕ_ℓ represent respectively the complex amplitude, propagation delay, elevation angle and azimuth angle of the ℓth path with UCA center as the reference point, d_ℓ denotes the distance from the UCA center to the spherical-wavefront center, $d_{\ell,m}$ indicates the distance from the mth array element to the spherical-wavefront center, c is the light speed, and $n(m, f)$ denotes the complex Gaussian noise. The parameters to be estimated for all the 50 positions are $\Theta = [\Theta^{(1)}, \ldots, \Theta^{(K)}]$ where $\Theta^{(k)} = [\alpha_\ell^{(k)}, \tau_\ell^{(k)}, \theta_\ell^{(k)}, \phi_\ell^{(k)}, d_\ell^{(k)}; \ell = 1, \ldots, L^{(k)}]$, and k is inserted for the reason that the path number at a different position can be different.

Since the so-called narrowband assumption in array signal processing [36] is not valid due to the 2 GHz bandwidth and the large array aperture, i.e., the array aperture is much larger than the inverse bandwidth multiplied by the light speed, the widely used Space-Alternating Generalized Expectation-Maximization (SAGE) algorithm [17, 25, 39] is not applicable in our case. The complexity of the Expectation-Maximization (EM) algorithm [40, 41] is prohibitively high due to the multiple-dimensional joint-parameter-searching. We hence exploit a low-complexity HRPE estimator [31] to estimate Θ. The basic procedure mainly includes three steps. *i)* Firstly, obtain the high-resolution delay-element trajectories by applying a HRPE principle (e.g SAGE) only in delay domain for all the M UCA elements individually. *ii)* Secondly, locate a path trajectory across the array. This is achieved by exploiting a beamformer

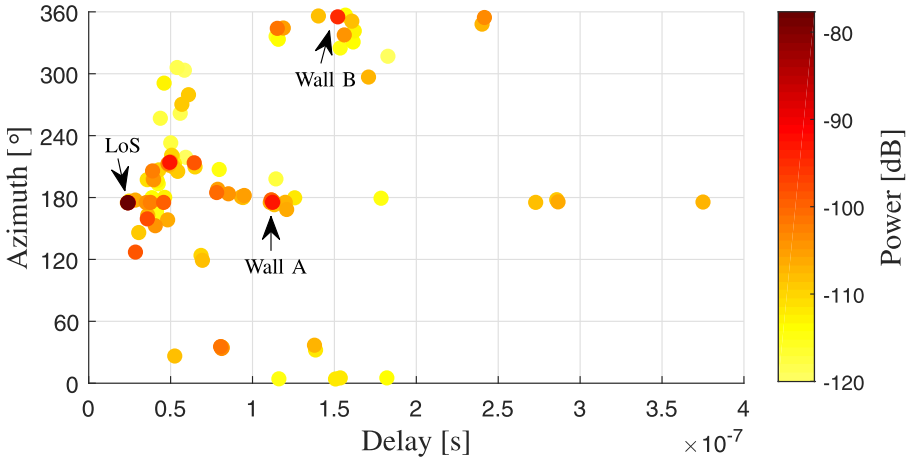

Fig. E.4: An example high-resolution delay-azimuth-power spectrum estimated using the HRPE algorithm at position 1 in the hall.

proposed in [42] to obtain roughly the delay and azimuth of this path trajectory. *iii)* Finally, retrieve the array transfer functions for this path according to the identified path trajectory. Then perform low-complexity parameter searching for the retrieved array responses, and update the original $H(m, f)$ by removing this path from it. Repeat steps *ii)* and *iii)* until the channel power is adequately extracted. Readers are referred to [31] for the detailed principle of the HRPE algorithm. In practice, total path number is set adequately large to fully extract the channel power above the noise floor in step *i)* of the HRPE algorithm, and the valid MPCs number $L^{(k)}$ can be automatically determined in step *ii)* of the HRPE algorithm [31]. Fig. E.4 illustrates an example estimated delay-azimuth-power spectrum at position 1 in the hall with its CCIRs illustrated in Fig. E.2(a). It can be observed more obviously in Fig. E.4 that the azimuths for LoS path and "Wall A" curves are near to 180°, and the azimuth for "Wall B" curves are near to 360° (or 0°). This demonstrates that the HRPE algorithm performs well to extract the high-resolution channel information. Moreover, it can be observed that MPCs are distributed in different groups. As conventionally termed in literature, we denote a group of MPCs with similar delays and angles as a cluster. In the sequel, cluster identification and tracking are elaborated.

4.2 Cluster identification and tracking

Several algorithms have been proposed to identify and/or track clusters in joint power-delay-angular domain. In [43], an algorithm combines K-Power-Means (KPM) and Kalman filter was proposed. KPM considers power in the MCD calculation and is a variant of KMeans [44]. The performances of KPM and

KMeans are highly dependent on the initialization of clusters number and centroids. In [45], a Kernel-Power-Density algorithm was proposed by assuming Gaussian kernel-density in delay domain and Laplacian kernel-density in angular domain, respectively. A Gaussian-mixture-model (GMM) based method was exploited in [18] by assuming the cluster data obey multivariate Gaussian distribution. Recently, a MCD-threshold based principle was proposed in [17]. The investigations in [18, 46] show that the threshold principle outperforms GMM, KPM and KMeans, since the optimum threshold is physically linked to the cluster size/distribution [46], and any prior assumptions of clusters in terms of number, shapes, distributions, etc. are not required. Therefore, the proposed cluster identification and tracking algorithm in this section is based on the MCD-threshold principle.

The MPC distance (MCD) was firstly introduced in [47] to quantify the multipath separation where the MPC parameters present in different units and orders of magnitude. It was then demonstrated in [48] that the clustering performance improves considerably with MCD as distance measures compared to that with squared Euclidean distance measures. In angular domain, the MCD between MPCs i and j is obtained as

$$\mathrm{MCD}_{\mathrm{Tx/Rx},ij} = \frac{1}{2}\left|\begin{pmatrix}\sin\theta_i\cos\phi_i\\ \sin\theta_i\sin\phi_i\\ \cos\theta_i\end{pmatrix} - \begin{pmatrix}\sin\theta_j\cos\phi_j\\ \sin\theta_j\sin\phi_j\\ \cos\theta_j\end{pmatrix}\right| \tag{E.4}$$

for Tx side and Rx side separately. In delay domain, the MCD is calculated as

$$\mathrm{MCD}_{\tau,ij} = \zeta \cdot \frac{|\tau_i - \tau_j|}{\Delta\tau_{\max}} \cdot \frac{\tau_{\mathrm{std}}}{\tau_{\max}} \tag{E.5}$$

where $\Delta\tau_{\max} = \max_{i,j}\{|\tau_i - \tau_j|\}$ for all pairs of (i, j), τ_{std} denotes the standard deviation of the delays, and ζ indicates an appropriate delay scaling factor that gives delay more "importance" when necessary which has advantageous effects when clustering real-world data [48]. The resulting MCD between two MPCs is then obtained as

$$\mathrm{MCD}_{ij} = \sqrt{\|\mathrm{MCD}_{\mathrm{Tx},ij}\|^2 + \|\mathrm{MCD}_{\mathrm{Rx},ij}\|^2 + \mathrm{MCD}_{\tau,ij}^2} \tag{E.6}$$

Note that for the channels observed in our case, $\|\mathrm{MCD}_{\mathrm{Rx},ij}\|^2$ in (E.6) is omitted since we only obtained the angular information at the UCA array side. Moreover, due to the low elevation resolution offered by the the 2D UCA, we also omit θ in the calculation of (E.4). For a cluster grouped by MPCs whose path indices are in set $\mathcal{S}_c$, its cluster centroid is calculated as

$$\mu_c = \frac{\sum_{\ell\in\mathcal{L}_c} |\alpha_\ell|^2 \cdot [\tau_\ell, \phi_\ell]^T}{\sum_{\ell\in\mathcal{L}_c} |\alpha_\ell|^2} \tag{E.7}$$

where T indicates transpose operation.

The proposed algorithm includes two parts. The first part is to identify clusters for all the K positions individually, and the second part is to track clusters between neighboring positions. The proposed cluster identification algorithm of the first part is elaborated in Algorithm 2. It is an improved variant of the algorithms reported in [17, 46]. The basic principle is to firstly initialize clusters by iteratively assigning MPCs adequately near to the current reference point which is chosen as the MPC with highest power among the remaining MPCs. The term "adequately near to" means that the MCD of a path to the reference path is lower than a pre-defined MCD threshold $\eta_{\mathrm{MCD},1}$. Then the overall intra-cluster MCDs are minimized by exploiting the previous cluster centroids as new reference points and updating the cluster centroids iteratively. The selection of the threshold $\eta_{\mathrm{MCD},1}$ is crucial. We exploit several cluster validity indices (CVIs) to choose a suitable value. The CVIs [46, 49–51] include Davies-Bouldin index, Calinski Harabasz index, generalized Dunn index, Xie and Beni index, Pakhira-Bandyopadhyay-Maulik index and SV index. Basically, these indices evaluate the compactness inside clusters and separativeness among clusters. As suggested in [50], the score fusion of all the CVIs is exploited as

$$\mathrm{SF_g} = \Big(\prod_{i=1}^{I} v_i\Big)^{1/I} \tag{E.8}$$

where v_i denotes the normalized score for the ith CVI, and I represents the number of CVIs. Note that for the CVI whose optimal solution is obtained at smallest value (e.g. the XB index), it was modified as $(1 - v_i)$ before inserted into (E.8) so that the optimal solution is obtained at the largest $\mathrm{SF_g}$ value. Fig. E.5 illustrates the $\mathrm{SF_g}$ variation (normalized to the largest value) versus $\eta_{\mathrm{MCD},1}$ variation for position 1. It can be observed that the largest $\mathrm{SF_g}$ value is obtained at $\eta_{\mathrm{MCD},1}$ equals 0.37 which is hence selected as the optimal threshold in the proposed clustering algorithm for position 1. The thresholds for the other positions are obtained with the same approach.

Based on the obtained clustering results, cluster tracking are performed by checking MCDs among cluster centroids between neighboring positions as elaborated in Algorithm 3. For each old cluster identified at the kth position, the closest new cluster is determined by finding the cluster at the $(k + 1)$th position with minimum MCD to this old cluster. The closest old cluster to each new cluster is determined vice versa. If an old cluster and a new cluster are mutually closest, and their MCD is lower than a pre-defined threshold $\eta_{\mathrm{MCD},2}$, these two clusters are associated as a tracked cluster. Old clusters that are not associated are considered "dead" clusters that stop existing, and new clusters that are not associated are considered as "born" clusters. In our case, $\eta_{\mathrm{MCD},2}$ is empirically chose as 0.35 to obtain reasonable tracking results.[5] Figs. E.6(a)

[5]The value of $\eta_{\mathrm{MCD},2}$ is selected practically. The attempt is to guarantee the cluster tracking results provide good match with the physical propagation mechanisms. In addition, it is noteworthy that the path-index set of tracked LoS cluster is associated as $\mathcal{L}_1^{(k)}$ in the algorithm since the power of the LoS cluster is the highest in the first array position.

Algorithm 2 The proposed MCD-threshold-based clustering algorithm for individual positions.

Input: MPC parameters $\Theta^{(k)}$ at the kth array position.
Output: Clustering results $\mathcal{L}_c^{(k)}; c \in \mathcal{C}^{(k)}$.

1: Initialize path-index set $\mathcal{L} \leftarrow \{1, \ldots, L^{(k)}\}$
2: Initialize cluster index $i \leftarrow 0$
3: **while** $\mathcal{L} \neq \emptyset$ **do**
4: $i \leftarrow i + 1$
5: Find the index of the path with highest power $\ell_{\mathrm{m}} = \arg\max_{\ell \in \mathcal{L}} |\alpha_\ell^{(k)}|^2$
6: Initialize path-index set for the ith cluster $\mathcal{L}_i^{(k)} \leftarrow \emptyset$
7: **for** $\ell \in \mathcal{L}$ **do**
8: **if** $\mathrm{MCD}_{\ell,\ell_m} \leq \eta_{\mathrm{MCD},1}$ **then**
9: $\mathcal{L}_i^{(k)} \leftarrow \mathcal{L}_i^{(k)} + \{\ell\}$
10: **end if**
11: **end for**
12: $\mathcal{L} \leftarrow \mathcal{L} \setminus \mathcal{L}_i^{(k)}$
13: **end while**
14: Let cluster-index set $\mathcal{C}^{(k)} \leftarrow \{1, \ldots, i\}$
15: Calculate all the cluster centroids $\mu_c^{(k)}; c \in \mathcal{C}^{(k)}$ by (E.7)
16: **while** $\mu_c^{(k)}$'s do not keep unchanged **do**
17: Initialize $\mathcal{L} \leftarrow \{1, \ldots, L^{(k)}\}$ and $\mathcal{L}_c^{(k)} \leftarrow \emptyset; c \in \mathcal{C}^{(k)}$
18: **for** $\ell \in \mathcal{L}$ **do**
19: Find the centroid index c_n with minimum MCD to the current MPC: $c_n = \arg\min_{c \in \mathcal{C}^{(k)}} \mathrm{MCD}_{\ell,\mu_c^{(k)}}$
20: **if** $\mathrm{MCD}_{\ell,\mu_{c_n}^{(k)}} \leq \eta_{\mathrm{MCD},1}$ **then**
21: $\mathcal{L}_{c_n}^{(k)} \leftarrow \mathcal{L}_{c_n}^{(k)} + \{\ell\}$, $\mathcal{L} \leftarrow \mathcal{L} \setminus \{\ell\}$
22: **end if**
23: **end for**
24: **if** $\mathcal{L} \neq \emptyset$ **then**
25: $i \leftarrow i + 1$, **do** lines 3 to 12.
26: **end if**
27: Update $\mathcal{C}^{(k)}$ and $\mu_c^{(k)}; c \in \mathcal{C}^{(k)}$
28: **end while**

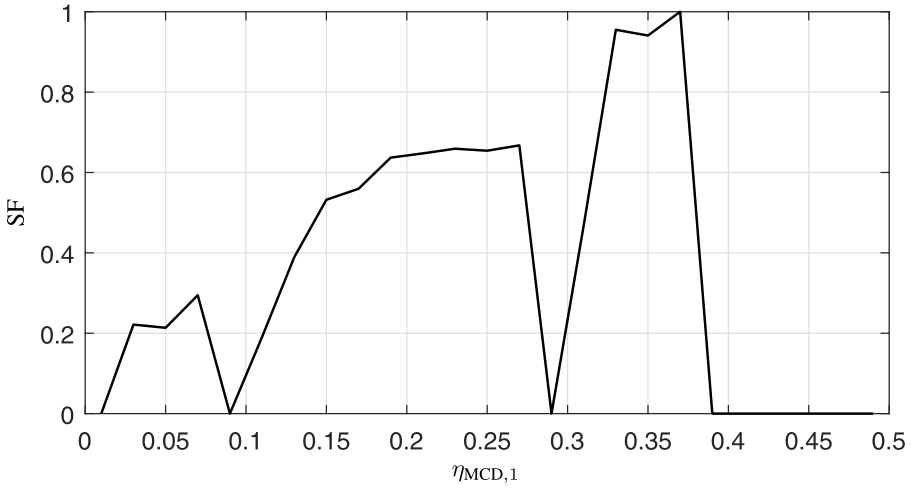

Fig. E.5: SF variation versus $\eta_{\mathrm{MCD},1}$ variation at position 1.

Algorithm 3 The proposed cluster tracking algorithm between neighboring positions.

Input: Clustering results at all positions.
Output: Cluster tracking results.

$i \leftarrow 1$
for $i \leq (K-1)$ **do**
  Obtain cluster centroids $\mu_c^{(i)}; c \in \mathcal{C}^{(i)}$
  Obtain cluster centroids $\mu_c^{(i+1)}; c \in \mathcal{C}^{(i+1)}$
  for $a \in \mathcal{C}^{(i)}$ **do**
    Find nearest cluster at the $(i+1)$th position: $b_n = \arg\min_{c \in C^{(i+1)}} \mathrm{MCD}_{\mu_a^{(i)}, \mu_c^{(i+1)}}$
    Find nearest cluster back at the ith position: $a_n = \arg\min_{c \in C^{(i)}} \mathrm{MCD}_{\mu_c^{(i)}, \mu_{b_n}^{(i+1)}}$
    if $a_n = a$, and $\mathrm{MCD}_{\mu_a^{(i)}, \mu_{b_n}^{(i+1)}} \leq \eta_{\mathrm{MCD},2}$ **then**
      Associate clusters a^i and b_n^{i+1} as one cluster
    end if
  end for
  Update cluster index set $\mathcal{C}^{(i+1)}$. The associated cluster-index values are set identical to previous values in $\mathcal{C}^{(i)}$, and un-associated cluster-index values accumulate referring to the largest value in $\mathcal{C}^{(i)}$.
  $i \leftarrow i+1$
end for

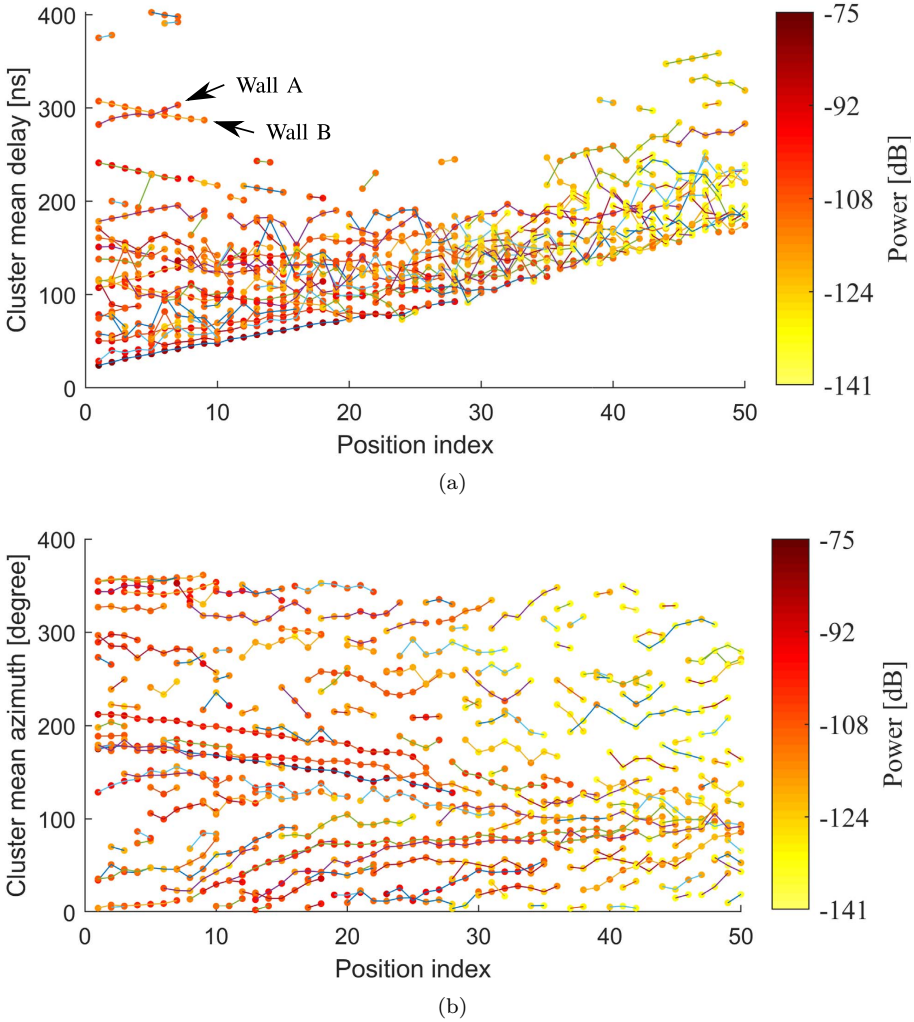

Fig. E.6: Dynamic clusters identified and tracked. (a) Delay domain. (b) Azimuth domain.

and E.6(b) illustrate the cluster identification and tracking results in delay and azimuth domains, respectively. Each dot represents a cluster's centroid in delay or azimuth. The colors of dots denote clusters power, and the dots belong to one cluster are connected with lines. It can be observed that clusters evolve in delay and azimuth domains. For examples, it can be observed in Fig. E.6(a) that the delay and azimuth of LoS cluster increases and decreases respectively along the route, and it stops at position 28 where the LoS link is starting to be blocked. Moreover, the clusters caused by "Wall A" and "Wall B" can also be easily located in Fig. E.6. A clearer illustration of them is in Fig. E.11. It can be observed that the cluster delays of them increases and decreases respectively, whereas the cluster azimuths almost keep unchanged as 180 and 360 (or 0) degrees, respectively. The demonstrated consistency between tracked clusters and the underlying propagation mechanisms validates the performance of the proposed cluster identification and tracking algorithm.

5 Dynamic channel model

Based on the cluster identification and tracking results, a dynamic channel model is established for the hall and corridor scenarios in this section. Basically, three aspects of the channel characteristics have been investigated. *i)* The composite-level parameters that include path loss, composite root-mean-square (RMS) delay spreads, composite RMS azimuth spreads are presented in Sect. 5.1. *ii)* In Sect. 5.2, cluster-level parameters, i.e. cluster delay spread, cluster azimuth spread, cluster power decay and correlations thereof, are elaborated. *iii)* Sect. 5.3 describes the "birth-death" behaviours of clusters. The investigated parameters include cluster survival length, cluster birth location, cluster evolution and cluster number. Note that the statistics obtained in *i)* and *ii)* can be exploited to reproduce random/wide-sense-stationary (WSS) channel realizations according to procedures similar to that as specified in, e.g. [52].[6] In cases where the spatial consistency (or dynamics) of the channel is crucial, statistics obtained in *iii)* can be further exploited to reproduce the realistic dynamic/non-WSS channels.

5.1 Composite level parameters

Path Loss PL

According to the clustering results, the received power at the kth position can be calculated as

[6] The term "random" here means that the channel parameters are generated independently for each snapshot according to the obtained statistics. In other words, the spatial consistency between neighboring channel snapshots are not considered. However, in 5G and beyond-5G communication systems where massive MIMO is considered as the key enabling technology, it is crucial to evaluated the beam-management [7, 53] (e.g. beam acquisition and beam tracking) performance of devices, which necessitates the investigation for aspect *iii)* in this contribution.

$$p = \sum_{\ell \in \{\mathcal{L} \setminus \mathcal{L}_1\}} |\alpha_\ell|^2 \tag{E.9}$$

where $\mathcal{L} = \{1, \ldots, L^{(k)}\}$, and the superscript k is omitted in (E.9) for notation convenience. The LoS cluster is not included for the following reasons. *i)* The challenging communication scenario at mm-wave frequency bands is usually the case where LoS direction is blocked. By removing LoS cluster in hall, a fair comparison can be obtained between the hall and corridor scenarios with only NLoS clusters considered. *ii)* Compared to that of NLoS clusters, the behaviour of LoS cluster is rather deterministic which is investigated in Sect.5.2 and can be easily included in the link budget estimation together with (E.9) if LoS communication is targeted. The floating-intercept (also known as alpha-beta) path loss model

$$PL(d)[\text{dB}] = \alpha + 10 \cdot \beta \log_{10}(d/d_0) + X_\sigma \tag{E.10}$$

is exploited, where α denotes the intercept, β indicates the path loss exponent (PLE), d and d_0 represent the Tx-to-Rx distance (the length of the straight line connecting the Tx and Rx positions) and reference distance (set as 1 m) respectively, and X_σ is the shadow fading modeled as a Gaussian random variable with zero mean and standard deviation σ. Fig. E.7 illustrates the path loss fitting in both hall and corridor scenarios. It can be observed the PLE in hall is small as 0.96. This can be explained by the fact that the hall is a nearly-closed scenario, the power of NLoS clusters change insignificantly with the array moving. However, the PLE in corridor is high as 5.9, mostly due to the large attenuation caused by the multiple reflections from the sidewalls in the corridor.

Composite delay spread σ_τ and composite azimuth spread σ_ϕ

The RMS delay spread is the most common parameter to characterize the delay dispersion of the channel, which is calculated as the second-order central moment of the power delay profile. Specifically, by using the HRPE estimation results, the RMS delay spread can be calculated as specified in [54, 55]

$$\sigma_\tau = \sqrt{\overline{\tau^2} - \overline{\tau}^2} \tag{E.11}$$

with

$$\overline{\tau^2} = \frac{\sum_{\ell \in \{\mathcal{L} \setminus \mathcal{L}_1\}} |\alpha_\ell|^2 \cdot \tau_\ell^2}{\sum_{\ell \in \{\mathcal{L} \setminus \mathcal{L}_1\}} |\alpha_\ell|^2}, \quad \overline{\tau} = \frac{\sum_{\ell \in \{\mathcal{L} \setminus \mathcal{L}_1\}} |\alpha_\ell|^2 \cdot \tau_\ell}{\sum_{\ell \in \{\mathcal{L} \setminus \mathcal{L}_1\}} |\alpha_\ell|^2} \tag{E.12}$$

The azimuth spread σ_ϕ can be calculated as [52]

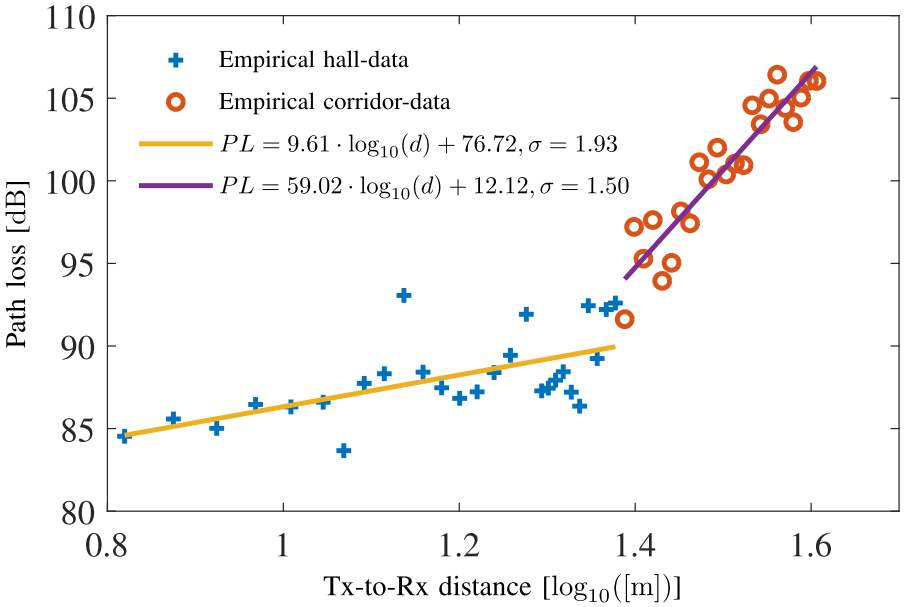

Fig. E.7: Path loss fitting for the hall scenario and corridor scenario.

$$\sigma_\phi = \sqrt{-2\log\left(\left|\frac{\sum_{\ell\in\{\mathcal{L}\setminus\mathcal{L}_1\}} \exp(j\phi_\ell)\cdot|\alpha_\ell|^2}{\sum_{\ell\in\{\mathcal{L}\setminus\mathcal{L}_1\}}|\alpha_\ell|^2}\right|\right)} \tag{E.13}$$

Fig. E.8(a) and Fig. E.8(b) illustrate the empirical cumulative distribution functions (CDFs) of σ_τ and σ_ϕ represented in logarithm scales respectively for both hall and corridor scenarios, and the empirical CDFs are well fitted with normal distributions.[7] It can be observed from Fig. E.8(a) that in most cases, the composite delay spread in hall scenario is larger than that observed in corridor scenario. We postulate that this is mainly due to the fact that the dimension of the hall is large, and MPCs with larger relative delays can exist. Meanwhile, in some cases, the delay spread in hall can be smaller than that of corridor. This is possibly due to that the objects in the hall can cause dominant paths which compress the whole spread. Moreover, it can be observed from Fig. E.8(b) that

[7] We exploit the Kolmogorov-Smirnov (KS) testing [56] to validate the consistency between the empirical distribution and the fitted analytical distribution. Specifically, if the p-value is larger than a pre-defined significance level α, the null hypothesis is accepted, say, the empirical and fitted distributions are consistent. Note that the value selection of α is rather artificial (conventionally at 0.05 meaning the probability of wrongly rejecting the null hypothesis), we thus directly show p-values throughout the paper. For example in the case illustrated here, the p-values are 0.74 and 0.97 that are much larger than 0.05, which indicates that the consistency between the empirical and fitted distribution are rather significant. All the p-values for the fittings throughout the paper can be found in Table E.4.

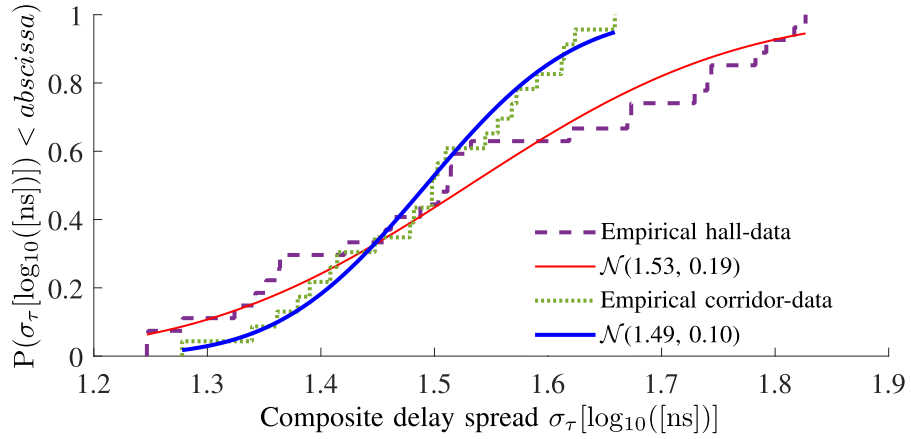

(a)

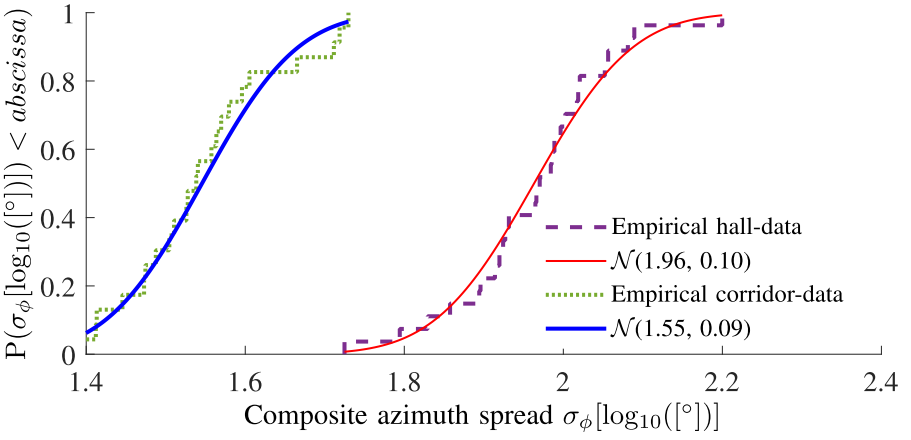

(b)

Fig. E.8: Empirical and fitted analytical CDFs for hall and corridor scenarios. (a) Composite delay spread σ_τ. (b) Composite azimuth spread σ_ϕ.

the composite azimuth spread in the hall is larger that that in the corridor. Basically, this is due to the large dimension of the hall, which implies that MPCs can have different azimuth angles. As a contrast, the corridor has a narrow opening to the hall, which leads to confined azimuth angles of the paths. Consequently, we can observe small composite azimuth spread in the corridor scenario.

5.2 Cluster level parameters

Cluster power decay behaviour

The cluster power decay PL_c is similarly modeled using (E.9) with PL replaced by the cluster path loss PL_c and d replaced by d_c calculated according to the cluster mean delay $\bar{\tau}_c$. Fig. E.9 illustrates the cluster path loss versus propagation distance in logarithmic scale for LoS cluster in hall, NLoS clusters in hall scenario and NLoS clusters in corridor scenario, respectively. It can be observed that PLE of LoS cluster is near to the free-space PLE 2, which is reasonable. It can also be observed that the PLE of NLoS clusters in corridor scenario is higher as 3.65. The possible reason is that the narrow corridor lead to larger reflection orders hence a larger PLE. However, as a contrast, the PLE of NLoS clusters in hall scenario is small. We postulate this is because the objects, e.g. the metal objects, in the hall can cause high-power clusters although with large propagation distances, which tilts down the slope. This also results in a large shadowing for the NLoS clusters in hall compared to that of LoS cluster. Basically, it can be observed that the spread of cluster path loss becomes larger with the cluster propagation distance increasing. We postulate it is due to the fact that with a larger propagation distance, the possibility of clusters experiencing multiple-bounces is higher. As different objects or scatterers can cause different losses, the path loss spread could thus be larger.

Intra-cluster delay spread σ_{τ_c} and azimuth spread σ_{ϕ_c}

The intra-cluster delay spread and azimuth spread are calculated similarly by using (E.11) and (E.13), respectively, with path index-set replaced by the corresponding cluster path-index set. Fig. E.10(a) and Fig. E.10(b) illustrate respectively the empirical CDFs of σ_{τ_c} and σ_{ϕ_c} for the LoS cluster and NLoS clusters in hall and corridor, and the fitted analytical CDFs are also shown. It can be observed from Fig. E.10(a) and Fig. E.10(b) that both the delay spread and azimuth spread of LoS cluster are smaller than that of NLoS clusters. This is reasonable since the high power of LoS path compresses the cluster dispersion in both domains. Moreover, it can also be observed that the cluster delay spreads and azimuth spreads of NLoS clusters in hall are smaller than that observed in corridor scenario. We conjecture this is because in the hall, sparsely placed objects such as pillars can cause clusters with dominant MPC(s). However, in the corridor, due to the narrow dimension, MPCs with similar power are grouped as a cluster which enlarges the cluster dispersion.

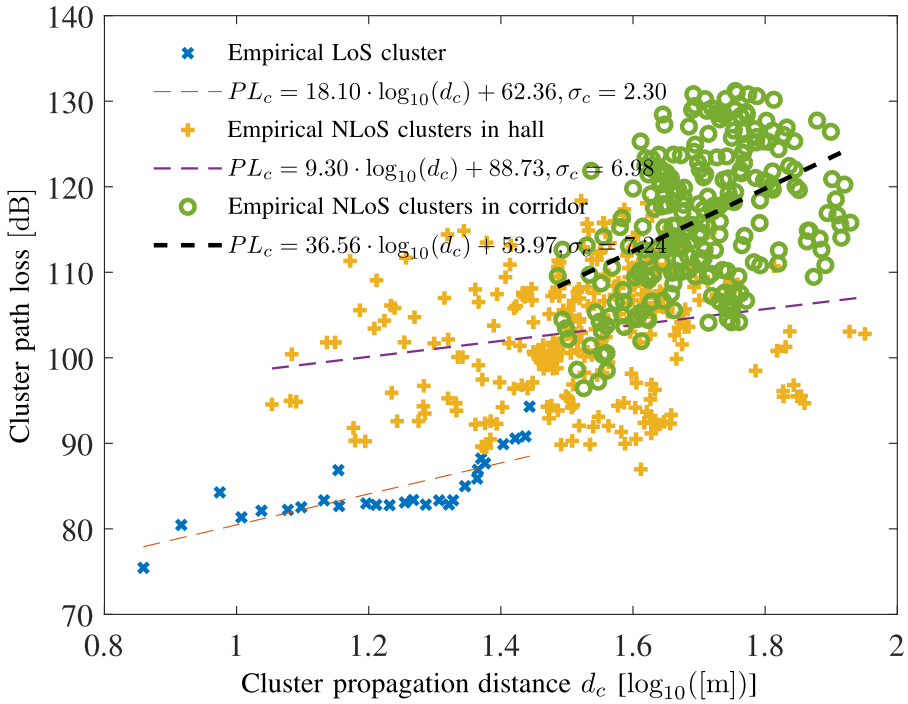

Fig. E.9: Cluster power decay behaviour for LoS cluster and NLoS cluster in hall and corridor scenarios.

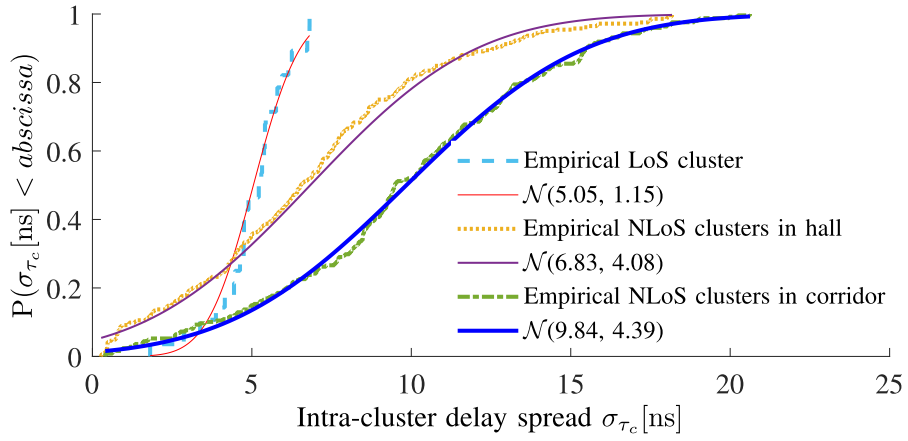

(a)

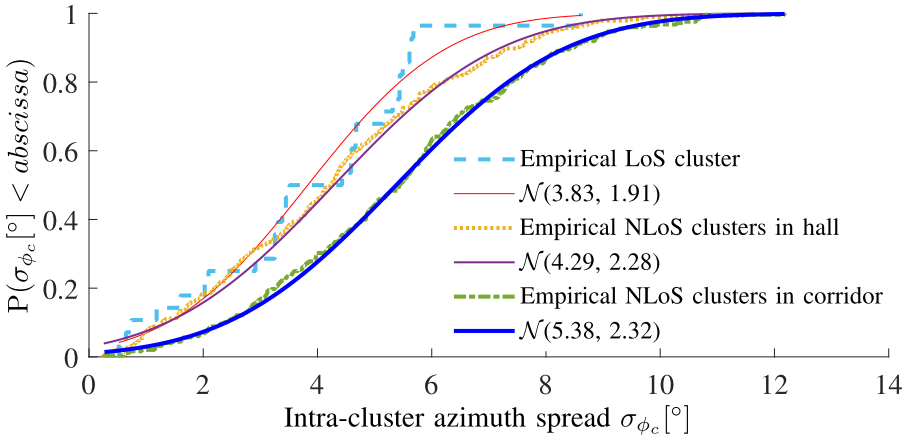

(b)

Fig. E.10: Empirical and fitted CDFs of intra-cluster delay spread and azimuth spread for LoS cluster, hall and corridor scenarios. (a) Intra-cluster delay spread σ_{τ_c}. (b) Intra-cluster azimuth spread σ_{ϕ_c}.

Table E.3: Correlations among cluster level parameters.

	LoS	NLoS in hall	NLoS in corridor
$\gamma(\sigma_{\tau_c}, \sigma_{\phi_c})$	0.28	0.14	0.05
$\gamma(\sigma_{\tau_c}, p_c)$	-0.56	-0.08	-0.08
$\gamma(\sigma_{\phi_c}, p_c)$	-0.48	-0.15	-0.02

Correlations of cluster level parameters

The correlation coefficient between two random variables X and Y is formulated as

$$\gamma_{XY} = \frac{\sum_i (X_i - \bar{X})(Y_i - \bar{Y})}{\sqrt{\sum_i (X_i - \bar{X})^2} \sqrt{\sum_i (Y_i - \bar{Y})^2}} \tag{E.14}$$

where $\bar{X}$ and $\bar{Y}$ represent the mean values of X and Y, respectively. Table E.3 summarizes the correlation coefficients among cluster power, cluster delay spread and cluster azimuth spread. It can be observed that the correlation coefficients $\gamma(\sigma_{\tau_c}, p_c)$ and $\gamma(\sigma_{\phi_c}, p_c)$ of LoS cluster are negative and significant. This is reasonable since the power of LoS cluster is mainly dominated by the LoS path, and with a higher LoS path power, the LoS cluster dispersions in both delay and azimuth are compressed. For the same reason, a positive $\gamma(\sigma_{\tau_c}, \sigma_{\phi_c})$ for LoS cluster is also observed. The NLoS clusters exhibit similar correlation trends among these cluster-level parameters. However, the absolute values are rather small. Therefore, it can be considered that no correlations have been found among cluster-level parameters for NLoS cluster in both hall and corridor scenarios.

5.3 Dynamic parameters

In this section, dynamic parameters that characterize the "birth-death" behaviors of clusters are investigated. The concerned parameters include the cluster survival length, cluster born point, slopes of cluster-trajectories in both delay and azimuth domains. Fig. E.11 illustrates two enlarged clusters selected from Fig. E.6 to demonstrate the definitions of the dynamic parameters. Note that to compromise the model accuracy and complexity, we use linear lines to fit the cluster-trajectories in both delay and azimuth domains. This is a reasonable approximation since it can be observed from Fig. E.6 and Fig. E.11 that the cluster survival length is usually not large, which means that during the "alive" distance, the relative geometry between a cluster and the scatterer do not change much, thus a first-order approximation is reasonable. Specifically, the variation of a dynamic cluster in terms of mean delay and mean azimuth can be formatted as

$$\bar{\tau}_c = a_\tau d + b_\tau + x_\tau, \quad \bar{\phi}_c = a_\phi d + b_\phi + x_\phi \tag{E.15}$$

where d denotes the distance the UCA moves along the route, and a, b and x represent the slope, intercept and fluctuation respectively with their subscripts τ and ϕ indicating delay and azimuth domains, respectively.

Survival length d_s

Fig. E.12 illustrates the empirical CDFs of cluster survival lengths in logarithm scale for both hall and corridor scenarios. It can be observed that the empirical CDFs of survival length in meter can be well fitted using log-normal distributions. This means that the survival length has moderate values with large probability. In other words, either the survival length is too small or too large, its probability becomes smaller. Moreover, it can also be observed that the cluster survival length in hall is larger than that observed in corridor scenario. This is consistent with the fact that the dimension of the hall is large which can result in large cluster survival lengths. Due to the multiple reflections in corridor, clusters cannot be alive for long distances.

Slopes a_τ and a_ϕ of clusters

By fitting the model as specified in (E.15), a_τ and a_ϕ are calculated for the NLoS clusters in both hall and corridor scenarios. Fig. E.13(a) and Fig. E.13(b) illustrate the empirical CDFs and fitted analytical CDFs for a_τ and a_ϕ respectively in both scenarios. It can be observed that the spread of the slopes in the corridor scenario is basically larger than that observed in the hall scenario. We postulate the main reason is that the scatterers are nearer to the transceiver in the corridor due to its smaller dimension. In addition, Fig. E.14(a) and Fig. E.14(b) illustrate respectively the empirical CDFs of x_τ and x_ϕ for both scenarios, which are found to be best fitted with stable distributions.[8] It can be observed that the mean values of x_τ and x_ϕ are near 0, which is expected in (E.15). Moreover, the fluctuations x_τ or x_ϕ are similar in both scenarios.

Born delay τ_0 and born azimuth ϕ_0

As illustrated in Fig. E.11, τ_0 and ϕ_0 of a cluster are defined as the delay (relative to LoS path delay) and azimuth of the cluster born point, respectively. Fig. E.15(a) illustrates the empirical CDFs and fitted analytical CDFs for τ_0 in logarithmic scale in both scenarios. It can be observed that the range of τ_0 in hall scenario is larger than that observed in corridor. We postulate that this is due to the fact that the scatterer with large relative distance in hall can still cause non-negligible clusters. However, in the corridor scenario, larger relative delay probably means more bounces between two sidewalls, and the power of clusters decreases fast. Fig. E.15(b) illustrates the empirical CDFs and the corresponding fitted CDFs for ϕ_0 in both scenarios. It can be observed that the empirical CDFs of born azimuth in both scenarios can be well fitted with

[8] Readers are referred to [57] for the definition of stable distribution.

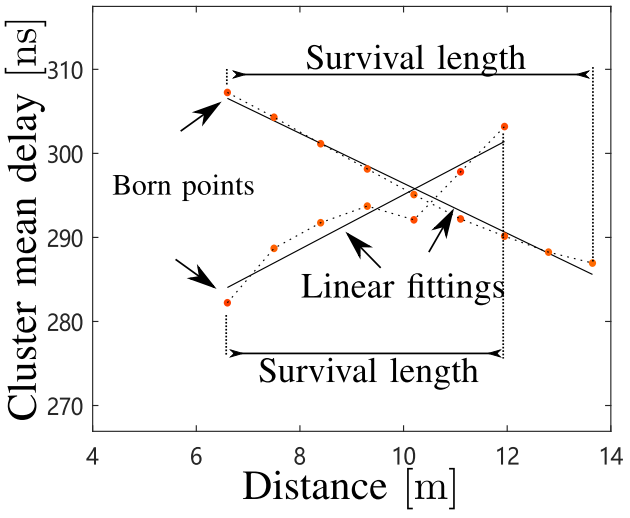

(a)

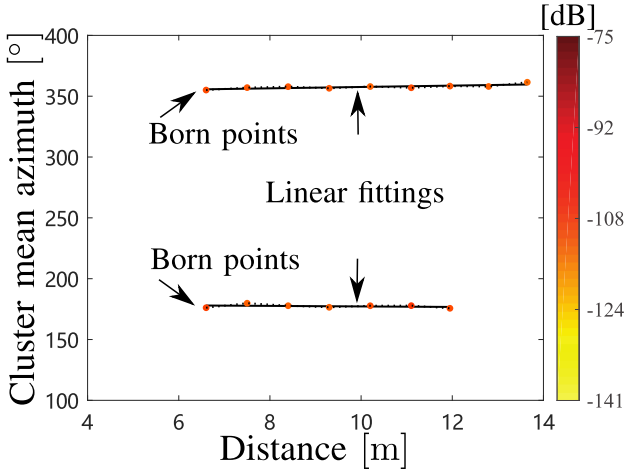

(b)

Fig. E.11: An example demonstration of dynamic parameters with two clusters enlarged from Fig. E.6.

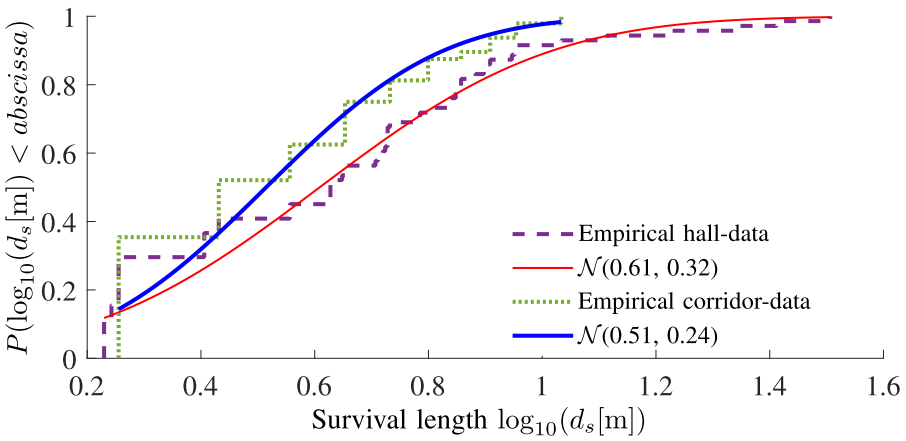

(a)

Fig. E.12: Empirical and fitted CDFs of survival distance d_s in logarithm scale for NLoS clusters in hall and corridor.

uniform distributions. This is reasonable since the walls and objects as well as bounces in both scenarios can cause clusters with various angles. Besides, due to the dimension of the hall is larger, the whole angle range is larger than that observed in corridor.

Born clusters number N

Fig. E.16 illustrates the empirical CDFs and the fitted CDFs of born clusters number for both scenarios. It can be observed that the mean number of born clusters in hall scenario is slightly larger than that observed in corridor, which we postulate is due to the larger dimension and more objects in hall scenario. However, the born clusters number are basically similar in both scenarios. The possible reason is that although the dimension of the corridor is smaller, with a glass wall on one side, the outside objects may also cause new-born clusters. It is noteworthy that if the cluster born-process can be considered as a Possion process, the mean value of N can be considered as the born rate of dynamic clusters. In addition, the statistics extracted for the established dynamic model are summarized in Table E.4.

6 Conclusions

In this contribution, a millimeter-wave channel measurement campaign at 28-30 GHz was conducted along a pre-defined 48 m route in an indoor area from a hall to a corridor. Based on the estimation results using a high resolution parameter estimation (HPRE) algorithm, a novel cluster identification and track-

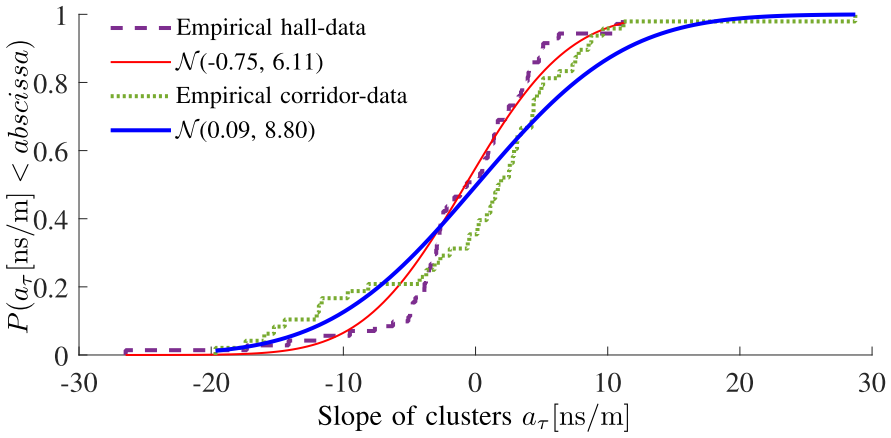

(a)

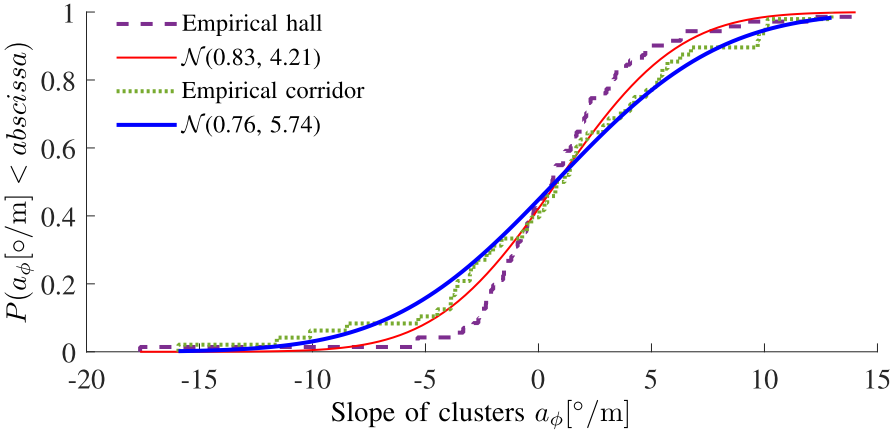

(b)

Fig. E.13: Empirical and fitted CDFs of the slope for the NLoS clusters in hall and corridor scenarios. (a) Delay domain a_τ. (b) Azimuth domain a_ϕ.

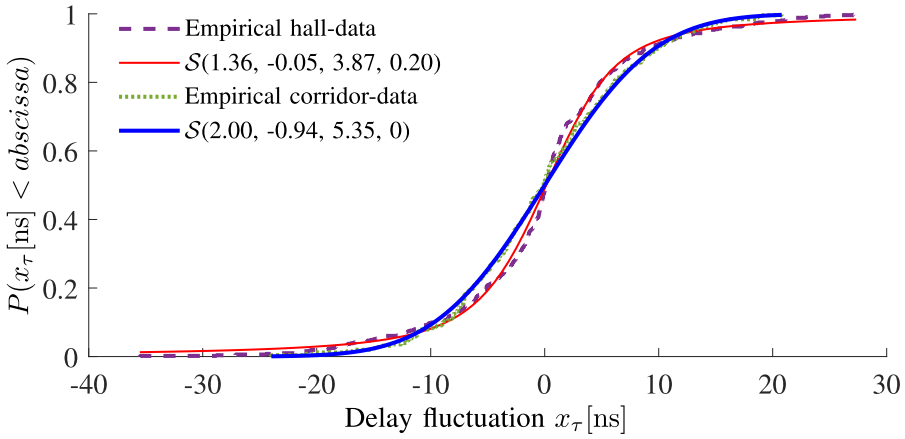

(a)

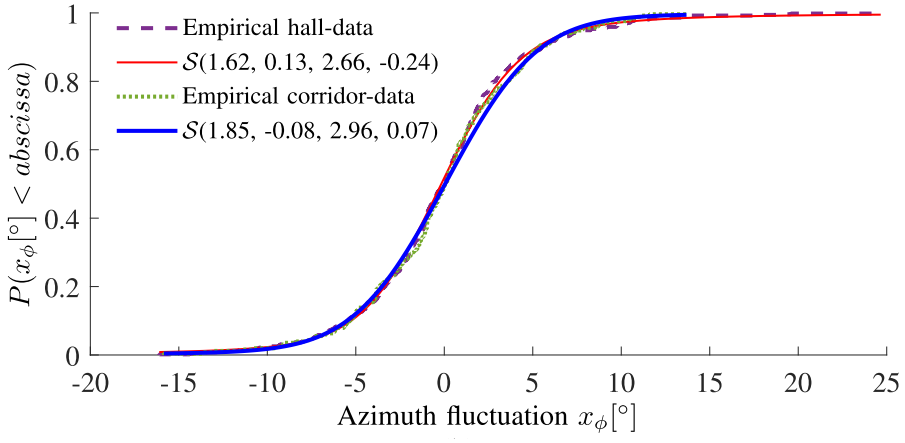

(b)

Fig. E.14: Empirical and fitted CDFs of the delay and azimuth fluctuation for NLoS clusters in hall and corridor scenarios. (a) Delay fluctuation x_τ. (b) Azimuth fluctuation x_ϕ

.

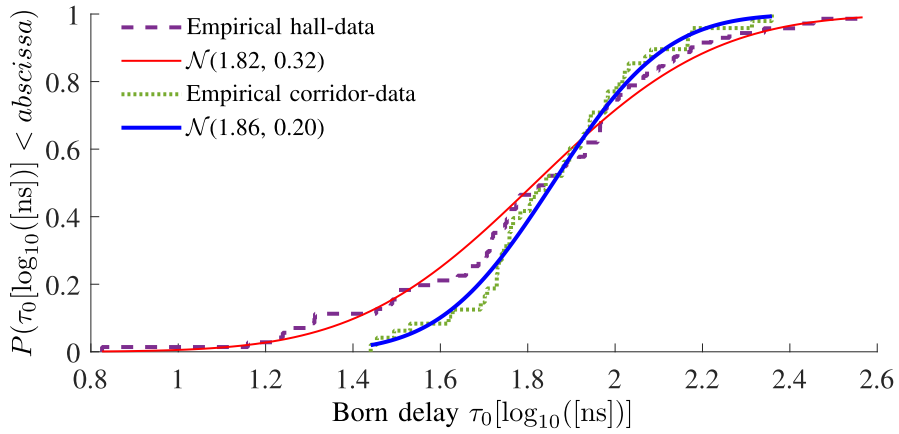

(a)

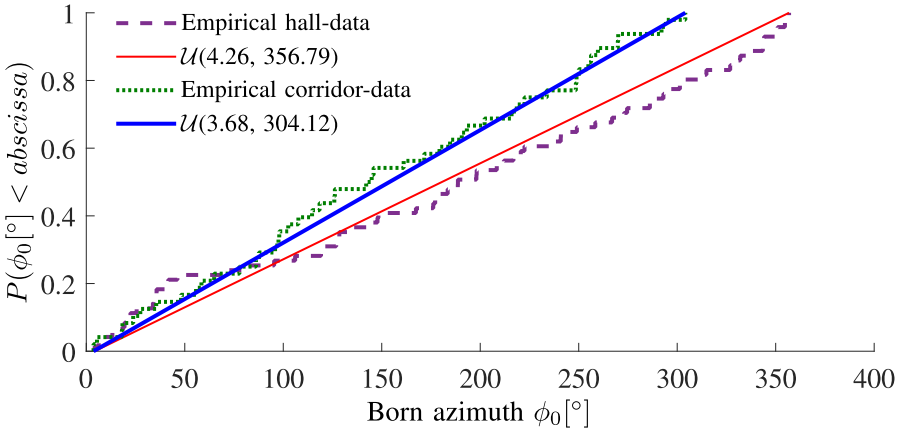

(b)

Fig. E.15: Empirical and fitted CDFs of the born delay and born azimuth for NLoS clusters in hall and corridor scenarios. (a) Born delay τ_0. (b) Born azimuth ϕ_0.

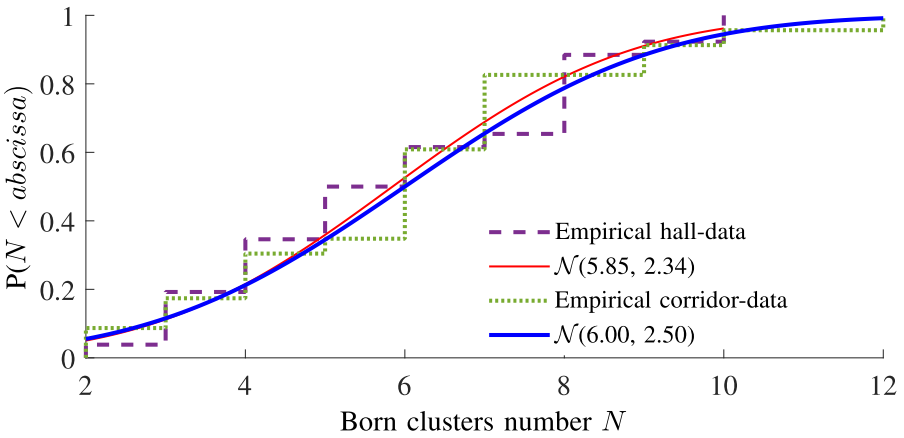

(a)

Fig. E.16: Empirical and fitted CDFs of the born clusters number at each position for NLoS clusters in hall and corridor.

Table E.4: Statistics extracted for the established dynamic model.

		Parmeters	Hall (Dist.; p-value)	Corridor (Dist.; p-value)
Composite level		$\sigma_\tau[\log_{10}([\text{ns}])]$	$\mathcal{N}(1.53, 0.19)$; 0.74	$\mathcal{N}(1.49, 0.10)$; 0.97
		$\sigma_\phi[\log_{10}([^\circ])]$	$\mathcal{N}(1.96, 0.10)$; 0.93	$\mathcal{N}(1.55, 0.09)$; 0.96
		$(\alpha, \beta, X_\sigma)$	(76.72, 0.96, 1.93)	(12.12, 5.90, 1.50)
Cluster level	LoS cluster	σ_{τ_c}[ns]	$\mathcal{N}(5.05, 1.15)$; 0.77	-
		$\sigma_{\phi_c}[^\circ]$	$\mathcal{N}(3.83, 1.91)$; 0.68	-
		$(\alpha, \beta, X_\sigma)$	(62.36, 1.81, 2.30)	-
	NLoS clusters	σ_{τ_c}[ns]	$\mathcal{N}(6.83, 4.08)$; 0.26	$\mathcal{N}(9.84, 4.39)$; 0.71
		$\sigma_{\phi_c}[^\circ]$	$\mathcal{N}(4.29, 2.28)$; 0.55	$\mathcal{N}(5.38, 2.32)$; 0.96
		$(\alpha, \beta, X_\sigma)$	(88.73, 0.93, 6.98)	(53.97, 3.66, 7.24)
Dynamic behavior		$d_s[\log_{10}([\text{m}])]$	$\mathcal{N}(0.61, 0.32)$; 0.04	$\mathcal{N}(0.51, 0.24)$; 0.02
		a_τ[ns/m]	$\mathcal{N}$(-0.75, 6.11); 0.11	$\mathcal{N}(0.09, 8.80)$; 0.17
		$a_\phi[^\circ/\text{m}]$	$\mathcal{N}(0.83, 4.21)$; 0.25	$\mathcal{N}(0.76, 5.74)$; 0.85
		x_τ[ns]	$\mathcal{S}(1.36, -0.05, 3.87, 0.20)$; 0.11	$\mathcal{S}(2.00, -0.94, 5.35, 0)$; 0.77
		$x_\phi[^\circ]$	$\mathcal{S}(1.62, 0.13, 2.66, -0.24)$; 0.76	$\mathcal{S}(1.85, -0.08, 2.96, 0.07)$; 0.59
		$\tau_0[\log_{10}([\text{ns}])]$	$\mathcal{N}(1.82, 0.32)$; 0.49	$\mathcal{N}(1.86, 0.20)$; 0.88
		$\phi_0[^\circ]$	$\mathcal{U}(4.26, 356.79)$; 0.37	$\mathcal{U}(3.68, 304.12)$; 0.95
		N	$\mathcal{N}(5.85, 2.34)$; 0.42	$\mathcal{N}(6.00, 2.50)$; 0.46

ing algorithm was exploited to trace dynamic clusters observed in the channel. The composite-level, cluster-level and "birth-death" behaviours were investigated. It has been found that the composite path loss exponent (PLE) in the corridor can be high as 5.9, while its counterpart in the hall can be as small as 0.96, which is possibly due to the large attenuation caused by the multiple reflections in the corridor. The mean composite delay spread in the hall is slightly larger than that observed in the corridor, both of which are around 30 ns. Meanwhile, the mean composite azimuth spread in the hall was observed much larger than that observed in the corridor, which are around 91° and 35°, respectively. However, the cluster delay spread and cluster azimuth spread in the hall scenario are smaller than that observed in the corridor, mostly due to the fact that the objects in the hall can cause dominant paths. Moreover, cluster power decay behaviors are very different among the line-of-sight (LoS) cluster, non-LoS (NLoS) clusters in the hall and NLoS clusters in the corridor. The cluster survival length in both hall and corridor scenarios can be well fitted with log-normal distributions, and the mean survival lengths in hall and corridor were found as around 4.07 m and 3.24 m, respectively. The cluster born delay and born azimuth in both scenarios were found to obey log-normal and uniform distributions, respectively. In addition, it has been found that the born rate of clusters are similar in both scenarios. The overall statistics can be found in Table E.4. The established dynamic model can provide valuable reference for evaluating the performance of 5G and beyond systems. Future works include further enhancing the model's ability by also including the dynamic behavious in the elevation domain, applying the proposed algorithm and analysis for outdoor propagation scenarios and adopting the developed dynamic cluster channel models for wireless system performance testing.

References

[1] M. Agiwal, A. Roy, and N. Saxena. Next generation 5G wireless networks: A comprehensive survey. *IEEE Communications Surveys Tutorials*, 18(3):1617–1655, thirdquarter 2016.

[2] J. G. Andrews, S. Buzzi, W. Choi, S. V. Hanly, A. Lozano, A. C. K. Soong, and J. C. Zhang. What will 5G be? *IEEE Journal on Selected Areas in Communications*, 32(6):1065–1082, June 2014.

[3] C. Wang, F. Haider, X. Gao, X. You, Y. Yang, D. Yuan, H. M. Aggoune, H. Haas, S. Fletcher, and E. Hepsaydir. Cellular architecture and key technologies for 5G wireless communication networks. *IEEE Communications Magazine*, 52(2):122–130, February 2014.

[4] A. Osseiran, F. Boccardi, V. Braun, K. Kusume, P. Marsch, M. Maternia, O. Queseth, M. Schellmann, H. Schotten, H. Taoka, H. Tullberg, M. A. Uusitalo, B. Timus, and M. Fallgren. Scenarios for 5G mobile and wireless communications: the vision of the METIS project. *IEEE Communications Magazine*, 52(5):26–35, May 2014.

[5] W. Roh, J. Seol, J. Park, B. Lee, J. Lee, Y. Kim, J. Cho, K. Cheun, and F. Aryanfar. Millimeter-wave beamforming as an enabling technology for 5G cellular communications: theoretical feasibility and prototype results. *IEEE Communications Magazine*, 52(2):106–113, February 2014.

[6] S. Sun, T. S. Rappaport, R. W. Heath, A. Nix, and S. Rangan. MIMO for millimeter-wave wireless communications: beamforming, spatial multiplexing, or both? *IEEE Communications Magazine*, 52(12):110–121, December 2014.

[7] Marco Giordani, Michele Polese, Arnab Roy, Douglas Castor, and Michele Zorzi. A tutorial on beam management for 3GPP NR at mmwave frequencies. *IEEE Communications Surveys and Tutorials*, 2019.

[8] L. Tian, V. Degli-Esposti, E. M. Vitucci, and X. Yin. Semi-deterministic radio channel modeling based on graph theory and ray-tracing. *IEEE Transactions on Antennas and Propagation*, 64(6):2475–2486, June 2016.

[9] B. Ai, K. Guan, R. He, J. Li, G. Li, D. He, Z. Zhong, and K. M. S. Huq. On indoor millimeter wave massive MIMO channels: Measurement and simulation. *IEEE Journal on Selected Areas in Communications*, 35(7):1678–1690, July 2017.

[10] D. He, B. Ai, M. Schmieder, Z. Zhong, J. Kim, B. Hui, H. Chung, I. Kim, and Y. Hao. Influence analysis of typical objects in rural railway environments at 28 GHz. *IEEE Transactions on Vehicular Technology*, 68(3):2066–2076, March 2019.

[11] S. Hur, S. Baek, B. Kim, Y. Chang, A. F. Molisch, T. S. Rappaport, K. Haneda, and J. Park. Proposal on millimeter-wave channel modeling for 5G cellular system. *IEEE Journal of Selected Topics in Signal Processing*, 10(3):454–469, April 2016.

[12] J. Chen, X. Yin, L. Tian, and M. Kim. Millimeter-wave channel modeling based on a unified propagation graph theory. *IEEE Communications Letters*, 21(2):246–249, Feb 2017.

[13] T. S. Rappaport, G. R. MacCartney, M. K. Samimi, and S. Sun. Wideband millimeter-wave propagation measurements and channel models for future wireless communication system design. *IEEE Transactions on Communications*, 63(9):3029–3056, Sep. 2015.

[14] G. R. Maccartney, T. S. Rappaport, M. K. Samimi, and S. Sun. Millimeter-wave omnidirectional path loss data for small cell 5G channel modeling. *IEEE Access*, 3:1573–1580, 2015.

[15] G. R. Maccartney, T. S. Rappaport, S. Sun, and S. Deng. Indoor office wideband millimeter-wave propagation measurements and channel models at 28 and 73 GHz for ultra-dense 5G wireless networks. *IEEE Access*, 3:2388–2424, 2015.

[16] C. Zhang, X. Yin, X. Cai, and Z. Yu. Wideband 39 GHz millimeter-wave channel measurements under diversified vegetation. In *2018 IEEE 29th Annual International Symposium on Personal, Indoor and Mobile Radio Communications (PIMRC)*, pages 1–6, Sep. 2018.

[17] C. Gustafson, K. Haneda, S. Wyne, and F. Tufvesson. On mm-wave multipath clustering and channel modeling. *IEEE Transactions on Antennas and Propagation*, 62(3):1445–1455, March 2014.

[18] C. Ling, X. Yin, R. Möller, S. Häfner, D. Dupleich, C. Schneider, J. Luo, H. Yan, and R. Thomä. Double-directional dual-polarimetric cluster-based characterization of 70-77 GHz indoor channels. *IEEE Transactions on Antennas and Propagation*, 66(2):857–870, Feb 2018.

[19] C. Ling, X. Yin, H. Wang, and R. S. Thomä. Experimental characterization and multipath cluster modeling for 13-17 GHz indoor propagation channels. *IEEE Transactions on Antennas and Propagation*, 65(12):6549–6561, Dec 2017.

[20] J. Blumenstein, A. Prokes, A. Chandra, T. Mikulasek, R. Marsalek, T. Zemen, and C. Mecklenbräuker. In-vehicle channel measurement, characterization, and spatial consistency comparison of 3-11 GHz and 55-65 GHz frequency bands. *IEEE Transactions on Vehicular Technology*, 66(5):3526–3537, May 2017.

[21] J. Huang, C. Wang, R. Feng, J. Sun, W. Zhang, and Y. Yang. Multi-frequency mmwave massive MIMO channel measurements and characterization for 5G wireless communication systems. *IEEE Journal on Selected Areas in Communications*, 35(7):1591–1605, July 2017.

[22] J. Li, B. Ai, R. He, M. Yang, and Z. Zhong. On modeling of dense multipath component for indoor massive MIMO channels. *IEEE Antennas and Wireless Propagation Letters*, 18(3):526–530, March 2019.

[23] F. Zhang and W. Fan. Near-field ultra-wideband mmwave channel characterization using successive cancellation beamspace UCA algorithm. *IEEE Transactions on Vehicular Technology*, 68(8):7248–7259, Aug 2019.

[24] S. Sangodoyin, V. Kristem, A. F. Molisch, R. He, F. Tufvesson, and H. M. Behairy. Statistical modeling of ultrawideband MIMO propagation channel in a warehouse environment. *IEEE Transactions on Antennas and Propagation*, 64(9):4049–4063, Sep. 2016.

[25] J. Chen, X. Yin, X. Cai, and S. Wang. Measurement-based massive MIMO channel modeling for outdoor LoS and NLoS environments. *IEEE Access*, 5:2126–2140, 2017.

[26] J. O. Nielsen, W. Fan, P. C. F. Eggers, and G. F. Pedersen. A channel sounder for massive MIMO and mmwave channels. *IEEE Communications Magazine*, 56(12):67–73, December 2018.

[27] S. Malkowsky, J. Vieira, L. Liu, P. Harris, K. Nieman, N. Kundargi, I. C. Wong, F. Tufvesson, V. Öwall, and O. Edfors. The world's first real-time testbed for massive MIMO: Design, implementation, and validation. *IEEE Access*, 5:9073–9088, 2017.

[28] P. Harris, S. Malkowsky, J. Vieira, E. Bengtsson, F. Tufvesson, W. B. Hasan, L. Liu, M. Beach, S. Armour, and O. Edfors. Performance characterization of a real-time massive MIMO system with LOS mobile channels. *IEEE Journal on Selected Areas in Communications*, 35(6):1244–1253, June 2017.

[29] L. Pometcu and R. D'Errico. Large scale and clusters characteristics in indoor sub-THz channels. In *IEEE 29th Annual International Symposium on Personal, Indoor and Mobile Radio Communications (PIMRC)*, pages 1405–1409, Sep. 2018.

[30] E. M. Vitucci, F. Yu, L. Possenti, M. Zoli, F. Fuschini, M. Barbiroli, V. Degli-Esposti, K. Guan, and T. Kürner. A study on dual-directional mm-wave indoor

channel characteristics. In *European Conference on Antennas and Propagation (EuCAP)*, pages 1–5, March 2019.

[31] X. Cai and W. Fan. A complexity-efficient high resolution propagation parameter estimation algorithm for ultra-wideband large-scale uniform circular array. *IEEE Transactions on Communications*, 67(8):5862–5874, Aug 2019.

[32] A. W. Mbugua, W. Fan, K. Olesen, X. Cai, and G. F. Pedersen. Phase-compensated optical fiber-based ultrawideband channel sounder. *IEEE Transactions on Microwave Theory and Techniques*, 68(2):636–647, 2020.

[33] W. Fan, A. W. Mbugua, X. Cai, and K. Olesen. Development and experimental validation of an ultra-wideband channel sounder. In *13th European Conference on Antennas and Propagation (EuCAP)*, pages 1–5, March 2019.

[34] A-INFO-SZ-2003000/P Datasheet. Technical report.

[35] S. S. Zhekov, A. Tatomirescu, and G. F. Pedersen. Antenna for ultrawideband channel sounding. *IEEE Antennas and Wireless Propagation Letters*, 16:692–695, 2017.

[36] H. Krim and M. Viberg. Two decades of array signal processing research: the parametric approach. *IEEE Signal Processing Magazine*, 13(4):67–94, Jul 1996.

[37] Constantine A Balanis. *Antenna theory: analysis and design*. 3rd ed. Hoboken, NJ, USA: Wiley, 2005.

[38] Y. Ji, W. Fan, and G. F. Pedersen. Channel characterization for wideband large-scale antenna systems based on a low-complexity maximum likelihood estimator. *IEEE Transactions on Wireless Communications*, 17(9):6018–6028, Sep. 2018.

[39] B. H. Fleury, M. Tschudin, R. Heddergott, D. Dahlhaus, and K. Ingeman Pedersen. Channel parameter estimation in mobile radio environments using the SAGE algorithm. *IEEE Journal on Selected Areas in Communications*, 17(3):434–450, Mar 1999.

[40] T. Moon. The expectation-maximization algorithm. *IEEE Signal Processing Magazine*, 1997.

[41] M. Feder and E. Weinstein. Parameter estimation of superimposed signals using the EM algorithm. *IEEE Transactions on Acoustics, Speech, and Signal Processing*, 36(4):477–489, April 1988.

[42] F. Zhang, W. Fan, and G. F. Pedersen. Frequency-invariant uniform circular array for wideband mm-wave channel characterization. *IEEE Antennas and Wireless Propagation Letters*, 16:641–644, 2017.

[43] N. Czink, R. Tian, S. Wyne, F. Tufvesson, J. Nuutinen, J. Ylitalo, E. Bonek, and A. F. Molisch. Tracking time-variant cluster parameters in mimo channel measurements. In *the second International Conference on Communications and Networking in China*, pages 1147–1151, Aug 2007.

[44] Jerome Friedman Trevor Hastie, Robert Tibshirani. *The Elements of Statistical Learning: Data Mining, Inference, and Prediction, Second Edition (Springer Series in Statistics)*. Springer Series in Statistics. Springer, 2nd ed. 2009. corr. 3rd printing edition, 2009.

[45] R. He, Q. Li, B. Ai, Y. L. Geng, A. F. Molisch, V. Kristem, Z. Zhong, and J. Yu. A kernel-power-density-based algorithm for channel multipath components clustering. *IEEE Transactions on Wireless Communications*, 16(11):7138–7151, Nov 2017.

[46] S. Cheng, M. Martinez-Ingles, D. P. Gaillot, J. Molina-Garcia-Pardo, M. Liénard, and P. Degauque. Performance of a novel automatic identification algorithm for the clustering of radio channel parameters. *IEEE Access*, 3:2252–2259, 2015.

[47] Martin Steinbauer, Huseyin Ozcelik, Helmut Hofstetter, Christoph F. Mecklenbrauker, and Ernst Bonek. How to quantify multipath separation. *IEICE Transactions on Electronics*, E85-C(3):552–557, Mar 2002.

[48] N. Czink, P. Cera, J. Salo, E. Bonek, J. . Nuutinen, and J. Ylitalo. Improving clustering performance using multipath component distance. *Electronics Letters*, 42(1):33–45, Jan 2006.

[49] U. Maulik and S. Bandyopadhyay. Performance evaluation of some clustering algorithms and validity indices. *IEEE Transactions on Pattern Analysis and Machine Intelligence*, 24(12):1650–1654, Dec 2002.

[50] Krzysztof Kryszczuk and Paul Hurley. Estimation of the number of clusters using multiple clustering validity indices. In Neamat El Gayar, Josef Kittler, and Fabio Roli, editors, *Multiple Classifier Systems*, pages 114–123, Berlin, Heidelberg, 2010. Springer Berlin Heidelberg.

[51] Malay K. Pakhira, Sanghamitra Bandyopadhyay, and Ujjwal Maulik. Validity index for crisp and fuzzy clusters. *Pattern Recognition*, 37(3):487 – 501, 2004.

[52] Study on channel model for frequencies from 0.5 to 100 GHz. Technical report, 3GPP TR 38.901 V15.0.0, Jun. 2018.

[53] Pekka Kyösti, Lassi Hentilä, Jukka Kyröläinen, Fengchun Zhang, Wei Fan, and Matti Latva-Aho. Emulating dynamic radio channels for radiated testing of massive MIMO devices. In *IET Conference Publications*, 2018.

[54] X. Cai, J. Rodríguez-Piñeiro, X. Yin, N. Wang, B. Ai, G. F. Pedersen, and A. P. Yuste. An empirical air-to-ground channel model based on passive measurements in LTE. *IEEE Transactions on Vehicular Technology*, 68(2):1140–1154, Feb 2019.

[55] X. Cai, B. Peng, X. Yin, and A. P. Yuste. Hough-transform-based cluster identification and modeling for V2V channels based on measurements. *IEEE Transactions on Vehicular Technology*, 67(5):3838–3852, May 2018.

[56] Frank J. Massey. The kolmogorov-smirnov test for goodness of fit. *Journal of the American Statistical Association*, 46(253), 1951.

[57] John P Nolan. Numerical calculation of stable densities and distribution functions. *Communications in statistics. Stochastic models*, 13(4):759–774, 1997.

Paper F

A Scatterer Localization Method Using Large-Scale Antenna Array Systems

Guojin Zhang, Xuesong Cai, Jesper Ødum Nielsen, Gert Frølund Pedersen and Fredrik Tufvesson

The paper has been published in the
IEEE Conference on Antenna Measurements and Applications (CAMA),
2022.

The layout has been revised.

Abstract

As ultra-massive multiple-input multiple-output (UM-MIMO) has emerged as a key technology for millimeter-wave and terahertz communications, the spherical wave propagation should be considered for channel modeling. Therefore, it is critical to identify the locations and evolving behaviors of scatterers, i.e., the sources of the spherical wavefronts. In this contribution, a novel space-alternating generalized expectation-maximization (SAGE) based scatterer localization algorithm is proposed, where a large-scale antenna array is divided into multiple sub-arrays. Due to the decreased aperture of each sub-array, plane wave assumption can be applied to estimate the angles of departure/arrival, delays and amplitudes of multipath components (MPCs). Based on the angle variations of MPCs observed at different sub-arrays, the corresponding scatterers can be located. The proposed algorithm is verified in a simulation using a large-scale uniform circular array (UCA) system. Moreover, we apply this algorithm to an indoor measurement campaign conducted at 27-29 GHz in a hall scenario. Dominant scatterers are identified, which can be used for the development of further geometry-based stochastic channel models.

1 Introduction

To establish realistic geometry-based stochastic channel models for ultra-massive multiple-input multiple-output (UM-MIMO) communications, it is necessary to consider spherical wave propagation [1–3]. In [4–6], under spherical wavefront assumption, propagation delays, angles of departure or arrival (AoD or AoA), amplitudes, and the distances from the array to the first or last hop scatterers of the multipath components (MPCs) are estimated using a whole large-scale antenna array. The locations of the scatterers were estimated by checking the distance and angular information. As the distances between the array and the first or last hop scatterers have to be considered in the estimation, it leads to high computational complexities. To decrease the complexity of the estimation algorithm, a novel scatterer localization method is proposed in this contribution, where a large-scale antenna array is divided into multiple sub-arrays, to make it feasible to estimate the parameters of the MPCs under the plane wave assumption. According to the estimated angles of MPCs observed at each sub-arrays, the corresponding locations of the scatterers can be estimated.

The performance of the proposed scatterer localization algorithm is verified by a simulation with a large-scale uniform circular array (UCA). Furthermore, the proposed algorithm is applied to a measurement campaign conducted in an indoor hall scenario at 27-29 GHz. Eleven consecutive elements are formed as a sub-array moving across the UCA. Due to the narrow beamwidths of the transmitter (Tx) and receiver (Rx) biconical antennas in elevation domain and that they were placed with the same height, we do not consider elevations in

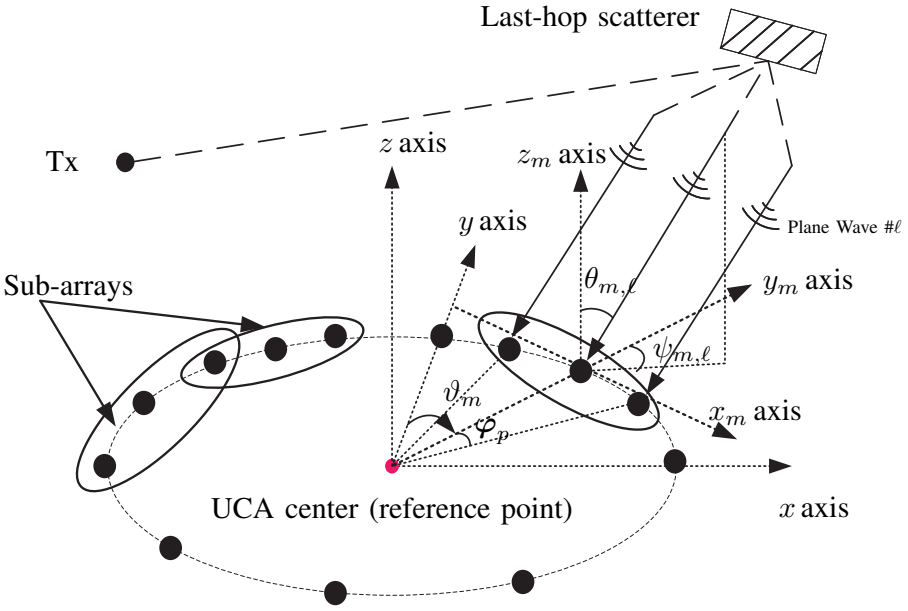

Fig. F.1: Sub-arrays moving across the UCA.

our estimation. The parameters, i.e., the delays, azimuths and amplitudes of the MPCs observed at each sub-array, are independently estimated using the space-alternating generalized expectation-maximization (SAGE) algorithm [7] under the plane wave assumption. Based on the azimuths of MPCs estimated at different sub-arrays, the scatterers are located using an iterative non-linear least squares algorithm, i.e. the Levenberg and Marquard algorithm [8]. The performance of the proposed scatterer localization method is verified by mapping the estimated scatterers to the real physical objects in the indoor hall scenario. Moreover, with the estimated parameters obtained from each sub-array across the whole UCA, the spatial non-stationary for the large-scale array can also be observed.

The rest of the paper is organized as follows. Sect. 2 presents the signal model and the proposed scatterer localization algorithm. In Sect. 3, simulation results in a line-of-sight (LoS) scenario are elaborated to evaluate the performance of the proposed algorithm. Moreover, the measurement campaign conducted in the indoor hall scenario and measurement-based estimation results are presented in Sect. 4. Finally, conclusive remarks are included in Sect. 5.

2 Signal model and scatterer localization

To apply the SAGE algorithm with the plane wavefront assumption, let us consider a UCA with M elements that is divided into multiple sliding sub-arrays as shown in Fig. F.1. The mth sub-array contains P elements with its center as the mth element of the UCA, resulting in a total number of M sub-arrays. The UCA with a radius r is located in the x-y-z plane, with its center as the origin. The mth sub-array is located in its local x_m-y_m-z_m plane, with the center of the sub-array as the origin. The angle between x and x_m is $\vartheta_m = \frac{2\pi m}{M}$. A finite number of L_m plane waves are assumed to impinge into the mth sub-array. in the x_m-y_m-z_m coordinate system, the complex amplitude, delay, azimuth and elevation of the ℓth path that impinges into the mth sub-array are denoted as $\alpha_{m,\ell}$, $\tau_{m,\ell}$, $\psi_{m,\ell}$, $\theta_{m,\ell}$, respectively. The direction vector $\mathbf{\Omega}_{m,\ell}$ can be written as

$$\mathbf{\Omega}_{m,\ell} = [\sin\theta_{m,\ell}\sin\psi_{m,\ell},\ \sin\theta_{m,\ell}\cos\psi_{m,\ell},\ \sin\theta_{m,\ell}]^T. \tag{F.1}$$

The coordinate $\mathbf{S}_{m,p}$ of the pth array element of the mth sub-array in the x_m-y_m-z_m system can be written as

$$\mathbf{S}_{m,p} = [r\sin\boldsymbol{\varphi}_p,\ -r + r\cos\boldsymbol{\varphi}_p,\ 0]^T \tag{F.2}$$

where $\boldsymbol{\varphi}_p$ denotes the angle between the pth array element and the center of the sub-array. The channel transfer functions $\mathbf{H}_{m,\ell}(\mathbf{f})$ of the ℓth path at the reference point (the center of the mth sub-array) in the frequency range $\mathbf{f}$ can be described as

$$\mathbf{H}_{m,\ell}(\mathbf{f}) = \alpha_{m,\ell}e^{-j2\pi\mathbf{f}\tau_{m,\ell}} \tag{F.3}$$

where $\mathbf{f} = [f_1, \ldots, f_N]$ contains N frequency points that sweep the bandwidth of interest. Due to the propagation distance difference between the reference point and the pth element, the frequency response $\mathbf{H}^p_{m,\ell}(\mathbf{f})$ at the pth element can be described as

$$\mathbf{H}^p_{m,\ell}(\mathbf{f}) = \mathbf{H}_{m,\ell}(\mathbf{f}) \odot e^{j2\pi\mathbf{f}(\frac{\mathbf{\Omega}_{m,\ell}\cdot\mathbf{S}^T_{m,p}}{c})} \tag{F.4}$$

where c is the speed of light and $\odot$ means the element-wise product. The signal $\mathbf{H}(\mathbf{f};\mathbf{\Psi}_{m,\ell})$ contributed by the ℓth path for the mth sub-array can be described as

$$\mathbf{H}_m(\mathbf{f};\mathbf{\Psi}_{m,\ell}) = [\mathbf{H}^1_{m,\ell}, \ldots, \mathbf{H}^P_{m,\ell}]^T. \tag{F.5}$$

The output of the mth sub-array contributed by all the L_m MPCs can be written as

$$\mathbf{H}_m(\mathbf{f};\mathbf{\Psi}_m) = \sum_{\ell=1}^{L_m}\mathbf{H}_m(\mathbf{f};\mathbf{\Psi}_{m,\ell}) + \mathbf{N}(\mathbf{f}) \tag{F.6}$$

where $\mathbf{N}(\mathbf{f})$ denotes complex Gaussian noise. With the signal model above, the SAGE algorithm is applied independently to estimate the propagation param-

eter set $\mathbf{\Psi}_m = [\alpha_{m,\ell}, \tau_{m,\ell}, \psi_{m,\ell}, \theta_{m,\ell}; \ell = 1, \ldots, L_m]$ of the MPCs for the mth sub-array in the x_m-y_m coordinate system[1].

Based on the SAGE estimation results, a multipath-component-distance (MCD) threshold method [9] is applied to associate the estimated paths at different sub-arrays using their delay and angular information, since the same path could experience death-birth behaviour across the large aperture of the whole array. Note that the estimated azimuth angle $\hat{\psi}_{m,\ell}$ in the local coordinate system is converted to the angle $\hat{\phi}_{m,\ell}$ in the global system as $\hat{\phi}_{m,\ell} = \hat{\psi}_{m,\ell} + \vartheta_m$ for path association/tracking. Based on the path tracking results (e.g., as shown in Fig. F.5), the locations of scatterers are obtained using an iterative non-linear least squares algorithm, i.e. the Levenberg and Marquard algorithm [8] as follows.

For an associated path with its azimuths and elevations at different sub-arrays estimated as $\hat{\phi}_{m,\ell}$ and $\hat{\theta}_{m,\ell}$, let us denote the location of the corresponding scatterer in x-y-z system as $\mathbf{V}_\ell$. The location vector of sub-array centers is known as $\mathbf{R}_m$. Then, in x-y-z system the ground-truth unit vector of the direction of arrival $\mathbf{\Theta}_{m,\ell}$ of the ℓth path observed at the mth sub-array can be calculated as

$$\mathbf{\Theta}_{m,\ell} = \frac{\mathbf{V}_\ell - \mathbf{R}_m}{\|\mathbf{V}_\ell - \mathbf{R}_m\|} \tag{F.7}$$

The unknown location $\mathbf{V}_\ell$ can be obtained by minimizing the cost function

$$c(\mathbf{V}_\ell) = \Sigma_m(\hat{\mathbf{\Theta}}_{m,\ell} - \mathbf{\Theta}_{m,\ell})^T(\hat{\mathbf{\Theta}}_{m,\ell} - \mathbf{\Theta}_{m,\ell}) \tag{F.8}$$

as

$$\hat{\mathbf{V}}_\ell = \arg\min_{\mathbf{V}_\ell} c(\mathbf{V}_\ell) \tag{F.9}$$

where $\hat{\mathbf{\Theta}}_{m,\ell}$ is the estimated direction vector of arrival according to $\hat{\phi}_{m,\ell}$ and $\hat{\theta}_{m,\ell}$.

3 Simulation

To evaluate the performance of the proposed scatterer localization algorithm, a simulation of a LoS scenario is considered. A UCA is used as the Rx side, and a single antenna as the Tx side. The radius of the UCA is set as 0.24 m. The distance between Tx and the UCA center is set as 3.75 m. The delay, azimuth, elevation, and amplitude of incident wave towards the center of the UCA are set as 12.5 ns, 40 °, 90 ° and 1, respectively. In the simulations, both P=3 and P=11 are considered to investigate the effect of sub-array sizes. Moreover, signal-to-noise ratios (SNRs) of 30 dB and infinite (i.e., no noise) are considered. The estimated azimuths $\hat{\psi}_{m,\ell}$ in local coordinate system and azimuths

[1] As mentioned earlier, we consider 2D transmission in this paper. However, to generalize the signal model, we have elevation angels throughout this section.

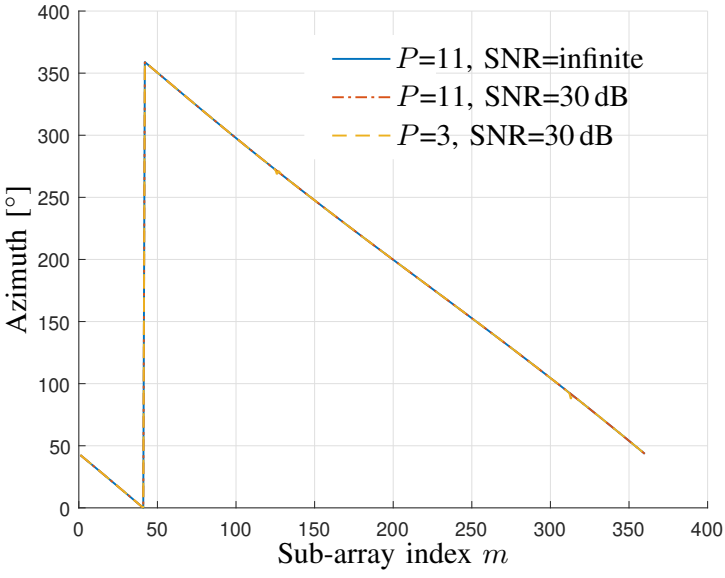

(a)

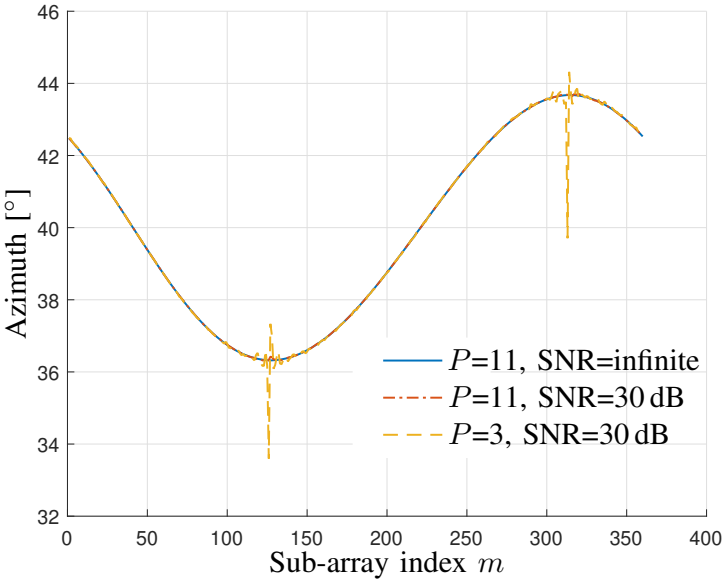

(b)

Fig. F.2: The estimated azimuths $\hat{\psi}_{m,\ell}$ and azimuths $\hat{\phi}_{m,\ell}$ obtained at each sub-array in the simulation. (a) Estimated azimuths $\hat{\psi}_{m,\ell}$ in local coordinate system. (b) Estimated azimuths $\hat{\phi}_{m,\ell}$ in global system.

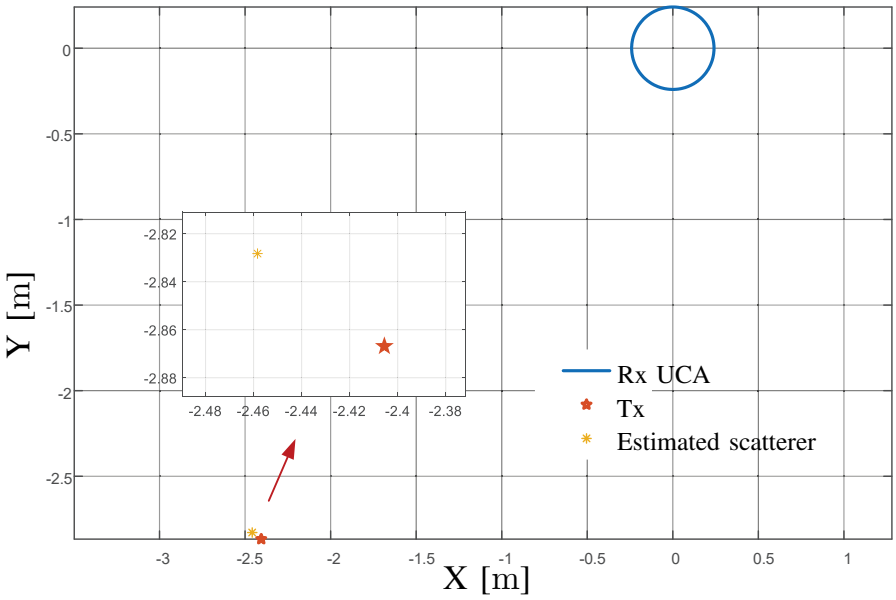

Fig. F.3: Simulation with noise data for the scatterer localization of LoS scenario.

$\hat{\phi}_{m,\ell}$ in global system obtained at each sub-array are shown in Fig. F.2(a) and Fig. F.2(b). In Fig. F.2(a), it can be observed that the estimated azimuth $\hat{\psi}_{m,\ell}$ decreases 1° as the center of the sub-array moves one element, which is reasonable according to the geometry. It can also be observed that the trajectory of azimuths $\hat{\phi}_{m,\ell}$ is a sine-alike shape in Fig. F.2(b), which is caused by the near-field effect as expected. Significant fluctuations of estimated azimuths are observed in the noisy situation. It is caused by the fact that the accuracy of angular estimation decreases, as the direction of the incident waves are parallel to the sub-array, leading to larger estimation error. Moreover, it can be found that the estimation accuracy is significantly affected by the noise, especially with a smaller number of elements within each sub-array. Considering the Rayleigh distance, the number of the elements within a sub-array should be less than nineteen, if the nearest scatter is two meters away. Therefore, to balance the accuracy of the estimation and effects of the near field, eleven consecutive virtual elements are practically chosen as a sub-array for the scatterer localization. According to the azimuths $\hat{\phi}_{m,\ell}$ in global system and the location of each sub-array, the location of the last hop scatterer (Tx antenna position here) is estimated as shown in Fig. F.3. The distance errors between the estimated scatterer and Tx antenna are 0.0655 m and 0.0654 m, in the noisy and noise free cases, respectively. One may expect that the estimation accuracy should be zero in the noise free situation. In fact, the non-zero error is because of the model mismatch herein. In other words, when the scattterer is too near to the sub-array (e.g., as shown in this simulation), near field propagation still

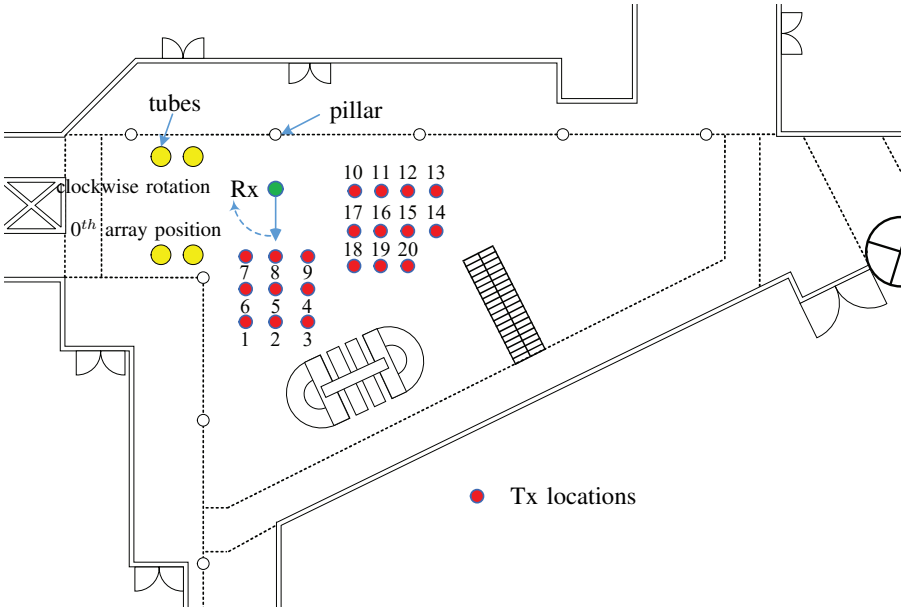

Fig. F.4: The top-view of the hall scenario.

exist. Therefore, in our future work, we will investigate the suitable number of antennas used in one sub-array more comprehensively.

4 Measurement

A measurement campaign was conducted in an indoor hall scenario at 27-29 GHz as illustrated in Fig. F.4. A vector network analyzer (VNA)-based channel sounder [10] was used to collect channel transfer functions. Four yellow ventilation tubes (marked as yellow circles) and six white pillars (marked as white circles) are located in the hall scenario. The shape of the hall is irregular and the dimension is approximately $39\times20\times10$ m^3. A commercial biconical antenna SZ-2003000/P [11] and a homemade biconical antenna [12] were utilized as the Tx and Rx antennas, respectively. The heights of the Tx and Rx antennas are both 1.50 m. A total of 20 snapshots were recorded by moving the Tx antenna 1 m apart. For each Tx position, the Rx antenna was rotated clockwise to form a large-scale UCA with a radius of r=0.24 m. For each snapshot, N=750 frequency points were swept. M=360 UCA elements were collected by the VNA.

Using the SAGE algorithm and the MCD threshold tracking method, the examples of the tracking results in delay and angular domain obtained from the measurement at Tx position 5 are shown in Fig. F.5(a) and Fig. F.5(b), respec-

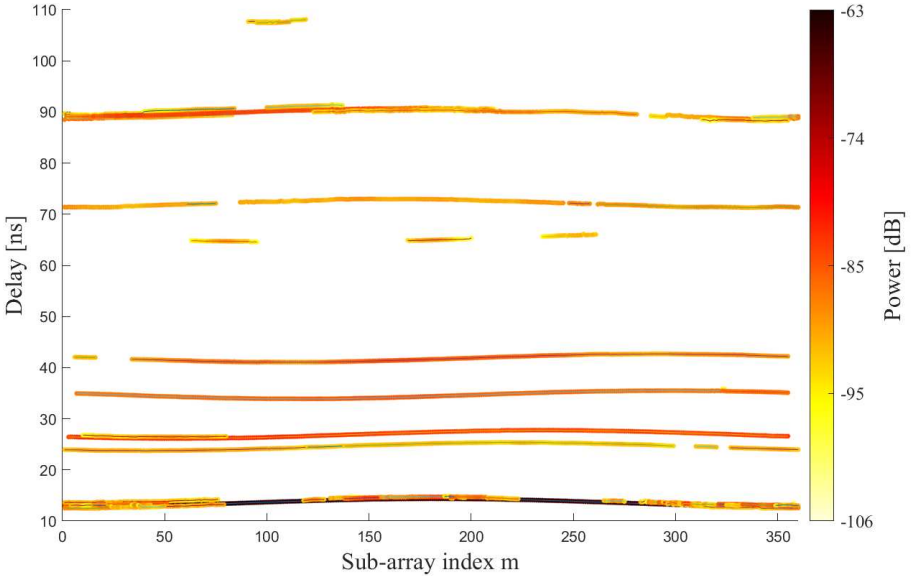

(a)

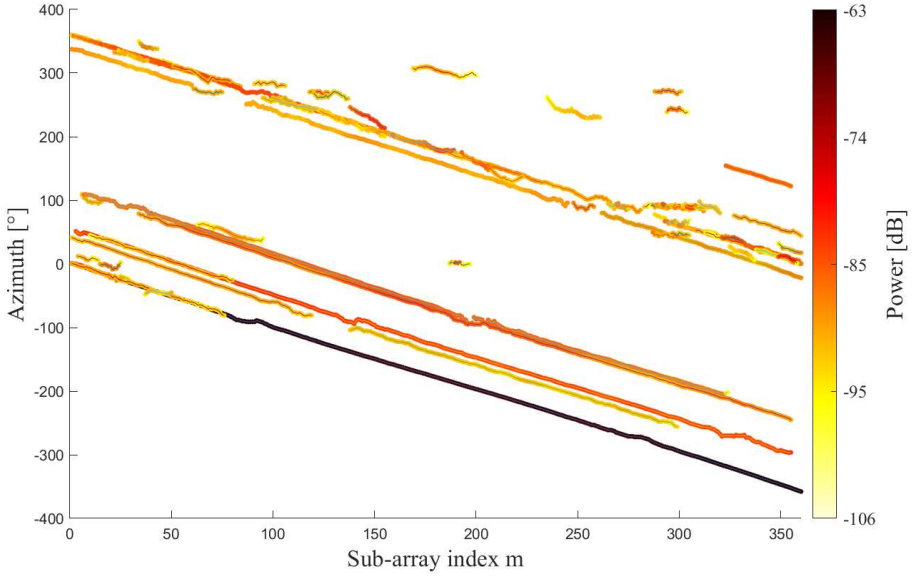

(b)

Fig. F.5: Path tracking/association results in the measurement campaign. (a) Delay domain. (b) Azimuth domain.

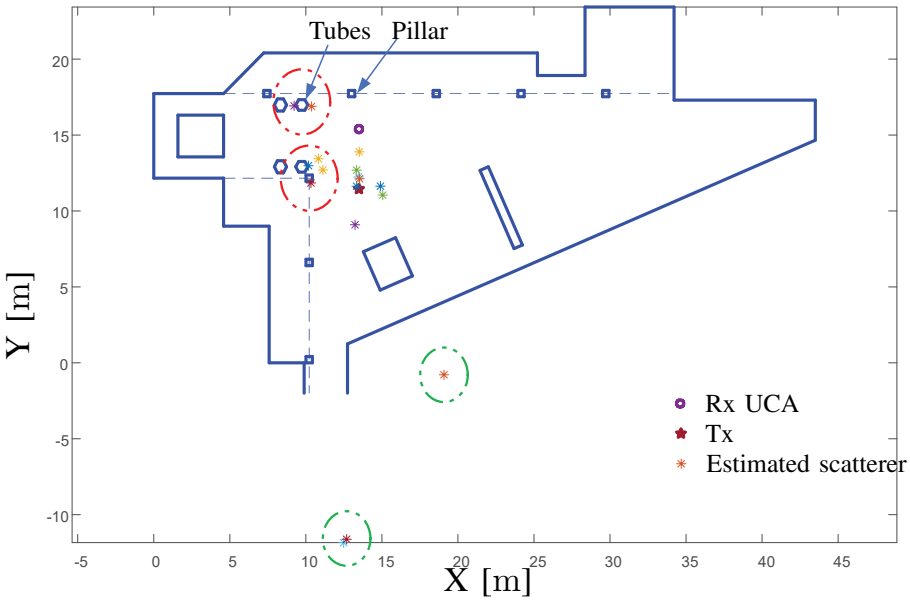

Fig. F.6: The map of the hall scenario with physical objects and the estimated last hop scatterers obtained from the measurements.

tively. The spatial non-stationary across the elements of the large-scale array can be observed. The locations of the last hop scatterers are estimated as shown in Fig. F.6, which shows a good match with actual physical objects. For example, some scatterers (highlighted by red circles) are identified closely around the tubes and the pillars. Furthermore, it is also observed that some scatterers (highlighted by green circles) are located outside the hall, which are called "virtual scatterers". These scatterers are probably due to specular reflections from smooth surfaces, resulting in the mirror positions of Tx.

5 Conclusions

A novel space-alternating generalized expectation-maximization (SAGE) based scatterer localization algorithm is proposed. The large-scale antenna array is divided into multiple sub-arrays. Plane wave propagation parameters, i.e., amplitudes, delays and directions of departure/arrival, of the multipath components (MPCs) impinging to each sub-array are estimated independently using the SAGE algorithm. Using the estimated angles and the locations of each sub-array, the locations of scatterers can be estimated. The performance of the proposed algorithm is verified in the simulation. Moreover, the estimated scatterers in the measurement campaign shows consistency to the actually physical objects. Future work will investigate the optimal number of antennas in a sub-

array, and establish scatterer-based channel models. Moreover, computational complexity of the proposed algorithm will be compared with that of the method using the entire array under spherical-wave assumption.

References

[1] X. Cai and W. Fan. A Complexity-Efficient High Resolution Propagation Parameter Estimation Algorithm for Ultra-Wideband Large-Scale Uniform Circular Array. *IEEE Transactions on Communications*, 67(8):5862–5874, Aug 2019.

[2] Y. Ji, W. Fan, and G. F. Pedersen. Near-Field Signal Model for Large-Scale Uniform Circular Array and Its Experimental Validation. *IEEE Antennas and Wireless Propagation Letters*, 16:1237–1240, 2017.

[3] Xuesong Cai, Wei Fan, Xuefeng Yin, and Gert Frølund Pedersen. Trajectory-Aided Maximum-Likelihood Algorithm for Channel Parameter Estimation in Ultrawideband Large-Scale Arrays. *IEEE Transactions on Antennas and Propagation*, 68(10):7131–7143, 2020.

[4] X. Yin, S. Wang, N. Zhang, and B. Ai. Scatterer Localization Using Large-Scale Antenna Arrays Based on a Spherical Wave-Front Parametric Model. *IEEE Transactions on Wireless Communications*, 16(10):6543–6556, Oct 2017.

[5] J. Chen, S. Wang, and X. Yin. A Spherical-Wavefront-Based Scatterer Localization Algorithm Using Large-Scale Antenna Arrays. *IEEE Communications Letters*, 20(9):1796–1799, Sept 2016.

[6] Yilin Ji, Johannes Hejselbæk, Wei Fan, and Gert F. Pedersen. A Map-Free Indoor Localization Method Using Ultrawideband Large-Scale Array Systems. *IEEE Antennas and Wireless Propagation Letters*, 17(9):1682–1686, 2018.

[7] B. H. Fleury, M. Tschudin, R. Heddergott, D. Dahlhaus, and K. Ingeman Pedersen. Channel Parameter Estimation in Mobile Radio Environments Using the SAGE Algorithm. *IEEE Journal on Selected Areas in Communications*, 17(3):434–450, Mar 1999.

[8] Martin Schmidhammer, Christian Gentner, and Benjamin Siebler. Localization of Discrete Mobile Scatterers in Vehicular Environments Using Delay Estimates. In *2019 International Conference on Localization and GNSS (ICL-GNSS)*, pages 1–6, 2019.

[9] Xuesong Cai, Guojin Zhang, Chao Zhang, Wei Fan, Jinxing Li, and Gert Frølund Pedersen. Dynamic Channel Modeling for Indoor Millimeter-Wave Propagation Channels Based on Measurements. *IEEE Transactions on Communications*, 68(9):5878–5891, 2020.

[10] Johannes Hejselbaek, Wei Fan, and Gert F. Pedersen. Ultrawideband VNA based channel sounding system for centimetre and millimetre wave bands. In *2016 IEEE 27th Annual International Symposium on Personal, Indoor, and Mobile Radio Communications (PIMRC)*, pages 1–6, 2016.

[11] LB-SJ-180400-KF Datasheet. Technical report.

[12] S. S. Zhekov, A. Tatomirescu, and G. F. Pedersen. Antenna for Ultrawideband Channel Sounding. *IEEE Antennas and Wireless Propagation Letters*, 16:692–695, 2017.

ISSN (online): 2446-1628
ISBN (online): 978-87-7573-708-6

AALBORG UNIVERSITY PRESS